Advances in Signal Processing for Non Destructive Evaluation of Materials

Proceedings of the VIth International Workshop

and of

NDT in Canada 2009

J. Baron, D. Craig, X. P. V. Maldague, Editors

É. du CAO

à la frontière des connaissances
at the cutting edge of knowledge

publié par:

X. Maldague
É. du CAO
38, Chemin du Cap-aux-Oies
Les Éboulements (Québec)
CANADA
G0A 2M0

ISBN 978-2-9809199-2-3

Dépôt légal - Bibliothèque nationale du Québec, 2010
Dépôt légal - Bibliothèque et Archives Canada, 2010

Imprimé au Canada
Printed in Canada

Table of contents

Message from the « NDT in Canada 2009 » Conference Chair

On behalf of the Organizing Committee I would like to welcome everyone to « NDT in Canada 2009 » - our first National Conference dedicated to a broad spectrum of NDE issues, ideas and applications. The Conference is jam-packed with events and information from leading edge R & D papers, papers dedicated to application of methods and techniques, workshops on failure analysis, ground penetrating radar applied to concrete structures and phased array ultrasonics plus an extensive array of vendors exhibiting their latest instruments, equipment and services. Clearly, there is something for all those with an interest in NDT.

We are seeing revolutionary change in NDT technologies, largely driven by developments in digital signal processing, computer control and the ability to store immense amounts of data in small packages. Such rapid change provides both opportunities and challenges. Opportunities in the way of doing things faster, smarter and cheaper; challenges in terms of being able to exploit the latest developments to their full capability. This Conference facilitates consideration of both the opportunities and the challenges.

We hope that you find this important Conference a fulfilling and rewarding event.

John Baron
Chair, NDT in Canada 2009

Preface

The 6th International Workshop on *Advances in Signal Processing for Non Destructive Evaluation of Materials* was held August 24 - 27, 2009, in London (Ontario), Canada. This Proceedings volume includes most of the presentations given at the Workshop. Interestingly, the 6th International Workshop was held jointly with the First «***NDT in Canada 2009***» Conference. This global event was admirably organized by the *Canadian Institute for NDE* (CINDE). In fact Proceedings are available either through CINDE or through the 6th International Workshop organization and besides some details they are both the same and include the two tracks *Advances in Signal Processing for Non Destructive Evaluation of Materials* and *NDT Technology and Applications*.

Scientific content

Non Destructive Evaluation (NDE) is playing an increasing role in our modern global economy. For instance NDE is essential in various safety sensitive industries such as in power generation, aerospace, manufacturing. The complexity of the inspection task and the requirement for higher quality standards impose more operator-assisted or fully-automated signal processing NDE stations. This event had the particular goal to bring together people from both fields of expertise: NDE and signal processing with the underlying idea to stimulate mutual cross-fertilization, for instance through the mix of papers from both fields in tracks.

Ideal production processes should only produce quality, consequently there should be no need for NDE. In fact, NDE is an added cost to the industry and there is an economic trade-off which opposes costs for increased NDE processing to traditional procedures: added procedures and processing should pay for themselves if to be accepted by the industry. NDE solutions must then always be realistic, fast, robust and cost-effective.

On the signal processing side, advanced algorithms for data extraction and processing, specialized techniques such as wavelets, inverse reconstruction, image processing emerge strongly to handle complex problems. In fact, it appears that in many fields, thanks to quantitative reliability, the technology is now mature for plant floor applications, especially with the availability of number-crunching digital computers combined with sensitive sensors, such deployment is possible thanks to rigorous reliability studies and dedicated modeling.

On the NDE side, enhanced techniques are emerging with for instance innovative applications of laser ultrasonics, ultrasonics phase arrays, acoustic pulse reflectometry among others. More traditional NDE techniques such as eddy currents, ultrasonics, X rays or infrared techniques are expanding with availability of finer quantitative diagnosis and internal specimen reconstruction based on inverse methodologies.

The event was organized with a double track (Tracks 1 and 2) over two and half days (as part of *NDT in Canada 2009* as stated above). With the success of the 6th Workshop edition, another International *Workshop is already planned*: the **7th International Workshop**, four years from now, in **August 2013**! The Seventh Workshop is expected to report on emerging techniques and new developments. This should further encourage the many exchanges that are a landmark of this meeting. In fact, this specificity of the Workshop has always been found to be one of its strongest aspect. Information about the Workshops is available on the web site located at:

http://intl.gel.ulaval.ca/

On the agenda this year for the third time, was the *International Workshop best presentation Award*: Dr. W. Weber was selected to receive the 2009 Award (see p. *xii*).

International Workshop Context

The *VIth Workshop* edition has deep grounds since we have to go back in August 1993 when the *II*nd *Workshop* took place, on Université Laval's (Quebec City, Quebec) campus. At the wrap-up session, attendees were quite enthusiastic about a Workshop Series with editions to be held every four years. Hence the *Vth Workshop* took place in 2005, *IVth Workshop* took place in 2001 and the *III*rd *Workshop* was held in 1997 commemorating the tenth anniversary of the *I*st *Workshop* which was organized in August 1987 by Professor Chen of the Southeastern Massachusetts University in Lac Beauport, a nice resort area located in the hills, at some 20 minutes North of Québec City. Besides the VIth edition held in London (Ontario), all the Workshops took place in Quebec City (Quebec).

For the 6th edition, the support of the *Canadian Institute for NDE* (CINDE) was much appreciated, particularly of J. Baron, L. Cote, D. Craig, D. Marshall. Mr. J. Baron chaired the *NDT in Canada 2009* Conference. Mr. Cote is Managing Director of CINDE. Mr. Craig chaired the "NDT Technology and Applications" track. Mr. Marshall is Director of CINDE. Many other people contributed to make the event a big success and we thank them all, particularly the members of the *NDT in Canada 2009* Organizing Committee: J. Baron, L. Cote, D. Craig, B. Delong, D. Domenichini, C. Finley, P. Kaszuba, D. Luey, D. Marshall, R. Robichaud, E. Sjerve, J. Zirnhelt.

More than one hundred (106 to be exact) people attended this combined event *NDT in Canada 2009 / 6th International Workshop* with a nice exhibition of 17 booths. These are interesting figures revealing the interest of the community in such gathering, especially considering the bad economic situation of 2009.

A special thank is also due to all participants for their kind cooperation and participation which was *essential* to the success of the meeting. Primary was also the efforts of the International Scientific Committee members.

Finally, on behalf of all those who helped to make the conference *NDT in Canada 2009* and the *6th International Workshop* a success, I sincerely wish these Proceedings will bring new ideas, and will help a little the progress of Mankind towards a better world, a flawless world!

See you in 2013!

Prof. Xavier P. V. Maldague
VIth International Workshop Director
August 2009

6th International Workshop - Scientific Committee

• N. Avdelidis	Hellenic Aerospace Industry,	Athens, **Greece**
• A. Bendada	Université Laval, Elect. & Comp. Eng. Dept.,	Québec, **Canada**
• P. Bison	National Research Council - ITEF,	Padova, **Italy**
• J. F. Bussière	Industrial Materials Institute - NRC,	Boucherville, **Canada**
• E. Grinzato	National Research Council - ITEF,	Padova, **Italy**
• D. Lévesque	Industrial Materials Institute - NRC,	Boucherville, **Canada**
• R. Maev	IRAMC - University of Windsor,	Windsor, **Canada**
• X. Maldague	Université Laval, Elect. & Comp. Eng. Dept.,	Québec, **Canada**
• A. Mandelis	CADIFT - University of Toronto,	Toronto, **Canada**
• S. Marinetti	Istituto per le Tecnologie della Costruzione, CNR,	Padova, **Italy**
• C. Müeller	Federal Institute for Materials Research and Testing,	Berlin, **Germany**
• H.G. Walther	Institut für Optik und Quantenelektronik,	Jena, **Germany**

International Workshop 2009
Best Presentation Award

presented to

Dr. W. Weber

from

Utex Canada

for the excellence of his presentation :

Advanced Ultrasonic Inspection Systems

Picture (left to right): X. Maldague, M. Klein and W. Weber (holding the Award plate).

The *Best Presentation Award*, instituted in 2001, materializes the strong dedication of the Workshop to excellence. It is awarded to the best presentation. Selection proceeds through a secret polling with all attendees being invited to cast their vote at the end of the event.

Keynote talk

Keynote Speaker: Dr. Eric Sjerve

Eric Sjerve has a B.Sc. in honours Physics from the University of British Columbia (1990), and a Ph.D. from the University of Toronto in the area of applied laser physics (1996). His Ph.D. thesis involved an experimental and theoretical investigation of polarization dynamics in gas laser systems under the influence of external magnetic fields. He has been involved with commercialization of NDT technology for over ten years, primarily in the petrochemical sector in Western Canada. This time has primarily been spent working on practically-oriented technique developmenf for field usage in a variety of different NDT mefhods such as automated ultrasonic testing, computed radiography and EMAT inspection. He is also the chairman of ISO TC 135 in Canada and for the past six years has been chairman of fhe IIW sub-commission VC on ultrasonic testing of welds. The IIW work has been focused on publication of IIW Handbooks on automated ultrasonic testing, austenitic weld inspection and phased arrays, with future work involved in standardization of phased array ultrasonic inspection techniques. He has written and presented over 30 papers in NDT. His position at IRISNDT is currently vice president working in the areas of fechnology development and mentoring the operational groups.

The Evolution of NDT

Non-destructive testing (NDT) is a discipline that is used to detect the presence of discontinuities in components, with the end goal of determining their fitness for service. This has primarily been done using the five basic Canadian General Standards Board NDT methods:
radiographic testing, ultrasonic testing, magnetic particle testing, liquid penetrant testing and eddy current testing. This NDT structure has been in place for many years providing quality assurance across many industries.

Currently, this structure is in a state of flux as new NDT technologies and ideas about quality assurance are entering into the NDT field. This process is being driven by the introduction of computerized systems, by new physical concepts that are being used to detect degradation and by novel ways of providing quality assurance. The result is that the process of delivering NDT products is rapidly changing.

This talk will provide some background on this transition, drawing examples from a variety of industries and their novel use of NDT technologies and signal processing techniques. The issue of probability of detection and confidence intervals will be discussed, in the context of how merging multiple NDT technologies can improve these techniques.

Track 1

Advances in Signal Processing for Non Destructive Evaluation of Materials

Trackleader - Xavier Maldague, Université Laval

Xavier Maldague, Ph. D., P. Eng. is professor at the Department of Electrical and Computing Engineering of Université Laval, Québec City, Canada. He has trained over 50 graduate students (M.Sc. and Ph.D.) with more than 300 publications. His research interests are in infrared thermography, NonDestructive Evaluation (NDE) techniques and vision / digital systems for industrial inspection. Since 2004, he has held a Tier 1 Canada Research Chair in Infrared Vision. In 2009, he was elected Fellow of the Engineering Institute of Canada (FEIC). He is active in several (international) organizations working in infrared NDE, such as CINDE, ASNT, SPIE Thermosense, QIRT among others. He launched the “International Workshop Advances in Signal Processing for Non Destructive Evaluation of Materials (IWASPNDE)” Series in 1993. In 2010, he will chair the 10th International conference on *Quantitative Infrared Thermography* ($QIRT^{10}$) in Quebec City, Canada.

Advanced Ultrasonic Inspection Systems

Walter Weber

Abstract not available at time of printing.

Signal-Injection for Building POD Qualification and Sizing Performance Data Sets

R. Lakhan, L. Davey and D. Hawley
Atomic Energy of Canada Limited
Chalk River, ON, K0J 1J0 Canada
613-584-8811

lakhanr@aecl.ca daveyl@aecl.ca hawleyd@aecl.ca

ABSTRACT

Qualification of eddy current techniques can be a costly and complex endeavour; however, the use of signal injection can reduce these costs and can be applied in most situations. This process allows for field and laboratory data to be combined and incorporated into qualification exercises, and provides a well-controlled data set that is suitable for round-robin testing with lower subjectivity.

This presentation compares the signal-injection method for generating data, needed to produce probability of detection (POD) curves and estimate flaw-sizing performance, to that of conventional laboratory or field-based methods. POD curves and sizing error calculations were used to compare the methods and determine if signal injection is a valid method for conducting performance demonstrations. In this case study of fretting wear at support plates, it was found that the signal injection method produced similar results, with the differences ≤ 1% of the steam-generator tube-wall thickness and well within the uncertainty and repeatability of eddy current measurements.

Wavelet Signal Processing of Magnetic Flux Leakage Signals - Implementation of a Multichannel Wavelet-Filter for Nondestructive Testing Systems in Steel Tube Mills

Thomas ORTH*, Till SCHMITTE Salzgitter Mannesmann Forschung, Duisburg, Germany
Robert PETERS, Klaus-Dieter MÜLLER, Ashraf KOKA, Stefan NITSCHE,
V&M Deutschland, Düsseldorf, Germany

Abstract. Magnetic flux leakage testing is one of the most important NDT methods for seamless steel tubes. In order to increase the sensitivity of the inspection, diverse signal processing techniques are already applied. As an alternative to conventional filter techniques, wavelet filtering reveals a higher separation of the signal to the noise level together with an improved adaptation to the signal structure. For the implementation of wavelet filtering into existing third party systems, a multichannel DSP-hardware has been developed, which is capable to filter 32 sensor signals simultaneously. The results show a significant improvement of the signal to noise ratio. Furthermore, it is possible to dispend with the commonly applied differential sensor technique so that a wider range of defect types can be detected.

Introduction

In the production of seamless steel tubes, made of ferromagnetic steel grades, the use of electromagnetic inspection is often favored compared to UT inspections. In addition, certain customer specifications demand EMI as a second NDE method.

For seamless pipe production the magnetic flux leakage technique is a good compromise, because flaws at the outside and inside of pipe walls can be detected for DC flux excitation. However, the ability to detect flaws at the pipe-inside is limited and decreases with increasing wall thickness. The demand to shift this limit towards higher walls is essential. Furthermore, seamless pipe production usually leads to significant magnetic background signals, so called seamless pipe-noise, which makes it necessary to implement a more sophisticated filter technique for data processing.

We have researched in this field and developed a wavelet-based technique, which increases the signal to noise ratio and suppresses the background signal reliably. We will discuss several threshold techniques and adaptive threshold methods. Several wavelets (orthogonal and biorthogonal) were tested for this purpose.

The selected technique is based on wavelet analysis using a stationary algorithm which omits any data-blocking. The wavelet coefficients are subjected to adaptive thresholds and afterwards subjected to inverse transformation. The denoised signal is fed back into existing installations. The method was implemented on a DSP-based system, resulting in a 32-channel parallel system for real-time evaluation of the signals. The system is installed at existing MFL installations for longitudinal flaw detection at Vallourec&Mannesmann mill in Mülheim, Germany, and a new MFL installation at Vallourec&Mannesmann mill in Düsseldorf, Germany [1].

*) Salzgitter Mannesmann Forschung GmbH, Ehinger Str. 200, 47259 Duisburg, Germany, t.orth@du.szmf.de

The testing of the system was done in collaboration with Institut Dr. Foerster, one of the world leading suppliers for magnetic flux leakage inspection systems, using their ROTOMAT system [2]. Foerster also provided an analogue interface for the ROTOMAT system. The 32-channel DSP system has been tested under mill conditions. The aim for the implementation of the wavelet filtering was:

- increase of the signal to noise ratio
- improvement for the detection of inner defects
- substitution of the differential sensor technique by absolute mode detection
- development of methods for defect classification

Overall, the application of magnetic flux leakage should be extended, resulting in significant reduction of costs.

The paper will discuss the system-design and results from the running installations.

Technical Realisation

Wavelet- filtering

In this chapter only a short review of wavelet filtering will be given. For a more comprehensive description see [3-5].

The signals, which are superimposed by noise of different origins, are wavelet transformed into the wavelet domain (see Figure 1). This is similar to a spectral analysis of the signal, but instead of using a sine function, a wavelet ("little wave") is chosen as a basic function. By a suitable choice of the wavelet an improved resolution for transient signals can be achieved. These types of non-stationary signals are typical for ultrasonic testing, magnetic flux leakage, acoustic emission and others.

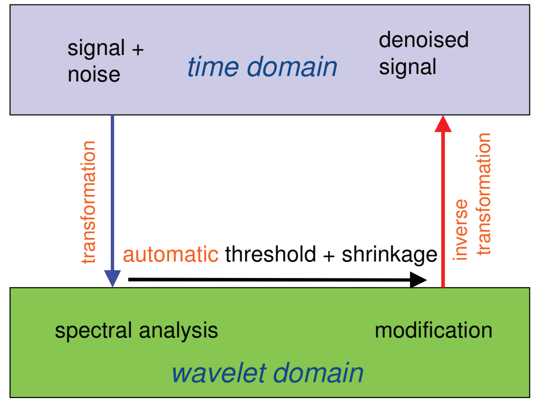

Figure 1: Basic principle of wavelet filtering

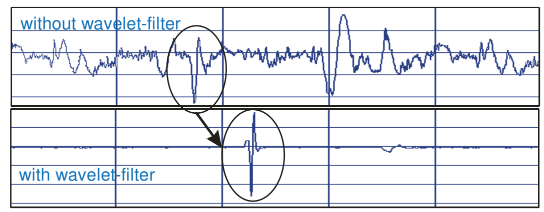

Figure 2: Filtering of a single magnetic flux leakage signal trace by wavelet analysis. The defect indication is marked by a circle. The filtering leads to a short time delay. The denoised signal is clearly visible in the lower diagram.

After transformation of the signal into the wavelet domain the resulting wavelet coefficients have to be modified to achieve a denoising effect. In this process one has to differ between shrinkage and threshold determination. For shrinkage, several methods are available which cut the wavelet coefficients, which means certain big coefficients are kept while the others are reduced or even set to zero [6]. Which coefficients are finally relevant is decided by the threshold, which can be varied dynamically. For the system discussed in this paper, the threshold is determined by analysing the statistical properties of the wavelet coefficients. The threshold is dynamically corrected. Afterwards the modified wavelet coefficients are inversely transformed back into the time domain. Figure 2 gives the filtering of a typical magnetic flux leakage signal. Another example is given in Figure 3, which shows the 100% inspection (C-scan) of a test tube, in which several artificial defects have been prepared.

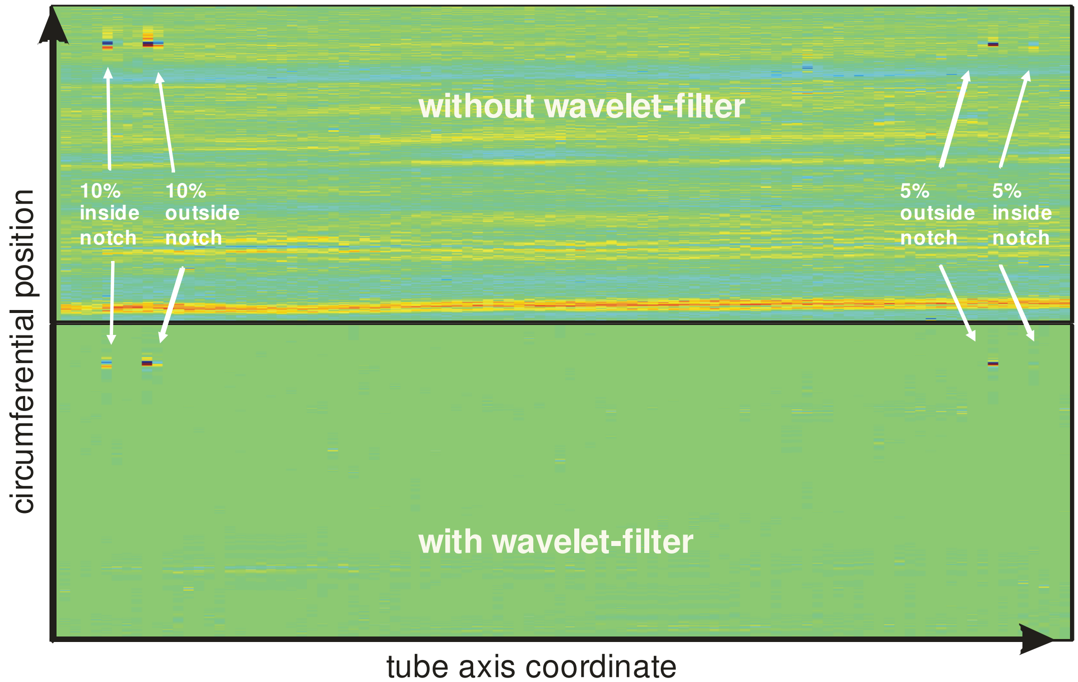

Figure 3: complete measurement (C-Scan) of a test tube, wall thickness = 10.36 mm, with one single sensor. The tube has been scanned spirally. The y-axis represents the circumferential position, the x-axis the longitudinal coordinate of the tube. The colour coding relates to the signal amplitude. The upper diagram shows the non-filtered data, the lower diagram gives the result after wavelet denoising. The following artificial notches have been prepared at the tube ends (left to right): 10% inside, 10% outside, 5% outside, 5% inside. The percentages give the notch depth relative to the wall thickness.

Design of the 32-channel system

To realise the wavelet denoising for mill application, the wavelet filtering has been implemented on DSP-based signal processing systems. For this purpose, the filter has been programmed eight times in parallel, so that one single DSP is filtering eight channels. In addition to the DSP, each channel is equipped with an AD and DA converter. The converters are set in parallel, so that delay times due to multiplexing can be excluded. Four of these units are mounted in one 19” rack. The final 32-channel system is shown in Figure 4. Depending on the type of filtering, sampling rates up to 25 kHz can be achieved. This is by far sufficient for most of the MFL applications during seamless pipe production. By slight modifications of the hard- and software higher sampling rates would be possible. The system reveals analogue inputs and outputs to ensure a simple integration into the analogue signal path (black box principle). No change of the existing system control is therefore necessary. The system is parameterized from a PC via an Ethernet connection.

The system presented here has been developed for the ROTOMAT system of the NDT company Institut Dr. Foerster and has been tested intensively in the mill. The ROTOMAT is provided with two sensor shoes, each equipped with an array of 8 induction sensors. The measured signal is fed into analogue bandpass filters and is separated into a high frequency outside channel and a low frequency inside channel. Subsequently, these analogue signals are given to the wavelet filter, which consequently filters inside and outside channel separately. In summary, 32 wavelet filter channels are necessary for the complete system. The effect of the analogue band pass filtering is shown in Figure 5. The ROTOMAT system offers the possibility to perform differential measurements. This is realised on a software basis (right after the wavelet filtering) where the difference of two channels is calculated and finally evaluated.

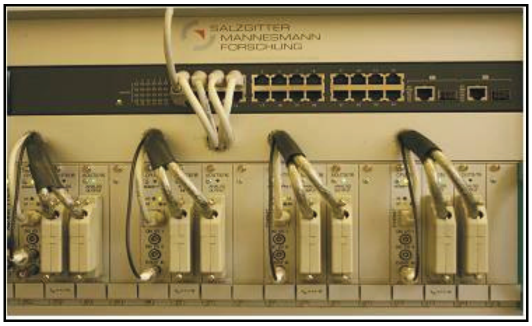

Figure 4: 32-channel wavelet-signal processing system. The 4 DSP-based systems are clearly visible, each equipped with 8 analogue inputs and outputs.

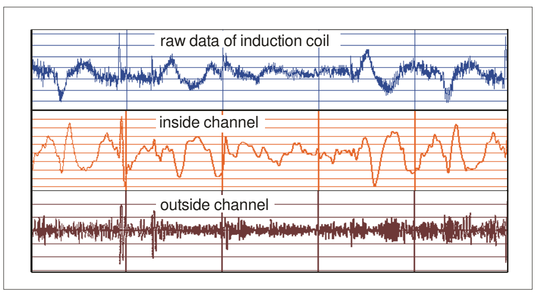

Figure 5: Separation of the stray flux signals in the ROTOMAT system: the upper diagram gives the non-filtered signal. The centre and lower diagram represent the low frequency inside channel and high frequency outside channel respectively.

System test in the mill

Below some examples originating from the mill trials are presented. All experimental data have been recorded within the ROTOMAT system, comprising screenshots from the ROTOMAT software or extracts from the ROTOMAT database. All data have been measured under mill conditions.

Test tube

During inspection of the first test tube (177.8 x 10.36 mm) only the absolute sensor mode (no differential technique) has been used. The test tube has been inspected several times, while the different parameters of the wavelet filter were tested. The result of optimal filtering is given in Figure 6. The upper part of the diagram (without wavelet filtering) shows a clear separation between the outside defect (5% longitudinal notch) and inside defect (12.5% longitudinal notch). The noise content of the signal becomes quite evident in the inside channel.

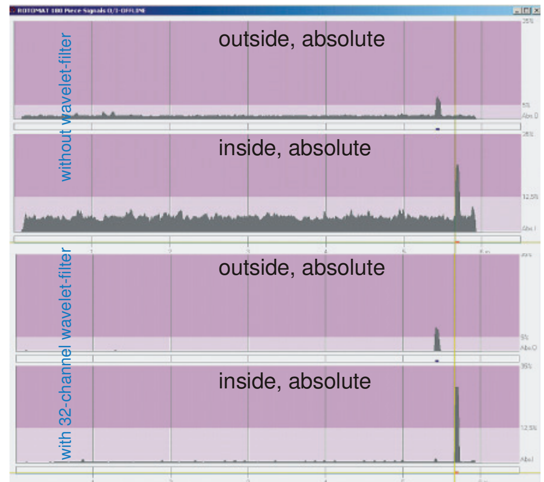

Figure 6: Screenshots of the ROTOMAT-software: test tube (177.8 x 10.36 mm): 12.5 % inside notch, 5% outside notch. This measurement has been performed in absolute mode only. The two upper diagrams show the results without wavelet filter. The two lower ones with applied wavelet filtering**.**

After passing the wavelet filter the situation changes: without changing the amplification of the electronics, the signal amplitudes of the indications stay constant while the background signal has been removed nearly completely.

Natural imperfections

The next examples show the characteristics for natural imperfections, in this case two small outer defects, shown in Figure 7. The tube dimension was 139.7 x 7.72 mm. The tubes have been inspected five times and the evaluation of the ROTOMAT system has been recorded repetitively, without wavelet filter and with varying wavelet filter adjustments. The result for optimised filter settings is given in Figure 8a and 8b. In contrast to the inspection of the test tube with artificial defects (see above), both

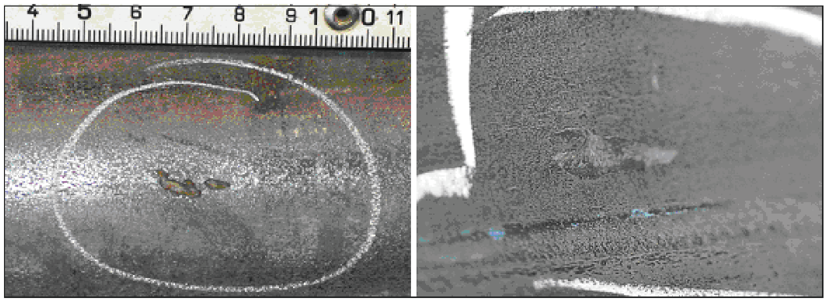

Figure 7: natural imperfections: example 1 (left) and example 2 (right), tube dimension 139.7 x 7.72 mm.

inspection modes have been used, absolute as well as differential mode. It can be clearly seen, that the outside defect is indicated in the inside channel, which is a typical drawback of conventional band pass filtering defect classification.

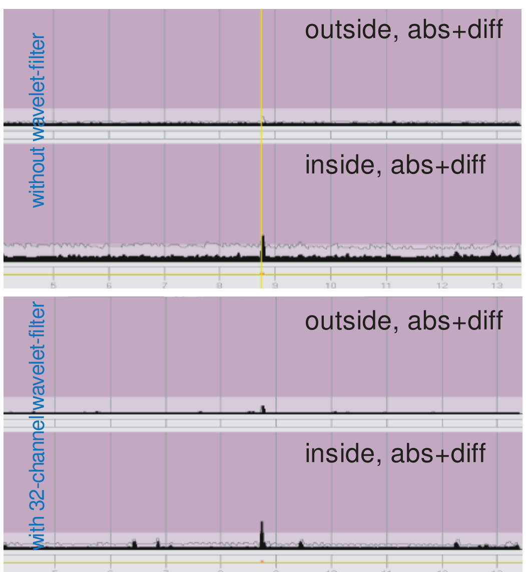

Figure 8a: Screenshots of the ROTOMAT-software: natural outside imperfections example 1. The upper part of the diagram shows the results without wavelet filtering, the lower with activated wavelet filter. The measurements were recorded in absolute as well as differential mode. The grey solid lines represent the absolute mode measurement, the black bar graph the differential mode result

For this reason the wavelet filtering works especially in the inside channel. Again the noise is significantly reduced while the indication amplitude stays constant.

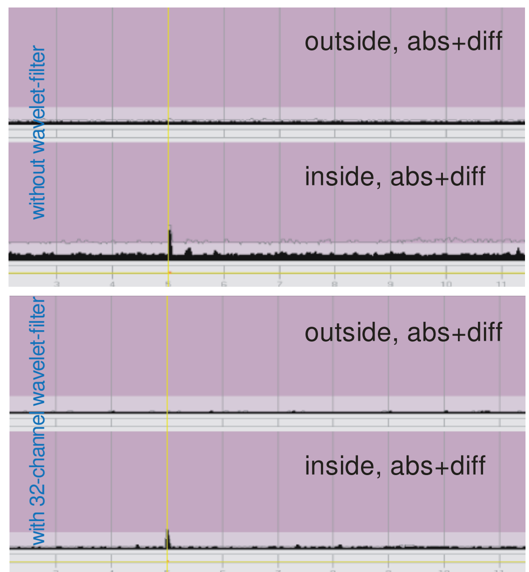

Figure 8b: Screenshots of ROTOMAT-software: natural outside imperfection example 2. See caption to Figure 8a for details.

In addition, the rather high background signal of the absolute mode result can be reduced to the level of the differential mode, which essentially means that with filtering an absolute mode measurement becomes practically possible.
In the following the measurements will be evaluated statistically. The five runs with identical settings have been averaged and are represented together with results for different wavelet filter settings in Figure 9.

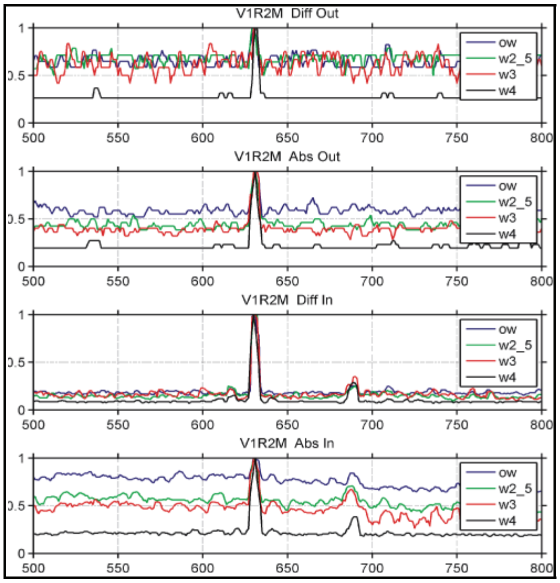

Figure 9a: statistical evaluation of the measurements from example 1. The curves given in the diagram represent the results without wavelet filtering („ow“ blue) and with 3 different setting of the wavelet filtering („w2_5“ green, „w3“ red, „w4“ black, with increasing filter strength in that order). The diagrams given are from top to bottom: differential evaluation of outside channel, absolute evaluation of outside channel, differential evaluation of inside channel, absolute evaluation of inside channel.

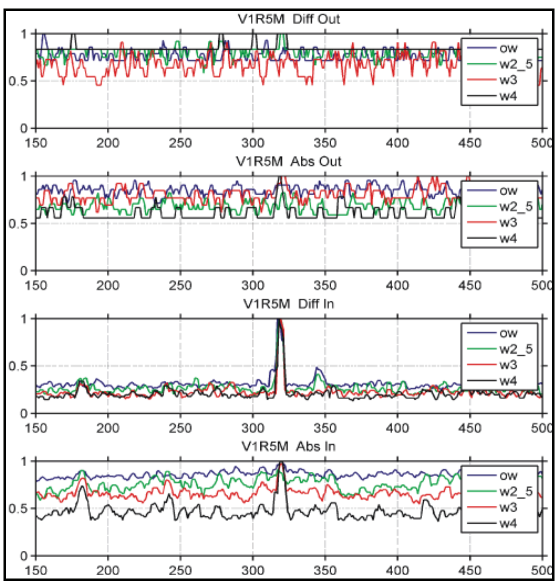

Figure 9b: statistical evaluation of the measurements from example 2. For details see caption to Figure 9a.

For the sake of better comparison, all results are normalised to the biggest indication amplitude and are spread in the axial direction of the tube. In each diagram, curves are given in color coding (green, red, black) corresponding to increasing filter strength (in this order) and blue for no wavelet filtering. It can be clearly seen that wavelet filtering is very much effective for the absolute mode measurement. In case of the differential mode measurement a quite strong filter setting has been set in order to obtain a considerable effect. In case of the outside channel of example 2 the filter effect is negligible, probably because the indication amplitude is rather small. On the basis of the results of Figure 9a and 9b the improvements for the signal to noise ratio (SNR) have been quantified (see Table 1 and Table 2).

Table 1: Statistical evaluation of the results for example 1. Improvement of the SNR given in dB relative to the situation without wavelet filtering.

.

Δ dB	Diff Out	Abs Out	Diff In	Abs In
Wavelet 2.5	0	2.81	1.5	2.57
Wavelet 3	0.95	3.67	1.5	4.58
Wavelet 4	7.77	8.03	7.52	10.61

Table 2: Statistical evaluation of the results for example 2. Improvement of the SNR given in dB relative to the situation without wavelet filtering.

Δ dB	Diff Out	Abs Out	Diff In	Abs In
Wavelet 2.5	n.a.	n.a.	1.16	0.36
Wavelet 3	n.a.	n.a.	1.8	1.94
Wavelet 4	n.a.	n.a.	4.08	4.89

Conclusions

In the scope of the work presented here a multichannel wavelet filter has been successfully adapted to an existing commercial magnetic flux leakage inspection system and has been tested under mill conditions. The filter hardware has been realised on the basis of digital signal processors and has been integrated in the ana-

logue signal path as a black box element. As a consequence, only minor modifications of the regular inspection electronics were necessary. The required space for the DSP-hardware is moderate due to effective programming which allows an 8 channel filtering on one DSP board.
The results indicate that a significant improvement of the signal to noise ratio has been achieved. As a consequence, also small indications can be detected reliably. Furthermore, it could be demonstrated, that it is possible to avoid the differential sensor mode, resulting in a higher lateral resolution and a wider range of imperfections which can principally be detected.

References

[1] Orth, T.; Kaack, M.; Fischer, G.; Weingarten, W.; Koka, A.; Nitsche, S.; Arzt, N.: DACH Tagung St. Gallen, P33 (2008), NDT.net
[2] www.foerstergroup.de
[3] Wickerhauser, M. V.: *Adaptive Wavelet-Analysis*, Vieweg, 1996
[4] Addison, P. S.: *The Illustrated Wavelet Transform Handbook*, Institute of Physics, 2002
[5] Bäni, W.: *Wavelets*, Oldenbourg (2005)
[6] Jansen, M.: *Noise Reduction by Wavelet Thresholding*, Springer, 2001

Author

Dr. rer. nat. Thomas Orth has studied physics at the Ruhr-University in Bochum, Germany until 1994. He researched in the group of Prof. Dr. J. Pelzl in the field of solid state spectroscopy. After subsequently working in the research for the automobile industry dealing with adhesive bonding, he changed in 1998 to the Salzgitter Mannesmann Forschung GmbH (former Mannesmann Forschungsinstitut, MFI). Since 2004 he is the head of department for non-destructive testing, dealing with all conventional and less conventional NDT methods.

email: t.orth@du.szmf.de

Wavelet-based Denoising of EMAT Signals – from Development to Industrial Real-time Application

Till SCHMITTE*, Thomas ORTH, Salzgitter Mannesmann Forschung, Duisburg, Germany
Andre GERMES, Stefan NITSCHE, V&M Deutschland, Düsseldorf, Germany

Abstract. EMAT is used whenever a coupling medium like water shall be omitted. However, signal quality sometimes needs improvement, especially if surface quality of the product under test is poor. In this situation wall thickness measurements may be a challenging task. Signal filtering using wavelet based techniques proved to be suited well for improving SNR in situations with pulse-shaped signals. Therefore we developed a system for wavelet-filtering of UT signals in real-time under production situations.

Introduction

In steel tube industry, electromagnetic acoustic transducers (EMAT) are used for ultrasonic testing (UT) of wall-thickness and laminations, whenever the use of a coupling medium like water can not be accepted, for hot products or in cases where UT is combined with other dry NDT techniques like magnetic flux leakage. However, in some cases the advances are paid with a poor signal-to-noise ratio, especially for rough surfaces and high wall-thicknesses.

We present a wavelet-based approach to significantly increase the signal-to-noise ratio (SNR) in these situations. We have researched several wavelet-techniques like adapted wavelets, biorthogonal wavelets, discrete and continuous wavelet-transformations and static and adaptive thresholding techniques. As an outcome of this work we designed and programmed a FPGA-based hardware for adaptive wavelet denoising in real-time of UT-signals. The system, which could not be purchased of the shelf, is running at Vallourec & Mannesmann (V&M) mill in Düsseldorf-Rath in Germany. It comprises 4 channels in parallel and is capable to denoise UT signals at a pulse-repetition rate of up to 5 kHz and sampling rates of up to 125 MHz. The wavelet-denoising uses a well suited wavelet-transform specially adapted to the NDT signals. Additionally, an adaptive thresholding is implemented. The pre-amplified analog EMAT signals are fed into the digital filter electronics, being wavelet-denoised, and subsequently transformed back to analog signals which are transferred into the conventional UT-system. This "black-box" philosophy allows for usage in almost any standard UT-system. The paper describes the basic design of the system and presents results from trials and mill application.

System Design

General

Instead of using a frequency filter, e.g. a band-pass, to reduce the noise, the wavelet filtering enables to filter in the time-frequency domain, thus taking also time aspects (pulse-shaped signals) into account. In addition, mathematics of the

*) Salzgitter Mannesmann Forschung GmbH, Ehinger Str. 200, 47259 Duisburg, Germany, t.schmitte@du.szmf.de

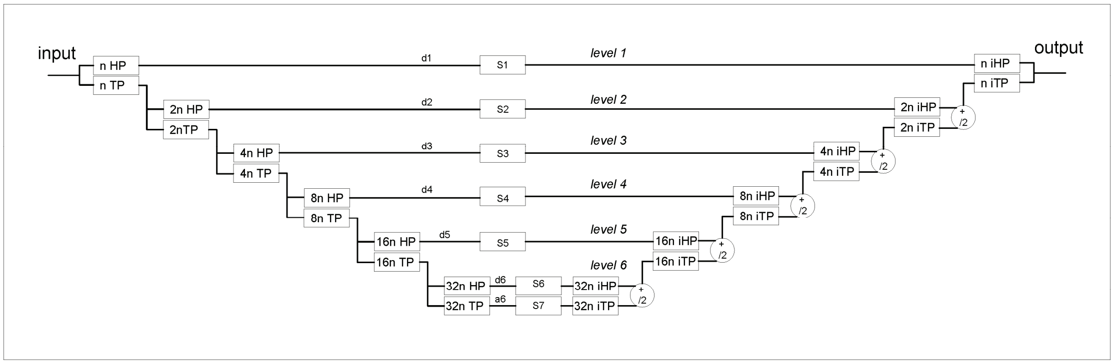

Figure 1: Wavelet filtering scheme. nHP and nTP etc denote the high pass and low pass FIR filters of length *n*. S1 … S7 denote the shrinkage functions**.**

wavelet transformation also allows for using different wavelets which may be adapted to the actual signal shape and thus leads to a better signal discrimination.

The actual wavelet filtering consists of three parts: first the signal in the time domain is transformed into the wavelet domain by the wavelet transformation, in the next step the signals in the wavelet domain are modified (shrinkage) and last the modified signals are transformed back into the time domain by an inverse transformation.

This procedure is very demanding with respect to computing power if the complete filtering should be carried out in real time during the measurement.

In recent years we have gained experience in wavelet filtering for stray flux (MFL) signals [1, 2]. This research resulted in the successful filtering of MFL signals in several installations at V&M mills. Because the MFL signal rate is comparatively slow, the realization could be done with standard DSP techniques. Unfortunately, this could not directly be transferred to UT systems, because the data rate is approximately a factor of 1000 faster. Only a hardware based on modern field programmable gate arrays (FPGAs) will have sufficient computing power for performing the necessary transformations in real time.

Setup

The realized wavelet filter programmed on FPGA hardware is mainly optimized for UT wall-thickness (WT) measurement which is a pulse echo method. The hardware enables for a pulse repetition frequency (PRF) of up to 5 kHz. Typically pulses with central frequency around 2 - 10 MHz are used. The reflected signal (an echo from the back wall) is digitized during a limited span of time (*window*) after the initial pulse. The sampling frequency can be selected up to 125 MHz and the time window has up to 4096 samples. The sampling frequency of the AD and the DA converters are identical.

The time window of the measurement starts with a defined delay time after the trigger. During the recording phase the samples in the time window are recorded and fed into a FIFO (first in - first out buffer). At the same time the filtered data of the previous cycle is passed to the DA converter. During the time between two trigger pulses the data is copied into the FPGA for processing. At the same time the results of filtering of the previous cycle are copied into the output FIFO. The remaining time of the cycle – until the recording starts again – is used for actual filtering the data.

The complete system consists of one circuit board with FPGA, memory, AD- and DA- converter, which is parameterized via PCIe-bus from a standard PC. An additional board stacked upon the first is designed for analog input and output signal conditioning. The system is mounted together with power supply and cooling into a 19'' rack which can hold up to four channels (10 height units).

Wavelet-Transformation

The mathematics of wavelet transformations is documented in a broad range of books and articles, some of them are given in [3, 4]. Here we concentrate on aspects of the actual algorithm, which we developed for a wavelet based *filtering* of UT-signals. The wavelet filter consists of a cascading arrangement of finite impulse response filters (FIR filters); also called a *filter-bank*. By processing the signal through this structure (Figure 1) the signal is transformed into the wavelet domain.
This is also called the *decomposition*. This process can be compared to the Fourier transformation from the time into the frequency domain.
The signal in the wavelet domain consists of *wavelet coefficients,* which exist in different *levels*. The number of levels is the number of identical steps in the cascading FIR filter algorithm. After transformation, the wavelet coefficients are modified (shrinkage). This is done by comparing the amplitude of the wavelet coefficients in one level with a threshold value. If the magnitude of the wavelet coefficient is below the threshold the coefficient is set to zero, if it is above the threshold is subtracted in case of positive coefficient and added in case of negative coefficient. This procedure is called *soft thresholding*. As an alternative to the soft version there is a *hard thresholding* where the coefficients above the threshold survive unmodified, and those below are set to zero [6]. After the modifications the wavelet coefficients are transformed back into the time domain. This is done with an equivalent FIR filter scheme, see Figure 1. The inverse transform is also called the *reconstruction*. If all thresholds are zero the wavelet coefficients pass unmodified and the signal is perfectly reconstructed: The output is identical to the input signal.
Instead of using the usual *fast wavelet transformation* algorithm [5] or the *wavelet packet transformation* [6], we use the *stationary wavelet transform* (SWT) algorithm [6]. This algorithm has the advantage that the signal is stationary after filtering and no additional *jitter* is introduced by wavelet filtering. However, the disadvantage is a higher demand of computing power and memory. The SWT is easily implemented in the scheme depicted in Figure 1. The decomposition is done with *N* levels. Therefore the decomposed signal exists in the wavelet domain as details d1 … d*N* and approximation a*N*. The first level set of FIR filters (high pass HP and low pass TP) has *n* filter taps. For subsequent levels the number of filter taps increased such that for the *N*th level the number of filter tabs is $2^{N-1}n$. The increase of filter length is done by inserting zeros between the original filter tab values. After decomposition the values in wavelet domain are subjected to shrinkage function S*N*. A delay line has to be inserted into the signal path for d*N* for proper phase overlay. The reconstruction is done accordingly. This scheme directly allows for point-by-point filtering of the signals if a signal buffer is associated to each FIR filter. In this manner it is possible to filter virtually endless signals without the need of storing the complete signal and without introducing block-artefacts after filtering. The point-by-point method is thus implemented and the endless signal consists of the A-scans to be filtered.

Shrinkage and Thresholds

As shrinkage function the well explored soft- or hard thresholding is selected. May *k* be the index of the discretized signal, *i* the number of the level and λ_i the threshold for this level, than e.g. hard threshold is given by

$$Si : d_{i,k} \to \begin{cases} 0 : d_{i,k} \le \lambda_i \\ d_{i,k} : d_{i,k} > \lambda_i \end{cases} .$$

It remains the question of choosing a good threshold value. One strategy may be to use the global threshold level wise, i.e. calculate the threshold using [6]

$$\lambda_i = \sigma_i \sqrt{2\ln(M_i)} \,,$$

with M_i is the number of values in ith level on which the standard deviation σ_i is calculated upon. The problem here is that the filtering scheme as discussed above, if performing the SWT in a point-by-point manner, has only one wavelet-coefficient in a given level per sampling time interval. Therefore we add an additional memory where the last M values are to be stored. The threshold is calculated just on this last M values by performing standard deviation calculation and is valid for the next M values. This standard deviation is denoted σ_i^M for level i.

Furthermore, the above formula relies on the fact that the noise in the signal to be filtered is white noise, which in most cases in NDT is not fulfilled. Therefore an adjustable number f is introduced such that

$$\lambda_i = f\sigma_i^M \,.$$

The values of f and M are adjustable by the user and have to be optimized. It should be pointed out that both parameters are identical for all levels. In this manner a compromise between complete automatic threshold determination on one hand and the necessity of controlling all thresholds manually on the other hand is obtained.

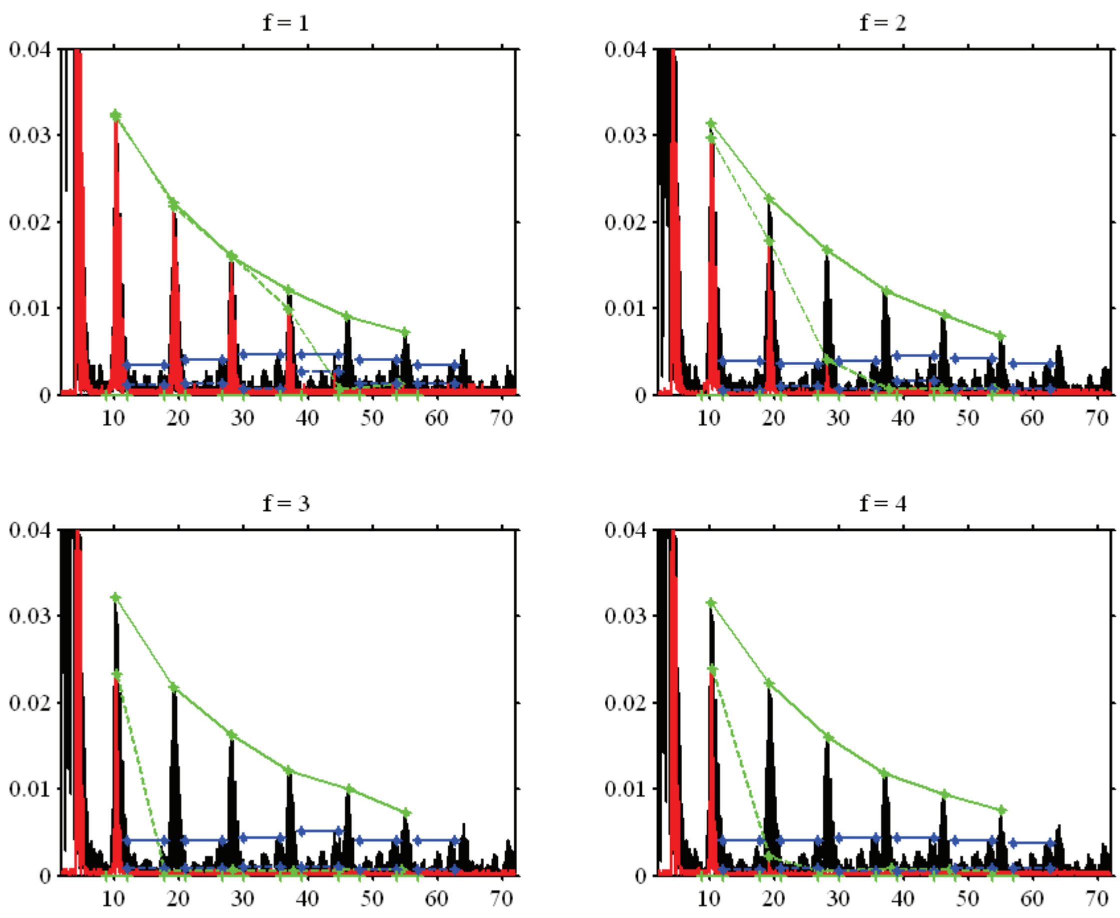

Figure 2: Static testing of the wavelet filter at 100 MHz, 4000 samples and 1 kHz PRF at a sample of 14.5 mm wall-thickness. Four a-scans are given for different values of f as defined in the figure. The red curves show the wavelet-filtered rectified signals and the black curves are non-filtered a-scans. The green curve displays the damping in the filtered (dashed) and non-filtered (straight) case. The green bars display the region of the BWE and the blue straight and dashed bars show the noise level in the filtered and non-filtered case, respectively.

Selected Wavelets

The choice of wavelets is quite important and we performed trials and simulations with a broad variety of different wavelets. Due to performance reasons the first laboratory trials were carried out using Daubechies wavelets with 4 filter coefficients. The mill trials reported here were performed with Daubechies wavelets with 10 coefficients because they proved a better performance than wavelets of shorter length. More complex wavelets were not used because of performance reasons. Other families of wavelets were also tested, but proved less viable for the case of EMAT wall thickness measurements.

Results

All results presented here were carried out at the NDT facilities of the pipe mill of Vallourec & Mannesmann in Düsseldorf-Rath (Germany). This mill is producing large diameter and large wall thickness seamless tubes in the Pilger process. The wall thickness is measured using electromagnetic ultrasonic transducers (EMAT). The system scans the pipe under test in a helical manner. For installation and maintenance purposes a plate or test piece can be placed at the measuring head. Details of the system can be found in [7].

Static measurements

The first presented results were carried out in static operation with a sample tube shell of 14.5 mm wall-thickness. The data was recorded using an oscilloscope. The wavelet-filtering was performed at 100 MHz at a pulse repetition frequency (PRF) of 1 kHz. The lift off of the EMAT head is 1 mm.

Examples of raw and filtered data are presented in Figure 2 for different values of the tuning factor *f*. It can be clearly seen that the noise level, the response in-between the back-wall echoes (BWEs), is reduced. At the same time the damping of the pulse sequence of the BWEs is observed. For usual signal processing only the first or the first and the second BWE is relevant. It can be clearly seen that the increase of *f* leads to a decrease of noise and also to a stronger damping of the signals.

In order to find a good compromise between optimal noise and minimal signal suppression the signal-to-noise ratio (SNR) is calculated for all recorded situations. The signal amplitude is the maximum of the rectified BWE of a given order. Noise is defined as the maximum rectified amplitude in the region between the BWEs. SNR is given in dB. The time window of the BWE is denoted by green bars, the time between the BWE and the level of noise is denoted by blue lines in Figure 2.

In this manner the SNR is calculated for different *f* and for different order of BWEs. Obviously, the interesting parameter is the change of SNR for the situation with and without filter. This is expressed by

$$\Delta SNR = SNR^{filtered} - SNR^{non-filtered}.$$

The values for ΔSNR defined like this are plotted as a function of the order of the BWE for different values of *f* in Figure 3 and as a function of *f* in Figure 4.

From the above analysis it can be deduced that the optimal value for *f* depends on the measurements situation. If one uses only the first BWE for measuring the time of flight and detecting wall thickness it is possible to use up to highest tested values $f < 4$. However, if the wall thickness is deduced from time of flight between first and second BWE, $f \sim 2$ shall be maximum.

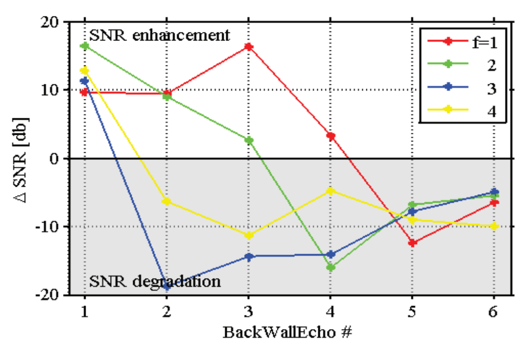

Figure 3: SNR for the same situation as in Figure 2. The change in SNR is plotted as a function of the order of the BWE for several values of *f*.

Dynamic mill test

One main objective to be proved is if the wavelet filtering may lead to any phase shift or signal deformation and may thereby change the results of wall thickness measurements: All A-scans recorded so far did not show any hint towards such behaviour, if f is not too high. The values deduced above ($1 < f < 4$) do not change the shape of the first BWE.

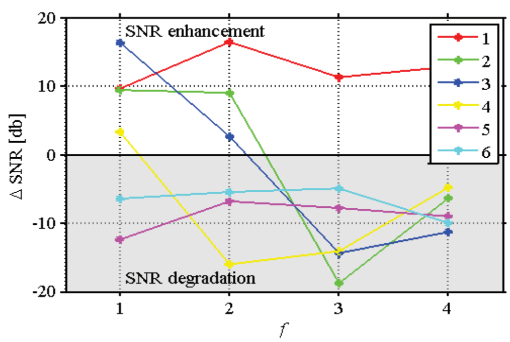

Figure 4: SNR for the same situation as in Figure 2. The change in SNR is plotted as a function of f for the first six BWEs.

In order to prove this we performed a trial recording all A-scans (filtered and non-filtered) from a wall-thickness measurement with EMAT sensor for one rotation of a pipe. From this data the wall-thickness was calculated utilizing the time of flight between first and second BWE. The filtering was done with a moderate value of f. The result from approx. one half of the rotation is displayed in Figure 5.

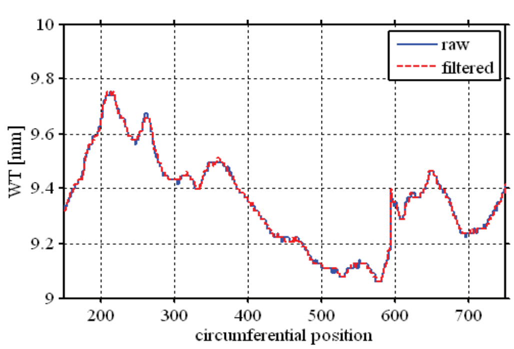

Figure 5: Result of wall thickness measurement of a test pipe. The wall thickness is evaluated from time of flight between 1. and 2. BWE. The data for approx. one half rotation is shown.

This argument can be supported with Figure 6 which displays one example A-scan collected during standard operation of the EMAT wall thickness device in the mill. It is clearly seen that no distortion of the signal takes place. The filtering was performed with $f = 2$. From the same measurement a B-scan is constructed and reported in Figure 7. This figure displays a fraction of the rotation of the pipe. From both figures an overall increase in SNR of approx. 10 dB can be concluded which is consistent with the static measurements discussed above. In addition, a more practical approach was performed in order to estimate SNR improvement: During calibration of the UT system first the wall thickness was calibrated using a reference plate of 40 mm thickness without wavelet filtering.

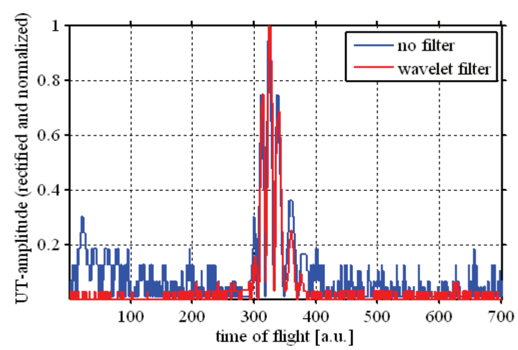

Figure 6: Example A-scan from dynamic tests. One filtered and non filtered part of a rectified A-scan is displayed around the first BWE.

The amplification of the system was adjusted such that noise level is sufficiently low not disturbing the wall thickness measurements. Next, the wavelet filter with $f = 2.5$ was switched on and the calibration was repeated with the same objective. In this case the operator could increase the amplification of the system by 12 dB without increasing relative noise level.

Conclusions

In this project a real-time wavelet-filtering of UT signals was realized and tested. To

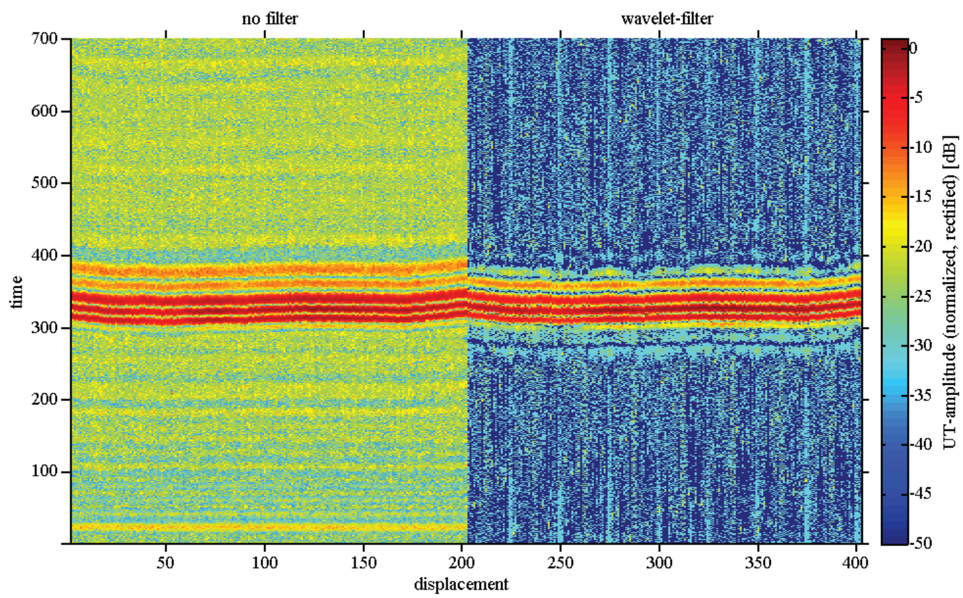

Figure 7: Time-displacement plot (B-scan) of pipe during production (wall thickness = 18.5 mm). Axes are not calibrated. The displacement axis displays approximately 1/5 of pipe rotation. The left part is the non-filtered signal; the right part displays the same data after wavelet-filtering.

our knowledge this is the first setup which can be operated at technically relevant pulse-repetition frequencies of up to 5 kHz and necessary resolution for wall thickness measurements of 125 MHz sampling. It could be proved that SNR could be improved by 10 to 15 db in different situations, laboratory as well as static and dynamic operation during production. The realized automatic threshold selection works well and an optimum filtering can be found depending on how many back-wall echoes are to be recorded. The algorithm is operating reliably on a FPGA board – also for long term operation.

The proposed wavelet filter scheme leads to a linear modification of the damping, depending on the threshold factor *f* and the number of detected back-wall echoes and the filtering does not lead to any major distortion of the signal. Thus, the results of wall thickness measurements are not altered.

Main parts of the presented algorithms and techniques have been applied for patent.

References

[1] Orth, T.; Kaack, M.; Fischer, G.; Weingarten, W.; Koka, A.; Nitsche, S.; Arzt, N.: DACH Tagung St. Gallen, NDT.net P33 (2008)
[2] Orth, T.; Schmitte, T.; et al.: 6th International Workshop Advances in Signal Processing for Non Destructive Evaluation of Materials (2009)
[3] Bäni, W.: *Wavelets*. Oldenbourg, 2005
[4] Addison, P. S.: *The Illustrated Wavelet Transform Handbook*. Institute of Physics Publishing, 2002
[5] Press, W. H.; et al.: *Numerical Recipes.* Cambride University Press, 2002
[6] Jansen, M.: *Noise Reduction by Wavelet Thresholding*. Springer, 2001
[7] Graff, A.; Arzt, N.; Nitsche, S.; Sy, D.: ITA Conference Bilbao/Spain 2001, NDT.net 7 (2002) 03

New and Innovative Non-Destructive Testing (NDT) Techniques for Inspection and Monitoring of Metal Smelting Furnaces

Afshin Sadri, Pawel Gebski, Koorosh Mirkhani and Gordon McGarrie
Hatch Ltd.

Abstract

In this paper, three (3) different NDT techniques are introduced: Acousto Ultrasonic-Echo (AU-E), Taphole Acoustic Monitoring (TAM) and Ultrasonic pulse-echo (UT) for copper cooling element inspection. All three (3) techniques have been developed and implemented for applications in metal smelting furnaces.

The AU-E technique was developed to determine refractory thickness in operating furnaces. In addition, AU-E is capable of determining metal penetration within furnace lining, determining position of cracks in the bricks and delaminations within the sidewall and hearth lining.

TAM is a monitoring system based on the acoustic emission (AE) principals that is utilized to determine the remaining refractory thickness in tapholes, as the furnace is in operation.

UT has been used to determine the remaining copper thickness in cooling elements in finger coolers, staves, plate coolers, breast coolers, and waffle coolers. To achieve accurate measurements, a temperature correction factor for longitudinal wave was used.

Following a brief introduction to the above techniques, various applications and case studies will be discussed.

Introduction

Smelting furnaces are the most volatile manmade structures which undergo severe thermo mechanical chemical deterioration and wearing. Molten metals and aggressive gasses are the main cause of vessel deterioration. To inspect and monitor the integrity of the metallurgical furnaces; elastic waves, including stress waves, ultrasonic waves and acoustic emission waves are the most reliable and practical measuring systems. Based on the above NDT principals, various techniques have been developed to determine the integrity of the refractory lining, vessel shell, tapholes and cooling elements.

These techniques are Acousto ultrasonic-echo (AU-E) which uses stress wave reflection technique to asses refractory thickness condition in operating furnaces; Taphole Acoustic monitoring system (TAM) which uses acoustic emission (AE) principals to monitor refractory wear in tapholes; and ultrasonic testing to monitor thickness and integrity of copper cooling blocks that are installed on the furnace sidewalls..

Acousto Ultrasonic – Echo (AU-E) Technique

Acousto Ultrasonic-Echo is a stress wave propagation technique using frequency data analysis. A mechanical impact on the surface of the structure (via hammer or a mechanical impactor) generates a stress pulse propagating into the furnace layers. Where the impact head is spherical or semi-spherical, it generates spherical waveforms which are simple to analyze. The generated waves are broadband and the diameter of the “impact head” dictates the range of frequencies: when the impact head is small the bandwidth is high frequency and when the impact head is large the bandwidth is low frequency.

The waves are partially reflected by the change in refractory layer properties, but the main energy propagates through the solid refractory layers. The signal is mainly reflected by the refractory/molten metal interface or refractory/air interface between internal layers or external boundaries. A receiver beside the impactor picks up surface vertical displacements caused by reflections from internal and external reflectors. The vertical displacements are mainly reflected P-waves (or longitudinal waves) received by a sensor close to the impact source. The signals are analyzed both in time and frequency domain, where the changes in thickness and wave speed are the controlling factors.

In this methodology, the principal stress wave captured and analyzed for quality assessment is the primary wave or the P-wave. Velocity of the P-wave varies form material to material based on the density and elastic properties. A drastic change in density and/or elastic properties of the material results in partial or total reflection of the waveform.

Two major elements are considered important in AU-E computations. First, the shape and dimension effect of the refractory layers on the resonance frequency of the P-wave, which causes a change in wave speed. For the refractory layers that are well bonded, the shape factor, β, is considered used to correct the wave speed. For a metallurgical furnace the shape of the layers are either flat or slab shape such as walls, or concave up or down, such as electrical furnace hearth and roof; or circular or semi circular, like rotary kilns, converters and reactors. Second, since each layer contains bricks of different composition and thickness, the wave speed in each layer and their known thickness must be taken into consideration in the overall assessment of the furnace. The compressive or P-wave velocities are affected by the temperature. The effect of the temperature or α-factor is unique for each type of refractory, for each range of temperature.

The resonance of the P-wave arrivals to the surface causes a periodic spectrum that can be best viewed by converting the time-domain spectrum to a frequency domain using the fast

Fourier transform (FFT) technique. Equation 1 is the fundamental AU-E equation, where the T is the thickness and f_p is the frequency of the P-wave reflecting between the two interfaces.

$$T = \frac{\alpha \beta V_P}{2 f_P} \qquad (1)$$

In the above equation, α is the thermal correction for the P-wave speed and the β factor is the shape factor correction for the P-wave speed. Equation 1 is correct when the refractory material is limited to a single brick or single layer. For multilayer refractory lining, the resonance frequency of the P-wave is a result of the total (sum) of responses from each layer of the refractory lining. The waveform is affected by the material properties from each layer. Knowing the thickness of the layers are not changing on the cold face, using the frequency of the wave from the full thickness and the known parameters, the thickness of the final layer is computed.

Correct knowledge of both temperature and shape factors (α and β) are important in computations of thickness and material quality by the acousto ultrasonic-echo technique.

The AU-E technique has been used for detection of refractory and accretion thickness in following vessels:

- Blast Furnace
- Electrical Arc Furnaces
- Six-in-Line Furnace
- Flash Smelting Furnaces
- Rotary Kilns
- ISASMELT Furnaces
- AUSMELT Furnaces
- Mitsubishi Process
- KIVCET Furnace
- Pierce Smith Converter
- Anode Furnaces
- Teniente/Noranda Reactors
- Tunnel Furnaces
- Reheat Furnace

In addition to detecting refractory and accretion thicknesses, AU-E has been used for detecting:

- Molten metal penetration within the lining layers in furnace hearth
- Detection of frozen metal within hearth lining
- Taphole refractory thickness
- Detection of brittle zones in blast furnaces
- Cracks and delamination within refractory lining and individual bricks
- Refractory qualification
- Identification of refractory hydration areas

All the above AU-E measurements are done as the furnace is in operation.

Furnace condition monitoring plans are organized to detect and foresee the lining issues prior to become an issue resulting in break-outs and metal run outs. The optimum plan is to conduct a baseline inspection after the first furnace start-up and later the same areas to be inspected within a decided known time pattern. This type of condition monitoring will demonstrate the wearing and deterioration pattern for the refractory lining and could be used as a predictive maintenance tool.

Figure #1: The sensor and impactor arrangement on the shell

Taphole Acoustic Monitoring (TAM) System

Water-cooled tapblocks are essential components of modern smelting furnaces. Uninterrupted operation of a tapblock is critical both for the structural integrity of a furnace and for the optimal operation and process control. This critical function together with the exposure to extreme conditions (thermal, chemical and mechanical) creates the need for efficient and reliable means for tapblock monitoring. A typical tapblock with and without the refractory inserts installed is shown in Figure2. The inside of the block is lined with refractory inserts, forming a tapping channel, through witch the molten metal is tapped. These bricks wear out due to thermal deterioration and need to be replaced on regular basis. The water-cooled tapblocks have cast-in Monel pipes that serve as cooling circuits. These coils enable constant flow of water within the copper block and in consequence they provide efficient means for the heat exchange.

Figure #2: Typical water-cooled tapblock removed from a furnace: LEFT - with the refractory inserts installed right) without the refractory inserts

Principles of the TAM System

The primary objective of the taphole monitoring system was to detect any wear and deterioration of the inner taphole refractory lining, with the ultimate objective of identifying any wear or shrinkage in the distance between the copper element and the cooling Monel pipe. For this purpose Acoustic Emission (AE) methodology was chosen.

Acoustic Emission for Tapblock Monitoring

Acoustic Emission is a powerful technique for evaluating the conditions of materials and structures. AE may be defined as a transient elastic wave generated by the rapid release of energy within a material. This technique is used to safeguard against catastrophic failures, to assess structural integrity and to enhance safety in a wide range of structures. This is often combined with monitoring of the manufacturing processes. For the tapblock monitoring, the AE system was used to detect changes in refractory and copper thickness and to evaluate their integrity.

In this application, the primary source of the signals is related to the flow of the molten metal. The signals (AE events) are generated on the interface between the molten metal and the inner refractory lining, and their occurrence is caused by the motion of the molten material and by the resulting thermal expansion of the refractory. The elastic wave propagates through the refractory and copper, and then approaches the cooling pipe. While both refractory and copper significantly attenuate the signals, the Monel pipe is a good medium for propagation. The elastic waves propagate through the Monel pipe towards the sensors installed on the inlet and outlet. Since significant attenuation takes place while the signal propagates through the refractory and copper, the changes of the signal's parameters will be related to the remaining thickness of the refractory lining and the copper. In general, the stronger the signal, the less attenuation, hence there is less material remaining. This concept is illustrated in Figure3.

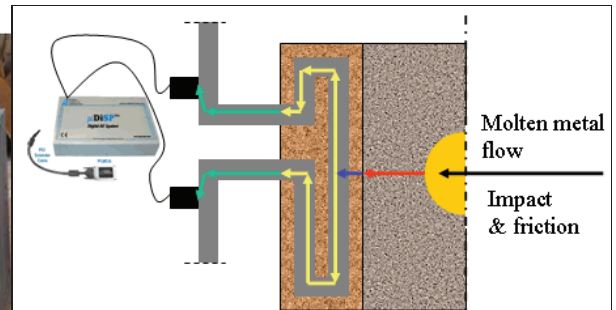

Figure #3: AE signal propagation path within a tapblock

As shown in Figure3 there are four components of the attenuation that should be considered for the tested tapblock (A_R – attenuation within refractory, A_C – attenuation within copper, A_{MC} – attenuation within the section of the Monel pipe that is cast in copper, A_M – attenuation within the Monel pipe not cast in copper). The total attenuation of the signal on its path from the source to the sensor is a summation of these components, see Equation2.

$$A = A_R + A_C + A_{MC} + A_M$$

Equation #2: Signal attenuation components

For the purpose of the refractory wear evaluation, out of the four distinct attenuation components one is variable, namely: A_R. The values of this component change when the thickness of the refractory changes. This relates back to the foundation of this Taphole Acoustic Monitoring technique: reduced thickness results in less attenuation and stronger AE signals.

Pattern Recognition for Damage Evaluation Based on AE

In order to process the large number of AE data in an efficient way, Hatch developed Pattern Recognition software. Using various combinations of signals' features it is possible to identify the ones related exclusively or predominantly to individual tapping events. This is schematically shown in Figure 4. Based on the experience of the furnace operators it was later possible to assign the most probable deterioration modes to those events. This work, together with the signal source location, established basics for the qualitative condition monitoring of tapblocks using Acoustic Emission technique.

	Amplitude	Energy	Duration	Rise Time
Class1	Low	Low	Low	Low
Class2	High	High	High	Low
…	…	…	…	…
Class N	High	High	High	High

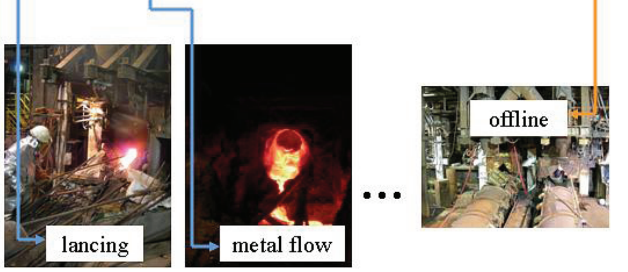

Figure #4: Various events and the related AE signal parameters

TAM Software

The key software modules of the TAM system are:

- The Detection Module – including the data acquisition software.
- The Source Location Module – computing physical location of the tapping related signal sources.
- The Signal Processing Module – responsible for digital filtering of the acoustic signals.
- The Pattern Recognition Module – with learning algorithms for recognizing the off-center lancing / tapping signal features.

The TAM is continuously monitoring the tapping intensity at various areas of the tapping channel, relating it to the refractory deterioration. Selected screen captures from the monitoring software are shown in Figure 5.

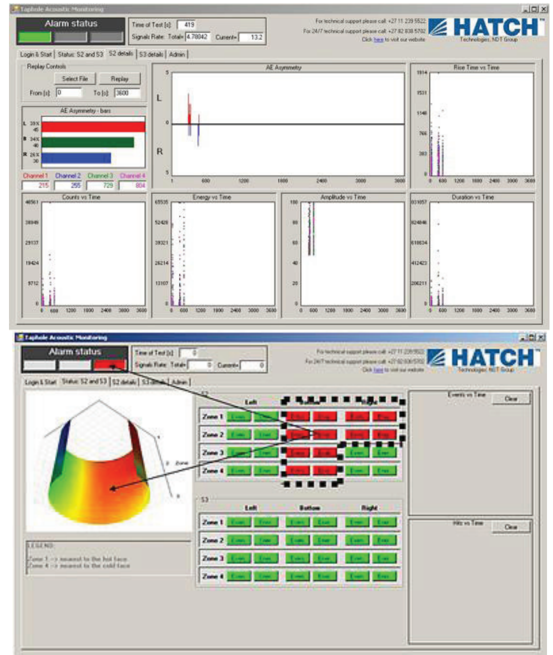

Figure #5: TAM software screen captures: LEFT – directional tapping control; RIGHT – detected area of high lancing intensity

TAM Performance History

The TAM system has been installed on two tapholes for two years. The main purpose of that installation was to monitor the taphole refractory wear and to ensure that the copper block remains intact. The system was validated during several minor tapping incidents. The data collected during these events was added to the knowledge base and used to recalibrate the alarms/warnings thresholds. The TAM system has served its purpose well without any major software or hardware malfunctions. Several software upgrades were successfully conducted on-line, using the Virtual Private Network (VPN) connection.

Cooler inspection using ultrasonic testing method

Methodology

Considering the critical role of the copper coolers, strict monitoring of their performance is essential. Such a monitoring is accomplished by precise measurement of the cooler's hot face thickness. Several non-destructive testing techniques have been benchmarked for this purpose. Ultrasonic testing method is one of the promising methods for inspection of copper coolers. Portability, accuracy, high sensitivity and ease of use are among the advantages of ultrasonic testing method.

The normal beam ultrasonic pulse-echo method is regarded as one of the most practical schemes for monitoring the thickness of copper coolers. As is shown in ***Figure*** , in this technique piezoelectric transducers are manually mounted on the cold face of the coolers using a viscous couplant

(jel). Ultrasonic waves launched by the transducers propagate in the copper medium. They are then partially reflected back at copper/Monel or copper/molten metal boundaries due to change in mechanical properties of the media at the interfaces. The reflected waves propagate toward the transducers and are detected by them.
Having the ultrasonic wave speed in copper medium and the total propagation time of the longitudinal wave to travel through the cooler and reflect back, the thickness is calculated.

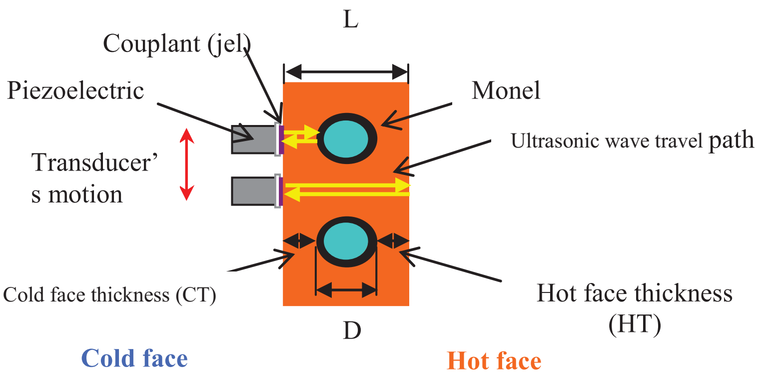

Figure #6: Schematic view of pulse echo technique for thickness calculation

Acoustic Wave Speed Calibration

Dependency of ultrasonic wave speed on copper temperature demands correction of the wave speed in advance of calculating the cooler thickness. Lack of such a correction introduces significant errors in thickness calculation.

Experimental and numerical studies on temperature dependency of ultrasonic wave speed in copper were accomplished by the Hatch NDT group. The results of these studies are briefly described.

Numerical Studies

A finite element model for propagation of a typically used 500 kHz acoustic wave in copper was developed using ANSYS software. The model was solved for different types of acoustic pulses such as transient and continuous, various grades of copper materials and different temperatures of copper.

For all different temperature values tried in the program, the acoustic wave speed exhibited a reduction against an increase in temperature. ***Figure*** 7 illustrates the relationship between the ultrasonic wave speed and temperature for a particular copper grade.

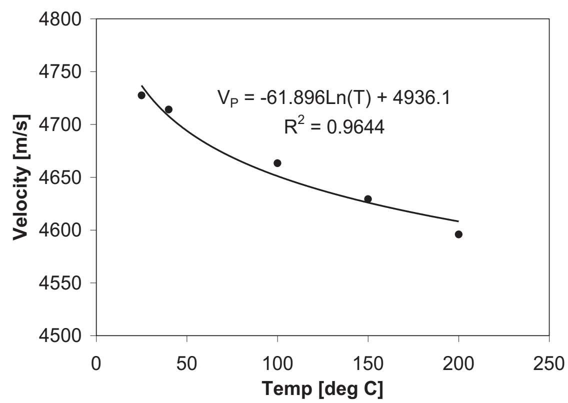

Figure #7: Dependency of acoustic wave speed on temperature for a particular copper grade.

Experimental Study

A series of tests were conducted to determine changes of wave speed in copper due to an increase in temperature and samples sizes. Two (2) copper rods of 130mm and 250 mm long were heated at equal time intervals, and longitudinal wave speed was measured using an ultrasonic thickness gauge system. A series of acoustic wave speeds were collected as the temperatures were increased in equal intervals up to 215°C. The measured wave speed data demonstrated that the sample length has no effect on the wave speed.

Figure 8 illustrates the relationship between the measured ultrasonic wave speed and temperature for a particular copper grade.

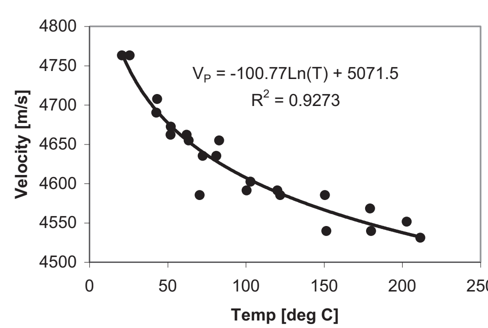

Figure #8: Measured Acoustic Wave velocity vs. temperature in copper rods

The empirical relationship between the acoustic wave speed and temperature, shown in ***Figure*** 8, are in agreement with that for the numerical study demonstrated in ***Figure*** 7.

Conclusions

Despite of complexities involved with material heterogeneity, temperatures and difficult working environments, NDT techniques have been developed and used for monitoring and inspection of the metallurgical vessels and furnaces.

Study of the Variations of Probe Parameters by Finite Element Modeling of Transient Eddy Currents in Multilayer Aluminum Structures

V. K. Babbar, D. Harlley and T. W. Krause
Department of Physics, Royal Military College of Canada, Kingston, ON, K7K 7B4

ABSTRACT

Transient eddy current inspection is being developed for detection of flaws located at depth in airplane wing structures. The input transient signal induces eddy currents, which interact with the flaws in a conducting structure to produce an output signal that provides information about the flaw. The output signal may depend strongly on a number of probe design parameters in addition to probe lift-off from the sample surface. The present work is aimed at investigating the effect of some of these parameters on the output signal by using three-dimensional finite element modeling employing the COMSOL Multiphysics commercial package. The model incorporates a reflection-type probe that consists of a driver coil, a pickup coil and a ferrite core and is placed on a multilayer aluminum structure with a variable lift-off. The parameters such as number of turns of the driver, length of the ferrite core and permeability of the core were varied to study the variation in current distribution and penetration depth within the sample. The modeled results were validated against experimental observations taken in the laboratory by using a probe configuration of identical geometry and electrical parameters. A TecScan System was employed to record and analyze the data. The variation of pickup voltage with lift-off revealed the existence of a lift-off intersection point for flat plates in agreement with experiment. The variations of pickup voltage with number of turns of the driver, length of the core, and permeability of the core are presented and discussed.

Keywords: Pulsed Eddy Current, Electromagnetic Modeling, Transient Electromagnetic Fields
PACS: 81.70.Ex, 85.70.Ay

INTRODUCTION

Non-destructive transient eddy current (TEC) testing is an emerging technology that is being developed for investigation of multilayer aircraft wing structures where fatigue induced crack growth may occur in the inner layers [1-5]. Locations of cracks in the second layer are not normally inspectable by conventional techniques, such as eddy current or ultrasonics. TEC employs a square wave excitation of the coil to induce a transient response from electromagnetic field interactions deep within the conducting aluminum structures. Such electromagnetic inspections are advantageous over ultrasonic inspections (both with and without sealant) and applicable to aircraft inspections, such as CC130 hat section inspection and CP140 second layer wing plank inspection. A number of publications on this subject are aimed at theoretical understanding of the phenomenon, development of appropriate probes, improvements in experimental test systems, and finite element (FE) modeling of the input and output signals [6-12]. In a recent publication, the authors demonstrated the success of finite element modeling, using COMSOL commercial software [13], to model coaxial and reflection type probes to simulate input and output signals that matched closely with those obtained from the experimental set-up of identical geometry and electrical circuit [14]. Thus the FE modeling has the potential to aid in optimizing probe characteristics for detection and sizing of cracks in multilayer structures. The present work is an attempt to improve the signal response of the flat reflection-type TEC probe by changing the probe parameters, such as number of turns of the driver, and length as well as permeability of the ferrite core, by using FE modeling that is validated by experimental observations. The effect of probe position relative to defect location on the pickup signal is also investigated.

EXPERIMENTAL DETAILS

The circuit diagram of a typical transmit/receive probe used for both experimental work as well as FE modeling is shown in Figure 1. The primary circuit consists of a driver of resistance R_{PC} connected in series with a source of emf ε and internal resistance R_{IN} of 53 Ω. The driver current is determined by connecting an additional series resistance R_{PV} of 2 Ω and measuring the voltage across it. The secondary circuit contains a pickup coil of resistance R_{SC} that is coaxially coupled to the driver and connected across an external load of 51 Ω. The coil dimensions and other circuit parameters are given in Table 1.

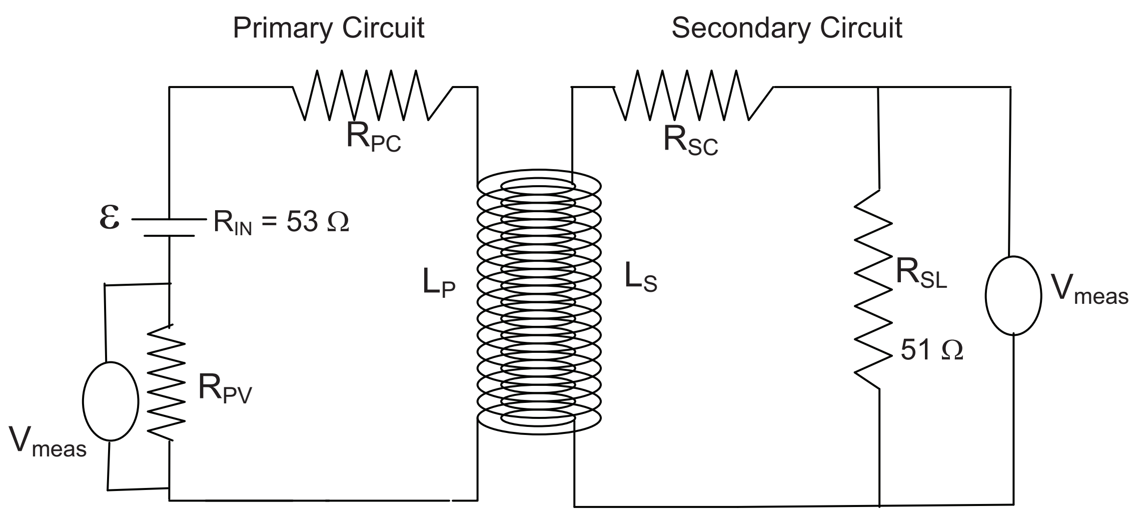

Figure 1. Circuit diagram of a typical reflection-type probe.

The experimental set-up of the TEC scanning system, also called pulsed eddy current (PEC) system, is shown in Figure 2. The pickup coil is located concentrically within the driving coil with a cylindrical ferrite core at the center to produce a reflection-type probe, as shown in the inset of Figure 3. The set-up uses a TecScan system manufactured by TecScan Systems Inc., Montreal and includes the TecView PEC software to capture and analyze the data. An external pulse generator (HP214B) is used to produce a driver signal of amplitude varying from 15 to 30 V, which is sent directly to the driving coil. The induced voltage in the pickup coil drives a current through the secondary circuit resulting in a voltage drop across 51-Ω termination to be sensed by the TecScan system. The System also provides motion control capability through a THK X-Y gantry system, which moves the probe placed in a probe holder.

The measurements were made on multilayer aluminum specimens produced by stacking thin plates (200 mm × 200 mm × 0.40 mm) of Al2024T3 on top of each other with the lowermost plate having a hole of diameter 5 mm. To eliminate the air gaps between the plates, the stack was placed inside a vacuum bag attached to a vacuum pump that maintained a constant pressure on the outer surface of the plates. The total lift-off of the probe from the sample surface was 0.23 mm.

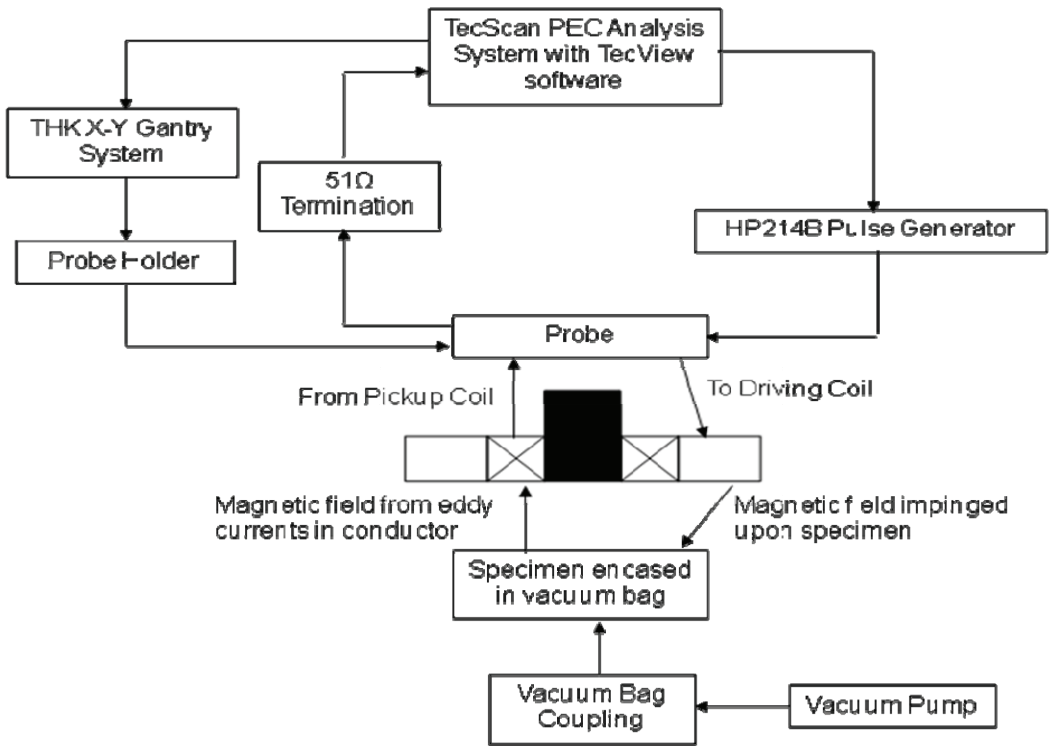

Figure 2. Block diagram of the experimental set-up used for the scanning system.

FINITE ELEMENT MODELING

The probe and samples described above were modeled using COMSOL3.4 Multiphysics commercial software. Both two-dimensional (2D) and three-dimensional (3D) models were used depending on the geometry of the measurement set-up. For example, it was convenient as well as economical to use a 2D model for a 'no defect' sample geometry that was used to study the effect of probe lift-off from the sample surface. For sample geometries involving localized defects, such as circular holes or rectangular cracks, 3D half-models were used. Figure 3 shows a typical 2D quarter-model of a driver-pickup probe placed over a set of three conducting plates. The plates have no defect, so it was possible to use cylindrical symmetry. The corresponding 3D half-model geometry of a multilayer sample with a hole in the lowermost layer is shown in Figure 4. The models were run for a number of plates varying from 0 (air case) to 10, each of thickness 0.4 mm. The modeled plates had no air gap between them, so the plate region is essentially a continuum. The complete model parameters of three different probes used in this work are given in Table 1.

Table 1. Specifications of the probes used for experimental work and FE modeling.

	Driver Coil			**Pickup Coil**
	D400	**D800**	**D1600**	
Length, mm	20.0	20.0	20.0	1.0
Inner diameter, mm	18.9	18.9	18.9	5.9
Outer diameter, mm	20.9	22.8	23.9	8.2
Number of turns	405	809	1635	300
AWG	34	34	34	44
Resistance, Ω	26.0	56.2	121.6	63.2
Length of ferrite core, mm	20, 30, and 40			
Diameter of ferrite core, mm	4.0			
Permeability of ferrite	1500, 2300, and 3100			
Conductivity of ferrite, S/m	0.5			
Conductivity of aluminum, S/m	2.46×10^7			

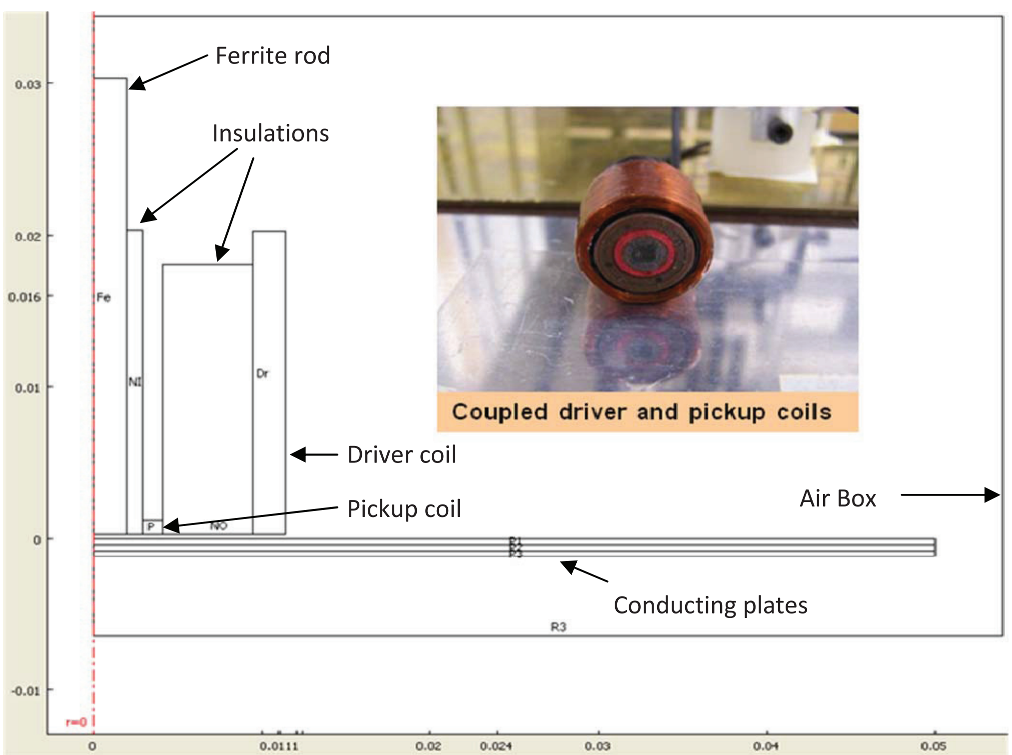

Figure 3. Quarter section of a 2D FE model of a driver/pickup coil probe geometry near a set of three plates. The inset shows the experimental probe of the same geometry.

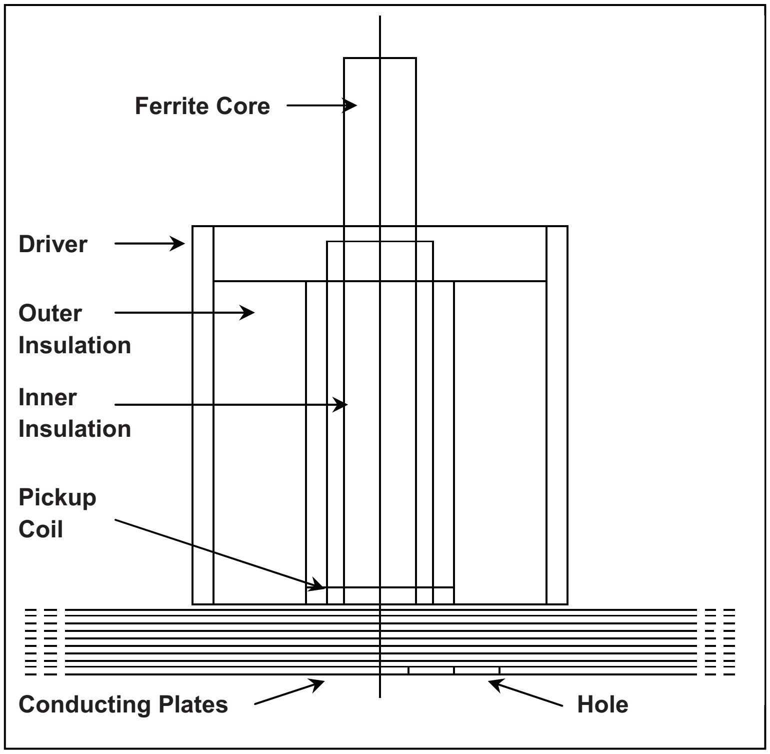

Figure 4. Half-section of a 3D model of 9 plates with a hole in the lowermost plate.

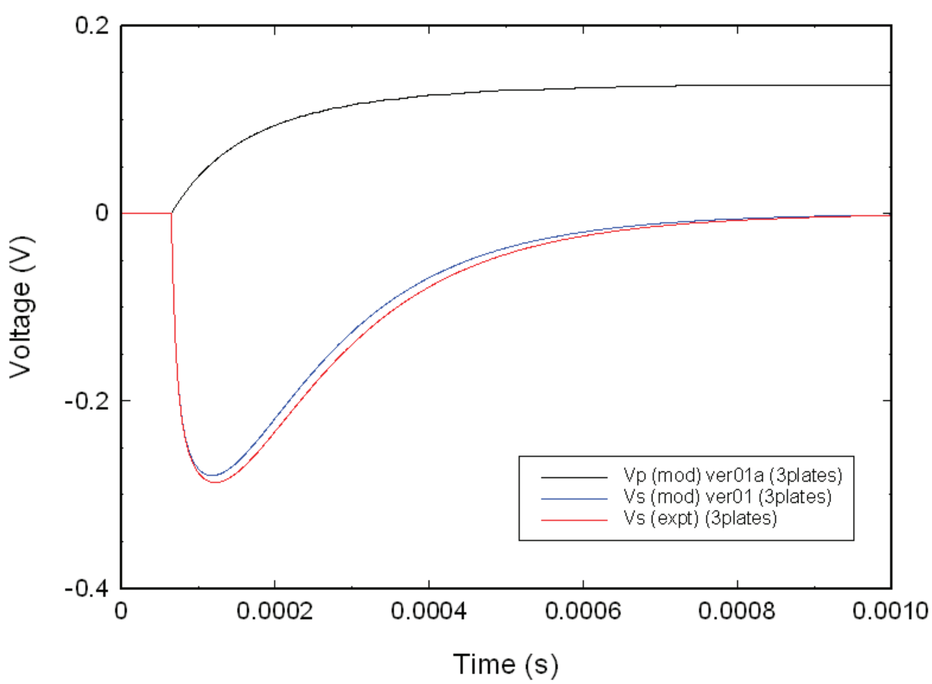

Figure 5. Driver voltage, V_p, and pickup voltage, V_s, for the 'no defect' model of 3 plates shown in Fig. 3. The corresponding experimental pickup signal is shown for comparison.

RESULTS

(a) 'No Defect' Case (2D Model)

Comparison of Modeled and Experimental Signals

The variations of driver voltage and pickup voltage as a function of time are shown in Figure 5 for the 'no defect' case of 3 plates. The corresponding experimental pickup voltage is also shown for comparison. There is reasonably good agreement between the two signals considering that the model runs under ideal conditions. For example, the plates are all stacked together in the model, which may not be strictly true in the experiment. The surface current density at about 0.1 ms, which corresponds to the peak signal amplitude in Figure 5, is shown in Figure 6. It gives a visual distribution of currents that penetrate inside the conducting plates.

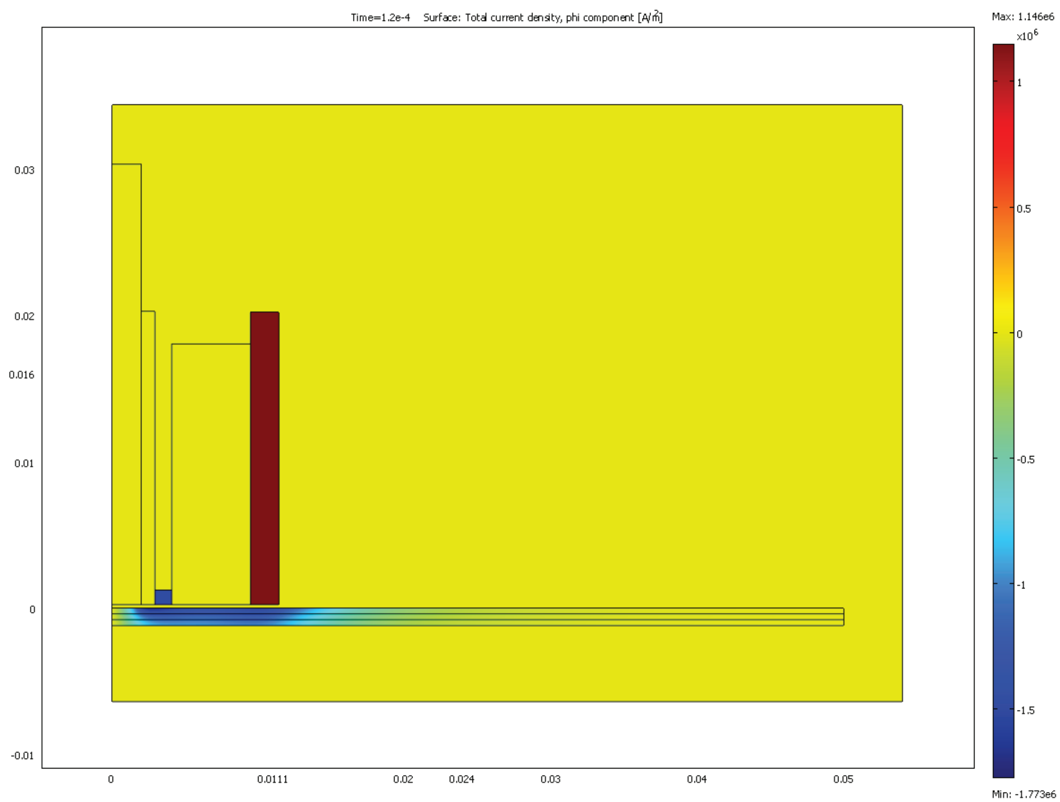

Figure 6. Surface current density corresponding to the peak amplitude of the pickup signal shown in Figure 5.

Effect of Lift-Off

The effect of lift-off was studied by increasing the distance between the probe and the plate up to 2.0 mm. The results are shown in Figure 7. The number of plates in each case was 10. All the pickup voltages, except the one for air, pass through a common point, which is called the lift-off intersection (LOI) point. The point has been observed experimentally by some researchers [2, 3]. The current models thus provide the experimental verification of the LOI point for flat plates.

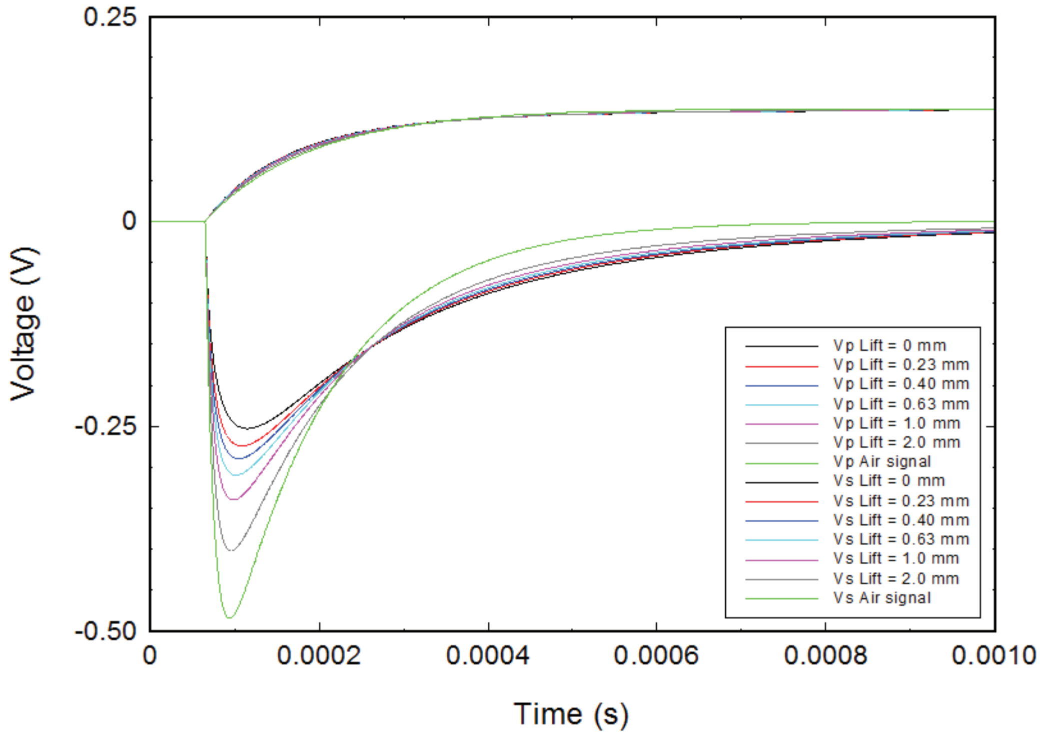

Figure 7. Variation of driver and pickup signals with lift-off for 10 plates case.

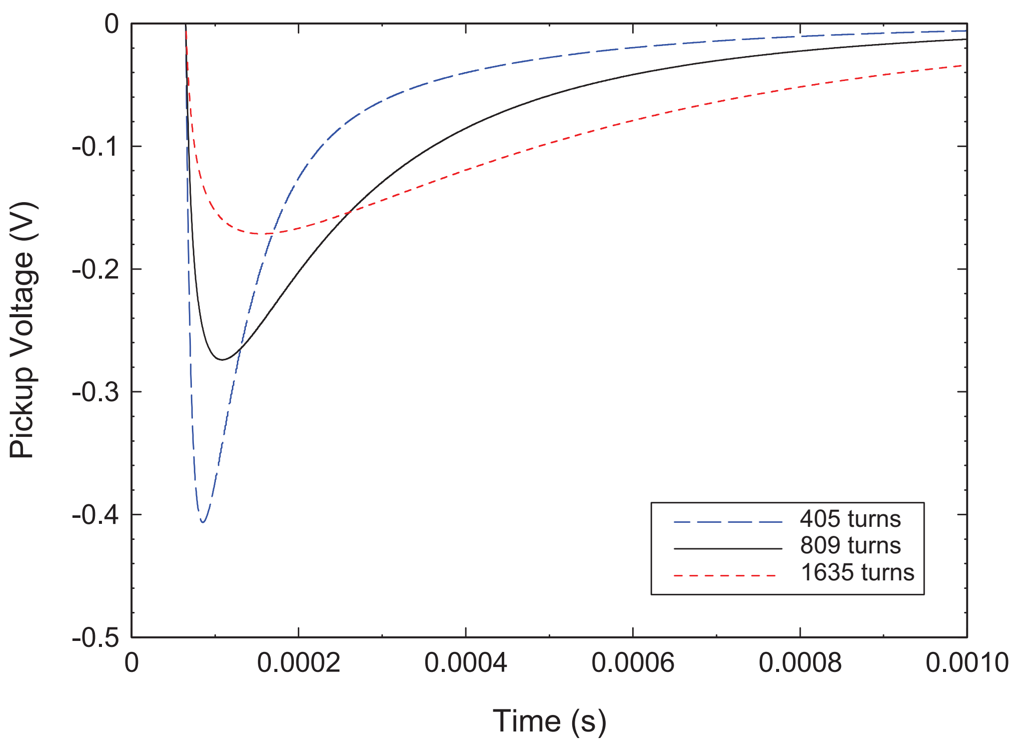

Figure 8. Variation of pickup signal with number of turns of the driver.

Variation of Pickup Signal with Number of Turns of the Driver

The magnitude as well as shape of the pickup signal is significantly affected by the change in the number of turns of the driver. The pickup voltage obtained from three different probes designated as D400, D800, and D1600, where driver has 405, 809 and 1635 turns respectively, is shown in Figure 8. Since each driver uses the same wire gauge, there is concomitant change in the outer diameter, as given in Table 1. The driver D400, which has the least number of turns, produces the greatest signal amplitude that decays at the fastest rate. This is attributed to the cumulative effect of resistance and inductance of the driving circuit with inductance playing a dominant role. Higher inductance contributes greater relaxation time, which acts to slow down both growth and decay of the driver voltage, thus causing a corresponding variation in the pickup voltage. While a greater driver voltage is an advantage, a larger relaxation time is vital to detection of deep-lying defects by TEC where the diffusing currents usually interact with defects later in time. For the driver D1600, the signal amplitude gets too low. So the driver D800 seems to be a better trade-off between greater relaxation time and larger peak amplitude.

Effect of Core Length and Permeability

The pickup signal for three different core lengths is shown in Figure 9. The signal, in general, increases with the length of the core; the increase is more pronounced for a change in length from 20 to 30 mm than from 30 to 40 mm. Long cores generate flux that can penetrate deeper into the sample and produce greater current density throughout the sample parallel to the surface. Although a longer core can produce stronger signal, it makes the probe bulky. A core length of 30 mm was found to be optimum for the present work. To investigate the effect of permeability, models were produced with core permeability of 1500, 2300 and 3000, but the pickup signal was found to be the same for each case. A ferrite core of permeability 2300 was used for the experimental work.

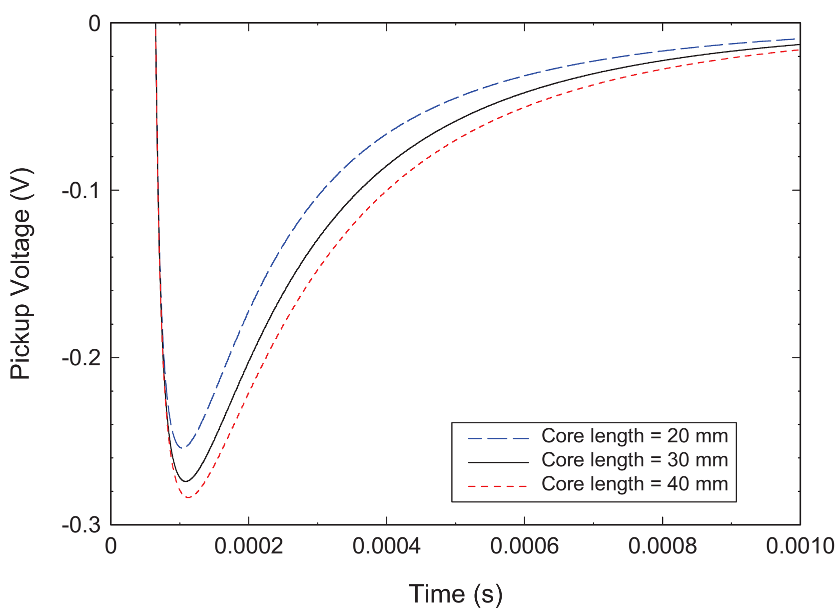

Figure 9. Effect of core length on pickup signal.

(b) 'Defect Case' (3D Model)

Background-Subtracted Signal

The pickup signal from 'no defect' case looks similar to the 'defect' case except for a slight difference in peak amplitude and shape. The information about defect is obtained only when the 'no defect', reference, or background signal is subtracted from the 'defect signal'. An example of a reference-subtracted signal for a hole in a single plate is given in Figure 10, which also shows the original pickup signals. The magnified subtracted signal (Figure 11) shows two peaks, which have different magnitudes and opposite polarities with the smaller peak occurring later in time. As will be discussed later, the first peak occurs because of Lenz's law, as in the case of sinusoidally excited eddy currents, while the second one is related to currents induced by the decay of the primary currents (transients). Although the amplitude and position of both the peaks are affected by the change in thickness of the multilayer structure, the shallower peak undergoes a greater shift in position and slower change in amplitude.

Variation of Signal with Thickness of Multilayered Structure

The variation of the reference-subtracted signal with increased number of plates (or thickness of the multilayer structure) is shown in Figure 12 for a particular probe position relative to the center of the hole. The hole exists in the lowermost plate. The amplitude of both the peaks decreased and the peaks shifted to later times with increase in thickness; the shift was more prominent in the second peak, which is associated with secondary induced currents within conducting structure. The signal response is believed to be associated with a diffusion wave, which penetrates through the thickness of the conductor with a velocity at the peaks that is given by the slope of the position-time plot, as shown in Figure 13. The plot corresponding to each peak is almost a straight line. The experimental points are also plotted for comparison and were found to be in good agreement with the model results. The velocity corresponding to the first and second peaks is about 22 and 8 m/s respectively. These results are discussed in the next section.

INTERPRETATION OF RESULTS

The electrodynamic response of the aluminum plate conductor to the application of a transient magnetic field can be described in terms of the induced electric and magnetic fields within the conductor. For the timescales over which the measurements are obtained here ($\sim 10^{-4}$ s), this is a two stage process [15]. First, the expulsion of the dynamic electric and magnetic fields occurs and, second, the surface currents and wave fields are damped. The initial expulsion of electromagnetic fields from within the conducting material arises by induced eddy currents as expressed by Lenz's law, with their depth of penetration limited by the skin depth [16]. Within the body of the sample, these induced currents, in turn, decay (are damped), and the changing magnetic field associated with this process, in turn, results in opposing eddy currents deeper within the sample. This may also be described in a process similar to that of a damped wave [17]. With the presence of the discontinuity this damping occurs more rapidly because of increase of resistance.

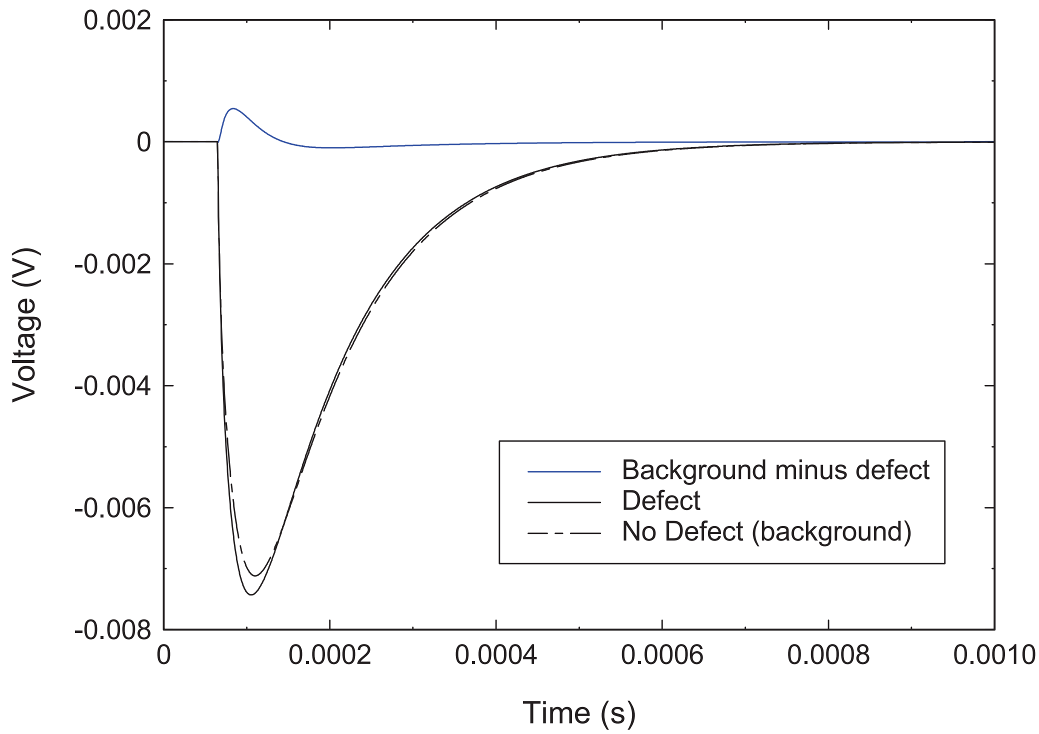

Figure 10. Original and subtracted pickup signals from a single plate sample.

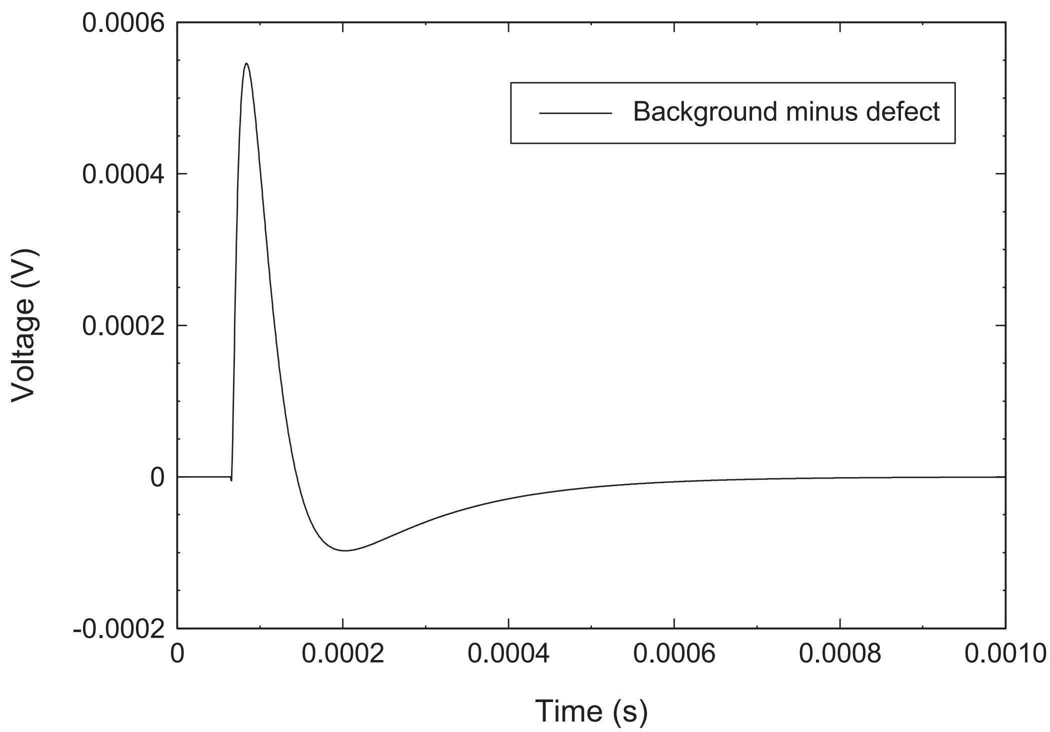

Figure 11. Magnified reference-subtracted signal shown in Figure 9.

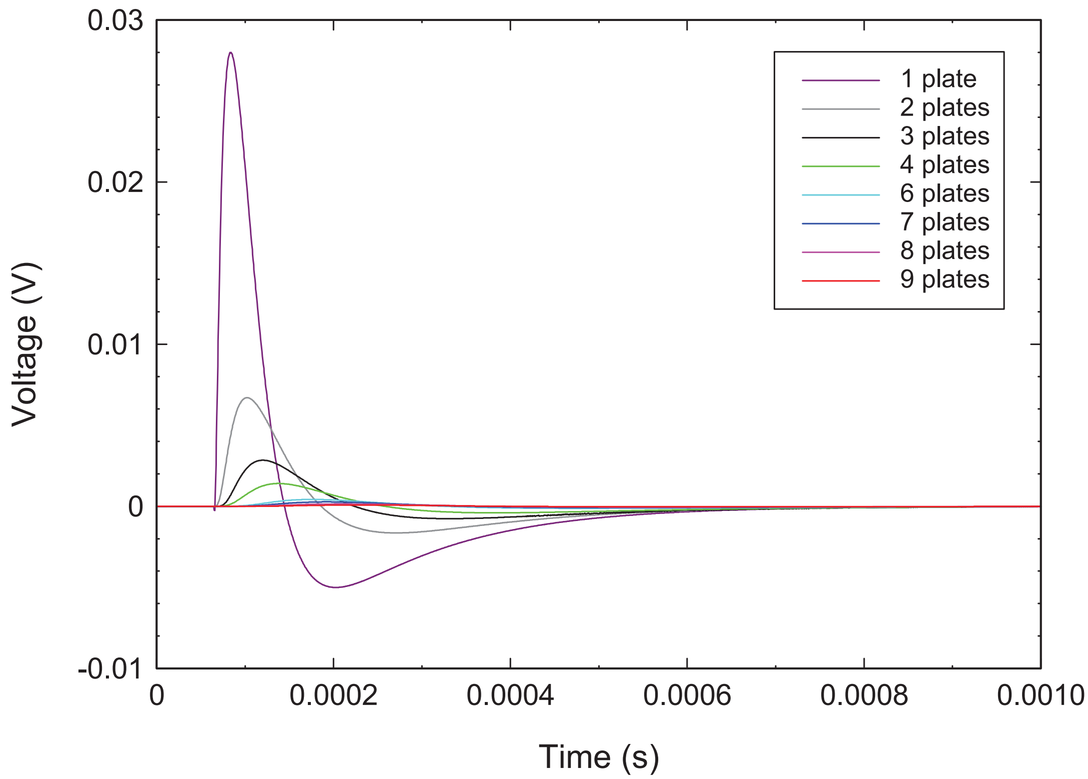

Figure 12. Variation of reference-subtracted pickup signal with number of plates.

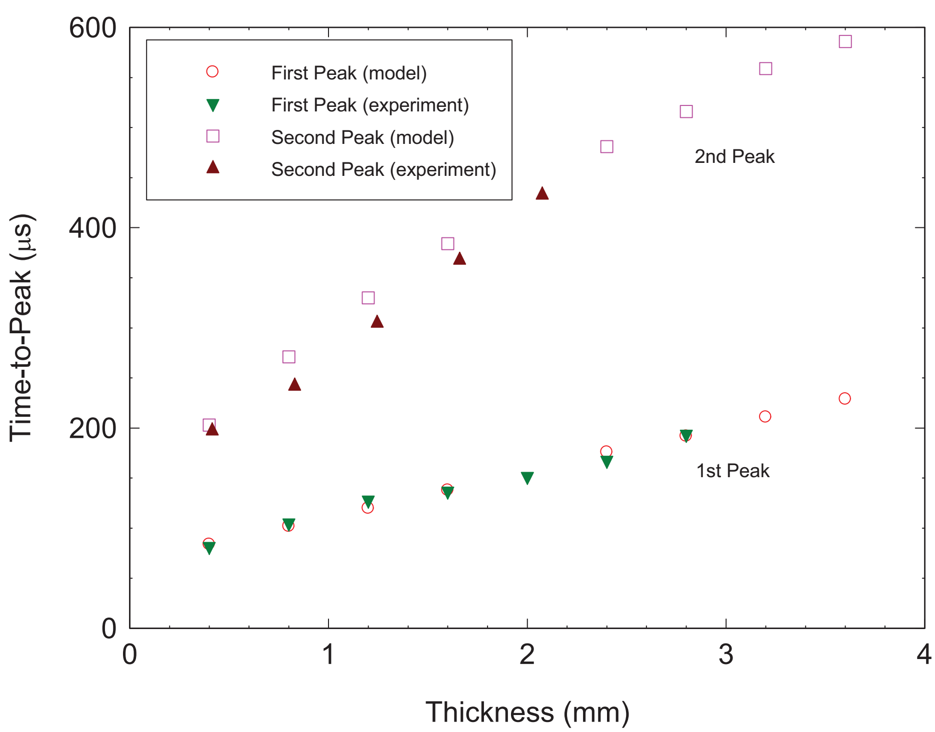

Figure 13. Time-to-peak versus total thickness of the conducting layers.

Referring to Figure 11, the initial positive peak is associated with the induced eddy currents produced due to the Lenz's law. As the primary induced currents decay, the associated changing field induces currents deeper within the sample. These currents are reversed and more diffused than the primary currents and are associated with the minimum response shown in Figure 11. For deeper defects, the interaction of induced currents gets weaker and occurs later in time as is evident from Figure 12, which shows decrease in amplitude of both primary and secondary peaks, and peaks arising later in time. The time position of both the first and second peaks varies linearly with thickness of the plate, as shown in Figure 13, with the second peak occurring at a proportionately later time (3×) than the first. This is attributed to the progression of diffusion wave fronts into the stack of plates. Also, the rate of decay of the secondary peak is not as rapid as that of the first, suggesting that greater depth-of-penetration is possible with the secondary currents. Recent measurements have demonstrated that enhanced signal-to-noise of the hole can be attained with analysis techniques applied in the region of the second peak [11], which is consistent with the interpretation of the greater depth of penetration achievable with the secondary induced eddy current process.

CONCLUTION

FE modeling was successful in simulating the TEC response in multilayered aluminum structures containing circular defects. It verified some known experimental results, such as the existence of the lift-off intersection point, and contributed in investigating different probe configurations and finding the optimum probe parameters. The existence of two peaks and the shifts of the peaks were indicative of diffusion wave phenomena, where the second peak was associated with the secondary induced currents that have greater depth-of-penetration within the material. The modeling appears to be a very promising technique to study multilayered airplane wing structures having cracks near the ferrous fasteners.

ACKNOWLEDGEMENT

The authors thank Mr. Kevin Wannamaker for technical assistance. This work is supported by the Natural Sciences and Engineering Research Council of Canada, the Academic Research Program at the Royal Military College of Canada and Defense Research and Development Canada.

REFERENCES

1. M. Gibbs and J. Campbess, *Mater. Eval.*, **49**, pp. 51-59 (1991).
2. S. Giguere and J. M. S. Dubois, "Pulsed Eddy Current: Finding Corrosion Independently of Transducer Lift-off," in *Review of Progress in QNDE*, **19**, edited by D. O. Thompson and D. E. Chimenti, AIP Conference Proceedings, American Institute of Physics, Melville, NY, 2000, pp. 449-456.
3. S. Giguere, B.A. Lepine and J.M.S Dubois, "Pulsed Eddy Current Technology: Characterizing Material Loss with Gap and Lift-off Variations," in *Review of Progress in QNDE*, **20**, edited by D. O. Thompson and D. E. Chimenti, AIP

Conference Proceedings, American Institute of Physics, Melville, NY, 2001, pp. 119-129.
4. Y. A. Plotnikov, S. C. Nath and C. W. Rose, "Defect Characterization in Multilayered Conductive Components with Pulsed Eddy Current," in *Review of Progress in QNDE*, **21**, *op. cit.*, 2002, pp. 1976-1983.
5. T. W. Krause, C. Mandache, and J. H. V. Lefebvre, "Diffusion of Pulsed Eddy Currents in Thin Conducting Plates," in *Review of Progress in QNDE*, **27**, *op. cit.*, 2008, pp. 368-375.
6. J. R. Bowler, D. J. Harrison, "Measurement and Calculation of Transient Eddy Currents in Layered Structures," in *Review of Progress in QNDE*, **11**, *op. cit.*, 1992, pp. 241-248.
7. D. J. Harrison, "The Detection of Corrosion in Layered Structures Using Transient Eddy Currents," in *Nondestructive Testing of Materials*, edited by R. Collins, W. D. Dover, J. R. Bowler and K. Miya, IOS Press, Tokyo, 1995, pp. 119-124.
8. J. R. Bowler, Pulsed Eddy Current Interaction with Subsurface Cracks," in *Review of Progress in QNDE*, **18**, *op. cit.*, 1999, pp. 477-483.
9. R. A. Smith, D. Edgar, J. Skramstad and J. Buckley, *Insight*, **46**, pp. 88-91 (2004).
10. F. Fu and J. Bowler, *IEEE Trans. Mag.*, **42**, pp. 2029-2037 (2006).
11. T. J. Cadeau, "Increased Field Depth Penetration with Pulsed Eddy Current", M.Sc. Thesis, Royal Military College, Kingston, Ontario, Canada (2008).
12. T. J. Cadeau and T.W. Krause, "Pulsed Eddy Current Probe Design Based on Transient Circuit Analysis," in *Review of Progress in QNDE*, **28**, *op. cit.*, 2009, pp. 327-334.
13. COMSOL Inc., Burlington, MA 01803. http://www.comsol.com/
14. V. K. Babbar, P. V. Kooten, T. J. Cadeau and T. W. Krause, "Finite Element Modeling of Pulsed Eddy Current Signals from Conducting Cylinders and Plates," in *Review of Progress in QNDE*, **28**, *op. cit.*, 2009, pp. 311-318.
15. H. C. Ohanian, "On the approach to electro- and magneto-static equilibrium", Am. J. Phys., **51**, pp. 1020-1022 (1983).
16. D. J. Griffiths, Introduction to Electrodynamics, 3e (Prentice-Hall, Upper Saddle River, New Jersey) 1999, pp. 303, 315 and 393.
17. M. Namkung, B. Wincheski, S. Nath, and J.P. Fulton, "Transient Electromagnetic Fields in Highly Conductive Media", in *Review of Progress in QNDE*, **18**, *op. cit.*, 1999, pp. 523-529.

Wave Propagation Concrete NDT Techniques for Evaluation of Structures and Materials

Afshin Sadri[1] and Koorosh Mirkhani[2]

Abstract
The useful life and work capacity of concrete structures largely depend on their construction practice, maintenance performance, and material capabilities. As such, an accurate estimate of the structure's remaining service life as part of a quality control program, demands precise condition assessment of the structure. Both by applying intrusive extraction of samples and by non-destructive testing methods have been applied to measure the strength of the structures in addition of identifying weak areas of deterioration, cracking and defect formations. A review of wave propagation non-destructive testing methods to test concrete structures is the subject of this article. The non-destructive testing methods discussed here utilize stress and electromagnetic waves to obtain the information required from the structure. Applications of each testing method have been briefly described.

Introduction
The life cycle and load-bearing capacity of concrete structures depend in great part on their thicknesses, original mixes, placing consolidations, curing conditions, reinforcements and later deterioration. The common practice for quality evaluation of concrete structures is the application of intrusive testing, applying drilling, sampling and laboratory testing. A more rapid and inexpensive methodology would apply the use of nondestructive testing (NDT) techniques.

In the inspection of metals and homogeneous–isotropic materials, NDT is an accepted practice. For example, radiographic and ultrasonic techniques are routinely used to identify anomalies in steel pipelines and rail lines, and there are recognized national and international standards on their use. However, in the inspection of concrete, the use of nondestructive testing methods is relatively new. The instrumentation and application of nondestructive testing techniques to concrete is at an early stage, mainly due to the complex nature of the material.

In the past few years, there has been progress in the development of nondestructive methods for testing concrete, and in recent years several methods have been standardized by the American society for Testing and Materials (ASTM), American Concrete Institute (ACI), the International Standards Organization (ISO) and the British Standards Institute (BSI).

Among the various NDT techniques for concrete, the stress wave propagation techniques such as impact-echo, impulse-response, pulse-echo, spectrum analysis of surface waves (SASW), ultrasonic through transmission and electromagnetic techniques such as short-pulse radar or ground penetrating radar (GPR) are the most popular and best understood methods by the engineers. All the above methods have shown that the common feature of them is that interferences about internal conditions of concrete structures are made based on the effect that the structure has on the propagation of stress and electromagnetic wave. The methods differ in the source of wave generation, the testing configuration, the characteristics of measured response and the signal processing techniques that are used. These differences make each method particularly suitable for specific applications.

Here, a brief description of stress and electromagnetic wave propagation principle and techniques in addition to the capabilities of each technique is presented.

Stress Wave Propagation Principles
A disturbance on a solid causes the entire body to respond by linear and angular accelerations. The applied force causes deformation in the solid body. Stress waves are generated, if the deformation is in elastic range and the applied force is rapid and changes with time, such as piezoelectric transducers or the collision of two solid bodies. Two types of stress waves propagate in a solid: compression waves or P waves and shear waves or S wave. The third type of stress waves propagates along the surface and is known as Rayleigh waves or R-wave. Particle motion at the wavefront for P wave is parallel to the direction of propagation, which produces compressive or tensile stress. For S waves, particle motion is vertical to the direction of propagation, which produces shear stress. R wave have a retrograde elliptical particle motion. P waves travel at higher velocities, followed by S wave and R waves, in that order. Stress wave follow the fundamental equation of waves:

$$C = f \times \lambda \qquad 1$$

where C is the wave velocity, f is the wave frequency and λ is the wavelength.

Stress wave velocity in a solid depends upon the elastic properties and the density of the material from which it is composed. In an infinite elastic solid, the velocity of P wave is computed by the following equation:

[1] Afshin Sadri, Ph.D., P.Eng., Global Director of Hath NDT Group, Hatch Ltd., 2800 Speakman Dr., Mississauga, Ontario L5K 2R, Canada.

[2] Koorosh Mirkhani, Ph.D., P.Eng., NDT Specialist, Hatch Ltd., 2800 Speakman Dr., Mississauga, Ontario L5K 2R7, Canada.

$$C_P = \sqrt{\frac{E(1-\nu)}{(1+\nu)(1-2\nu)\rho}} \qquad 2$$

where E is the Young's modulus of elasticity, C_P is the P wave velocity, ρ is the density and ν is the Poisson's ration. In rod-shaped structures, where the diameter of the cylinder is much smaller than its length, $d \langle\langle l$ m the P wave velocity is slower than in an infinite elastic solid and is given by the following equation:

$$C_P = \sqrt{\frac{E}{\rho}} \qquad 3$$

The shear wave velocity C_S, is calculated by the following equation:

$$C_S = \sqrt{\frac{E)}{2(1+\nu)\rho}} \qquad 4$$

Rayleigh wave velocity C_R, can be determined by the following equation:

$$C_R = \frac{0.87+1.12\nu}{1+\nu} C_S \qquad 5$$

The encounter of stress waves with an acoustic interface causes reflection, refraction and mode conversion of the waveforms. An acoustic interface is a boundary between two materials with different acoustic impedances. Acoustic impedance, Z is defined by the following equation:

$$Z = \rho \times C_P \qquad 6$$

The acoustic impedance of each material and the wave's angle of incidence, control the stresses associated with the wave reflection and refraction. For a P wave with a normal angle of incidence, the incident and reflected stresses are computed by the following equation:

$$R_P = I_P \times \frac{Z_2 - Z_1}{Z_2 + Z_1} \qquad 7$$

where I_P is the stress associated with incident P waves, R_P is the stress associated with reflected P waves, Z_1 is the acoustic impedance for the first medium and Z_2 is the acoustic impedance for the second medium. For example if P waves are reflected from a medium with lower Z_2, than the initial medium ($Z_2 \langle Z_1$), their sign (polarity) changes (i.e. concrete/air interface). This means that a compression wave changes to a tension wave. However if Z_2 is higher than Z_1 ($Z_2 \rangle Z_1$), the reflected wave remains with the same sign as the incident wave.

Stress Wave NDT Techniques

Impact-Echo

N.J. Carino and M. Sansalone developed the technique called impact-echo for nondestructive testing of concrete structures at the United States National Institute of Standards and Technology[1]. This testing technique is based upon a simple concept: a mechanical impact is generated on the surface of the test object, and the surface displacements close to the impact point are measured. The stress waves, which propagate into the object, undergo multiple reflections between the test surface and the internal defects of the opposite boundary of the test object. The path length of reflected P waves is twice the distance from the surface to the internal defect *2T*. Hence the travel time, *t*, between the successive arrivals of reflected P waves relies on the P wave velocity C_P, and is computed by the following equation:

$$t = \frac{2T}{C_P} \qquad 8$$

By monitoring the vertical surface displacements caused by the arrival of the multiple P wave reflection (echoes), the depth of the reflecting surface can be determined.

While a similar approach (impulse-response) has been used successfully for the evaluation of one-dimensional structures (piles and piers), the impact-echo method has the potential to be very successful in the evaluation of three-dimensional structures. Currently, several State departments of transportation are experimenting with the impact-echo method to measure pavement thickness.

The impact-echo test system is composed of three components: an impact source, a receiving transducer and a waveform analyzer, which is used to capture the transient output of the transducer to store the digitized waveforms and to perform the signal analysis. The contact time duration, t_C and the time history of the impact is critical in determining the depth and size of internal defects which can be detected; the contact time determines frequency of the stress pulse. As a general rule, the highest frequency component with significant amplitude has a frequency value that is approximately equal to the inverse of the contact time, and the shortest wavelength (wave speed divided by maximum frequency) has to be approximately equal to or less than the dimension of the smallest flaw to be detected. The receiving transducer must be broadband so that it will respond over a wide range of frequencies. This is a low frequency approach, which is the main reason why it has the potential to be successfully used in the inspection of large concrete structures. However, the complex waveforms make the time domain analysis difficult and impractical. The periodical arrival of P waves on the surface can be expressed in frequency by the following equation:

$$t = \frac{1}{f_P} \qquad 9$$

The resulting time domain spectra can be converted to the frequency domain by using the fast Fourier transform (FFT). Equation (8) can be written in to the following format:

$$T = \frac{C_P}{2f_P} \qquad 10$$

Equation (10) is valid only for the pulses reflecting from a free or low stress boundary (i.e. concrete/air or concrete/soil boundary). Where the second boundary has higher acoustic properties than the first boundary (i.e. concrete/steel or concrete/rock), based on equation (7), the reflection characteristics of the signal change. As a result, this doubles the period of signal arrivals on the surface of the concrete. Hence, equation (10) should be re-written in the following format:

$$T = \frac{C_P}{4f_P} \qquad 11$$

A frequency analysis has been the recommended method for interpreting the results of the impact-echo tests. Peaks in the amplitude spectrum can be readily converted to the depth of the reflecting interfaces. A spectral peak plotting technique is usually used to construct an "image" of the interior of the test object. For accurate detection of defects and thickness, shape condition of the structures must be taken in to consideration. The impact-echo inspection is performed according to ASTM C1383.

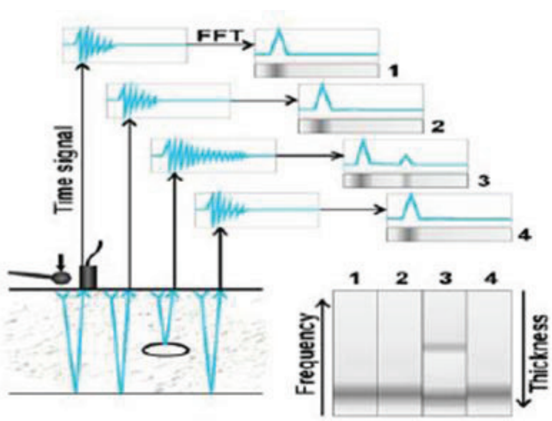

Figure #1: Impact-Echo Principle

Applications
The impact-echo system has been used to measure plate thickness, early age concrete strength, detection and location of cracks and voids in plate-like structures, columns and piles. Detection of shallow delaminations, unconsolidated concrete, honeycombing, depth of surface opening cracks, bond quality at internal interfaces, plates with asphalt overlays, hollow cylinders, mines shafts and tunnel linings and the position of reinforcement bars. Most recently the impact-echo technique has been applied in order to identify micro-cracks (generated by freeze-thaw cycles or AAR) density in structures.

Spectral Analysis of Surface Waves (SASW)
The spectral analysis of surface waves (SASW) is based on the principle that the various wavelength components in the impact-generated surface wave penetrate to different depths in layered pavements[2]. Because a layered system is a dispersive media for R waves, different frequency components of the R wave will propagate different speeds. Therefore, velocity of a given R wave, C_R, is a function of material properties of the layer it propagates.
The SASW system consists of an impact device, two surface displacements transducers, and a waveform analyzer. The system is used to determine the stiffness profile of layered structures. The R wave velocity for each frequency components is also known as the "phase velocity". The phase velocity is calculated by the travel time between the two receivers. The travel time is determined by measuring the phase difference of the frequency components when they arrive at the receivers, where the distance between the two receivers is known. A digitized waveform analyzer is used to determined phase information of the cross power spectrum between the two receivers for each frequency. The schematic presentation of the SASW system is shown in Figure #2.

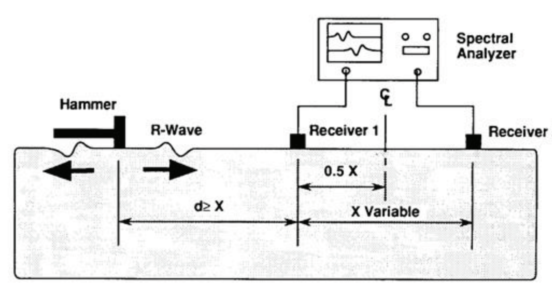

Figure #2: Principle of SASW system

The R wave velocity, C_R, is obtained by dividing the receiver spacing, *X,* by the travel time Δt, at a frequency:

$$C_R = \frac{X}{\Delta t} \qquad 12$$

The Δt for a given wavelength is measured from the phase difference ϕ :

$$\phi = \frac{\Delta t}{t^*} 360^\circ = \Delta t . f .360^\circ \qquad 13$$

Or

$$\Delta t = \frac{\phi}{360^\circ f} \qquad 14$$

where t^* is the characteristic period and f is a given frequency.
Therefore equation (12) can be written as:

$$C_R = \frac{360}{\phi} .X.f \qquad 15$$

The wavelength Λ is related to the phase velocity and frequency by:

$$\Lambda = \frac{C_R}{f} = \frac{360}{\phi} .X \qquad 16$$

The calculation are repeated for each component frequency and a plot of the wavelength versus phase velocity is obtained; it is known as"dispersion curve", it is used to obtain the dynamic modulus of elasticity. A process called "inversion" is used to approximate the dynamic modulus of elasticity.

Applications
The SASW technique is used for the determination of the stiffness profile of flexible and rigid pavement system. The SASW technique has extensively been used for pavement (with or without overlay) quality control.

Ultrasonic Through-Transmission
The ultrasonic through-transmission (UTT) technique exploits the relationship between the quality of concrete and the velocity of an ultrasonic pulse through the material. The equipment consists of a transmitting and a receiving transducer, a digital waveform analyzer or a UTT meter. The transducers are coupled to the concrete (usually the opposite faces of a section) with petroleum jelly or grease.

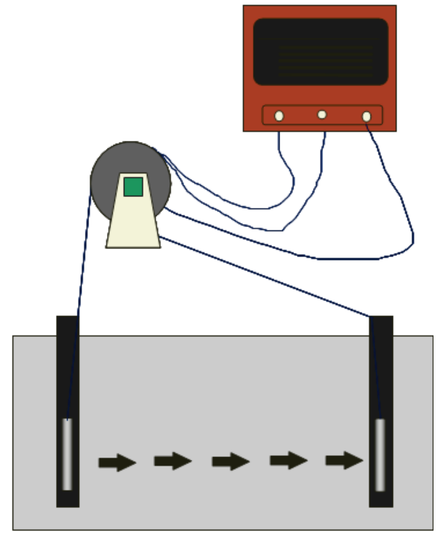

Figure #3: Ultrasonic through transmission

The test involves the travelling of an ultrasonic pulse into a concrete section with a known thickness or transducers separation distance. The pulse velocity computed by the following equation:

$$C_P = \frac{X}{t} \qquad 17$$

where X is the distance between the two transducers and t is the travel time for the pulse travelling between the transmitting transducer and the receiving transducer.
Fairly extensive research has been done in an attempt to correlate the pulse velocity with the compressive strength[3]. The idea is that pulse velocity is a function of material density and stiffness, both of which have been correlated with compressive strength. In practice, however, the results have been mixed. The number of variable, which affect concrete compressive strength, is large. Water-cement ration, aggregate size and shape, size of sample and cement content all directly relate to strength[4]. However, not all of these variables affect the pulse velocity. Thus it is difficult to universally apply pulse velocity methods to concrete. It has been generally accepted that pulse velocity can be a good indicator of strength gain of concrete at early ages (up to a few days). The *Ultrasonic through transmission* technique, Figure #3 can be applied in order to evaluate uniformly of the concrete in a structure. This type of measurement is generally qualitative in nature, and yield little quantitative information. Ultrasonic through transmission is extensively used in laboratories and on larger scale structures, such as concrete dams and bridges. In large structures ultrasonic tomography is often used in order to create an acoustic image of the structure[5]. In acoustic tomography, the object is reconstructed from the spatial distribution of stress wave propagation

velocity, which depends on the characteristics of the medium. As a result, areas of high and low wave velocity are characterized by various contouring techniques. In some applications water immersion transducers are used in boreholes in order to characterize to concrete mass between two holes. This technique is called crosshole sonic or ultrasonic (depends on the frequency of signal propagation) logging and parallel ultrasonic logging.

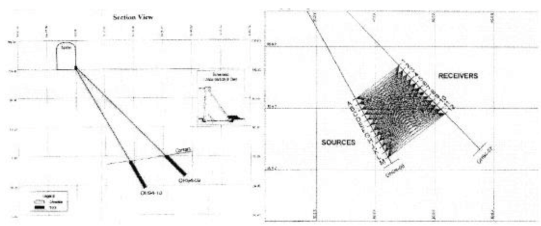

Figure #4: Crosshole sonic (ultrasonic) logging

The *Ultrasonic Pulse-echo* system, Figure #5 is used to detect the position of the cracks and discontinuities in the structure. Both transmitting and receiving transducers are placed on the same face of the structure. The position of the discontinuity is computed based on the change in the travel time of the ultrasonic signal. In the recent developments particular filters (Split Spectrum Processing or SSP) are used in order to remove the effect of inherent noise caused by aggregates and air bubbles. The UTT inspection is performed according to ASTM C 597.

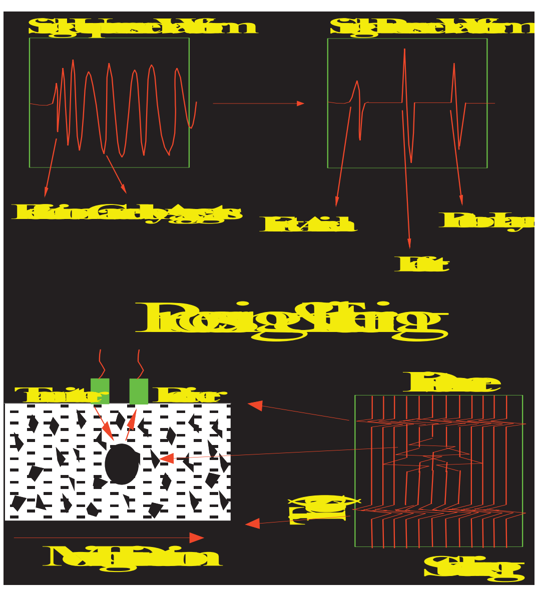

Figure #5: Pulse-echo technique

Applications
The through transmission technique is mainly used to qualify a concrete structure, monitor early-age strength and to evaluate the modulus of elasticity. Crosshole sonic or ultrasonic (depends on the frequency of signal propagation) logging and parallel ultrasonic logging is to qualify deep foundations, piles, bridge columns and dams. The pulse-echo technique is used to measure thickness and detect flaws and discontinuities in thin concrete structures. Pulse-echo systems are particularly useful for detection of discontinuities and thickness in concretes having less than 10 cm thickness such as concrete pipes.

Miniature Seismic Reflection (MSR)
The Miniature Seismic Reflection (MSR) system functions based on impact-echo principle, Figure #6, illustrates the schematic diagram of the MSR system.

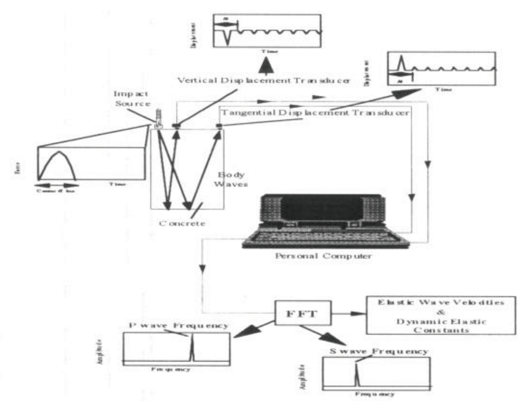

Figure #6: The MSR system

A supplemental tangential displacement transducer enables the user to evaluate the dynamic elastic properties of concrete directly and in-situ. Therefore, the MSR system consists of a vertical and tangential transducer, impact source and a waveform analyzer. The P wave velocity is calculated by re-writing equation (10) to the following format:

$$C_P = 2T.f_P \qquad 18$$

The output of the tangential displacement transducer is used to generate a frequency spectrum. The maximum peak of the frequency spectrum is the indicator of the shear wave reflections. Knowing the thickness and frequency, the S wave velocity can be calculated by the following equation:

$$C_S = 2T.f_S \qquad 19$$

Once the density and the P and S wave velocities of a concrete element are known, the Poisson's ration, Young's modulus, shear modulus and bulk modulus can be calculated. Important advantages of the MSR system over traditional techniques are its capability of operating from one free surface and the fact that the effects of shape and dimensions of the structure are minimal. MSR can also be used to detect flaws and delaminations within the structure.

Applications

The MSR system is used for the determination of elastic properties of plate-like, rod shape and hollow circular concrete structures.

Impulse Response (IR)

The impulse-response (IR) method is a surface reflection technique that relies on the identification of compression wave reflections. The method was developed as a means to quickly and inexpensively evaluate shaft integrity with minimal pile head preparation. Its beginning can be traced back to the late 1970's in France, when it arose as an extension of a vibration test which involved harmonically vibrating a known mass at frequencies up to 2kHz at the head of a shaft and measuring the shaft response with a geophone (Higgs, 1979).

The test involves impacting the top of a drilled shaft (or a pile) with an impulse hammer, which induced transient vibrations with frequencies as high as 2kHz. Both the impact force and particle velocity are measured on the impacted surface. Shaft response is recorded in the time-domain with a geophone or a broadband transducer, and the signal is digitally converted to the frequency-domain for analysis. To calculate the dynamic response of a structure to a given input, the force-time function of the input is convoluted with the impulse response function of the structure. The impulse response is the structure's response to an input having a force-time function that is a single spike at time zero (impulse). The impulse response function is a characteristic of a structure and it changes depending on geometry, support conditions and the existence of flaws or cracks. Alternatively, the impact response can be calculated in the frequency-domain by multiplying the Fourier transform of the force input with Fourier transform of the impulse response function.

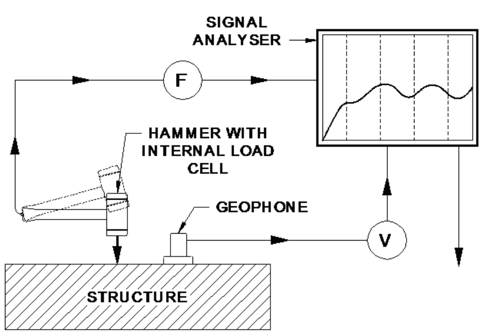

Figure #7: Impulse response data collection on a structure

For analysis, the time history of the impact force and the time history of the structure's response are recorded and the impulse response is calculated. This can be accomplished by de-convolution or in frequency-domain, by dividing the Fourier transform of the response waveform by the Fourier transform of the impact force-time function. In the frequency-domain, the resultant response spectrum indicated structural response as a function of the frequency components of the input. Digital signal processing techniques are used to obtain the impulse response function, often referred to as the transfer function. The transform function is computed through the following steps:

1. Calculate the Fourier transforms of the measured force-time function, f(t) and the measured response, v(t). These will be denoted as $F(\omega)$ and $V(\omega)$.
2. Using the complex conjugate of the Fourier transform of the force-time function $F^*(\omega)$, compute the cross power spectrum, $V(\omega).F^*(\omega)$.
3. Compute the power spectrum of the force-time function, $F(\omega).F^*(\omega)$.
4. Divide the cross-power spectrum by the power spectrum to obtain the transfer function:

$$H(\omega) = \frac{V(\omega).F^*(\omega)}{F(\omega).F^*(\omega)} \qquad 20$$

The test results can be repeated and average power spectra can be used to compute the transfer function. The calculations can be carried out automatically, using a dynamic signal analyzer.

Velocity is measured and the resulting impulse-response spectrum has units of velocity/force, which is referred to as mobility and the spectrum is also called mobility plot. At frequency values corresponding to resonant frequencies of the structure, mobility values are maximum.

The length of the pile can be calculated by the following equation:

$$L = \frac{C_P}{2\Delta f} \qquad 21$$

where C_P is the P wave velocity, *L* is the length of the pile and Δf is the fundamental longitudinal frequency of the pile. Δf is calculated from the mobility plot and is the difference between two adjacent peaks. Figure #8 illustrates a typical mobility plot.

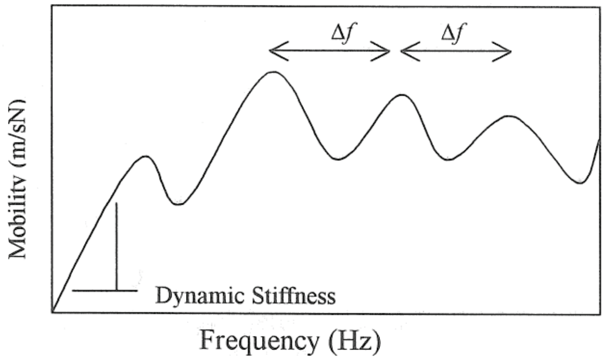

Figure #8: Mobility plot for a pile

At low frequencies, the pile and soil vibrate together and the mobility plot provides information on the dynamic stiffness of the soil/pile structure (Stain, 1982; Davis and Dunn 1974). The slope of the mobility plot represents the dynamic flexibility of the pile head. The dynamic stiffness is the inverse of the dynamic flexibility. Therefore, mobility plots with steeper initial sloped correspond to a lower dynamic stiffness of the pile head. The pile head stiffness is a function of the dynamic stiffness of the pile and the dynamic stiffness of the surrounding soil.

Applications

The impulse-response technique is mainly used to qualify columns and piles in terms of modulus of stiffness. However, IR has been extensively used to detect defects and cracks in columns and pillar like structures.

Short-Pulse Radar (SPR) or Ground Penetrating Radar (GPR)

Electromagnetic wave propagation principles

Short-pulse radar (SPR) is a powerful scientific tool with a wide range of applications in the testing of concrete. SPR waves are electromagnetic (EM) waves that propagate through air at the speed of light. A schematic view of the technique basics is shown in Figure #9.

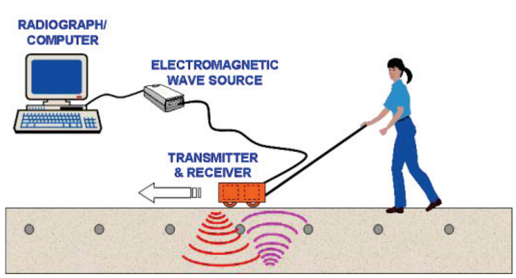

Figure #9: Basics of short-pulse radar technique

The way EM waves behave in other material is governed by the material's dielectric and conductivity properties. Any EM wave that encounters an interface between two materials of different dielectric constants will have part of its energy reflected from the interface, and part of its energy transmitted through the interface. At the air/concrete interface approximately %55 of the signal strength is transmitted into the concrete.

$$\rho = \frac{R}{I} = \frac{\sqrt{\varepsilon_1} - \sqrt{\varepsilon_2}}{\sqrt{\varepsilon_1} + \sqrt{\varepsilon_2}} \qquad 22$$

where ρ is the reflection coefficient, *R*, is the amplitude of reflected energy, *I* is the amplitude of incident energy, ε_1 is the dielectric constant fro material 1 and ε_2 is the dielectric constant for material 2. If material 2 has larger relative dielectric constant than material 1, then ρ would have a negative value.

The receiving antenna will detect the signals that are reflected from an interface. Any defect in a concrete structure, such as air, water, salt water or an air gap, will cause a new dielectric interface in concrete. This interface will cause a reflection that the radar equipment records, then the type of severity of the defect can be estimated. Only defects that are perpendicular to the direction of travel of the radar pulse are detected.

The larger the difference in the dielectric properties between the two materials at an interface is, the larger the reflection from that interface will be. The GPR inspection is performed according to ASTM D 4748.

Applications

Short-pulse radar is capable of rapid detection of delaminations and other types of defects in bare or overload reinforced concrete bridge docks. It has also been used to detect voids underneath pavements and within the concrete mass. In addition to the detection of delaminations in concrete, radar shows potential for other applications such as the monitoring of cement hydration or strength development in concrete, the study of different admixture and additives on concrete, the rapid determination of water content in fresh concrete, the measurement of the thickness of concrete members and the location of reinforcement bars.

Short-pulse radar has also been used to successfully locate underground concrete masonry units, buried utilities, determining dowel bar alignment and areas of high chloride concentration on bridge decks.

The accuracy of the SPR and its ability to detect other types of defects existing in concrete bridge decks and other structures need improvements in the resolution of antenna and by increasing the understanding of the various radar encountered in these structures.

References

1. Sansalone, M.J., and Streett, W.B., *Impact-Echo: Nondestructive Evaluation of Concrete and Masonary.* Bullbrier Press, Ithaca, N.Y.

2. Nazarian, S., Stokoe, K.H., II, and Hudson, W.R, *Use of Spectra-Analysis of Surface Waves Method for Determination of Moduli and Thickness of Pavement Systems,* Trans. Res. Rec., 930, 38, 1983
3. Jones, R., *A. Nondestructive Method of Testing Concrete During Hardening,* Concrete & Constructional Engineering, April, 1949, pp. 127-129.
4. Naik, T.R and Malhotra V.M., *The Ultrasonic Pulse Velocity Method,* Handbook of Nondestructive Testing of Concrete, CRC Press, Edited by Malhotra and Carino, 1991, pp. 188.
5. Rhazi J., Kharrat, Y., Ballivy, G., and Rivest, M., *Application of Acoustical Imaging to the Evaluation of Concrete in Operating Structures,* Innovations in Nondestructive Testing of Concrete, ACI-SP-168-10, 1997, pp. 221-232.
6. Sadri A., *Development of the Miniature Seismic Reflection (MSR) System for Nondestructive Evaluation of Concrete Shaft and Tunnel Linings,* Ph.D., Thesis, McGill University, Montreal, Canada 1996, pp. 423.
7. Goldsmith, W., *Impact: The Theory and Physical Behavior of Colliding Solids,* Edward Arnold Press Ltd., 1965, pp. 250-257.
8. Davis, A. and Dunn, C., *From theory to field experience with the nondestructive vibration testing of piles,* Proc. Inst. Of civil Engineers, vol. 57, Part 2, December 1974, 571.
9. Higgs, J., *Integrity testing of piles by the shock method, Concrete,* October 1979, 31.
10. Stain R., *Integrity testing,* Civil Eng. (London), April 1982, 53.

Automatic Indoor Environmental Conditions Monitoring by IR Thermography

Alberto Pretto, Emanuele Menegatti, Paolo Bison and Ermanno Grinzato

Abstract— **This paper presents a new approach to monitor an indoor environment on thermodynamic basis. It uses temperature as the driving parameter and is especially suited for comfort analysis or evaluation of moisture. The method is based on infrared (IR) thermography, which proved to be very effective in this application. The system measures all fundamental environment parameters (e.g., air temperature, relative humidity and air speed) by imaging with a thermal camera a set of special targets arranged in a grid, which can be placed close to a wall or in any other place of the room . At the same time, the system images the wall surface behind the grid and so can measures the wall's temperature, as well. The thermal camera was mounted on a pan-til unit to realize the monitoring process in an automatic way. The core of the device is a software that can process the thermal images online and control the pan-tilt unit. A fast automatic learning procedure enables to recognize the special target on the grid also in challenging environments and in very different environment conditions. This coupled with the advanced features of modern off the shelve IR cameras allows effective and robust results. This paper illustrates the developed device (both the hardware and the software) and shows the current application of evaluating the decay risk of a heritage building covered by Italian renaissance frescoes. However, the presented approach can be applied in different applications, for instance: indoor environmental monitoring, energy saving, NDT of buildings, and information technology with geomatics.**

I. INTRODUCTION

The instruments utilized to monitor the environmental conditions are not appropriate to map local values such as temperature, light, humidity, air velocity inside buildings. For instance it is totally unpractical to move a measurement head comprising a temperature sensor, anemometer, hygrometer every 10 cm in a given room! Moreover, variations of interest are sometimes below the range of common instrumentation. For instance, low limit for ordinary anemometers is about $0.5\ ms^{-1}$ while natural convection occurring in buildings could be even smaller than $0.1\ ms^{-1}$. Tight building envelopes are another rising problem, since, in case of poor air exchange, the risk of high levels of humidity might conduct to health problem related to the development of fungi.

Another issue is the Non-destructive moisture detection, because moisture is the main reason for building damages. Currently, the moisture survey of buildings, performed using equipment such as moisture meters, is slow and prohibits the monitoring of hard-to-reach locations. An infrared thermal imaging camera helps to monitor moisture by imaging the different temperatures of wet versus dry building materials, making it a useful tool for a building moisture survey. Areas surveyed by the IR camera can be located before standard moisture detection equipment can. Sometime, a moisture survey of water damage can be performed with the infrared camera simply by walking through the affected building. Nondestructive testing of water intrusion can be performed using the IR camera in modern buildings, but could fails when high relative humidity and low temperature decrease the evaporation process. More important, the relation between moisture and temperature is much more complex as expected and a much deeper knowledge is needed [12].

Generally, the study of the indoor thermal and humidity

Fig. 1. The IR camera in front of the reference grid used to monitor the environmental conditions of the Masino castle (Italy) with the proposed approach.

conditions is a problem addressed by many authors, since a

Pretto and Menegatti are with the University of Padova, Dep. of Information Engineering (DEI), via Gradenigo 6/B - 35131 Padova (Italy)
Bison and Grinzato are with CNR-ITC, corso Stati Uniti 4 35127 Padova (Italy) http://www.itc.cn.it

long time ago [4]. The distribution of the surface temperature is of course very important, but the correct approach is to measure the boundary air conditions, at the same time. It is a matter of fact that the main limiting factor is the difficulty to analyze the environmental conditions using a suitable time and space scale. In fact, for a detailed study the density of measurement required is much more extensive than the ones practically available using ordinary techniques. Furthermore, the required accuracy of measurements is hardly matched at a reasonable cost. Indeed, the temperature of the surface could be hardly measured with contact probes, due to the contact thermal resistance. Therefore, IR thermography is the best way to fulfill such a task. It is worth saying that the low gradients to be measured requires special tools in order to achieve an accuracy of the order of $0.1\ K$. Finally, the normal indoor conditions are strongly affected by the operator, during the measurement.

The paper illustrates a new approach to solve such a problem (patent pending [7]). The main issue addressed here is the automatic measurement of different ambient parameters, exploiting as much as possible thermal images. Basically, the new deal is to measure the surface and air thermodynamic status starting from temperature measurements on special set of targets (Fig. 3(b)), distributed on the inspected volume (e.g., Fig. 1). Finally, the local conditions are recovered by means of an automatic processing, based on a robust mathematical model.
For all these reasons, the scanning of the wall surfaces and targets by the IR camera is the correct approach to obtain a high-resolution map of the physical phenomena distribution [1]. The automatic scanning device detects the targets in the right order, even if they are not in a regular pattern, in order to follow the geometry of a complex building. After that, the camera focus a partial fields of view and record the images. The needed values are extracted and all the fields are added up to a total view of the surface. Within any Elementary Field of View (EFOV), the thermodynamic quantities are evaluated. Finally, a resampling process gives a very detailed spatial distribution of the air and surface thermal hygrometric conditions. Of course, the arrangement of different thermograms composing a mosaic of the entire wall surface underlies the hypothesis that no significative changes happened during the scanning time. Therefore, the faster the scanning, the better it is.

II. HARDWARE SETUP

The prototype is made of four main hardware components: 1) the sensor device (the IR camera); 2) the pan-tilt camera mount; 3) the controlling PC and 4) the reference grid.

1) Thermal camera: The chosen thermal camera is a FLIR A320 (Fig. 3(a)), equipped with the standard lens (Field of View $25° \times 19°$; focal distance: $18\ mm$; F number 1.3; spatial resolution: $1.36\ mrad$). The detector is an uncooled microbolometer Focal Plane Array of 320×240 pixels, working in the $7.5 - 13\ \mu m$ spectral band, with

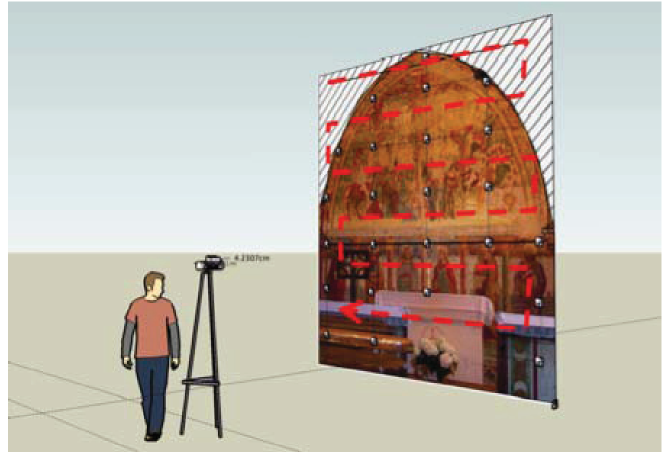

Fig. 2. The hardware setup of the system: the system automatically detects and tracks the positions of the targets during the scanning process. The red dashed line represents a possible scanning path.

(a) (b)

Fig. 3. (a) The FLIR A320 thermal camera mounted on the pan-tilt motor; (b) The special target used to compose the reference grid: it is patched with multiple squared surfaces, the top right surface is composed by a wet lint that is exploited in the target tracking process.

$70\ mK$ of thermal resolution at room temperature. The frame rate is $9\ Hz$. This device is mainly conceived for automatic industrial process control, due to dedicated features and advanced interconnection.

2) the pan-tilt camera mount: The position of the thermal camera is controlled by a simple and cheap pan-tilt motor with a constant velocity of $6°$ degrees per second for the horizontal movement (pan) and $3°$ degrees for the vertical movement (tilt). The device is controlled by the PC via a RS232 serial connection and it doesn't provide any feedback information (e.g., the odometry).

3) The controlling PC: The thermal images acquisition and the camera motion control are performed in real-time using a 2GHz Core 2 Linux-based latop. The target positions are tracked and matched with a reference grid (Fig. 2, see below). The camera position is continually changed in agreement with a given sampling sequence. For every cluster of targets a set of parameters are sampled.

4) The reference grid: The innovative features of the method are mainly based on the extraction of useful radiative data by means of a set of special targets (Fig. 2 and 3(b), patent pending [7]). A light metallic frame is placed in the field of view of the IR camera holding on the targets. This reference grid serves for the following purposes:

- makes easier the identification of the running surface patch at the particular time;
- allows image registration and correct geometric scaling;
- allows a precise temperature compensation for the reflected thermal energy;
- over the targets the IR camera is able to record particular temperature values needed for the measuring of the air temperature map; also the air speed parallel to the surface is mapped on each target point;

Furthermore, a reference passive device is used to calibrate the temperature values measured by thermography and to measure the relative humidity of the air [11], [2].
A precise thermographic reading of an object that is not a black-body, requires at first the knowledge of the reflected IR radiation by the inspected surface and the surface emissivity [10]. A practical way to achieve such a data is to use a diffusive-reflective material placed close to the surface. Any target supported by the grid is patched with multiple squared surfaces where these informative radiative fluxes can be detected by the thermal camera and used for the heat flux estimation. One of these surface is composed by a wet lint ant it will be exploited in the target tracking process. Generally, characteristics of thermal images are more sophisticated than trivial visual images as produced by a vision system, because they are radiometrically calibrated. In other words, the quantitative content, in terms of radiance within a particular IR band, must be preserved for any image processing steps. Therefore, the processing of thermograms has to be performed on the raw data coded according to the manufactured proprietary format.

III. Targets detection

In order to automatically detect the targets inside the environment, we focus on the wet lint that is embodied in each target (Fig. 3(b)). In fact, such a slice appears usually well-defined inside the thermal images (e.g., Fig.4(a)). Our process starts detecting a set of putative targets inside every thermal image using an efficient blob-detection technique. Every candidate is therefore classified as inlier or outlier using a trained Adaptive Boosting (AdaBoost) machine learning algorithm.

A. Selecting putative targets

Given the known distance of the IR camera from the grid, we can approximately fix the size of the targets in the thermal images, and the radius (say σ) of its squared surfaces as well. The surface composed by the wet lint usually appears roughly as a uniform and well-defined squared region. Therefore, we start the process looking into the image for all the blob structures with approximately radius σ. As blob detector, we use the difference of Gaussians (*DoG*) operator, that is a computational efficient approximation of the Laplacian of the Gaussian (*LoG*) filter, one of the most common blob detectors.

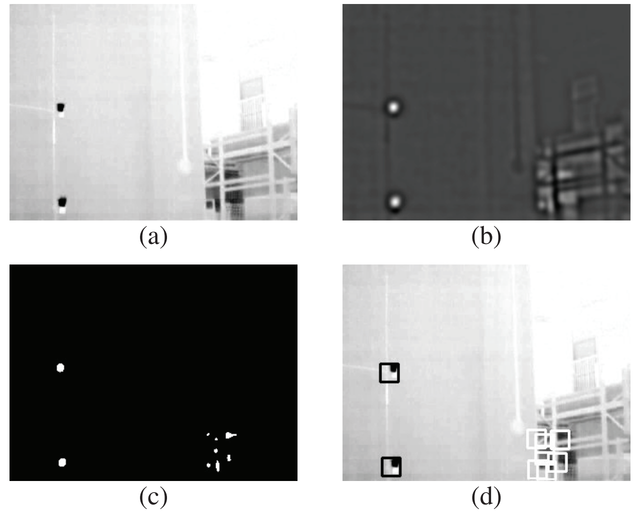

Fig. 4. (a) The input gray-level thermal image: two targets are visible in the left side of the image; (b) The difference of Gaussians (DoG) filter applied to the input image; (c) The adaptive thresholding operator applied to the DoG image (b): every white blob represents a putative target; (d) The putative targets detected in (c) are classified as inlier or outlier based on sourrinding pixels in (a) using the AdaBoost machine learning algorithm.

We can define $l(x, y, \sigma)$ as the convolution of the original thermal image $f(x, y)$ with a bivariate Gaussian kernel $g(x, y, \sigma)$ with zero-mean and diagonal covariance matrix with all non-zero entries equals to σ^2:

$$l(x, y, \sigma) = g(x, y, \sigma) * f(x, y) \tag{1}$$

The difference of Gaussians is therefore defined as:

$$DoG(x, y; \sigma) = l(x, y; \sigma + \Delta\sigma) - l(x, y; \sigma - \Delta\sigma) \tag{2}$$

where $\Delta\sigma$ is chosen in order to well approximate the LoG operator. The application of the *DoG* filter results in strong positive responses for dark blobs (e.g., the wet lints of the targets) of radius σ (Fig.4(b)).
Finally, we need to select a set of connected dark regions that represent our putative targets. We transform the DoG grayscale image to a *binary* image $th(x, y)$ using an adaptive thresholding operator [9], according to the following equation:

$$th(x, y) = \begin{cases} 1 & \text{if } DoG(x, y; \sigma) > T(x, y) \\ 0 & \text{otherwise} \end{cases} \tag{3}$$

where $T(x, y)$ is a threshold calculated individually for each pixel as a gaussian weighted sum of pixels neighborhood ($b \times b$), summed by a positive parameter s. We typically use $b = 25$ while s depends on the contrast of the wet lints inside the thermal images. An example of the application of the adaptive thresholding operator is depicted in Fig.4(c).
For each detected blobs (i.e., connected dark regions), it is hence computed the centroid, the area in pixels and the size ratio ($width/length$) of its bounding box.

B. Classify targets

As we have seen, every detected blob represents a putative target: we turn now to the problem of the classification of those regions in real (*inlier*) and fake (*outlier*) targets. This is a 2-class categorical classification problem: we use a method similar to the Viola-Jones object detection technique [14], based on the AdaBoost (*Adaptive Boosting*, [6]) learning algorithm applied to a set of Haar-like features efficiently extracted from the input thermal images.

1) Feature extraction: As most of the classification algorithms, also AdaBoost needs a discrete representation (i.e., a features vector) of the object that should be classified. For each putative target, we consider in the input gray-level image (Fig. 4(a)) a squared region of fixed size that should cover all the surface of the viewed target (e.g., the black and white boxes depicted in Fig. 4(d)), and not only the wet lint surface (see Fig. 3(b)).

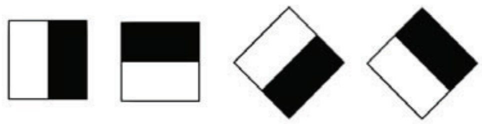

Fig. 5. The four Haar-like features used in the classification: the white regions is interpreted as "add that area", while the black regions as "subtract that area".

Similarly to [14], we compute in that region a small number (four in our case) of Haar-like visual features (Fig. 5): the white regions is interpreted as "add that area", while the black regions as "subtract that area". The sums and differences of the pixel values over the squared regions are calculated efficiently using integral images [5]. We include in our features vector also the two values representing the area in pixels and the size ratio ($width/length$) computed during the selecting of the putative targets (Sec. III-A).

2) Classification using boosting: Boosting is a classification method that works by sequentially applying a simple classification algorithm (in most cases, a *decision tree*) to re-weighted versions of the training data, and then taking a weighted majority vote of the sequence of classifiers thus produced. Boosting is a *supervised* learning technique, that means it generates a function that maps inputs (the features vector) to a class label (inlier or outlier in our case) given a set of training data. This dataset is composed of a number of pairs of input features vector and the desired class label. AdaBoost (Adaptive Boosting) is an instance of the boosting machine learning algorithm that try to modify the sequence of the simple classifiers giving higher weight to training samples that are currently misclassified [6].
In our case the training stage is performed off-line before the scanning process. We develop a specific graphical tool for this task (Fig. 6). The user chooses a set of representative thermal images: for each, the application automatically select the putative targets (Sec. III-A). Using a point-and-click strategy, the user decides the class label of the putatives: inlier (green boxes in Fig. 6) or outlier (gray boxes in Fig. 6). The collected set of input feature vectors and the corresponding class labels (inlier/outlier) are therefore used to train the AdaBoost algorithm: in other words, the algorithm learn the

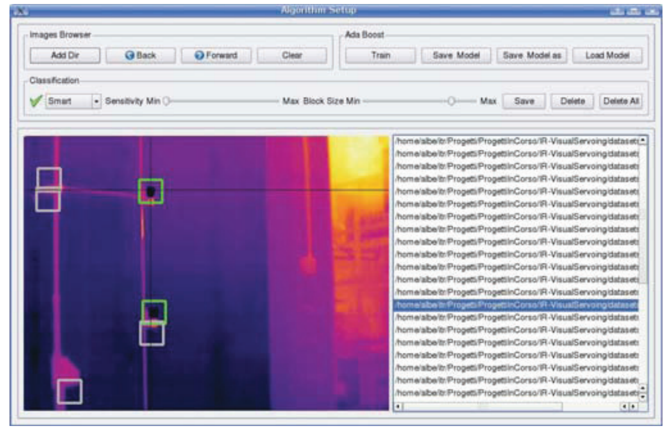

Fig. 6. The graphical user interface (GUI) of the application developed for the training stage of the AdaBoost algorithm. The user select each putative targets and assign to it a label (green boxes are inlier, gray boxes are outlier).

functional relationship $F : y = F(x)$ between input feature vectors x and the output labels y. This relationship will be used during the real classification stage to predict the class label of a putative target given its incoming feature vector.

IV. Automatic monitoring process

The presented monitoring process involves an accurate computation for each location of some fundamental parameters as the air temperature and speed, the relative humidity and the wall temperature. Those thermodynamic quantities are evaluated given the measures extracted from the recorded thermal images during the scanning process. On the other hand, the IR camera focus only a partial fields of view (here's called Elementary Field of View, EFOV) of the desired area. In order to automatically perform the whole monitoring process, it is therefore essential to accurately track the location of every EFOV inside the area of interest during a complete scan. For every recorded thermal image, we are then able to recover the metrical positions where the measures are taken. We propose to cope such a task exploiting the relationship between the IR camera image plane and the planar surface of the reference grid (Fig. 2, see Sec. II).
Given the 2D metrical map of the reference grid (i.e., the location of every target) and a thermal image with the projection of at least four *known* targets (i.e., we know *which* are the projected target), it is possible to compute the *homography* H between image points and grid points solving a linear system [8] (Fig. 7). Given the homography H, it is possible to map every image point p_i to a world point P_i inside the surface of the reference grid as:

$$P_i = Hp_i \tag{4}$$

As we have seen, the computation of the homographies involves the knowledge of *which* target is actually inside the EFOV (i.e., which target is actually projected inside the thermal image). We therefore propose to estimate the position of the intersection point between the optical axis of the camera ($\hat{z}_{cam}$) and the planar surface of the reference

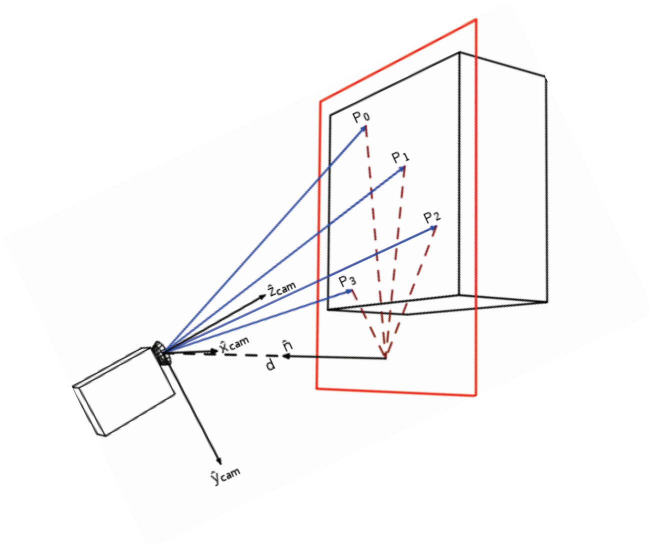

Fig. 7. The IR camera looking at a plane with four point correspondences ($P_0, P_1.P_2, P_3$) needed to determine H. During the scanning process, we track the position of the intersection point between the optical axis of the camera ($\hat{z}_{cam}$) and the planar surface of the reference grid .

grid (Fig. 7): given the knowledge of this location (the *state* of the system), the four targets correspondences and hence the corresponding homography can be easily recovered.

It is important to note that no geometric calibration of the IR camera is needed in our system: it is only assumed that the optical axis of the camera $\hat{z}_{cam}$ intersect the image plane in a point close to the image center.

A. Target tracking using a Particle Filter

Our approach is to represent the state of the system in a probabilistic fashion through a *posterior density function* (PDF) $P[x_t|z_0, \dots z_0; u_t, \dots u_t]$, where x_t is the state of the system at time t, $z_0, \dots z_t$ is the sequence of all the observations until time t and $u_0, \dots u_t$ is the sequence of all the performed actions until time t. In our case, a single observation is the set of the detected targets with their position inside the thermal images (see Sec. III), while a single action is a command sent to the pan-tilt motor (for example, pan clockwise).

The PDF can be estimated recursively over time using incoming observations and actions using the Recursive Bayes Filter, that exploits the Markov assumption of the stochastic process [13]:

$$Bel(x_t) = \eta P[z_t|x_t] \int P[x_t|u_t, x_{t-1}] Bel(x_{t-1}) dx_{t-1} \tag{5}$$

Here we define $Bel(x_t) = P[x_t|z_0, \dots z_0; u_t, \dots u_t]$ (also called *Belief*), while $P[x_t|u_t, x_{t-1}]$ is the *action model*, $P[z_t|x_t]$ is the *observation model* and η is a normalization factor.

The action model represents the probability density of the state at time t given the the state at time $t-1$ and the last action u_t (pan-tilt movement) performed.

The observation model represents the probability density of the observation at time t given the state at the same time.

To solve the Bayes Filter (Eq. 5) we use a Particle Filter, that is an approximated solution of the Bayes Filter. Particle Filters are well suited to cope with multi-modal PDF, as in our case, due to the strong spatial symmetry of the reference grid (Fig. 8).

The key idea of the Particle Filter is to represent the posterior density functions of the state by means of a set of N particles $(x_t^{[1]}, x_t^{[2]}, \dots, x_t^{[N]})$. Each particle represents an *hypothesis* of the state (i.e., in our case a *2D position* inside the grid): the denser a subregion of the state space is populated by particles, the more likely it is the true state falls into this region [13].

In detail, at time t our tracking process works as follow:

1) We detect targets (i.e., the observation z_t) within the incoming thermal image using the strategy presented in Sec. III.
2) All particles are *moved* inside the grid according to the action model, i.e. we replace each particle $x_{t-1}^{[i]}$ with a new particle $x_t^{[i]} \sim P[x_t|u_t, x_{t-1}^{[i]}]$, $i = (1, \dots, N)$. We use here an approximation of the motion: given the last command sent to the pan-tilt motor, the elapsed time from the command invocation and the (fixed) distance of the IR camera from the grid, it is possible to recover the relative movement of the intersection point inside the grid. In order to sample a new particle $x_t^{[i]}$, this relative movement is added to the position of each $x_{t-1}^{[i]}$ plus a zero mean gaussian noise that model the action's uncertainty.
3) All particles are weighted according to the observation model: for each particle $x_t^{[i]}$, we calculated the so-called *importance-factor* $w_t^{[i]}$, with $w_t^{[i]} = P[z_t|x_t^{[i]}]$, $i = (1, \dots, N)$. Given an hypothetical position $x_t^{[i]}$, we roughly estimate the association between the detected targets in the image and the real targets that lies in the neighborhood of that position. This is obtained comparing the relative distances and angles between the image center and the detected targets with the relative distances and angles between the particle position and the neighbour targets in the reference grid. With four or more target correspondences, it is possible to compute the homography $H^{[i]}$. We then project the image center p_c in the grid plane using this homography: $P_c^{[i]} = H^{[i]} p_c$. If the position of the particle $x_t^{[i]}$ falls close to the real position, the projection of the image center $P_c[i]$ should fall near the particle. In order to compute the importance-factor, we compute the distance $d^{[i]}$ between $P_c^{[i]}$ and $x_t^{[i]}$. $w_t^{[i]}$ is obtained computing the probability of $d^{[i]}$ using a zero mean gaussian distribution that model the observation noise.
4) The particles are finally *resampled* based on their importance-factors [13], i.e. we construct a new population of particles by selecting particles from the actual population with probability proportional to the weight

of each particle. Some initial particles may be forgotten and some may be duplicated.

B. Initialization and scanning

At the beginning of the process, the particles are uniformly distributed in the whole working area (Fig. 8(a)). A sequence of fixed movements is performed in order to estimate the real position inside the grid: all particles that fall outside the working area obtain an importance-factor equals to zero, then they will be discarded during the resampling process. At the end of the this initialization step, all particle are condensated around the real position (Fig. 8(f)). During the scanning of the wall surfaces, a set of special positions are automatically and sequentially reached by the moving IR camera: for each position a thermal image is recorded. These special positions (magenta boxes in Fig. 8) represent the centroids of the neighbour targets. Images taken in such location usually contain four or more targets, enabling the estimation of the homography that allows an accurate mapping between image points and world points. Given the homography, we rectify the image (i.e., remove the distortion due to perspective projection) in order to obtain a more accurate temperature sampling.

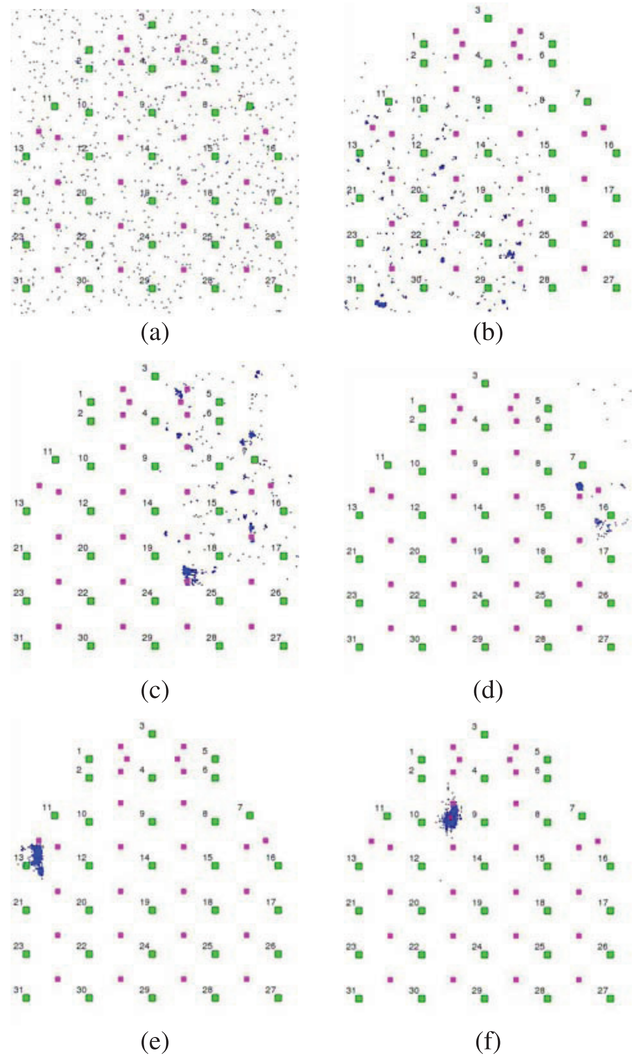

Fig. 8. A typical localization sequence. The green boxes represent the position of the targets inside the reference grid, while the magenta boxes represent the special positions that should be reached during the scanning process. (a) The particles are uniformly distributed in the whole working area; (b),(c),(d),(e) Due to the IR camera movements, the particles tends to come close to real position; (f) All the particle are condensated around the real position.

V. Experiments

We implemented our monitoring system in C++ using the efficient OpenCV image processing library[1] [3]: in Fig.9 the the graphical user interface of the application is depicted. The whole process runs in realtime with a frame-rate of 9 fps on a 2GHz Core 2 Linux-based latop.
Figure 1 shows the technique of measurement at work inside the main tour of the Masino castle in Italy.

The surface condensation of water vapour is extremely dangerous for building materials. Of course, this problem is emphasized if the wall finishing is, for example, a precious Italian Renaissance fresco. The purpose of the investigation is to find out the best ventilation scheme in order to avoid the condensation risk. A few cross sections has been measured according to the described method as shown in Fig. 11. Any map represents the air temperature in the range $3.5 \div 5.5°C$, as seen in Fig.10 (a). Similar maps refer to air speed distribution in the range $0 \div 0.5ms^{-1}$ (see Fig.10 (b)). All results are geometrically corrected, with horizontal and vertical coordinates expressed in cm.

VI. Conclusions

IR Thermography is an effective NdT method for the evaluation of the indoor thermal-hygrometric conditions and the materials decay.
Using the proposed grid of targets, the moisture damage could be detected in a much more reliable and non-destructive way. High thermal and spatial resolution are achieved with such a method allowing to follow the real physical process. The automatic scanning of the grid, with the automatic tracking of the targets and the IR image processing improves significantly the effectiveness of the method. Indeed, with a fully automatic scanning the presence of humans inside the monitored environment is not necessary, avoiding perturbations of the microclimate natural status. This was one of the main goal of the presented system.
In addition, the device allows a precise data fusion and registration of visible map and temperatures map of the site. This is very useful to visually locate the area at risk. Using such a data, a robust mathematical modelling allows to estimate the heat and mass transfer between air and wall. Future work is the intimate integration of thermographic findings with a 3-dimensional model of the building.

[1] http://sourceforge.net/projects/opencvlibrary/

References

[1] P.G. Bison, C. Bressan, E. Grinzato, and S. Marinetti. Automatic air and surface temperature measure by ir thermography with perspective

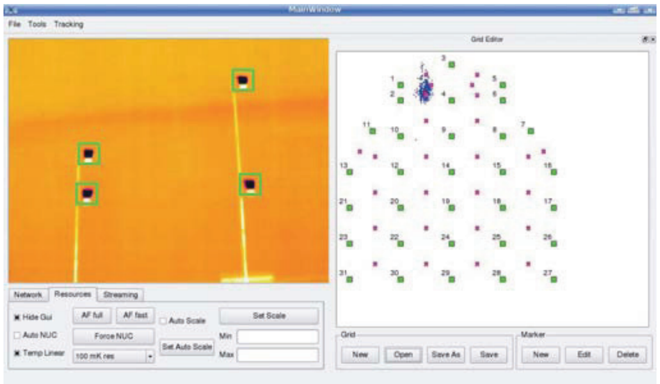

Fig. 9. The graphical user interface (GUI) of the developed application. On the left: the actual grabbed IR-image; On the right: the reference grid and the particles representing the probability distribution of the position of the IR camera's optical axis inside the grid.

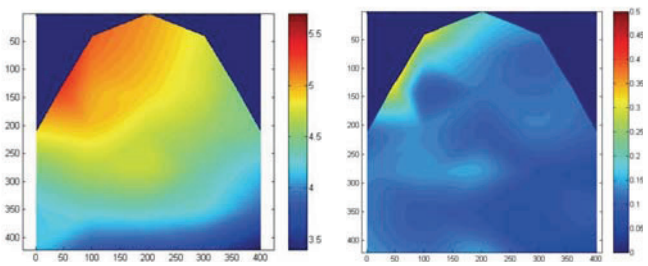

(a) (b)

Fig. 10. (a) Air temperature in the range $3.5 \div 5.5°C$; geometry corrected and space scale in cm ; (b) Air speed distribution in the range $0 \div 0.5ms^{-1}$; space scale in cm;

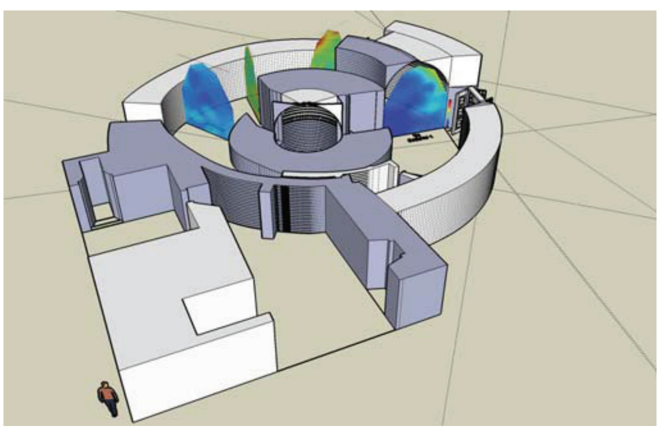

Fig. 11. The condensation risk studied by the new method inside the Masino castle (Italy)

correction. *SPIE*, 1821:252–260, November 1992, Boston (USA).

[2] P.G. Bison, G.M. Cortelazzo, E. Grinzato, and G.A. Mian. Automatic thermal reference detection in thermographic images. *XIIth Thermosense SPIE*, 1313:269–277, April 16-20 1990, Orlando (USA).

[3] Gary Rost Bradski and Adrian Kaehler. *Learning OpenCV*. O'Reilly, 2008.

[4] D. Camuffo. *Microclimate for cultural heritage*. Elsevier, 1998.

[5] Franklin Crow. Summed-area tables for texture mapping. In *SIGGRAPH '84: Proceedings of the 11th annual conference on Computer graphics and interactive techniques*, pages 207–212, 1984.

[6] J. H. Friedman, T. Hastie, and R. Tibshirani. Additive logistic regression: a statistical view of boosting. *Technical Report, Dept. of Statistics, Stanford University*, 1998.

[7] E. Grinzato. *Thermal-hygrometric monitoring of wide surfaces by IR Thermography*. Patent n.PD2006A000191.

[8] R. I. Hartley and A. Zisserman. *Multiple View Geometry in Computer Vision*. Cambridge University Press, ISBN: 0521540518, second edition, 2004.

[9] A. K. Jain. *Fundamentals of Digital Image Processing*. Prentice Hall, 1986.

[10] X. Maldague. *Theory and Practice of Infrared Technology for Non Destructive Testing*. John Wiley & Sons, 2001.

[11] C. Ohman. Practical methods for improving thermal measurement. *Development Department, AGA Infrared System AB, Box 3, S-182 Danderyd, Sweden*.

[12] J. Snell. The thermal behavior and signatures of water in buildings. *Thermosense XXIX SPIE*, 6541:654109.1–654109.9, April 9-13 2007, Orlando (USA).

[13] Sebastian Thrun, Wolfram Burgard, and Dieter Fox. *Probabilistic Robotics*. The MIT Press, 2005.

[14] Paul Viola and Michael Jones. Rapid object detection using a boosted cascade of simple features. In *Proceedings of the 2001 IEEE Computer Society Conference on Computer Vision and Pattern Recognition (CVPR)*, pages 511–518, 2001.

A new filter bank design for Split-Spectrum algorithm

Alberto Rodríguez
Departamento de Física y Arq. de Computadores
Área de Teoría de Señal y Comunicaciones
Universidad Miguel Hernández de Elche
e-mail : arodriguezm@umh.es

Luis Vergara
Departamento de Comunicaciones

Universidad Politécnica de Valencia
e-mail : lvergara@dcom.upv.es

Abstract- *The most important aspect when designing Split-spectrum algorithms is the filter bank design. There are two main trends commonly followed. One is based on constant bandwidth Gaussian filters equally spaced in frequency and the other one uses wavelets as a multi-resolution time-scale method. In this paper we present an alternative that combines both techniques taking advantage from the best of each. It is based in the use of variable bandwidth filters but in this case filters are equally spaced in frequency and are energy gain equalized so that all bands have the same contribution from the possible echo defect. With this new design we improve the insensitivity of the echo defect to the tuning frequency. Improvements in the signal to noise ratio gain after recombination are reported in this contribution. We show the results obtained after simulations using simple stationary models for the grain noise with a single defect. SNR enhancement factor was selected as the figure of merit to make the comparisons among the different methods. These results are contrasted with real processed signal obtained in laboratory from pieces of aluminum alloy, showing the interest of the proposed new filter bank structure and recombination methods.*

1. INTRODUCTION

The main objective of signal processing techniques in NDT is to eliminate or reduce as far as possible the effect of the grain noise to improve the SNR in detection [1][2].

Although there are many methods, most of them based on time-frequency decomposition, the most used method due to its simplicity and the good results provided is the Split Spectrum Processing (SSP) algorithm, widely studied and with a long history in the field of NDT [3]. Despite this, the processes involved in this algorithm which affects its improvement and optimization are not very clear yet, and it is not easy to find studies which justify the use of certain algorithms to the detriment of others, nor from standpoint of efficiency in terms of the gain neither in terms of complexity of calculation or interpretation of the results.

This work seeks to deepen in some of the parameters involved in the design of different algorithms based on SSP techniques, reviewing the influence they have on the results in order to establish objective criteria for selecting the different methods.

2. MODELING OF THE PULSE-ECHO SYSTEM

2.1 Approach to the problem

The basic principle of operation in ultrasonic NDE consists in the emission of an ultrasonic wave in a transducer coupled to the material, which propagates through it so that part of the energy is reflected when it collides a discontinuity, while the rest is scattered or reflected on the surface opposite to the emission. The amplitude of received echoes is directly related to the acoustic pressure of the reflected wave, including coherent and incoherent noise.

Dispersion experienced by the wavefront is dependent on frequency, depending on the size, number and distribution of the scatterers of the material, thus not all the frequencies will be reflected equally, phenomenon called frequency diversity [4]. Thus, when the wavefront collides on a reflector comparable to its wavelength, the reflector acts as an omnidirectional, spherical and frequency selective emitter, scattering better high frequencies than low.

For the evaluation of the methods used in structural noise reduction it is necessary to use models that describe the signals coming from the inspected material. If we wish to model the scattering processes through analytical models, it is necessary to know the exact mechanisms of the physical phenomena involved in the generation of the obtained ultrasonic signal, which is very difficult to achieve in practice, so generally, stochastic models are used considering the received signal as a random process.

2.2 Transducer Modeling

Regarding the transducer, the models used frequently are based on either deterministic Gaussian envelope signals or decreasing exponentials, depending on the transducer to be modeled (focused or not focused, for example).

In the first case, the response of the transducer can be modeled using a band pass signal with Gaussian envelope [5], and in the second with a growing potential term combined with a decreasing exponential, modulated to the desired central frequency. In both cases, the desired waveforms can be achieved by modifying the appropriate parameters.

Finally, beamforming techniques [5] can be used to achieve better control over the transducer frequency response.

2.3 Material modeling

The stochastic models consider the signal received from the material as an stochastic process that allows both modeling and perform simulations and deductions about the nature of the phenomenon as validate various algorithms used for the reduction of structural noise [6][7].

For modeling the ultrasonic signal coming from the structure of a dispersive material, the grain noise is usually regarded as the additive composition of the echoes from the small individual reflectors or inhomogeneities of the material, so the received signal could be expressed analytically as:

$$r(t) = \sum_{k=1}^{K} g_k(t-\tau_k)$$

with K the number of grains, g_k the echo from the k-th reflector and τ_k the scatterer located at the distance $z=\tau_k c/2$, being c the propagation velocity in the material. Depending on the criterion used to model this response, models can be classified in stationary and not stationary.

Stationary models assume that the statistical parameters of the process do not vary with the depth and, particularly, that the impulsional response of the scatterers and the attenuation coefficient do not depend on the frequency, just on the features of the material. Thus, received signal could be expressed as [8]:

$$r(t) = \sum_{k=1}^{K} e^{-2\alpha \cdot z_k} \cdot h_{sk}(t-\tau_k) * x(t)$$

where $x(t)$ is the mechanical transducer response, α is the attenuation coefficient and $h_{sk}(t)$ is the impulsional response of the *k-th* reflector.

In practice, the attenuation may be compensated easily, so the stationary model would be:

$$r(t) = \sum_{k=1}^{K} h_{sk}(t-\tau_k) * x(t)$$

This is a reasonably valid simplification if the length traveled by the ultrasonic wavefront is small, or the transducer is narrowband.

Combining this model with the transducer-material model, the material impulse response $h(t)$ is modeled as a random white process consisting of a sequence of deltas weighted by its reflection coefficient, assuming, by the central limit theorem, when the number of reflectors is high the sum adopts a Gaussian distribution.

$$h(t) = \sum_{k=1}^{K} \rho_k \delta(t-\tau_k)$$

The general expression would be as follows:

$$R(\omega) = X(\omega) \cdot \left\{ \sum_{k=1}^{K_s} \rho_{sk} \cdot e^{-j2\omega z_k/c} + \sum_{k=1}^{K_d} \rho_{dk} \cdot e^{-j2\omega z_k/c} \right\}$$

with ρ_{sk} and ρ_{dk} the reflection coefficients of the material and defects respectively.

In both cases, the first part of the sum would be the contribution due to the structure of the material (grain noise) and the second the due to the defects. Just would remain to add a fraction of white Gaussian noise to model the incoherent noise.

2.4 Model validation

Next figure shows (figure #1) the results obtained using a stationary model of material with a Gaussian-type envelope transducer and a sample taken on a piece of aluminum alloy in which a small hole has been done close to the end of the piece:

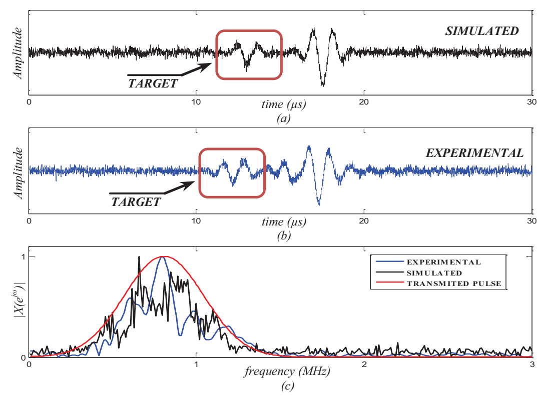

Figure #1: Simulated signal (a), experimental signal (b) and spectrum (c).

As can be seen, the model is able to reproduce quite accurately the environment of the real test by simply adjusting properly the parameters involved in the design. It is also found that in low dispersive materials, as in stationary models, the spectrum of the received signal occupies the same band that the spectrum of the transducer, but with random spectral contributions due to the fact that the reflections depend on the size of the grain.

3. THE SSP ALGORITHM

3.1 Approach to the problem

Preceding sections described the basic principles of operation of the inspection by ultrasound, and particularly the frequency diversity phenomenon, whereby when the transmitted wavefront collides with a reflector greater than its wavelength, part of the energy is reflected, regardless of frequency. Because of this, the spectral power density of the received signal should contain information on the same bandwidth that the transmitted pulse or, if it is a very dispersive material, at least in the lower part of the band due to the low pass filter effect of the material.

In other hand, when the wavefront collides with a reflector of size comparable to its wavelength, some of the energy is dispersed, so that the spectral power density of the received echo will contain information only on some localized bands. Since the distribution and size of these reflectors is random, it will also the received power distribution.

The following figure (figure #2) shows the spectrum of a signal generated according to the stationary model with a single defect located approximately in the centre of the scan.

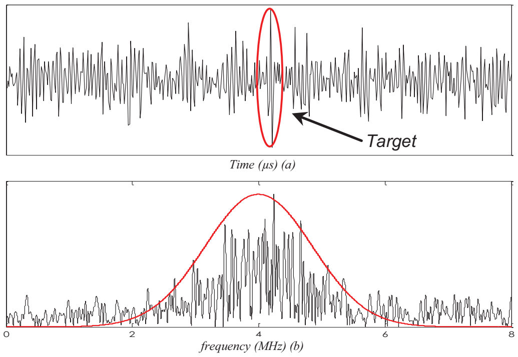

Figure #2: Scan obtained in a dispersive material with a defect at 16 µs using a 4MHz transducer with 2MHz bandwidth. (a) time (b) frequency

If its spectrogram is calculated, it can be appreciated (figure #3) that where the defect is present its power density spreads all around bandwidth of the transmitted pulse. However, in the rest, contributions occupy only one portion of the spectrum depending on the size, position and orientation of the reflectors that, as mentioned, will be random.

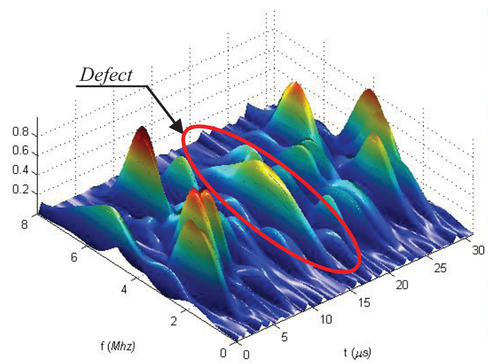

Figure #3: Spectrogram of the previous signal.

This shows that the most appropriate strategy would be to perform a time-frequency analysis and search the time in which the power of the echo is distributed homogenously in the bandwidth of the transmitted pulse.

3.2 The SSP algorithm

This algorithm exploits the frequency diversity phenomenon according to the foregoing previously. Its objective is to reduce as far as possible the grain noise by applying a frequency decomposition and discriminating the areas in which the spectral contribution is not homogeneous. To do this, a broadband signal is used and the received signal is filtered with a filter bank [8]. Then, resulting signals are processed on a non-linear combination providing information about the location of the possible defect.

Next figure (figure #4) shows the schema of the algorithm:

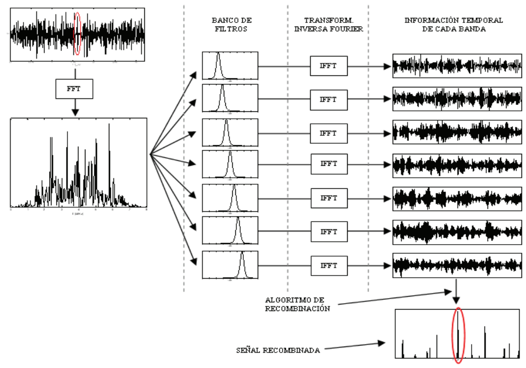

Figure #4 SSP algorithm schema

To perform the filter bank, the bandwidth of interest must be selected. Then, this bandwidth is split in equally spaced sub-bands obtaining information about the spatial distribution of the energy in each one. Finally, this information will be combined to highlight the areas where there is significant contribution of energy in all bands.

At this point, should be remarked that one of the main objectives of this work is to optimize the performance of the SSP algorithm in terms of improving the SNR with the lowest possible complexity, i.e. with the fewest number of bands and the simplest filters.

3.3 The SSP algorithm parameters: the Bank of filters.

The first step in the SSP algorithm is the division of the signal in different bands (figure #5b), which is done with a bank filter, whose specifications depend on the following factors:

- Number bands [9][10][11]
- Inspection bandwidth [12][13]
- Bandwidth of each filter [9][14][15][16]
- Overlap between different bands [9][15]
- Filter type [9][10][17]

3.4 New filter bank design: Filters equally spaced in frequency and energy gain equalized

In this work, it is studied the possibility of using an alternative design for the filter bank, based on equally spaced filters but in this case with variable bandwidth proportional to its central frequency and designed that they all have the same energy (figure #5a) in order to equalize the contribution of each band.

Thus accomplished:

- The transfer function of the filter bank is adapted to that of the transmitted pulse
- More influence of the lower bands is achieved
- More incidence of the prunning effect is achieved

Comparing the sum of the contribution of all the bands with that of the original design, it is shown that when using the new filter bank, all the bandwidth transmitted by the transducer is taken into account for the analysis, fitting it to the response of the material. Then, selecting properly the bank parameters (number of filters and bandwidth), it can be achieved a response adapted to that of the material.

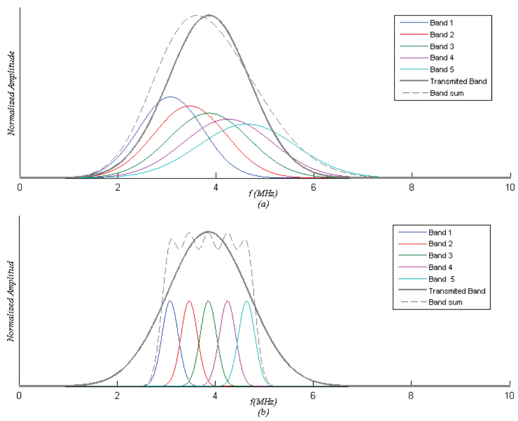

Figure #5: Filter bank example.
(a) Variable bandwidth (b) Fixed bandwidth

4. RECOMBINATION METHODS

4.1 Introduction

There are multiple methods of recombination, but the most frequently used due to its good results are Minimization (MIN) and of Polarity Thresholding (PT). However, in spite of its reliability, both have certain limitations: Minimization algorithm has very little resolution and high SNR values cannot be achieved, and Polarity Thresholding, although it is able to provide very good resolution, needs a lot of bands to achieve substantial gain in the SNR values.

In addition of these, two modifications of the previous algorithms will be explored: Normalization (NORM), based in Minimization method, and Scaled Polarity Thresholding (SPT), in order to check their behavior compared to previous, with both the traditional filter bank and the new one proposed.

Finally, in this paper we propose the use of the Frequency Multiplication method (FM), that provides very high resolution and achieves the best results in the SNR when combined with the new design of filter bank, with less number of bands than the rest of algorithms.

4.2 Recombination methods

Thereafter the following notation will be used; $y(n)=F\{x_1(n),x_2(n),x_3(n),\ldots,x_L(n)\}$ is the result obtained after processing and recombination of the signal at n, $x_i(n)$ is the result of the filtering of the i-th band at n , and L is the number of bands. Thus, algorithms are defined as follows:

- Minimization (MIN) [15][16]; for each instant in time (distance), takes the minimum of the absolute value from all bands

$$y(n) = min\{|x_1(n)|, |x_2(n)|, |x_3(n)|, \ldots, |x_L(n)|\}$$

- Normalization (NORM) [18]; for each instant in time (distance), takes the minimum of the absolute value from all bands, previously normalized by the maximum value of each of them

$$\hat{x}_i(n) = \frac{x_{i(n)}}{\max_n x_{i(n)}}$$

$$y(n) = min\{|\hat{x}_1(n)|, |\hat{x}_2(n)|, |\hat{x}_3(n)|, \ldots, |\hat{x}_L(n)|\}$$

- Polarity Thresholding (PT) [15][17]; for each instant in time (distance), takes the minimum of the absolute value from all bands, only when the value in all of them has the same sign, assigning a zero otherwise.

$$y(n) = \begin{cases} min\{|x_1(n)|, |x_2(n)|, \ldots, |x_L(n)|\} & \begin{cases} si\ x(n) > 0 \forall n \\ si\ x(n) < 0 \forall n \end{cases} \\ 0 & resto \end{cases}$$

- Scaled Polarity Thresholding (SPT) [19]; for each instant in time (distance), takes the minimum of the absolute value from all bands and scale it by a factor that depends on the number of samples with the same sign.

$$y(n) = \left|\frac{N_+ - N_-}{S}\right| min\{|x_1(n)|, |x_2(n)|, \ldots, |x_L(n)|\} \cdot 4L$$

With N_+ the number o positive samples, N_- the number of negative samples S the number of samples

- Frequency Multiplication (FM) [15]; for each instant in time (distance), takes the product of the samples from all bands.

$$y(n) = |x_1(n) \cdot x_{21}(n) \cdot x_3(n) \cdot \ldots \cdot x_L(n)|$$

5. EVALUATION OF THE SSP ALGORITHM

5.1 Previous considerations

To simulate the transducer pulse *x(t)* it will be considered an impulse response of Gaussian envelope centered at 4 MHz and with 2 MHz of bandwidth. To reproduce the SSP algorithm, it will be considered scans with a single defect in its centre and with variable reflection coefficient ρ, all that immersed in a dispersive environment modeled by the stationary model previously described (figure #2), adding certain amount of white noise to take account of the incoherent noise present in the scan. In all cases simulations are undertaken according to the Monte Carlo method with 1000 iterations by simulation, varying the number of filters of the Bank from 2 to 20 bands and the type filter Bank used, repeating the experiment for the two different filter bank designs.

Signal to noise ratio enhancement factor (Signal to Noise Ratio Gain SNRG) was selected as the figure of merit to make the comparisons among the different methods (GSNR), measured as the difference between SNR al the input (SNRin) and SNR after applying the algorithm (SNRout), taken that relationship as:

$$SNR = \frac{\sum_{D+\frac{P}{2}}^{D-\frac{P}{2}} y^2(n)}{\sum_0^{N-1} y^2(n)}$$

$$G\,SNR = \frac{SNR_{OUT}}{SNR_{IN}}$$

Where D is the defect location, P the pulse width and N the record length.

5.2 SNR Out Vs. SNR in

The following figure (figure #6) represents the average SNRout versus the average SNRin for the different recombination methods previously studied and for the two types of filter bank, varying in all cases the number of inspection bands from 2 to 20.

The effectiveness of the method is given by the slope of the RSNout curve, which shows the ease with which the algorithm is able to detect a defect. Values close to 1 SNRout indicate that the noise (coherent and incoherent) is absolutely removed from the scan after processing it.

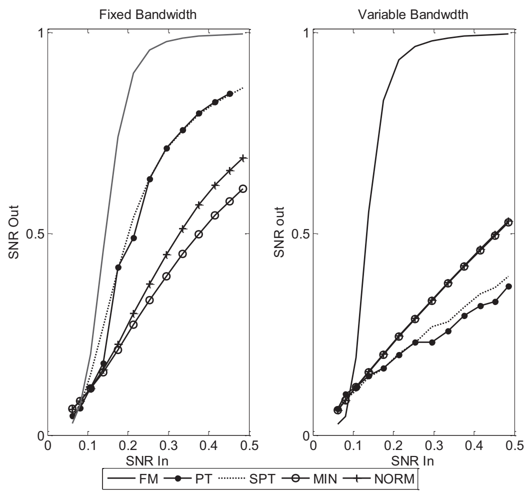

Figure #6: SNRout Vs. SNRin using fixed bandwidth filters (left) and variable bandwidth filters (right)

As shown in the figure, in both cases the most effective recombination method is the FM, being slightly steeper the slope when using the new filter bank. In the traditional model, PT and SPT methods also provide good results, followed finally by methods based on Minimization, being slightly better NORM than MIN. It should be noted that using fixed bandwidth filter, in all cases the slope is more than ½, which implies that the SNR gain will be greater than 1. However, using variable bandwidth filters, the slope of PT-based methods is less than ½ and therefore the SNR gain will be less than 1.

5.3 Variation of the SNR Gain vs. number of bands

The following figures (figure #7) show the average SNR gain vs. the number of bands used, with either the fixed and variable bandwidth filters and for all the recombination methods.

As can be seen in figures, the MF method is not only the method that get the best values for the SNR gain, but also the one which needs the less number of bands to achieve high values, so that using these methods the system complexity would be considerably reduced.

The best gain values and the higher speed of convergence are achieved when combining the new filter bank with the MF method, although it is true that for the rest of methods the gain worsens.

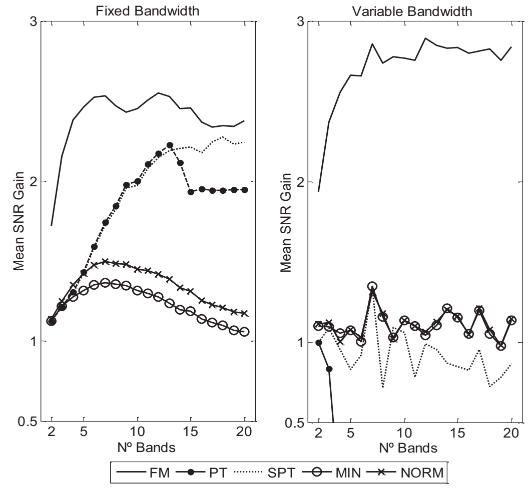

Figure #7: Mean SNR Gain Vs. number of bands using fixed bandwidth filters (left) and variable bandwidth filters (right)

5.4 Experimental results

After the analysis of the behavior of the different algorithms with simulated signals, it is time to check if the observed effects are reproduced with signals coming from real ultrasonic inspections, studying the SNR Gain obtained with each algorithm. Thus, it has been used a set of scans obtained from the inspection of a piece of Duralumin with a 1 cm diameter hole in its structure that simulates an effect, where has been used a transducer with a central frequency of 2 MHz and 1 MHz of bandwidth.

Next figure (figure #8) shows the results obtained after applying the different algorithms to one scan, where it is clearly seen the coincidence with the trends observed in simulations for the different methods and filter banks.

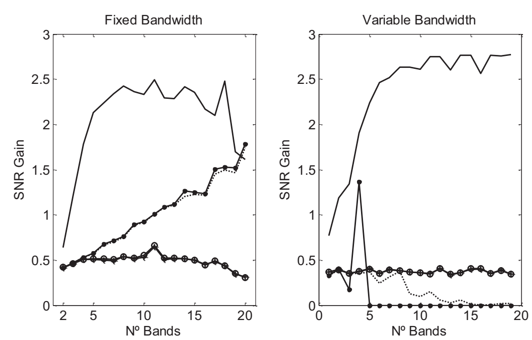

Figure #8: SNR gain Vs. number of bands of the scan using fixed bandwidth filters (left) and variable bandwidth filters (right)

In both cases, using fixed or variable filters, the FM method provides the best results, achieving very high values of SNR gain for a few bands. The maximum values are obtained with only 7 to 9 bands, decreasing slightly from this point in the case fixed bandwidth and increasing slightly in the case of variable bandwidth, which is the combination that best results provides. In fact, using the PT method with the fixed bandwidth design, it would be needed up to 35 bands to achieve the same results as with 7 bands in the case of FM and the new filter bank design.

The following figures show the results obtained after the application of the different methods to the scan of the example, with the traditional filter Bank (figure #9), and the new filter bank design (figure #10), using 9 bands in both cases. In these figures can be checked easily the improvement achieved in the time (space) resolution using the new design, in addition of all effects commented previously.

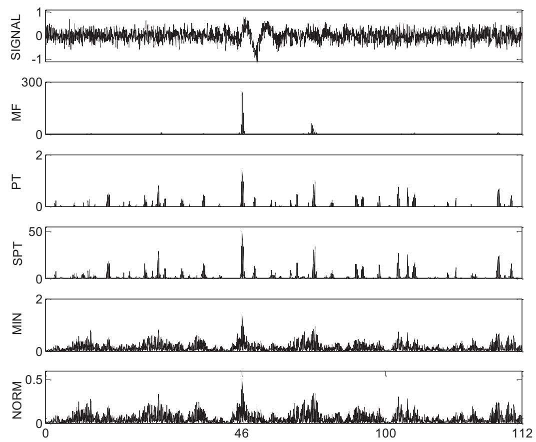

Figure #9: Output of the different methods of the scan using fixed bandwidth filters (time in microseconds)

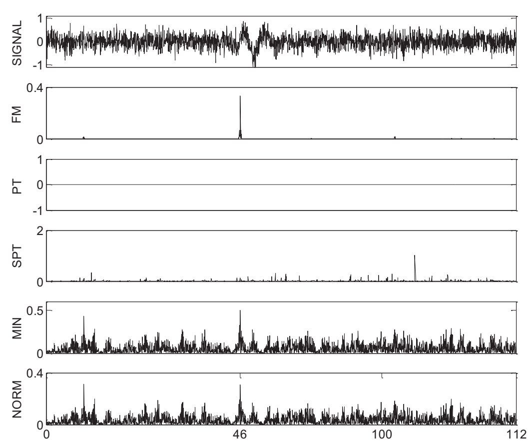

Figure #10: Output of the different methods of the scan using variable bandwidth filters (time in microseconds)

6. CONCLUSIONS

From the results it can be concluded that the stationary models used to simulate the signal and the algorithms assessment are adjusted enough to assume a valid approximation of real signals.

A new design filter Bank has been introduced, based on variable bandwidth filters, equally spaced and energy equalized, that has been demonstrated very efficient to maximize the SNR gain with the fewest possible bands in the filter bank.

On the behavior of the different algorithms, it has been proved that, in the case of a single defect, FM method provides the best values on the SNR gain, improving these considerably in the case of using the new filter bank proposed. In this case the gain remains approximately constant with the number of bands from the maximum, obtained between 5 to 9 bands. In any of the other methods, the use of this filter type worsens the result, so does not seem appropriate its use.

In future work will deepen into the behavior of the new filter bank and the FM method using not stationary models for the material and testing the obtained results with highly dispersive materials. The influence the rest of the parameters of the filter bank have in the behavior of the new design will also be the objective of a detailed study.

7. ACKNOWLEDGMENTS

This work has been supported by the Ministry of Fomento (Spain) and the Ministry of Science and Innovation (Spain), and FEDER funds under the projects T39/2006 and TEC2008-06728 and TEC2008-02975

8. REFERENCES

[1] N.M. Bilgutay et al., Flaw to grain echo enhancement, Proceedings, Ultrasonics International 1979, 1979 pp 157, Austria

[2] N.M. Bilgutay et al., The effect of grain size on flaw visibility enhancement using split spectrum processing, Material evaluations, Vol. 4, Nº2, May 1984, pp 808

[3] P. Rubbers, C. J. Pritchard, An overview of Split Spectrum Processing, NDTnet, August 2003, Vol.8 No.8

[4] Qi Tian and N.M. Bilgutay, Statistical analysis of split spectrum processing for multiple target detection, IEEE Transaction on ultrasonics, ferroelectrics and frequency control, Vol 45, Nº1, January 1998, pp 709

[5] Gabriella Cincotti, G. Cardone et al., Efficient transmit beamforming in pulse-echo ultrasonic imaging, IEEE Transactions on ultrasonics, ferroelectrics, and frequency control, Vol. 46, No. 6, pp. 1450-1458, November 1989

[6] Jafar Saniie, Tao Wang, Nihat M. Bilgutay "Statistical Evaluation of Backscattered ultrasonic grain signals". J. Acoust.Coc.Am 84 (1), July 88. pp 400-408

[7] Robert f. Wagner et al. "Statistics of Speckle in Ultrasound B-Scans". IEEE transactions on sonics and ultrasonics, vol 30, nº3, May1983.pp 156-163.

[8] Kevin D. Donohue "Maximum Likelihood Estimation of A-Scan amplitudes for coherent targets in media of unresolvable scatterers". IEEE Transactions on ultrasonics, ferroelectrics and frequency control vol 39 nº3 May 1992. pp 422-431.

[9] Kwong Ki Yau, Split-Spectrum Processing for Nondestructive Testing , NDTnet, August 1997, Vol.2 No.8

[10] J.D.Aussel. Split Spectrum processing with finite impulse response filters of constant frequency-tobandwidth ratio. Ultrasonics Vol. 28 July 1990.

[11] P.Karpur, P.Shankar, J Rose and V.L.Newhouse. Split spectrum processing: optimising the processing parameters using minimisation. Ultrasonics, Vol. 25, July 1987, pp. 204.

[12] M.Pollakowski, H.Ermert, L.von Bernus, T.Schmeidl. The optimum bandwidth of chirp signals in ultrasonic applications . Ultrasonics Vol.31 No 6, pp 417 1993

[13] P.Karpur, P.M.Shankar, J.L.Rose and V.L.Newhouse.Split. Spectrum processing: determination of the available bandwidth for spectral splitting. Ultrasonics Vol. 26, July 1988.

[14] J.Saniie. D.T.Nagle, K.D.Donohue. Analysis of order statistic filters applied to ultrasonic flaw detection using split spectrum processing. IEEE transactions on ultrasonics, ferroelectrics, and frequency control. Vol. 38 No 2 March 1991.

[15] Karaoguz, Meric; Bilgutay, Nihat; Akgul, Tayfun; Popovics, Sandor. Defect detection in concrete using Split spectrum processing. Proceedings of the IEEE Ultrasonics Symposium, Vol 1, 1998. pp 843-846

[16] V.L.Newhouse, V.L. Bilgutay, N.M.Saniie E.S. Furgason. Flaw-tograin echo enhancement by split spectrum processing . Ultrasonics, March 1982, Vol.20 pp. 59

[17] P.M.Shankar, P.Karpur, V.L.Newhouse, J.L.Rose.Split. Spectrum processing: Analysis of polarity thresholding algorithm for improvement of Signal-to-noise ratio and detectability in ultrasonic signals . IEEE transactions on ultrasonics, ferroelectrics and frequency control Vol. 36, no 1 January 1989.

[18] I. Bosch, L. Vergara, Normalized split-spectrum: A detection approach, Ultrasonics, Vol. 48, Issue 1, March 2008, pp 56-65

[19] E. C. Ifeachor, B. W. Jervis, Digital Signal Processing: A practical approach, Addison-Wesley.

Alberto Rodriguez was born in Salamanca (Spain) in 1973. He received the Ingeniero de Telecomunicación degree from Vigo University, Spain, in 1998. He worked for the Spanish Air Force as junior research engineer in the Logistics Transmission Centre in Madrid. After that he joined the Spanish branch of France Telecom for two years and finally he start his research activities in the Miguel Hernandez University of Elche, Spain, in 2001, focused in signal processing and specially in ultrasonic non destructive testing.

Contact:

Alberto Rodriguez
Universidad Miguel Hernandez
Avda. Universidad S/N
03203 Elche (Alicante) SPAIN
Tel. +34 966 658 825
Fax +34 966 658 825
Email: arodriguezm@umh.es

Luis Vergara was born in Madrid (Spain) in 1956. He received the Ingeniero de Telecomunicación and the Doctor Ingeniero de Telecomunicación degrees from the Universidad Politécnica de Madrid (UPM) in 1980 and 1983 respectively. Until 1992 he worked at the Departamento de Señales, Sistemas y Radiocomunicaciones (UPM) as an Associate Professor. In 1992 he joined the Departamento de Comunicaciones (Universidad Politécnica de Valencia UPV, Spain), where he has been Department Head until April 2004. From April 2004 to April 2005 he was Vice-rector of New Technologies at the UPV. He is now responsible of the Signal Processing Group of the UPV, a member group of the Institute of Telecommunication and Multimedia Applications (I-TEAM) of UPV.

Contact:

Luis Vergara
Universidad Politécnica de Valencia
Camino de Vera s/n
46022 Valencia SPAIN
Tel. +34 96 3658 825

Email: lvergara@dcom.upv.es

TIME OF FLIGHT INVERSE MATCHING RECONSTRUCTION OF ULTRASONIC ARRAY DATA EXPLOITING FORWARDS MODELS

S. Chatillon, A. Fidahoussen, E. Iakovleva, P. Calmon
CEA, LIST, F-91191 Gif-sur-Yvette, France;

Ultrasonic arrays provide improved flexibility and adaptability to complex configurations with comparison to conventional probes. Besides the usual application of focused beam, using electronic delays at emission and reception, more complete operating mode involving per-channel signals acquisitions are more and more encountered. To fully exploit this data, in order to localize and to characterize the defect, efficient imaging and reconstruction tools based on a direct modeling of the inspection are required.
A time of flight inverse matching reconstruction method has been implemented in the NDT software platform CIVA. The method consists in a coherent summation of the received signals for all points of the region of interest and can be used with different operating modes of the array. It exploits the forward models available on the platform and therefore it can deal with complex configurations (non canonical geometries, heterogeneous and anisotropic materials). In this communication we present results on both simulated and experimental data which show the performances of the method and its sensitivity to various acquisition parameters (inaccuracy of the probe position and orientation or surface description, etc…) .

Keywords: Non Destructive testing, ultrasonic, array, modeling, data processing

INTRODUCTION

Arrays techniques are increasingly used in ultrasonic non destructive testing industrial applications, thanks to their intrinsic versatility, combined to increased performances of commercially available acquisition systems and array probes. While regular operating modes such as focusing, steering and various electronic scanning or any combination of those have been implemented for a long time, they have been usually limited to 1D probes such as linear or circular arrays. However, the ever-increasing number of UT channels available within the acquisition systems enables the use of these techniques with matrix array probes. While 3D beam sweeping, focusing, electronic scanning and data reconstructions offer new inspection possibilities; it is crucial to conceive simulation tools and user-friendly interfaces that will help users exploit these tools to their full potential.

The French Atomic Commission (CEA) has been developing for years semi-analytical models dedicated to UT. These simulations tools allow computing delay laws, beam propagation, flaw scattering, as well as imaging tools. Those different features are available for simple (circular, linear) or more sophisticated (1.5D or 2D matrix arrays, sectorial arrays) patterns.
In this paper, we study reconstruction algorithms based on an inspection modeling, which allows dealing with complex configurations. The proposed algorithms derive from the synthetic focusing approach, which consists in coherently summing the received signals to have maximum amplitude where scatterers are really located. Basically, the algorithms exploit the time of flight, which is evaluated theoretically from existing forward models, which allow to deal with non-canonical situations (complex geometry, heterogeneous parts, anisotropic materials, etc…) [1, 2]. Moreover, the adopted approach is generic and can be applied to any inspection providing a set of ultrasonic signals. So a wide range of array operating modes (electronic scanning, beam steering, transmit-receive independent functions, per channel acquisition…) can be processed.
The simulation tools and their related configurations are first briefly introduced. In a second time, the so called FTP algorithm is described and several applications on both simulated and experimental data are proposed.

MODELING OF PHASED ARRAYS TECHNIQUES IN CIVA

Beam propagation and flaw response computation

UT semi-analytical models aim at fully predicting an inspection. In order to simulate the inspection, various flaw scattering approximations may be involved [2-4], depending on the configuration cases (type of inspection: pulse echo, tandem or TOFT technique) and on the flaw type (volumetric void flaws, crack-like flaws, solid inclusions), while the field incident over the flaw is modeled using a surface integral aperture over the transducer aperture [5]. Finally, the synthesis of the signal at reception is computed using an argument based on Auld's reciprocity [6]. This calculation is achieved for each scanning position of the probe and each applied parameters (delay and amplitude law) over the array, and for each elementary mode contribution: direct specular echoes in longitudinal and transverse modes, corner echoes with or without mode conversion occurring over the flaw or over the backwall, then the overall echo at reception is the summation of all these elementary modes.

Delay laws and operating modes

Because matrix array probes can perform full 3D volumetric inspections, it is necessary to develop user-friendly interfaces that allow the calculation of the most complex delay laws. One can now use the recent developments to define the pattern of the active source and reception. This pattern can be of any shape; a square and ring patterns are shown as example in red in Figure 1. These patterns can then be electronic scanned across the full aperture of the array. Two trajectories are presented in Figure 1, a crenel-like displacement and a displacement along the diagonal of the array. It is possible to assign two totally different trajectories for the source and reception for tandem application.

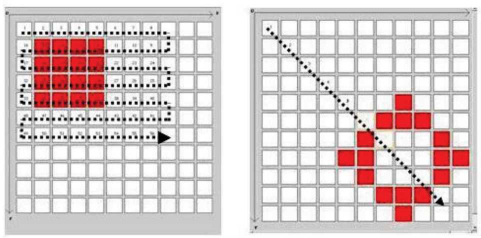

Figure 1 : Patterns (red elements) and trajectories across a matrix array probe (arrow).

After defining the patterns and trajectories, one can calculate delay laws to focus and/or deflect the beam in 2 or 3 dimensions according to the symmetry of the array. The delay law calculations take into account arbitrary component shapes (canonical or CAD defined) and structures (homogeneous or heterogeneous, each medium being isotropic or anisotropic). This skill is available for linear, matrix, circular, sectorial, encircling or encircled arrays and various operating probes (contact, immersion, flexible, dual T/R probes). Finally, a dynamic depth focusing delay law algorithm has been implemented to homogenize the beam spot within a desired inspection range of depths, with fixed or optimal aperture of the array pattern.

Imaging and reconstruction tools

The application of delay laws to drive the beam leads to a collection of different UT paths (for instance: multiple angles in sectorial scanning techniques) and potentially large amount of data collection (acquisition and storage of elementary signals received by each channel of the array for post-processing). For each applied delay and amplitude laws, it is possible, thanks to previously presented simulation tools, to determine the UT paths, time of flights or the amplitude of the radiated or scattered field inside the component. The knowledge of these allow to build true scan image (display of ultrasonic echoes according to the specimen frame coordinates) as well as post-processing summations of elementary signal to map a region of interest. Figure 2 shows some of these tools for measuring the focal spot dimensions of a circular array using different focal laws, evaluating the actual refraction angles (both features relying on a complete beam propagation), as well as a more simple (and very fast) ray tracing tool showing the UT paths used for focusing over a side drilled hole.

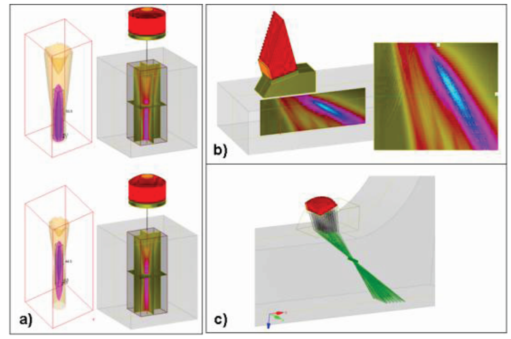

Figure 2 : Tools for evaluating phased arrays techniques: a) measure of the focal spot, b) estimation of the actual refraction angle, and c) ray tracing tool.

DATA RECONSTRUCTION OF ARRAY DATA

Principle of the method

New tools dedicated to the management of phased arrays data (both simulated and experimental using phased arrays acquisitions system developed by M2M [7]) have been added to the CIVA platform. These tools allow post-processing the data acquired in a phased array inspection by each element of the array [4]. The post-processing technique consists in summing the elementary contributions time shifted and weighted using model-based delay and amplitude laws:

$$E(P)=\sum_{n=1}^{N}W_{nP}S_{nP}$$

Where $E(P)$ is an estimation factor, representative of the probability of presence of a flaw at point P, S_{nP} is the amplitude of the n[th] signal at time of flight attributed to the point *P*, and W_{nP} is a weighting coefficient. The principle is described on the Figure 3.

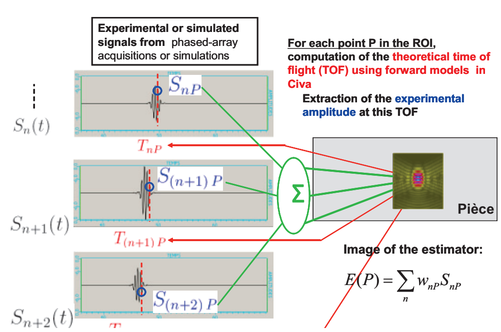

Figure 3 : Synthetic focusing: principle of the FTP method

Application to experimental data acquired through a complex profile

The application of such reconstruction technique is illustrated for an experimental tests carried out over a complex profile component, representative of irregular state of surface that may be observed in the vicinity of welds. A linear array of 64 elements lies over a ferritic steel of complex profile, containing 8 side drilled holes (4 side drilled holes are located below a planar part, while the 4 other reflectors are located below a complex part).

The acquisition is carried out as follows: the first element is used as a transmitter, and signals received by each element of the array are picked and stored, then the second element is used at transmission and all echoes are stored. Finally the complete set of transmitters and receivers (64x64 signals received for one position of the probe) are used to form the collection of UT data. This technique is sometimes referred as the full matrix capture (FMC) or transfer matrix by different authors. Figure 5 shows the Ascans received on the array, as the first element is used for transmission. The four echoes scattered by the side drilled hole are clearly observed by the array, although this configuration is somewhat unfavorable, as the array aperture is shifted with respect to the flaws position (one also has to note that the first element is the element closest to the side drilled holes). The observed echoes correspond to smooth hyperbolic curves, as this series of side drilled hole is located below the planar part of the component.

Using the collection of signals received in the FMC acquisition, the summation of echoes is performed in a region of interest in the component. Basically, this so called "FTP" time of flight inverse matching technique relies on the calculation of UT paths propagations from the transmitting element, a supposed point source scatterer lying in any position of a reconstruction area, and the receiving element.

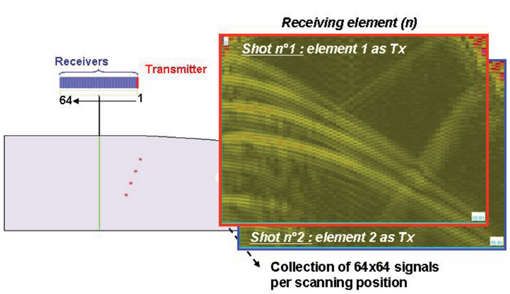

Figure 4 : Examples of signals acquired by the array, using the full matrix capture acquisition

Those paths are modeled using the previously detailed simulation tools for beam computation and flaw scattering and the amplitude at the corresponding time of flight is extracted on the elementary signal. These amplitudes are summed up to obtain the amplitude of the point in the reconstruction area.

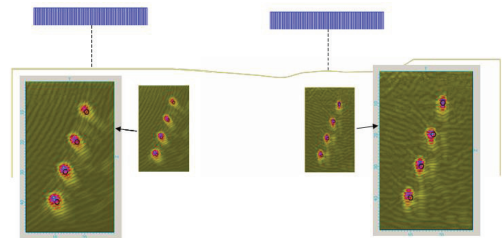

Figure 5 : Reconstruction over planar and irregular parts of the component

The results obtained for two positions (the first one corresponding to the previous figure, and the second one corresponding to the axis of the array probe aligned on the second series of side drilled hole, that is to say in front of the complex part of the component) are displayed on the Figure 5. It can be seen that both reconstructions give excellent results in terms of positioning of echoes (the reported circles correspond to the exact positions of the side drilled hole in the component), resolution, and signal-to-noise ratio.

Example of sensitivity of the method to the configuration parameters

To illustrate the influence of inaccurate position of the probe, reconstructions have been performed with the same experimental data using corrupted simulation configurations and are compared to that obtained with the exact model (Figure 6a). Loss of detection (around 4 dB) and wrong localization (less than 1 mm) can clearly be observed in the case of a 1mm misalignment of the probe (Figure 6b). These performances are significantly decreased (6 to 11 dB and 3 to 8 mm) with additional 1° disorientation of the probe (Figure 6c).

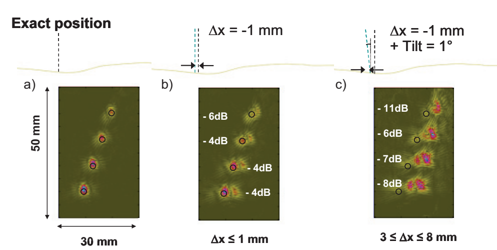

Figure 6 : Influence of inaccuracy on probe position

Multimode reconstruction

Using the forward simulation tools, the FTP method can deal not only with direct wave path, as in the previous case, but also with those including a backwall reflection. The Figure 7 describes all the possible corner echo wave paths, compared to the direct one. The indirect wave path can also be considered. Such multiple reconstruction modes have shown interest in literature [8].

Figure 7 : Definition of direct (a) and corner echo (b) wave paths

As an illustration, the FTP method as been applied on experimental data acquired with a 2.25 MHz flexible phased array transducer composed of 24 elements. The probe lies over a ferritic steel sample with a complex profile and complex backwall, representative of a welded component. A 10 mm high surface breaking planar defect is embedded before the weld root. The reconstruction obtained with the direct mode is compared to those obtained taking into account the most significant corner echo modes for this configuration, TLL, TLT and LLT. As expected, using the direct mode reconstruction, the two tip diffraction echoes are correctly localized at the edges of the defect. On the other hand, the reconstructions taking into account the corner echo wave paths give only one main indication, localized along the defect. Furthermore, the comparison with the same reconstructions obtained on simulated data give a very good agreement in all cases.

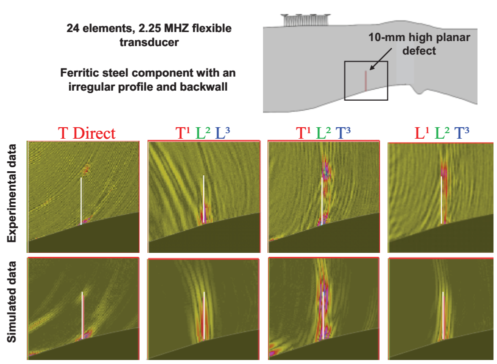

Figure 8: corner echo mode reconstruction in a complex profile component

Application to full 3D reconstruction

The FTP method is now used is the case of a matrix array probe (11x11 elements, pitch 6.5 mm, 1-MHz central frequency) in contact with a ferritic steel specimen (220 mm thick) containing various flat-bottom holes (FBH, 2 mm in diameter) of different height (5 mm to 60 mm). The position of the probe over the flat-bottom holes is shown in Figure 9.

The acquisition scheme used here is referred to as Full Matrix Capture (FMC). It can be explained as follow: an electronic commutation is performed for which each element of the array is successively being used as a source while all the elements are used as receivers. A set containing all combinations of transmitter and receiver elements (121x121 signals for one mechanical position of the probe) is being stored for post-processing. BScan and AScan from this set are shown in Figure 9; the signal-to-noise ratio associated with the FBH is relatively weak, which can be explained by the relatively long ultrasonic path and the small size of the sources and receivers (one element).

The reconstruction algorithm described before is used for experimental data along two perpendicular planes containing the holes. Figure 9 shows the superimposition of the two reconstructions upon a 3D view of the component containing the flat-bottom holes. It is important to notice that despite the poor signal-to-noise ratio observable in the individual ascans, the reconstruction technique leads to a clear detection of all the holes. The FMC acquisition combined with the reconstruction method presented here allows the detection of the defects without having to scan the specimen in all directions.

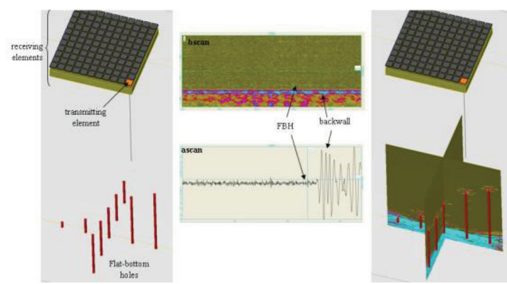

Figure 9 : Inspection configuration, examples of signals acquired during the FMC, and reconstruction result.

Reconstructions on simulated data obtained in an equivalent configuration have also been performed. To illustrate the full 3D data visualization, volumetric rendering using iso-surfaces are displayed on Figure 10. Using this 3D view, we can see that all the defects are correctly detected and localized in the component.

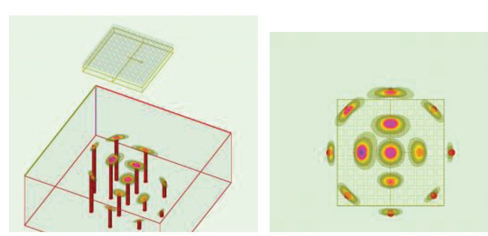

Figure 10: volumetric rendering with iso-surfaces

Conclusion

In this paper, we describe reconstruction algorithms based on the synthetic focusing approach. Unlike the classical reconstruction techniques, the algorithms have been coupled to existing forward models, which allow dealing with complex parts. We have presented some examples of results obtained on simulated and experimental data, which show the ability of the reconstruction to localize echoes in parts presenting irregular surfaces and backwall. Examples of multi-modes and full 3D reconstructions have been proposed on planar and complex components. A first estimation of the sensitivity to the control parameters has also been studied. Work in progress aims at accurately quantifying performances of the algorithms coupled to various operating modes of array inspection.

REFERENCES

[1] More details may be found at http://www-civa.cea.fr.

[2] Raillon R and Lecœur-Taïbi I, "Transient Elastodynamic Model for Beam Defect Interaction. Application to NonDestructive Testing", *Ultrasonics*, 2000, Vol 38, 527-530.

[3] Chaffaï S, Darmon M, Mahaut S, Menand R, "Simulation Tools for TOFD Inspection in CIVA Software", to be published in *proceedings of 6th ICNDE (2007)*.

[4] S. Chatillon, S. Mahaut, and P. Dubois, "*Simulation of advanced UT phased array techniques with matrix probes and dynamic settings for complex component inspections*, in *Review of Progress in Quantitative Nondestructive Evaluation*", Vol 28, (2008), pp 864-871.

[5] Gengembre N, "Pencil method for ultrasonic beam computation", in *proceedings of the 5th World Congress on Ultrasonic*s, 2003, pp. 1533-1536.

[6] Auld B, *Wave Motion* **1**, 3 (1979).

[7] O. Roy, M. Bouhelier,*"3D beam steering for improved detection of skewed crack"*, EPRI Piping & Bolting/Phased Array Inspection Conference, 2005.

[8] J. Zhang, B.W. Drinkwater, P.D. Wilcox, "The use of scattering matrix to model multimodal array inspection with the TFM", in *Review of Progress in Quantitative Nondestructive Evaluation*", Vol 28, (2008), pp 888-895.

Biography

Sylvain Chatillon was born near Paris, France, in 1970. He received the Engineering degree from *Ecole Nationale Supérieure des Telecommunication (ENST)*, Paris, France, in 1995, and the Ph. D. in Physical Acoustics from *Université Denis Diderot, Paris 7,* Paris, France, in 1999. Since December 1999, he has been working at the French Atomic Energy Commission (CEA/LIST) at Saclay, near Paris. He coordinates the implementation of the ultrasonic simulation tools in the Civa plate-form.
His interests include the simulation of ultrasonic beam propagation and interaction with defects in solids, arrays data simulation and reconstruction and signal processing.

Ultrasonic Based Process Monitoring Using Advanced Data Processing and Analysis

A. Shukla, A. Prakash* and S. Rohani
Department of Chemical and Biochemical Engineering
University of Western Ontario, London, Ontario N6A 5B9
CANADA

Abstract

The inherent ability of ultrasound to penetrate dense and optically opaque suspensions along with its fast response time makes it a desirable technique for online monitoring of industrial processes. A method based on ultrasonic attenuation spectroscopy for monitoring particle size distribution variations in dense and opaque suspensions is presented. Advances in the hardware required for ultrasound signal generation, maintaining signal stability and higher signal to noise ratio has provided the ability to accurately measure the attenuation spectra over a wide range of frequencies. Potential applications include online monitoring of nucleation /crystallization in pharmaceutical /food and mineral processing. In these processes it is essential to monitor changes in particle size to ensure product quality, conformity and to avoid complications in down stream processing by maintaining desirable operating conditions.

Although ultrasonic based methods suitable for dense suspensions of colloids and emulsions have been developed, their applicability in systems with larger particle size is limited due to unavailability of a reliable theoretical model for large particle/crystal sizes. Like many other techniques the accuracy of a deconvolution algorithm to determine particle size is limited by the adequacy of the underlying theoretical model. This study discusses a novel approach for predicting ultrasonic attenuation in the intermediate regime of wave propagation and an optimized deconvolution algorithm for signal processing and extraction of particle size information. The technique has been extensively tested in concentrated suspensions of inert particles. The performance has been further tested and validated with offline laser diffraction measurements for the crystallization of a model pharmaceutical compound. The novel technique will enable the development of an ultrasonic attenuation spectroscopy based online particle sizer capable of operating in concentrated suspensions (up to 30 vol.%) over a wide particle size range (1-1000μm).

Keywords: *Ultrasonic; Attenuation Spectroscopy; Particle Size Analysis; Dense Suspensions; Online Monitoring; Advanced Data Processing*

Introduction

The properties, handling and processing of powders are affected by the particle size distribution. Various techniques have been developed for the measurement of particle size. These can be classified under particle counting, fractionation and macroscopic techniques. Particle counting techniques generate number weighted size distributions and include electrozone/optical counters and optical/electron image analysis. Particle counting techniques generate a full size distribution as individual particles are counted. Full particle size distributions can also be obtained by fractionation techniques which rely on the separation of particles in different size fractions. These techniques include sedimentation and sieve analysis. Macroscopic techniques utilize the measurement of changes in physical phenomena (light or sound) which are affected by the presence of particles. These techniques relate the changes in the measured quantity with particle size using theoretical formulations. Depending on the measurement principle, different characteristics of the particles are measured and hence different measures of size are obtained. For example the sieve diameter is the width of the minimum square aperture through which a spherical particle will pass whereas the Stoke's diameter is the diameter of a free falling sphere. However, particles encountered in most industrial applications have an irregular shape and can not be described using a single geometrical parameter such as diameter. The size of these particles is generally expressed in terms of statistical diameters or equivalent spherical diameters (ESD). Statistical diameters (e.g. Feret's or Martin's) describe the mean value of sizes measured along different directions on the projected particle outline. The ESD is the diameter of a sphere that causes the same change in measured property as the particle. For example the Stokes diameter is equivalent to the size of a free falling spherical particle.

Equivalent spherical diameter shows a functional variation with shape depending on the method of measurement. Due to this reason, the ESD obtained using different techniques are not the same. However, it is possible for particle of different shapes to have the same ESD when measured using a particular technique. Hence, it is useful to define shape factors such as aspect ratio and sphericity to obtain a correlation between measured ESD and shape of the particles. Existing measurement techniques only predict the size distribution based on spherical equivalent diameter and assume that the particle shape is homogenous. Some studies [1] have tried to determine the shape factors by making measurements using various techniques and comparing them to estimate the aspect ratio.

Generally particulate systems in industrial processes are polydispersed in nature and consist of a distribution of different sizes occurring at specific frequencies. These systems are defined by the average and width of the distribution. The distribution average is a measure of its central tendency and includes the mode, median and mean. Mode is the most frequently occurring value in the distribution whereas median divides the distribution in to two equal parts and the mean value is the center of gravity of the distribution. The width of a distribution is defined by the standard deviation and is calculated with respect to the central tendency used to describe the distribution average.

There are various analytical distributions which can be used to define a particle size distribution (PSD) using mathematical expressions. Log-normal distribution is the most frequently occurring distribution in particulate systems and is used extensively for PSD measurements. Particle sizing techniques compare the measured size dependent physical phenomenon with theoretically computed values using different distribution parameters to obtain the best fit.

Particulate operations are dynamic in nature and the change in size distribution could be due to particle growth, attrition and/or agglomeration. Down-stream processing and end product quality in these systems can be significantly influenced by the particle size distribution. For example, changes in PSD during crystallization due to product classification can lead to open loop unstable behavior. A real-time knowledge of the PSD in these systems is essential for implementation of control algorithms to obtain desired end product quality. However, online size measurement is only possible with in-situ techniques. Hence, particle sizing techniques based on sieve analysis, sedimentation and optical/electron microscopy are inherently unsuitable for online applications due to the long delay-time associated with sample preparation/ measurement. Sampling itself can lead to errors if it is inadequate or unrepresentative.

Background- Particle Sizing Techniques

Online determination of particle size distribution requires in-situ measurements. The techniques capable of in-situ measurements include laser diffraction, laser reflectance and ultrasonic attenuation spectroscopy. These techniques are based on different measurement principles and hence give a different measure of PSD. Laser reflectance measures the number based chord length distribution whereas light scattering and ultrasonic spectroscopy generate volume-based distributions.

Laser diffraction measures the forward scattered light and is considered to be a standard technique for off-line particle sizing. The particles can be measured in a size range of 0.5 to 1000-μm. However, this technique cannot operate in opaque or dense suspensions due to the limited penetration depth of light. Furthermore, the theoretical models required for inferring PSD are only applicable at concentrations where multiple scattering is insignificant. Hence, online applications of this technique are limited to industrial processes which operate at very low solids concentration. Laser reflectance technique uses focused beam reflectance measurements (FBRM) from the particle surface. The particle size range obtained using this technique is from 0.5 to 2000-μm. Unlike laser forward scattering this technique can make in-situ measurements in dense suspensions. However, suspension transparency is required and limits its applicability to specific industrial processes. Ultrasonic techniques measure the change in energy loss as a function of frequency to determine particle size distributions and can operate in dense as well as opaque suspensions. It has the capability of operating in suspensions of particle sizes from 0.005 to 1000-μm. However, its online application is currently limited to particles in the size range of 0.005 to 100-μm due to the unavailability of theoretical models for sizing large particles in dense systems. The operating principles of these techniques along with their advantages and limitations are summarized in Table 1.

Table 1. Comparison of online PSD measurement techniques.

	Laser Forward Scattering	*Laser Reflectance Method*	*Ultrasonic Techniques*
Measurement Principle	Forwards scattered light	Back scattered light	Attenuation spectrum
Transparency	Required	Required	Not required
Nature of PSD	Volume weighted PSD	Unweighted chord length distribution	Volume weighted PSD
Penetration depth	4mm, for<1 vol. %	Only at probe surface	50 mm, for<20 vol.
Concentration	Dilute	Dense	Dense
Size range (Projected)	0.5 to 1000 μm	0.5 to 2000 μm	0.005 to 1000μm
Application	Mainly off-line	In-situ	In-situ

Recent advances have also been made in online microscopic image analysis. Although particle shape information will be more readily available using this technique it is not suitable for online PSD measurements. On-line microscopic analysis is not considered for further discussions here as this is a particle counting technique. A large number of particles have to be considered to obtain a reliable size distribution using this technique and suspension transparency is essential.

Laser Diffraction

Laser Diffraction is one of the most widely used techniques for determining particle size distribution. This technique is based on the principle of forward scattering of a broad laser beam passing through a suspension of particles. A Fourier lens is used to focus the forward scattered light on to an array of photo-detectors perpendicular to the laser source. Scattering may be caused due to diffraction at the particle edges, refraction of light passing through the particles and reflection from the external or internal surfaces. For larger particles (>4-μm) the Fraunhofer theory can be used as diffraction is the dominant scattering phenomenon whereas the Rayleigh theory is applicable to particles in the sub-micron region [2]. Most modern particle size analyzers based on this technique use the Mie theory as it can account for different types of scattering. The variation in scattered light intensity as a function of the scattering angle (ϑ) and particle size can be calculated using Equation 1 [3].

$$I(\vartheta) = I_o \int_0^\infty f(r) \left(\frac{rJ_1 \alpha_{ld}(\vartheta)}{\vartheta} \right)^2 dr \tag{1}$$

$$where, \quad \alpha_{ld} = \frac{2\pi\lambda}{r}$$

Particle size analyzers using laser diffraction assume a spherical particle shape and absence of multiple scattering. However, most industrial systems operate at high concentrations where this technique becomes inapplicable due to its limited penetration depth and multiple scattering. In such systems the measurements are made by continuously circulating the particles through a measurement cell after automatic slurry dilution.

Reproducibility of size measurement using laser diffraction depends on the accuracy of detector alignment with laser source. Misalignment was found to severely affect PSD measurements in simulated studies reported by Wang and Shen [4] for mono-sized particles. Various algorithms are available for deconvoluting particle size distribution and have been reviewed by [3]. However, Etzler and Deanne [5], Neumann and Kramer [6] and Pei et al. [7] have shown that the choice of deconvolution algorithm can effect the PSD.

The major drawback of laser diffraction technique is its inability to make in-situ measurement in dense suspensions. In-line mode of operation is essentially automatic slurry sampling as dilution is still needed to obtain the PSD. Slurry dilution also leads to error and increase in operating time as multiple measurements have to be made for obtaining a representative size distribution. Transport of slurry through a recirculation loop can also lead to changes in PSD due to particle breakage. Furthermore, design modification of the process itself is required to accommodate the re-circulation loop for in-line measurements.

Laser Reflectance

The focused beam reflectance method (FBRM) can be used for in-situ measurements in dense suspensions and is being rapidly adopted as a method of detecting particle growth and attrition in a number of industries. This technique is based on laser back reflectance and measures the chord length distribution of particles. Implementation of FBRM is done using a cylindrical probe [8], in which a laser beam with a wavelength of 780nm is rotated at high velocity (~4500rpm). This beam enters the suspension through a sapphire window at the probe tip and can be focused at various depths in the suspension. Particles crossing the focal point reflect the laser beam back into the probe where they are detected by optical sensors. These sensors convert the light energy into electrical signals which are passed through a discriminator circuit to filter signals with long rise times [9]. This helps in the elimination of signals generated from back reflection of particles at positions other than the focal point. The product of measured crossing time (of particle) and the beam velocity are used to calculate the chord length. These chord lengths are added to obtain finite number of chord length intervals or channels.

The FBRM technique measures thousands of chord lengths per second and gives an unweighted chord length distribution (CLD). Since the laser beam randomly scans the particle surface, it measures the chord lengths corresponding to the projected area of the particles. Various studies have been conducted to evaluate the effect of operating parameters such as solids concentration and focal point position on the measurement of CLD in suspensions. Heath et al. [8] have shown that the unweighted distributions are sensitive to fine particles with increase in solids concentration. This bias was attributed to the increase in the number of fines scanned by the FBRM probe. The effect of solid-volume fraction on distribution mode was negligible for equivalent spherical size, cube weighted and square weighted chord length distributions [8,10,11]. However, Sparks and Dobbs [10] have shown that laser-lens interactions may cause broadening of the beam due to high solids concentration and solution/particle surface characteristics. This can lead to changes in optimum focal point positions and cause errors in the CLD measurements [12]. Substantial changes were observed in the CLD as a function of focal position and have been investigated by various researchers. Monnier et al. [13] and Law et al. [14] have shown that focal length between 0.8 to 2mm in the solution gave better measurements for larger particles. However, Heath et al. [8] showed that although some improvement may be obtained using a larger focal position for dilute suspensions, the optimal setting for concentrated systems should be zero-microns from the probe window. They reported a drop in chord counts as the focal length was increased away from the probe window. Focal positions very close to the probe window can increase the sensitivity of the unweighted distribution to finer chord lengths as lesser number of larger chords is able to enter the viewing region. This effect can be minimized by using the square-weighted chord length distribution.

A number of studies have tried to correlate the CLD measurements with laser diffraction to obtain a relationship with average particle size [10,13,15]. Heath et al. [8] observed that the mean as well as median were affected by the sensitivity of FBRM measurements to fine particles. However, the mode of square-weighted distribution showed good agreement with the median size obtained using laser diffraction for particles between 20 to 500-μm. Various algorithms have also been developed for converting CLD measurements to size distribution data. Majority of the work dealing with theoretical methods for CLD-PSD conversion assume spherical particles or two-dimensional ellipses. Assumption of a spherical particle size simplifies calculations as orientation effects can be neglected. However, such assumptions are only valid for glass beads or latex suspension and can be considered reasonable in suspensions where the aspect ratio is approximately 1 [8]. Taddayon and Rohani [9] used a two dimensional model approach to obtain PSD from CLD for ellipsoidal and spherical particles. Ruf et al. [16] developed a 3-D model of chord length distribution for particles of general shapes. However, they concluded that CLD to PSD inversion is not possible unless the shape of particles is known.

This technique cannot operate in opaque suspensions and the measurements are not representative as they are localized at the probe tip. Particle opacity also has an effect on the measured CLD and transparent particles cannot be properly sized due to poor reflectivity [10]. FBRM measurements are susceptible to particle shadowing (due to the presence of fines), particle masking (due to coarse particles) and the assumption that the entire particle projection area has perfect back reflectance. Furthermore, CLD measurements are significantly affected by particle shape and can lead to large errors in PSD deconvolution unless the shape is known before hand.

Ultrasonic Spectroscopy

Ultrasonic techniques can be used for online measurement of volume-weighted particle size distribution in dense and opaque systems. This technique is based on the propagation of an acoustic pulse through the suspension and measures the change in its attenuation and acoustic velocity caused by the presence of particles (Figure 1). The ability of this technique to penetrate dense suspensions are shown in Figure 2 [17]. The settling characteristic of 43 and 168-μm mixed particle system was monitored using ultrasonic velocity. The measurements were made in through transmission mode with transducer separation of 25mm. It can be seen from the figure that segregation could be easily measured using ultrasound and the trends closely correspond to the theoretical model of Schneider et al. [18]. The measurements were also able to pick up concentration and size gradients.

The changes in the parameters of the acoustic pulse show frequency dependence with respect to particle size. Attenuation and velocity in suspensions are also affected by the properties of the liquid phase and the frequency dependence of these parameters becomes more pronounced with increasing viscosity and molecular scale relaxations in the liquid (e.g. oily liquids). However, irrespective of the liquid phase the presence of solids causes a substantial change in attenuation as compared to acoustic velocity measurements. Hence, majority of the ultrasonic techniques utilize attenuation spectrum measurements over velocity spectrum for particle sizing.

Loss of energy contained in the acoustic pulse can be due to different attenuation mechanism. These attenuation mechanisms can be classified under absorption and scattering losses. The dominant loss mechanism is dependent on the regime of wave propagation which is classified using a dimensionless parameter called the wavenumber ‘kr’. The wavenumber is calculated using the particle radius ‘r’ and ultrasonic wavelength ‘λ’. The various propagation regimes based on ‘kr’ are summarized in Table 2 along with the prevalent attenuation mechanism.

Table 2. Ultrasonic Propagation Regimes.

Wavenumber ($kr=2\pi r/\lambda$)	**Regime of Propagation**	**Loss Mechanism**
$kr<<1$	Long wave regime	Absorption losses are dominant
$kr\sim 1$	Intermediate regime	Scattering losses are dominant
$kr>>1$	Short wave regime	Geometrical scattering

Ultrasonic measurements in the long and intermediate wave regime are sufficient for obtaining PSD measurements for industrial processes as these can cover particles from the sub-micron to the micron region. Similar to other techniques ultrasonic attenuation spectroscopy optimizes the parameters of assumed distribution by minimizing the error between predicted and measured attenuation spectrum. Theoretical models available for attenuation predictions in dense suspensions are only applicable in the long wave regime. Hence this technique is limited to particles smaller than 100-μm. In this regime the absorption losses are dominant and the effect of scattering is insignificant. Absorption losses are hydrodynamic or thermodynamic in nature and are caused by the interaction of particles with the pressure field generated by the acoustic pulse.

The most widely used ultrasonic attenuation model was initially developed by Epstein and Carhart in 1941 for sound propagation in air with suspended fog droplets. Allegra and Hawley [19] modified this model for applications in colloidal suspensions and developed explicit equations for attenuation calculation. The ECAH (Epstein-Carhart and Allegra-Hawley) theory calculates the attenuation for a single particle and the total attenuation is obtained by superposition of the contributions of each particle. Under dilute conditions (<10 vol. %) the superposition theory is valid as particle-particle distance is sufficient to avoid the overlap of the viscous layers of individual particles. Gibson and Toksoz [20] developed a coupled phase model to account for the effects of viscous length overlap for mono-sized particles. Dukhin and Goetz [21] generalized the coupled phase model for poly-dispersed suspensions.

The major limitation of ultrasonic techniques is its inability to size larger particles due to the unavailability of theoretical models to predict scattering. Scattering is caused by the redirection of the energy contained in an acoustic pulse by the particles and is dominant when the wavelength is comparable to the particle size. Various attempts have been made to develop a scattering theory applicable at higher wave numbers [22,23,24,25,26]. However, these models did not show good agreement with measurements in dense suspensions.

In the absence of a reliable scattering model efforts were made using empirical models to obtain the relationship between particle size and measured attenuation. This technique is based on the measurement of particle size fractions using offline techniques such as laser diffraction. The attenuation spectrum of these particles was then measured and calibration equations were generated to obtain the frequency response of different size fractions. This technique can be used for a broad range of particle sizes but requires customized calibration for specific applications. Furthermore, changes in particle shape and/or size, fluid properties (e.g. density or compressibility) can lead to significant errors as the calibration model does not account for them. Hence, theoretical scattering models applicable in dense suspensions are desirable to extend the use of ultrasonic techniques for larger particles.

Novel Ultrasonic Technique- *Results*

Morse and Ingard [27] model, has the capability of operating in the intermediate regime of wave propagation. Equations 2 and 3 show the explicit equation for calculating the scattering and absorption cross sections using this model.

$$\Sigma_s = \frac{4\pi}{k^2}\sum_{m=0}^{\infty}(2m+1)\left|\frac{j_m'(kr)+i\beta_m j_m(kr)}{h_m'(kr)+i\beta_m h_m(kr)}\right|^2 \qquad (2)$$

$$\Sigma_a = \frac{k^4 r^4}{4\pi r^2}\sum_{m=0}^{\infty}\frac{(2m+1)\,\mathrm{Re}(\beta_m)}{\left[h_m'(kr)+i\,\mathrm{Im}(\beta_m)h_m(kr)\right]^2} \qquad (3)$$

A comparison with experimental results has shown that the model performance is extremely good at low concentrations (<2 vol.%) [28]. However the model tends to significantly deviate with increase in particles concentration. The deviations in this and other intermediate regime models have often been attributed to particle-particle interactions. However, Dukhin and Goetz [21] have experimentally shown that multiple scattering effects are minimal up to 40 vol.% concentration.

Shukla et al. [28,29] have shown that the model [27] non-performance in dense suspensions can be attributed to directional scattering. The original Morse and Ingard [27] model does not account for the finite sensor size and geometry. Model modification incorporating these effects leads to significant improvements in dense suspension attenuation predictions. The novel model along with an optimized deconvolution algorithm [28,30,31] has resulted in the measurement of PSD in dense suspensions of particles lying in the intermediate propagation regime.

Figure 3 shows the PSD measured using ultrasonic attenuation spectroscopy technique at 12 vol.% for 43 and 202-μm glass particles [28,29]. Offline PSD measured using Malvern Mastersizer ® at concentrations less than 1vol.% are also shown in the figure and is similar to the measurements obtained using the ultrasonic technique at higher concentrations. Figure 4 shows the online measured PSDs [30] using ultrasonic techniques during crystallization of a model pharmaceutical compound. A comparison with offline PSD measured using Malvern Mastersizer ® for a sample retrieved at the end of crystallization shows good agreement with the ultrasonic spectroscopic results.

Conclusions

Various particle size measurement techniques were compared with respect to their suitability for in-situ measurements. Laser diffraction technique can not operate in opaque and dense systems due to limited light penetration. This necessitates the use of in-line measurements to accommodate slurry dilution. However, this mode of measurement is not truly online due to the time-delay associated with slurry circulation and dilution. The removal of slurry from the process and dilution can also cause changes in the nature of the PSD. Unlike laser diffraction, FBRM measurements are capable of making in-situ measurements and hence can be used for online applications. However, this technique cannot be used for opaque suspensions and the measurements are non-representative as measurements are limited to the particles present at the probe surface. Ultrasonic techniques can overcome the limitations of light-based measurements as it can operate in opaque suspensions and has good penetration depth (>25mm) even under dense conditions. The measurements obtained using this technique is more representative when compared to laser diffraction as well as laser reflectance techniques. The current application of this technique was limited to particles smaller than 100-μm due to the unavailability of theoretical models for dense suspensions of large particles. These drawbacks have been overcome by the modified intermediate regime model proposed by Shukla et al. [28,30,31] and has the potential for online particle sizing in industrial applications.

Nomenclature

h_m, h_m'	Hankel function and its derivative
I	Final intensity (W.m^{-2})
I_0	Incident intensity (W.m^{-2})
j_m, j_m'	Bessel function and its derivative
kr	Non-dimensional wavenumber (-)
m	Integer (-)
r	Particle radius (m)

Greek Symbols

β_m	Surface Admittance (-)
λ	Wavelength (m^{-1})
ϑ	Scattering angle (rad)
Σ_a	Absorption c/s area (m^{-2})
Σ_s	Scattering c/s area (m^{-2})

Author Bio

Dr. Abhishek Shukla is a post doctoral fellow in the Department of Chemical and Biochemical Engineering at the University of Western Ontario (UWO).
Email- ashukla3@uwo.ca

Dr. Anand Prakash is a Professor in the Department of Chemical and Biochemical Engineering at UWO. He is a Steering Committee member of the Particle Technology Research Center (PTRC) at UWO.
Email- aprakas2@uwo.ca

Dr. Sohrab Rohani is a Professor in the Department of Chemical and Biochemical Engineering at UWO. He is a Director of PTRC and founder of Crystallization and Control of Pharmaceuticals Laboratory (CCPL) at UWO.
Email-srohani@eng.uwo.ca

Literature Cited

[1] J.W. Novak, J.R. Thompson, Extending the Use of Particle Sizing Instrumentation to Calculate Particle Shape Factors, Powder Technology 45 (1985) 159-167.

[2] P. Bowen, Particle size distribution measurement from millimeters to nanometers and from rods to platelets, Journal of dispersion science and technology 23 (5) (2002) 631-662.

[3] B.J. Azzopardi, in: N.G. Stanley-Wood, R.W. Lines (Eds.), 1992, pp. 108-132.

[4] N. Wang, J. Shen, A study of the influence of misalignment on measuring for laser particle analyzers, Particle and Particle Systems Characterization 15 (1998) 122-126.

[5] F.M. Etzler, R. Deanne, Particle size analysis: Comparison of various methods-II, Particle and Particle Systems Characterization 14 (1997) 278-282.

[6] A. Neumann, H. Kramer, J., M., A comparative study of various size distribution measurement systems, Particle and Particle Systems Characterization 19 (2002) 17-27.

[7] P. Pei, J. Kelly, S. Malghan, S. Dapkunas, Analysis of Zirconia Powder for Thermal Spray: Reference Material for Particle Size Distribution Measurement, Thermal Spray: Practical Solutions for Engineering Problems (1996) 263-273.

[8] A.R. Heath, P.D. Fawell, B.P. A., J.D. Swift, Estimating average particle size by fucused beam reflectance measurement (FBRM), Particle and Particle Systems Characterization 19 (2002) 84-95.

[9] A. Taddayon, S. Rohani, Determination of particle size distribution by Par-Tec ® 100: Modelling and experimental results, Particle and Particle Systems Characterization 15 (1998) 127-135.

[10] R.G. Sparks, C.L. Dobbs, The use of laser backscatter instrument for the online measurement of the particle size distribution of emulsions, Particle and Particle Systems Characterization 10 (1993) 279-289.

[11] E.A. Daymo, T.D. Hylton, Acceptance testing of the Lasentec focussed beam reflectance (FBRM) monitor for slurry transfer applications at Hanford and Oakridge, 1999.

[12] K.J. Reid, M.S. Stachowicz, Evaluation of the Partec 200 particle size analyzer, Soc. Min, Metall. Expl. Littleton, Cholorado, 1990.

[13] O. Monnier, J.P. Klein, C. Hoff, B. Ratsimba, Particle size determination by laser reflection: methodology and problems, Particle and Particle Systems Characterization 13 (1996) 10-17.

[14] D.J. Law, A.J. Bale, S.E. Jones, Adaptation of focused beam reflectance measurement to in situ particle sizing in estuaries and coastal waters, Marine Geol. 140 (1997) 47-59.

[15] F. Hobbel, R. Davies, F.W. Rennie, T. Allen, L.E. Butler, E.R. Waters, J.T. Smith, R.W. Sylvester, Modern methods of on-line size analysis for particulate process streams, Particle and Particle Systems Characterization 8 (1991) 29-34.

[16] A. Ruf, J. Worlitschek, M. Mazotti, Modeling and experimental analysis of PSD measurements using FBRM, Particle and Particle Systems Characterization 17 (2000) 167-179.

[17] A. Shukla, A. Prakash, S. Rohani, Particle settling studies using ultrasonic techniques, Powder Technology 177 (2007) 102-111.

[18] W. Schneider, G. Anestis, U. Schaflinger, Sediment composition due to settling of particles of different sizes, International Journal of Multiphase Flow 11 (3) (1985) 419-423.

[19] J.R. Allegra, S.A. Hawley, Attenuation of sound in suspensions and emulsions, Journal of the acoustical society of America 51 (1972) 1545-1564.

[20] R.L. Gibson, M.N. Toksoz, Viscous Attenuation of Acoustic Waves in Suspensions, Journal of the acoustical society of America 85 (1989) 1925-1934.
[21] A.S. Dukhin, P.J. Goetz (Eds.), Ultrasound for characterizing colloids- particle sizing, zeta potential, rheology, Boston, Elsevier, 2002.
[22] C.M. Atkinson, H.K. Kyotomaa, Acoustic wave speed and attenuation in suspensions, International Journal of Multiphase Flow 18 (4) (1992) 577-592.
[23] A.E. Hay, D.G. Mercer, On the Theory of Sound Scattering and Viscous Absorption in Aqueous Suspensions at Medium and Short wavelength, J. Acoust. Soc. Amer. 78 (5) (1985) 1761-1771.
[24] P.S. Waterman, R. Truell, Multiple Scattering of Waves, Journal of Mathematical Physics 2 (1961) 512-537.
[25] Y. Ma, V.K. Varadan, V.V. Varadan, Comments on ultrasonic propagation in suspensions, J. Acoust. Soc. Amer. 87 (1990) 2779-2782.
[26] P. Lloyd, M.V. Berry, Wave propagation through an assembly of spheres, Proceedings of the Physical Society 91 (1967) 678-688.
[27] P.M. Morse, K.U. Ingard, Theoretical Acoustics, McGraw Hill New york, 1968.
[28] A. Shukla, Ultrasonic Techniques for Dispersed Phase Characterization., Department of Chemical and Biochemical Engineering, University of Western Ontario (Ph.D.), London, Ontario, 2007.
[29] A. Shukla, A. Prakash, S. Rohani, Particle size distribution measurements in dense suspensions using ultrasonic spectroscopy with an improved model accounting for low angle scattering, Submitted to A.I.Ch.E. Journal Under review (2009)
[30] A. Shukla, A. Prakash, S. Rohani, Online Measurement of Particle Size Distribution during Crystallization using Ultrasonic Spectroscopy, Submitted to Industrial and Engineering Chemistry Research Under Review (2009)
[31] A. Prakash, A. Shukla, S. Rohani, Method and Apparatus for Ultrasound Monitoring of Particle Size Distribution, in: (Ed.), U.S. Patent Application, 2009.

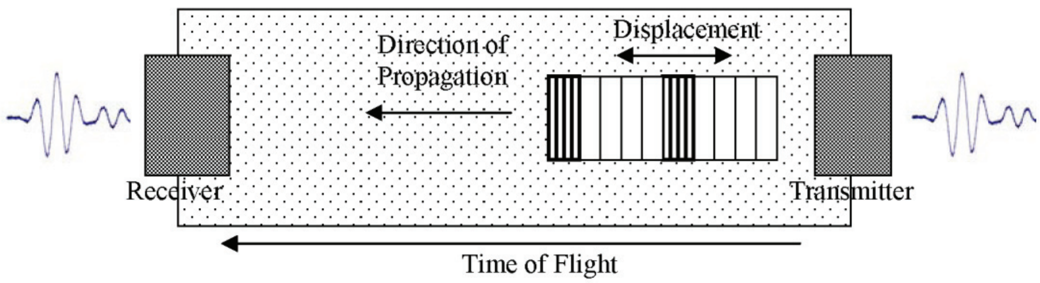

Figure 1. Propagation of longitudinal ultrasonic waves in suspensions

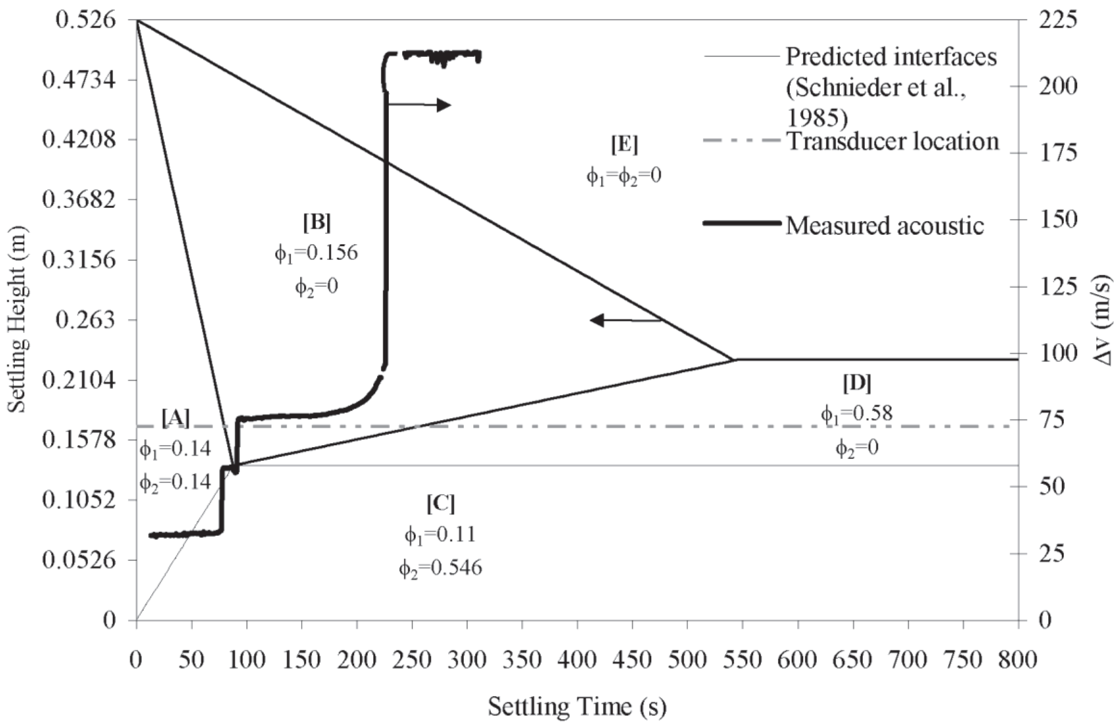

Figure 2. Simulation of bi-disperse suspension (43 and 168-μm) using Schnieder et al. [18] model and comparison with change in acoustic velocity measurements [17].

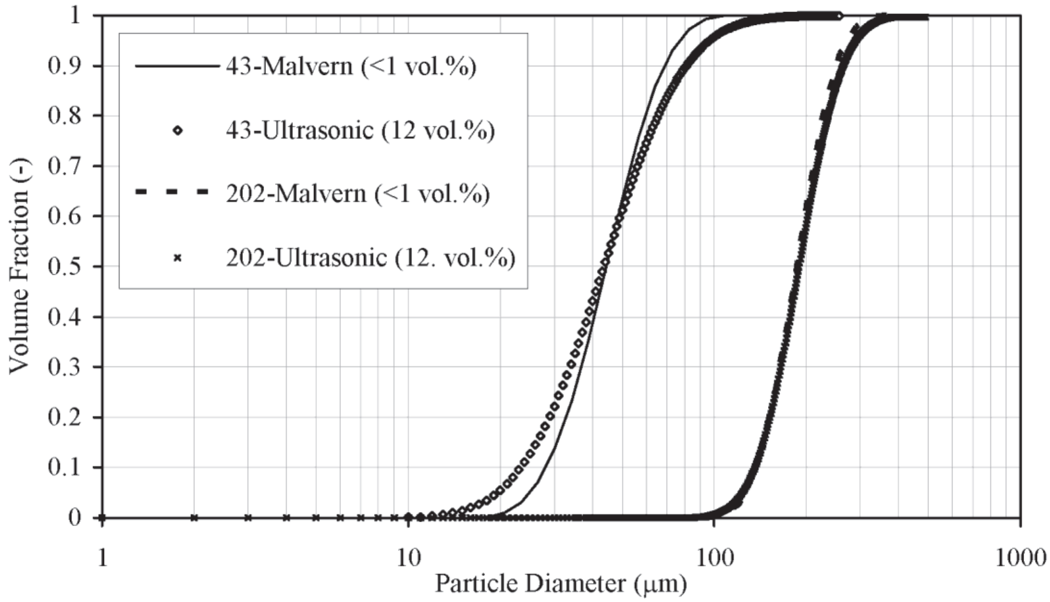

Figure 3. Comparison of PSDs (43 and 202-μm) [29] measured using the novel ultrasonic attenuation spectroscopy technique [28, 29, 31] at 12 vol.% with offline laser diffraction (<1 vol.%) results (Malvern Mastersize ®) for glassbeads suspended in water.

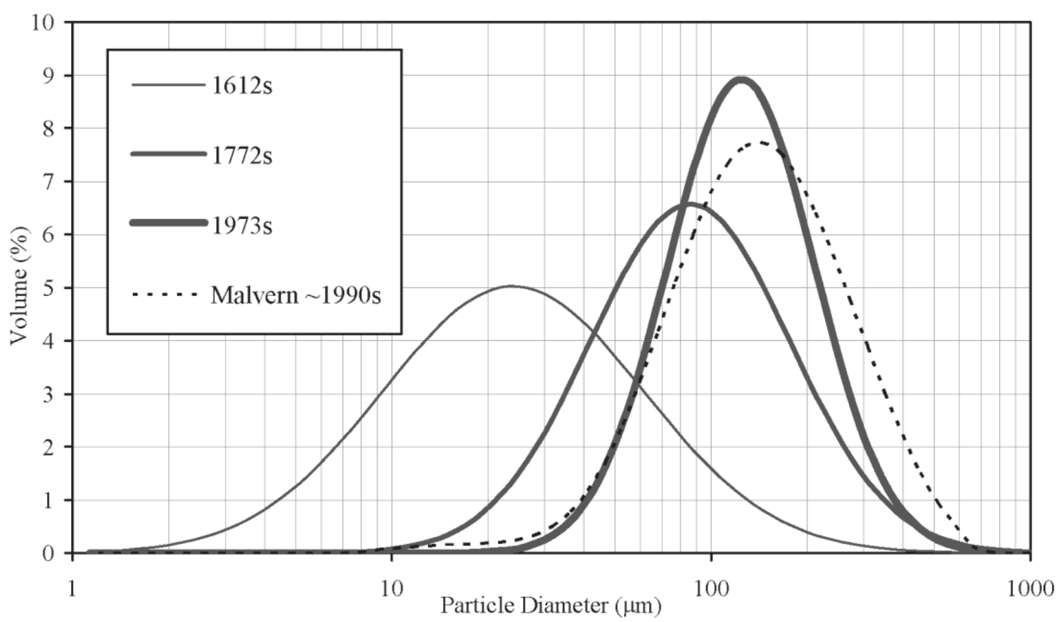

Figure 4. Online measurements of PSD [30] using Shukla et al. technique [28, 29, 31] at various times during crystallization. The offline measurement from Malvern Mastersizer ® is shown for comparison with the online ultrasonic PSD at the sample retrieval time.

Image Processing for Automated Flaw Detection in Pulsed Thermography

M. Genest

National Research Council Canada, Institute for Aerospace Research, 1200 Montreal Road, Building M-14, Ottawa, Ontario, Canada, K1A 0R6

Abstract

Infrared (IR) thermography has evolved in recent years from being an emerging nondestructive testing (NDT) technique to a viable approach for both aerospace manufacturing and in-service inspections. One of the drawbacks of thermography techniques is that no standard signal processing has been universally adopted and that different algorithms yield different sizing results. Additionally, the data interpretation is not as simple as with other NDT techniques. In this paper the most common signal processing techniques applied to pulsed thermography, which include derivative processing, pulsed phase thermography and principal component analysis, are applied in an attempt to simplify the damage detection and sizing process. The pulsed thermography experiments were carried out on 25 impacted panels made of carbon fiber epoxy material. Despite using similar panels and the same experiment parameters, the damage detection and sizing processes are not straight forward. It is concluded that some algorithms provide easier detection capability than others. However, on their own, the different algorithms lack the robustness to make the damage detection and sizing processes reliable and fully automated.

1 Introduction

In pulsed thermography (PT) energy is applied to the specimen using a pulsed excitation. Typically, the energy sources are flash lamps whose flash duration varies from a few milliseconds for good thermal conductors to a few seconds for low-conductivity materials.

The applied energy creates a thermal front that propagates from the specimen's surface throughout the specimen. During the cool down process the surface temperature decreases uniformly for a sample without internal flaws. When the thermal front intersects an interface from a high to low conductivity layer, like in the case of delamination, disbond and porosity, the cooling rate is locally disrupted. This results in an accumulation of heat above the flaw that is also manifested at the specimen's surface and can be detected by an IR camera. Thus, allowing defective areas to be distinguished from sound areas.

Image processing is commonly used for two purposes. Its first use is to improve the visual appearance of images to a human viewer. Filtering and colormap adjustments are commonly applied to make an image more pleasant to look at. Its second purpose is to prepare the images or data for the measurement of features present. This can include applying a threshold to create a binary image, applying morphologic filters, etc. The processed image allows the operator to measure the size of the features of interest and could also be used for automated flaw detection and measurements. Although NDT inspections are more and more automated, thanks to automated scanning systems, the inspector is still required to identify the presence of flaw and to perform the measurement of the features of interest.

The following paragraphs review the most common signal processing techniques applied to pulsed thermography data. In the open literature these algorithms are usually applied and demonstrated on laboratory samples that contain artificial and simple geometry flaws. In this paper, solid laminate samples that have been damaged by impact are used to investigate the capability of these algorithms for the development of robust and automated flaw detection and measurements.

Thermal Contrasts

The most basic data processing performed on pulsed thermographic data is the computation of thermal contrasts. Thermal contrasts have the advantages of being less sensitive to noise and to the surface optical properties[1]. The main problem with thermal contrast computation is that it requires a priori knowledge of a sound area. Although more recently new contrast methods have been developed to overcome this problem[2,3,4].

Pulsed Phase Thermography

Pulsed phase thermography (PPT) is a processing method in which the thermal images are transformed from the time domain to the frequency domain[5]. This can be performed by processing a sequence of thermal images (thermogram) with discrete Fourier transform (DFT):

$$F_n = \sum_{k=0}^{N-1} T(k) e^{-2\pi i k n / N} = \mathrm{Re}_n + i\,\mathrm{Im}_n \qquad (1)$$

Where n designates the frequency increments (n=0,1,…N-1), and Re and Im are the real and the imaginary parts of the DFT, respectively. For convenience, fast Fourier transform (FFT) a computationally efficient version of the DFT is generally used. Once the data has been converted into the Fourier domain, the phase (ϕ) and amplitude (A) images of the different frequencies can be calculated using:

$$A_n = \sqrt{\mathrm{Re}_n^{\,2} + \mathrm{Im}_n^{\,2}} \quad \text{and} \quad \phi_n = tan^{-1}\left(\frac{\mathrm{Im}_n}{\mathrm{Re}_n}\right) \qquad (2)$$

The phase is particularly advantageous since it is less affected by environmental reflections, emissivity variations, non-uniform heating, surface geometry and orientation. The phase characteristics are very attractive not only for qualitative inspections but also for quantitative ones[6,7].

Thermographic Signal Reconstruction

Thermographic signal reconstruction (TSR)[8] is a processing technique that uses polynomial interpolation to allow increasing the spatial and the temporal resolution of a thermogram sequence, while reducing the amount of data to be analysed. TSR is based on the assumption that temperature profiles for non-defective areas follow the decay curve given by the one-dimensional solution of the Fourier diffusion equation for an ideal pulse uniformly applied to the surface of a semi-infinite body[9], which is given by:

$$T(t) = \frac{Q}{e\sqrt{\pi \cdot t}} \qquad (3)$$

Where T(t) is the temperature evolution, Q is the energy applied at the surface and e is the thermal effusivity of the sample, which is defined as: $e = \sqrt{k\rho c}$; where k, ρ, and c are the thermal conductivity, the mass density and the specific heat, respectively. Equation 3 may be rewritten in a logarithmic notation and expanded into a polynomial series[10]:

$$\begin{aligned} \ln(\Delta T) &= \ln\left(\frac{Q}{e}\right) - \frac{1}{2}\ln(\pi t) \\ &= a_0 + a_1 \ln(t) + a_2 \ln^2(t) + \ldots + a_n \ln^n(t) \end{aligned} \qquad (4)$$

The noise reduction resulting from this polynomial interpolation[11,12] enables the use of derivate processing to enhance the contrast created by the presence of defects. The first and second derivatives of the thermogram sequence provide information on the rate of temperature variation. These measurements are analogous to the relations between position, velocity and acceleration in mechanics. The original thermogram corresponds to the surface temperature of the inspected object (position). The first derivative gives information on the cooling rate of the surface temperature (velocity), while the second derivative provides information on the acceleration or deceleration of this cooling rate (acceleration).

Principal Component Analysis

Principal component analysis (PCA)[13], also known as principal component thermography (PCT)[14], is an orthogonal linear transformation that transforms the thermogram sequence into a new coordinate system. The idea behind PCA is to remove possible correlation in the data by creating a new uncorrelated dataset called principal components. It has been applied in thermal NDT for data reduction and flaw contrast enhancement[13,14,15,16]. The algorithm is based on the decomposition of the thermogram into its principal components using singular value decomposition (SVD).

The first step of the PCA algorithm is to reshape the three-dimensional thermogram into a two-dimensional array where the columns and rows contain the spatial and temporal information, respectively. Thus, the original thermogram T(x,y,t) becomes A(n,m) where n = $\mathrm{Nx} \times \mathrm{Ny}$, m = Nt, Nx and Ny are the number of pixels per row and column of the IR camera and Nt is the number of thermal images in the thermogram sequence.

The two-dimensional array A is then adjusted by subtracting the mean along the time dimension, and decomposed into eigenvectors and eigenvalues[17]:

$$\mathrm{A} = \mathrm{U}\,\Gamma\,\mathrm{V}^{\mathrm{T}} \qquad (5)$$

Where U and V are orthogonal matrices which columns form the eigenvectors of AAT and ATA respectively, and Γ is a diagonal matrix that contains the singular values of ATA. Since the thermal images in the thermogram are non-erratic and vary slowly in time, the principal temporal variations of the dataset are usually contained within the first few eigenvectors. The principal component images are formed by calculating the dot product of the eigenvector and the measured temperature.

2 Experimental Work

Samples

This work used 25 generic samples of 6 inches wide by 4 inches long (15.2cm x 10.2cm) made of 24 plies of Toray T800S/3900-2B P2352W-19, with an areal weight of 0.0388 lbs/sqf (0.190 kg/m2) in a [+45/90/-45/0]3S layup configuration. The samples were all impacted using a one inch (2.54cm) diameter semi-spherical impactor head at 36.9 lbf (50J) impact energy level. Almost all of the samples had fibre breakage on the impacted side. Several of them also had fibre breakage at the back side.

Inspection

The pulsed thermography inspections were carried out using a 240x320 pixels IR camera that has a thermal sensitivity of 20mK at 303K and a spectral response in the long wave infrared, from 8.0 to 8.8μm. Two xenon flash lamps, each powered by a 2400J power supply, were used as energy sources. Each sample was inspected from both the front and the back surfaces, and each thermogram contained 740 frames that were acquired at 20Hz.

3 Results and discussions

In most papers available in the open literature, signal processing is applied to simple geometry simulated flaws such as square Teflon® inserts or flat bottom holes. Example of typical results obtained by processing PT inspection results of a composite sample that contains flat bottom holes are shown in Figure 2.

As seen in the images presented in Figure 2, typically, except for the edge effect[18], the flaws exhibit a uniform feature. The reason being that artificial flaws used in laboratory samples are usually at one specific depth. The reality is that a flaw can occur at different depths. For example an impact can cause fiber and matrix breakage resulting in a surface dent while creating delamination damage in several deeper layers. In addition, real components might be painted, be covered by a label or have information written on them that can affect the thermogram and make automated detection challenging. Examples of processed pulsed thermography results of impact-induced damage are presented in Figures 3 and 4.

Although simply applying a threshold on the data obtained on laboratory samples can yield good results for automated detection, it lacks the robustness required to deal with real damage. Besides, due to the edge effect it can either underestimate or overestimate the flaw size. In addition, real damage does not behave like simulated flaws and sizing techniques such as the full-width half-maximum[19,20] cannot be applied easily to estimate the flaw size. As it can be seen in Figure 4, amplitude, phase and principal component images provide different information and flaw sizes.

One of the challenges is to select the proper images to accurately estimate the flaw size. The amplitude, phase and principal component images tend to show the flaw within the first few images; while derivative processing algorithms require browsing through more images in the sequence to see the entire flaw. Therefore the former techniques were selected to develop the proposed algorithm.

The first step of the algorithm proposed is to compute the amplitude, phase and principal component images. Then, the marking and writing are automatically detected and removed from the images by creating a mask. For the samples used, it was found that the writing of the last amplitude image had values less than two times the standard deviation (STD) compared to the average of the panel.

Then the selected images: amplitude images 2 to 6, phase images 2 to 10, and PCA images 1 to 6 were further processed. For each of the selected amplitude images, each pixel that had a value of one STD above the average was considered being part of a flaw. Similarly, for the selected phase and PCA images each pixel that had a value of one STD above or below the average of the sample was considered to be a flaw. This resulted into several binary images that were summed up to give a “flaw likelihood” image as shown in Figure 5(a). After summation, each pixel that had a value superior to 4 was considered a flaw. An example of a binary image obtained after applying the threshold to the flaw likelihood image is presented in Figures 5(b). A series of morphological filters were then applied to remove what is considered to be noise and filling holes in such a way that only the large connected components of binary image were kept, as shown in Figure 6 (a). The agglomeration of pixels corresponding to the damage area was identified to be the one which had the highest pixel value in the second amplitude image (Figure 6 (b)).

The inspection results from both the front and the back of the samples were processed using this algorithm. In each case the algorithm successfully identified the damaged area and the false calls rate was zero. The final flaw image obtained (Figure 6 (b)) was used to calculate the flaw size and area. These measurements were similar to those obtained by an inspector measuring the flaw based on the regular processing techniques presented in section 2.

The measurements obtained were then compared to those obtained by pulse-echo ultrasonic. It was found that on average the measurements by thermography underestimate the flaw width and length by 15% and 10% respectively. Since the measurements obtained by the automated algorithm are similar to those obtained by an inspector, the differences may be caused by the samples geometries and its material characteristic. Further trial of the algorithm on different sample geometries should be carried out to better explain these differences.

It was found that the damage likelihood image is easier to interpret than typical amplitude, phase and principal component images. This can be seen by comparing the damage likelihood image of Figure 5 with the images obtained by other processing techniques presented in Figure 4, and in another example presented in Figure 7. The damage likelihood image has a stronger contrast than the others and better defined boundaries. In addition, the pixels from the damage area always have a greater value than the sound area which is not always the case with other processing techniques.

Although the process of creating this image is more computation intensive than other techniques used individually, it allows simplifying an entire thermogram sequence into a single image. Pulsed phase thermography and PCA significantly reduces the number of images to analysis, but combining these techniques reduces it even further.

4 Conclusions

An algorithm was developed for automated flaw detection and measurement of pulsed thermography inspection data. The algorithm was based on the combination of information from typical signal processing techniques used in pulsed thermography. The statistical divergence of the pixel value compared to the sample allowed identifying the damaged area. The algorithm provided measurements similar to that of a human eye. Moreover, the image obtained during the processing was easier to interpret by the inspector, provided the damage area with stronger contrast compared to other processing techniques used individually.

5 References

1. Maldague Xavier, "Theory and Practice of Infrared Technology for Nondestructive Testing", John Wiley & Sons Inc, New York NY, pp. 684, 2001.
2. D. Gonzalez, Clemente Ibarra-Castanedo, F.J. Madruga and Xavier Maldague, "Differentiated Absolute Phase Contrast Algorithm for the Analysis of Pulsed Thermographic Sequences", Infrared Physics and Technology, Volume 48, Issue 1, pp. 16-21, 2006.
3. Mirela Susa, Hernan Dario Benitez, Clemente Ibarra-Castanedo, Humberto Loaiza, Abdel Hakim Bendada and Xavier Maldague, "Phase contrast using differential absolute contrast method", QIRT (Quantitative InfraRed Thermography) Journal, vol. 3, no 2, pp. 219-230, 2006.
4. Hernan Dario Benitez, Clemente Ibarra-Castanedo, Abdel Hakim Bendada, Xavier Maldague, Humberto Loaiza and Eduardo Caicedo, "Modified Differential Absolute Contrast Using Thermal Quadrupoles for the Nondestructive Testing of Finite Thickness Specimens by Infrared Thermography", in CCECE 2006 - Canadian Conference on Electrical and Computer Engineering, (Ottawa (Ontario) Canada), May 7-10 2006.
5. Maldague X. and Marinetti S., "Pulse Phase Infrared Thermography", J.Appl. Phys., Vol. 79, pp. 2694-2698, 1996.
6. Ibarra-Castanedo C. "Quantitative subsurface defect evaluation by pulsed phase thermography: depth retrieval with the phase," Ph. D. thesis, Laval University, 2005, http://www.theses.ulaval.ca/2005/23016/23016.pdf
7. Ibarra-Castanedo, C. and Maldague, X. "Interactive methodology for optimized defect characterization by quantitative pulsed phase thermography," Research in Nondestructive Evaluation, Vol. 16, No. 4, pp1-19, 2005.
8. Shepard S. M. "Advances in Pulsed Thermography", Andres E. Rozlosnik, Ralph B. Dinwiddie (eds.), Proc. SPIE, Thermosense XXIII, Vol. 4360, pp. 511-515, 2001.
9. Carslaw, H. S. and Jaeger, J. C., "Conduction of Heat in Solids", 2nd edition, Clarendon Press, Oxford.
10. Martin R. E., Gyekenyesi A. L., Shepard S. M., "Interpreting the Results, of Pulsed Thermography Data," Materials Evaluation, Vol. 61, No. 5, pp 611-616, 2003.
11. Shepard, S. M, "Temporal Noise Reduction, compression and Analysis of Thermographic Image Data Sequence", US Patent 6,516,084, February, 2003.
12. Shepard, S. M., Ahmed, T., Rubadeux, B. A., Wang , D., Lhota, J. R., "Synthetic Processing of Pulsed Thermography Data for Inspection of Turbine Components", Insight Vol.43 No.9, September, 2001.
13. S. Marinetti, E. Grinzato, P.G. Bison, E. Bozzi, M. Chimenti, G. Pieri, O. Salvetti, "Statistical analysis of IR thermographic sequences by PCA", Infrared Physics and Technology 46 (2004) 85–91.
14. Rajic N., "Principal component thermography for flaw contrastenhancement and flaw depth characterisation in composite structures", Composite Structures 58, pp521–528, 2002
15. J.N. Zalameda, P.A. Howell and W.P. Winfree, "Compression Technique Computational Performance," Proceedings of SPIE Thermosense XXVII, Vol. 5782, pp. 399-406, 2005.
16. K. E. Cramer and W. P. Winfree, "The Application of Principal Component Analysis Using Fixed Eigenvectors to the Infrared Thermographic Inspection of the Space Shuttle Thermal

Protection System", Quantitative Infrared Thermography conference (QIRT) 2006, June 28-30, Padova (Italy), 2006
17. David C. Lay, *Linear Algebra and Its Applications* (2nd ed.), Addison Wesley and J. Ponce, March, 1997
18. Almond D. P. and Lau S. K. 1993, "Edge Effects and a Method of Defect Sizing by Transient Thermography," Appl. Phys. Lett., 62(25): 3369-3371.
19. Avdelidis N.P., Hawtin B.C., Almond D.P., "Transient Thermography in the Assessment of Defects of Aircraft Composites", NDT&E International, Vol. 36, pp. 433-439, Septembre, 2003
20. Saintey M.B., Almond D.P., "Defect Sizing by Transient Thermography II :A Numerical Treatment", Journal of Physic D: Applied Physics, Vol. 28, No. 12, pp. 2539-2546,1995

Biography

Mr. Marc Genest is a research officer at the National Research Council Canada, Institute for Aerospace Research. Since joining the NRC-IAR he has carried out research on thermography for non-destructive evaluation. He has worked on the development and optimization of thermographic inspection parameters. He also has worked on the enhancement of defect detection by developing data processing algorithms. His current research projects are focused on the development of new thermography inspection techniques for the support of military and commercial platforms.
(email: marc.genest@nrc-cnrc.gc.ca)

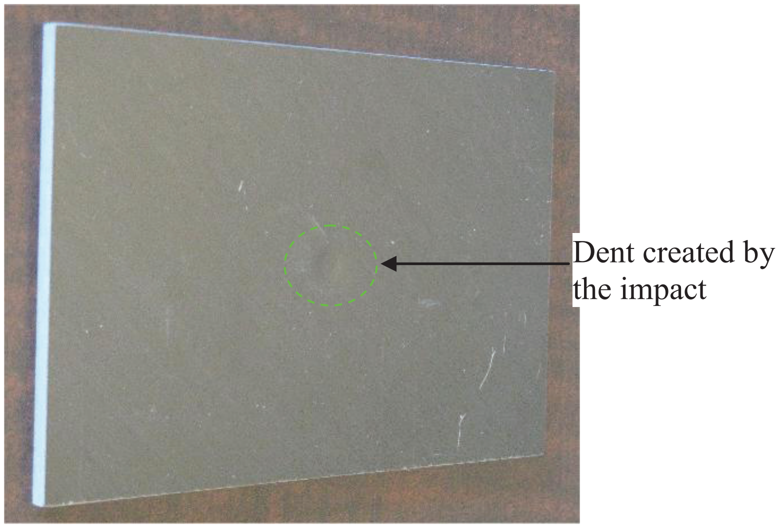

Figure 1: A photograph of an impacted sample.

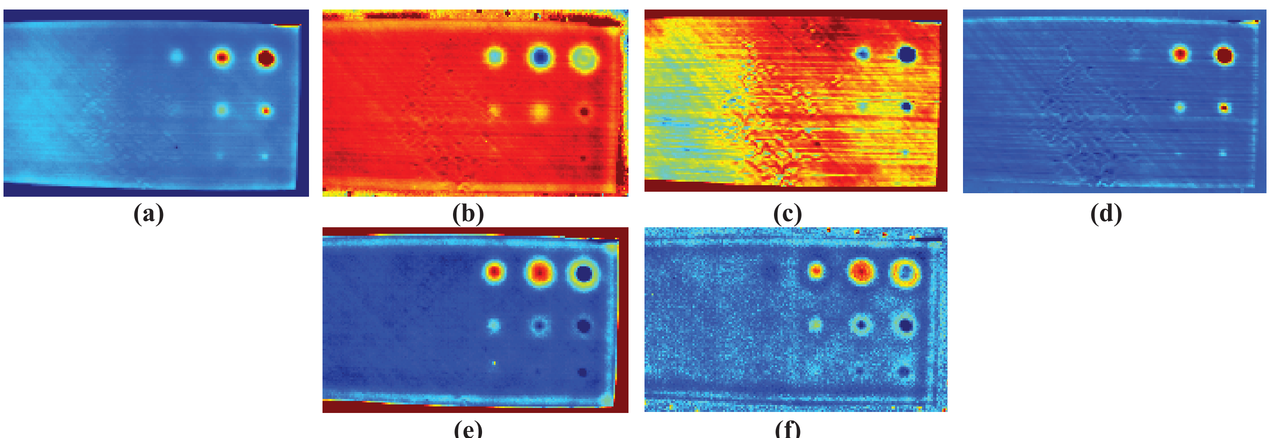

Figure 2: Typical images of (a) amplitude, (b) phase, (c) 1^{st} principal component, (d) 2^{nd} principal component (e) first derivative and (f) second derivative of a sample containing flat bottom holes.

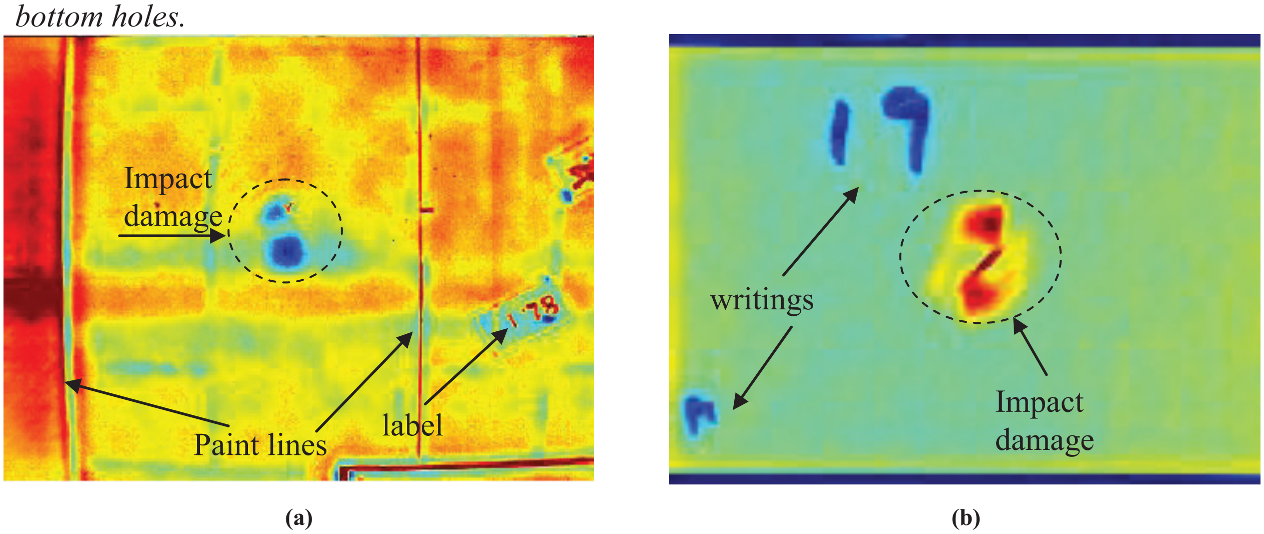

Figure 3: Pulsed thermography images of different samples containing impact damage, paint lines, sticker and marker writings.

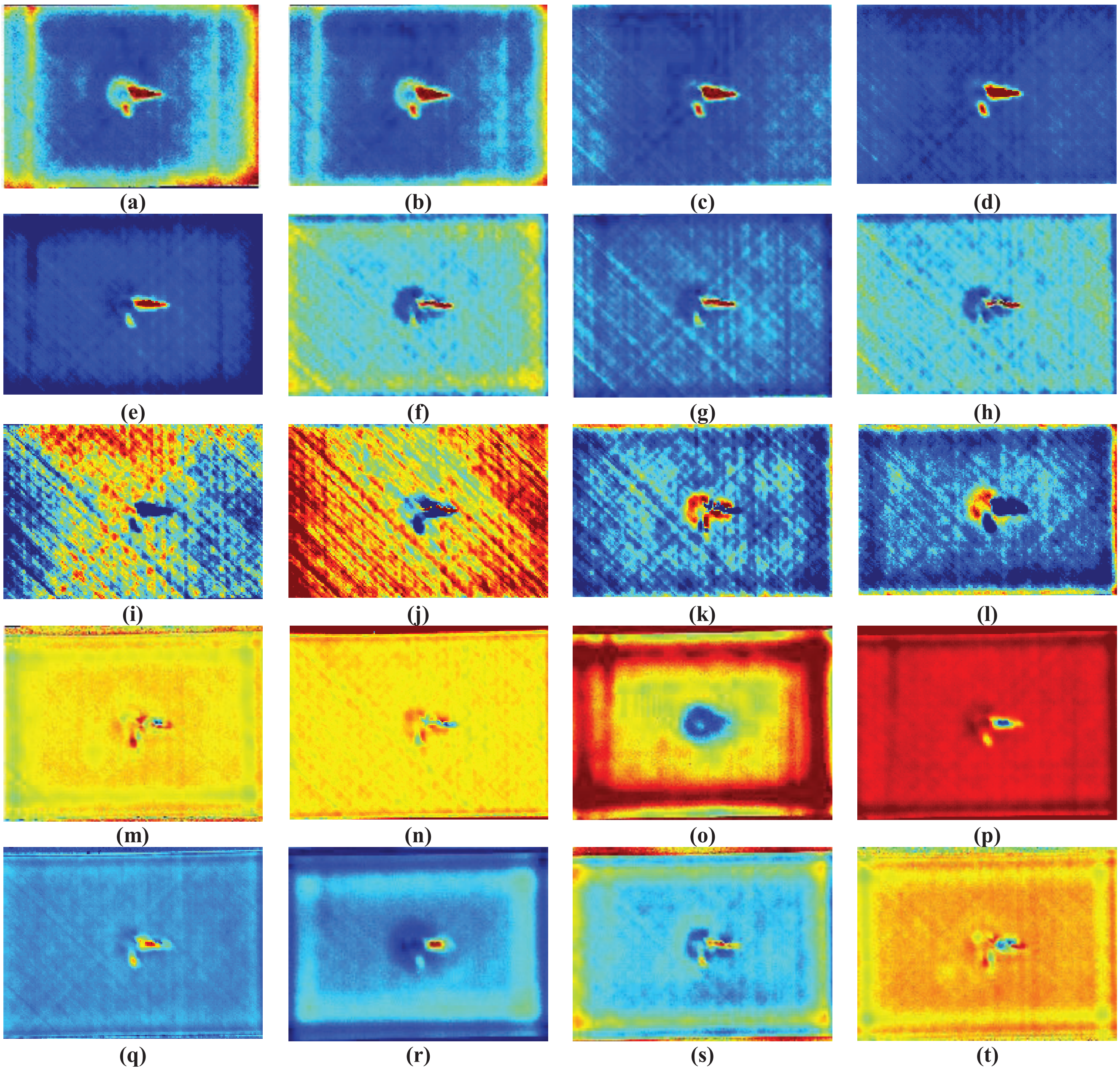

Figure 4: First four non-null images from (a-d) amplitude; (e-h) phase; and (i-l) principal components; and examples of 1st (m-p) and 2nd (q-t) derivative images of the same sample.

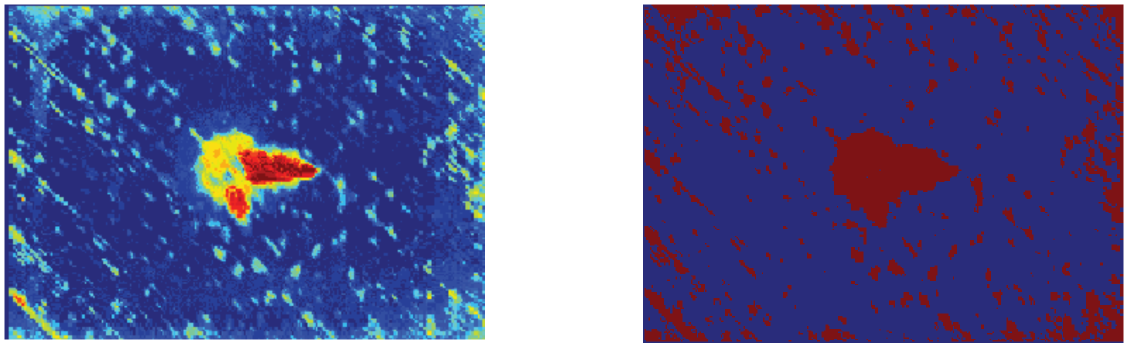

(a) (b)

Figure 5: An example of a (a) damage likelihood image (b) flaw image after applying threshold.

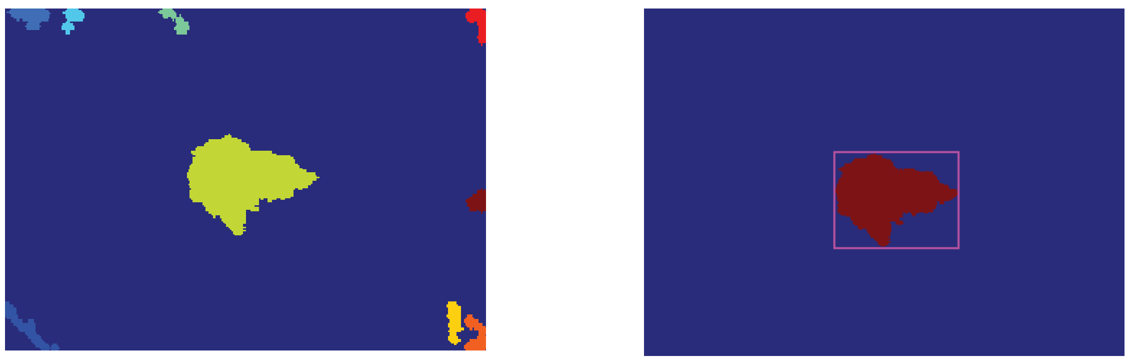

(a) (b)

Figure 6: An example of a (a) flaw image after applying morphological operations (b) flaw image after identifying the image blob corresponding to the damage area.

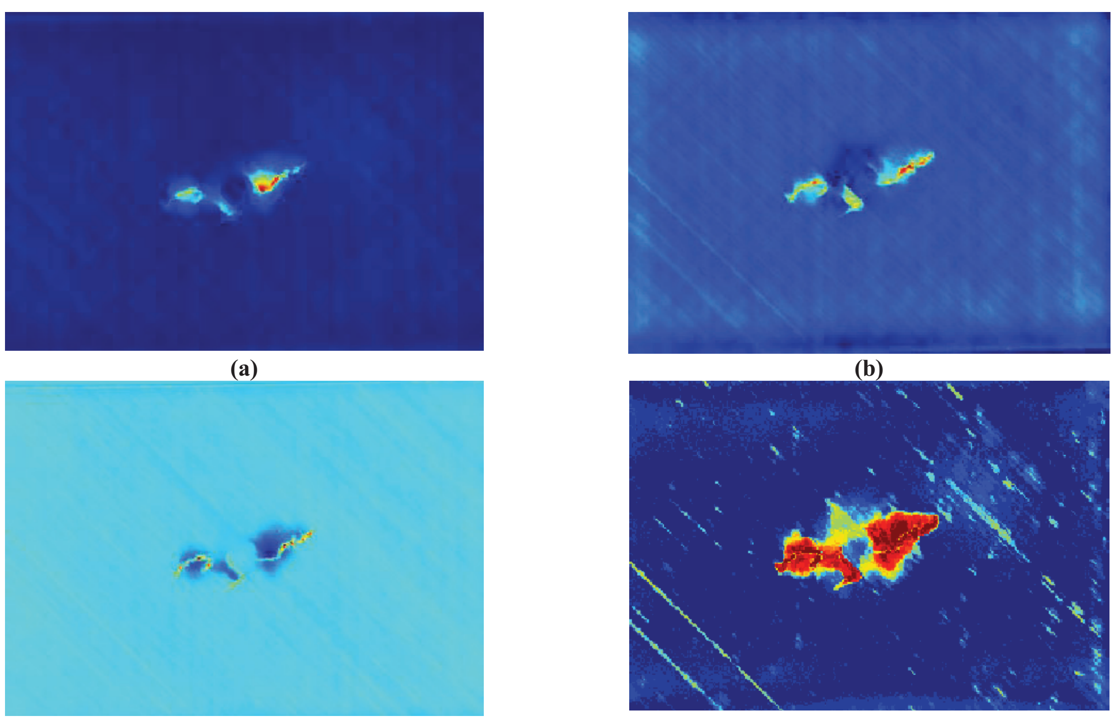

(a) (b)

(c) (d)

Figure 7: Example of images of (a) amplitude; (b) phase; (c) principal component; (d) damage likelihood.

ANALYSIS OF ULTRASONIC ELASTIC WAVES IN VIBROTHERMOGRAPHY USING FEM

A. Saboktakin[1] - C.Ibarra-Castanedo[1] - A. Bendada[1]- X. Maldague[1]
P. Bison[2], E. Grinzato[2], S. Marinetti[2]
[1]Electrical and Computing Engineering Department,
Université Laval, Québec (Quebec) Canada, G1V 0A6,
Saboktakin.Abbasali.1@ulaval.ca,{IbarraC, Bendada, MaldagX}@gel.ulaval.ca
[2] ITC-CNR,Corso Stati Uniti,4-35127 Padova, Italy
{paolo.bison, sergio.marinetti, ermanno.grinzato}@itc.cnr.it

Vibrothermography is a promising technique that uses elastic ultrasonic wave excitation in solids for quality maintenance, e.g. in aerospace and automotive industry to monitor the integrity of surface or subsurface features. Vibrothermography allows for defect selective imaging using thermal waves that are generated by elastic sound or ultrasound waves. The mechanism involved is local friction or hysteresis that turns a dynamically loaded defect into a heat source, which is identified by a thermography system. Efficient numerical modeling allows a deeper understanding of the physical mechanisms of ultrasonic wave propagation in solids and this paper summarizes some of the recent results in modeling elastic waves to non-destructive evaluation (NDE) of isotropic materials. In this paper, a finite element modeling (FEM) of vibrothermography is presented to investigate the elastic wave propagation around cracks and to predict the time history of elastic waves scattering and diffraction. A fully coupled thermoelastic response is computed by combining stress-strain analysis with the heat equations in order to analyse the influence of the damage for the wave propagation. This work is divided into two parts, the first part describes the theoretical background of elastic waves propagation in isotropic materials. The second part introduces numerical simulations of elastic waves propagating in structures containing cracks.

Keyword: Vibrothermography, FEM (finite element modeling), Heat Generation, Thermoelasticity, Elastic Waves

1.Introduction

Industries are continuously demanding more reliable, convenient and quicker nondestructive testing methods for the detection of small cracks and damage in metals. Several non-destructive testing techniques have been used to detect cracks and defects in metallic structures. These techniques include x-ray imaging, various ultrasonic methods, eddy current methods, magnetic particle inspection and IR thermography. Over recent years, many authors have turned their attention to explore high frequency ultrasonic elastic waves because elastic waves are capable of propagating long distances in specimens, and tend to interact with changes such as cracks and delaminations in a workpiece. Such interactions can be detected and further analysed to determine characteristics of the change[1]. Vibrothermography is a non-destructive testing method in which cracks in an object are made visible through frictional heating caused by high frequency ultrasound. In this technique the heat is generated through the dissipation of mechanical energy at the crack surfaces by vibration. The frequency range used for excitation of structures is from 20 kHz to 100 kHz. A schematic representation of the method is given in Figure 1.The presence of the crack results in a temperature rise around the area and the surface close to the crack. The temperature rise is measured by a high sensitivity infrared imaging camera whose field of view covers a large area. The method therefore covers large area from a single excitation position so it is much quicker than conventional ultrasonic or eddy current inspection that requires scanning over the whole surface and can also be a convenient and reliable inspection technique for structures with complex geometries that are difficult to inspect by conventional methods.

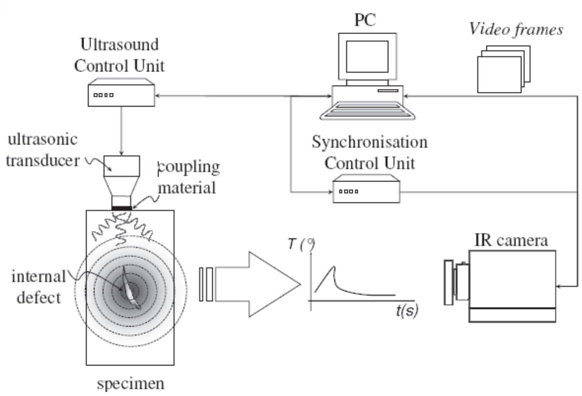

Fig.1 - Principle and ultrasonic thermography.

Vibrothermography is also particularly well-suited to the detection of closed cracks that can cause problems with other techniques such as conventional ultrasound and radiography [2]. In this technique, when ultrasonic waves reach the defects, their mechanical energy decay rapidly because of the friction between the interface of the cracks, or the elastic property of the crack areas is much more different than any other areas, so that thermoelastic effect and hysteresis effect are generated. Accordingly, vibrothermography is a very attractive and fairly recent NDT method many industries may benefit from . However, more systematic research is required to understand the physics behind vibrothermography in order to make it more reliable with repeatable results.

2.Finite element modeling (FEM)

Finite element modeling is used to understand the principle behind crack detection using vibrothermography and the effect of induced ultrasound pulse on the damage zones, and also to investigate the effect of complex parameters, such as geometry, material properties, loads and nonlinearities. By using a numerical analysis we can predict the optimal excitation parameters. FEM also provides a better understanding of the influence of different excitation parameters on the system resonance and of the characteristics of the coupling between the exciter and the test piece. Once the system characteristics resulting from the coupling of exciter and the test piece are known, it is possible to construct a more practical and efficient excitation system.

For instance, in parallel with experiment, Han et al. [3] created a basic finite element model for a metal fatigue crack in order to study the efficiency of chaotic vs. non-chaotic sonic excitation in generating heat around cracks. In ultrasonic thermography, the hysteresis induced by the elastic waves might be responsible of the thermoelastic stresses in the crack and the subsequent localized heating. Clearly the thermoelastic stresses could modify the acoustic loading necessary to initiate heat generation in a crack area. Another possible mechanism for observed hysteresis phenomena in ultrasonic thermography might be due to intrinsic nonlinearity of the interaction forces within the crack itself.

In a simulation model, the specimen is subjected to ultrasonic elastic wave that generates a significant amount of heat within the structure because of mechanical losses in the material and thermoelastic damping. This thermoelastic effect represents the energy transfer between the thermal and mechanical domains.

In this paper we model a plate with a notch crack under excitation and compute a fully coupled thermoelastic response for a model induced ultrasonic elastic wave combining the stress-strain analysis with the linearized heat transport equation. The crack is located 150 mm away the excited edge; its depth and width are 10 and 0.1 mm, respectively. The analysis is performed in the frequency domain.

With this model we can observe the temperature rise in the crack area. The corresponding heat transfer equation contains two source terms computed using the analysis results. These terms represent the heat generation due to mechanical losses in the material and the nonlinear effects related to the thermoelastic damping. In this paper we suppose the transducer vibrates at 20 kHz with constant amplitude.

Nowadays, commercial software such as COMSOL, ANSYS, ABAQUS, LS-DYNA are available for the analysis of elastic wave propagation. In this paper, ABAQUS was used to run and analyse the simulations. The ABAQUS element library provides a complete geometric modeling capability. We used coupled three-dimensional temperature-displacement elements. Thermoelastic effect is considered during the numerical simulation.

Heat convection is neglected in the numerical simulations and all degrees of freedom were restricted at one end (Fig.2). A time-dependent sinusoidal displacement load is applied on the other end, and then thermoelastic effect analysis is then performed. The applied displacement amplitude is of 0.06 mm at the position of excitation with a frequency of 20 kHz, and is applied over a 50 ms period to save computation time.

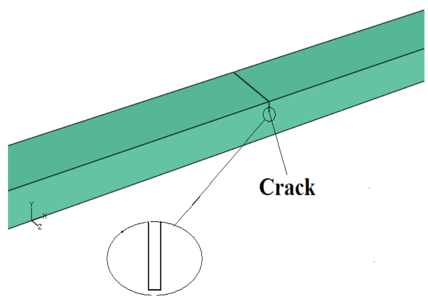

Fig.2 - Model with a crack under a sinusoidal force.

For the purpose of simulating the thermoelastic effect, a subroutine was created and the simulations were limited by the assumptions that the material is isotropic and applied stresses are within the limit of elasticity and the heat generation within the system is only caused by thermoelastic effect and hysteresis, which is based on the classical theory. The physical properties of the material are described by the following parameters: elasticity modulus, Poisson's ratio, density, linear thermal expansion coefficient which is considered as constant, specific heat capacity, thermal conductivity, surface emissivity and Stefan-Boltzmann constant. (Fig.3)

α (k^{-1})	λ (W/mK)	C_p $\left(J/kgK\right)$	E (MPa)	σ_y (MPa)	ν	ρ $\left(kg/m^3\right)$
12×10^{-6}	42.8	476	2×10^5	415	0.3	7840

Fig.3 – Physical properties of model.

3.Modeling Results

In the simulation, the ultrasonic elastic wave is induced into the sample until the wave hits a defect. Because the loading and unloading of solid material occurs at every cycle, the wave is damped and the material is warmed up by hysteretic effects and friction of crack lips. We used the monofrequency excitation. According to the modeling results, heat changes at the crack tip and the temperature distribution in the time domain can provide information about the depth where the defect is located.By using FEM we were able to directly calculate the temperature distribution on observed area of the specimen and to explain the mechanism of heat generation and the associated temperature evolution at the crack vicinity. (Fig. 3)

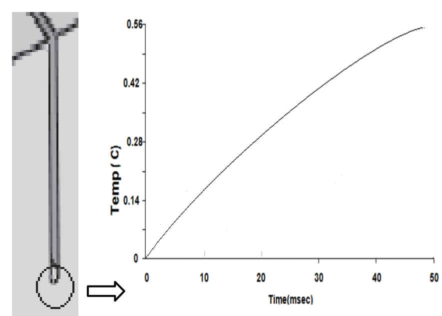

Fig.4 - Thermal changes at node in vicinity of crack.

Numerical simulation results revealed that the calculated stress generated under the excitation for the above mentioned frequency is lower than the material yield stress during the non-destructive testing.According to the observed heating in the sample, there was no standing wave present during this simulation and moreover, the excitation frequency did not match the resonance of the sample. It is clear that for the case of complex geometries or thin specimens, standing elastic waves can appear as temperature patterns causing misinterpretations. In other words, in the worst case the defect could be hidden in a node while the standing wave maximum might appear as a defect. This can be avoided by frequency modulation of the signal. In such a case, the standing wave pattern is superimposed by a field of propagating waves.

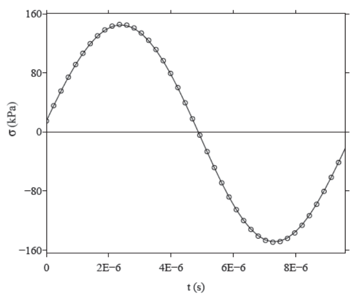

Fig.5 - Stress in crack at the beginning of heat generation.

4.Conclusion

In this study, a small open crack in a plate was assessed using vibrothermography. We observed the thermal evolution caused by the thermoelastic effect induced by the elastic waves and also stress concentration around crack and we analyzed the thermoelastic effect and the mechanical losses via FEM analysis. In this simulation, we observed that the thermoelastic effects and heat changes in the crack were proportional to the stress amplitude and the position of the crack can be clearly seen from the heat generation within the crack. To calculate the effect of thermoealsticity on sample during the excitation, we solved the coupled thermoelastic via a FEM simulation. By using the fully coupled thermoelastic response and combining stress-strain analysis with the heat equations we were able to directly calculate and analyse the influence of the damage for the wave propagation and the temperature distribution on the sample and explain the mechanism of heat generation and the associated temperature evolution at the crack vicinity.

Acknowledgements

The National Science and Engineering Research Council of Canada (NSERC) is thanked for its financial support as well as the Canada Research Chair MiViM – *Multipolar Infrared Vision Infrarouge Multipolaire* and the Canadian Foundation for Innovation through the LIVE installation (*Laboratory for Infrared Vision Excellence*).

Reference:

1) Mian, A., et al., "*Fatigue damage detection in graphite/epoxy composites using sonic infrared imaging Technique"* Composites Science and Technology, 2004. 64(5): p. 657-666.
2) J.-M.Piau,A.Bendada and X.Maldague,"*Ultrasound Vibrothermography Applications for Nondestructive Discontinuity Detection* " Materials Evaluation, 66[10]: 1047-1052, 2008.
3) Han, X., et al., "*Simulation of Sonic IR Imaging of Cracks in Metals with Finite Element Models"* Review of Progress in Quantitative Nondestructive Evaluation; Volume 25A. Vol. 25A, pp. 544-549. 2006.
4) Maldague, X.P.V., *Theory and practice of infrared technology for nondestructive testing*. Wiley series in microwave and optical engineering, ed. K. Chang. 2001: John Wiley & Sons. 684.
5) Mian, A., et al., *Response of sub-surface fatigue damage under sonic load - a computational study.* Composites Science and Technology, 2004. 64(9): p. 1115-1122.
6) ABAQUS User Manual.
7) Rantala, J., D. Wu, and G. Busse" *Amplitude-modulated lock-in vibrothermography for NDE of polymers and composites"*. Research in Nondestructive Evaluation (USA). Vol. 7, no. 4, pp. 215-228. 1996,
8) J. Rantala, D. Wu, A. Salerno and G. Busse, "*Lock-in thermography with mechanical loss angle heating at ultrasonic frequencies*," *Proc. Int Conf. Quantitative InfraRed Thermography (QIRT96)*, Stuttgart,
9) Germany, Sep.2-5, (1996). M. Reza Eslami "*Thermal Stresses –Advanced Theory and Applications"*
10) Clemente, Jean-Marc Piau, Stéphane Guibert, Xavier Maldague and Abdel Hakim Bendada, "*Inspection of aerospace materials by pulsed thermography, lock-in thermography and vibrothermography: A comparative study*", in SPIE - The International Society for Optical Engineering, Thermosense XXIX, (Orlando, FL, USA), 9-13 April 2007.
11) Renshaw, Jeremy; Holland, Stephen D, "*Full-Field Vibration Measurement for Vibrothermography* ",34th Annual Review of Progress in Quantitative Nondestructive Evaluation. AIP Conference Proceedings, Volume 975, pp. 498-503 (2008).
12) X.Y. Han, M.S. Islam, and G.M. Newaz, "*Finite element modeling of the heating of cracks during sonic infrared imaging*", Journal of Applied Physics, 99(7), 074905, 2006.

Reducing the Negative Effects of Grating through A-Scan Post Processing When Compensating for Poor Element Directivity

Shaddy Shokralla

Ontario Power Generation, Ajax, ON L1S 7J5, Canada

Abstract

Increase in computation power has made post-processing of ultrasonic array data a feasible alternative to traditional processing schemes. Instead of firing transmitter elements at staggered intervals to produce wave fronts, the full matrix of time domain signals (A-Scans) from every transmitter-receiver pair can be captured and post-processed, allowing for improved accuracy in imaging. A new signal processing technique is introduced in this paper, which massages full matrix A-Scans as part of post-processing algorithm implementation, compensating for poor element directivity in directions away from element normals. Utilization of this technique is shown to reduce the negative effects of grating lobes in imaging over another known directivity-compensating technique. Experimental results are presented to verify this.

Key words:

1. Introduction

Phased array systems are now commonly used by ultrasonic examination industry to perform non destructive examination. Transmitter elements are fired at staggered intervals to produce wave fronts. Signals acquired by receiver elements are used to judge depth and directionality of flaws. With respect to imaging inspection media, a superior alternative to using phased array systems with preprogrammed focal laws is to acquire ultrasonic data via full matrix capture (FMC) and post-process it. The main advantage

Email address: `shaddy.shokralla@opg.com` (Shaddy Shokralla)

Preprint submitted to NDT in Canada 2009 Conference *June 23, 2009*

of this setup is that any possible post-processing algorithm can be applied to image the inspection medium, since all possible raw data information is present in the FMC data set.

Full matrix capture denotes the acquisition of A-scans from every transmitter receiver pair in the array. The data can be conveniently represented by a 3D matrix where the first dimension contains transmitter indices, the second dimension contains receiver indices, and the third dimension contains A-Scans belonging to respective transmitter-receiver pairs. Once the full matrix capture data has been stored, any post-processing scheme can be applied to image the ultrasonic raw data, including the total focusing method (TFM) [1]. This method emulates phased array focusing at every point in the inspection medium, a prohibitive task using standard phased array technology. TFM has been termed the 'gold standard' of inspection by some authors [3].

A correction factor (Section 2.1) has been employed to account for beam directionality with the intention of emulating element omni-directionality [1]. Elements with omni-directional beams provide the best data for imaging. This paper highlights some shortcomings of this correction factor and introduces an alternative, albeit more raw-data-intrusive method to correct for beam directionality in Section 3. Experimental results are presented to verify improvement in imaging via the new method in Section 4.

2. Preliminaries

2.1. Total Focusing Method

We first state the Total Focusing Method [1] for imaging in a single medium where sound travels at speed c. Consider Figure 1. Elements i and j belong to aperture $a \in A$, where $A = \{a_1, a_2, \ldots, a_n\}$ is the set of apertures containing adjacent elements. Apertures in A all have equal size. $g_{(i)j}(t)$ is a data-set of analytic time-domain signals from transmitter i to receiver j (recall that $g_{(i)j}(t)$ is defined for every i and j, since the full matrix of ultrasonic transmit-receive array data is acquired). $e_{(i)}$ has i is enclosed in parenthesis here to denote it as a transmitter. j is not enclosed in parenthesis, representing it as a receiver. The intensity at r is defined as

$$I(\mathbf{r}, a) = \left| \sum_{i,j \in a} g_{(i)j} \left(t = \frac{|\mathbf{e_{(i)}} - \mathbf{r}| + |\mathbf{e_j} - \mathbf{r}|}{c} \right) \right|. \tag{1}$$

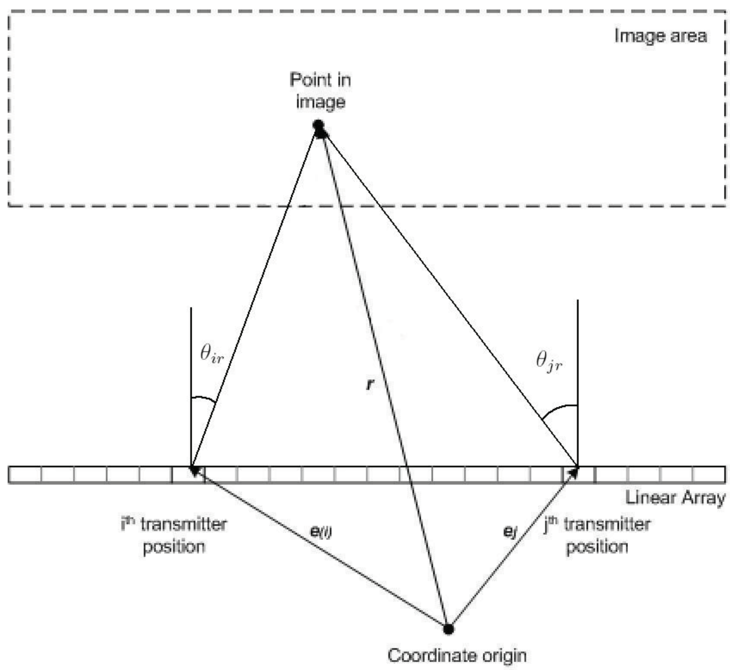

Figure 1: Illustration of vector notation

Phased array engineers as well as some authors ([1],[4]) employing the TFM methodology have utilized the approach of McNab and Stumpf [2] in using a far-field approximation of directivity to emulate beam omnidirectionality. Given the far field approximations for directivity of transmitter and receiver elements at $\mathbf{r}$,

$$p_{ir} = \left|\operatorname{sinc}\left(\frac{\pi f a \sin\theta_{ir}}{c}\right)\right| \text{ and} \tag{2}$$

$$p_{jr} = \left|\operatorname{sinc}\left(\frac{\pi f a \sin\theta_{jr}}{c}\right)\right|, \tag{3}$$

where f is the centre frequency of the elements and a is the element width, a version of Equation 1 can be written which corrects for element directivity. The corrected version is as follows,

$$I_c(\mathbf{r}, a) = \left|\sum_{i,j\in a} \frac{1}{p_{ir}p_{jr}} g_{(i)j}\left(t = \frac{|\mathbf{e_{(i)}} - \mathbf{r}| + |\mathbf{e_j} - \mathbf{r}|}{c}\right)\right|. \tag{4}$$

2.2. Grating Lobes

Given a focusing angle of α, aberrations due to grating will be imaged (in the far field) at angles θ_n, $n = 1, 2, \ldots$ which satisfy the following equation,

$$\sin\theta_n = \sin\alpha + \frac{n\lambda}{p}, \tag{5}$$

where p is the pitch of the array elements. Equation 5 can be derived from simple trigonometry, as θ_n is the angle such that the path length between adjacent elements is equal to the path length based on desired steering angle plus/minus an integer number of wavelengths. The condition for no grating is $p < \lambda/2$. This is obvious enough, since if $p < \lambda/2$, Equation 5 cannot be solved for any θ_n, as the right side of the equation is always greater than 1.

Grating is a common phenomenon in imaging ultrasonic data gathered by linear arrays, as p is usually greater than $\lambda/2$ due to manufacturing constraints.

3. Total Focusing with Beam Normalization

One obvious problem with using Equations 2 and 3 as correction factors in Equation 4 is that $I_c(\mathbf{r}, a)$ blows up to infinity when either p_{ir} or p_{jr} are equal to zero (currently the norm given practical element dimensions when performing scans in water). A more subtle problem is that the implementation of these correction factors presume signals found in $g_{(i)j}(t)$ are located in the direction of $\mathbf{r}$, when assigning a value to $I_c(\mathbf{r}, a)$. Clearly this is not true when intensities are assigned due to grating. While this may not be a problem of great concern when attempting to image small objects, which is the intent of many users of the TFM algorithm, when imaging surfaces this leads to amplified grating in cases where surface reflectors are oriented parallel to the probe array. Amplified grating can lead to a reduction in SNR in areas of the image where the true surface and grating aberrations overlap.

The method presented in this paper for normalizing beam spread is to normalize wave-packets found in the real and imaginary parts of $g_{(i)j}(t)$ such that the envelope of $g_{(i)j}(t)$, $|g_{(i)j}(t)|$, has peak(s) equal to an arbitrary constant. For simplicity we choose this constant equal to 1. This procedure measures the directivity of a transmitter/receiver combination at a reflector by the value of the peak of the envelope of the reflector wave-packet, irrespective of reflector orientation and amplitude. Thus, if $g_{(i)j}(t)$ contains wave packets $W = \{w_1, w_2, \ldots, w_n\}$ and $|g_{(i)j}(t)|$ has peaks $P = \{p_1, p_2, \ldots, p_n\}$, to normalize the peaks of $|g_{(i)j}(t)|$ to 1, all must be done is to scale the wave packets W by $\{p_1^{-1}, p_2^{-1}, \ldots, p_n^{-1}\}$. We let $g'_{(i)j}(t)$ denote $g_{(i)j}(t)$ with normalized wave packets. Figures 2 and 3 illustrate our concept of analytic time domain wave packet normalization.

This type of beam normalization is very direct as the raw data is normalized to emulate beam omni-directionality. Reflectors having poor orientations delivering weak responses to receivers will be imaged brighter than if no normalization routine were performed at all. At the same time, grating intensity due to reflectors having good orientations delivering strong responses to receivers will be largely unaffected. Thus, in imaging areas where grating from reflectors with good orientations interferes with correctly identified reflectors with poor orientations, the SNR will be increased such that the reflectors with poor orientations will be imaged more brightly, while the grating intensity will not change very much.

If we replace $g_{(i)j}(t)$ with $g'_{(i)j}(t)$ in Equation 1, total focusing with normalized element beam spread via wave packet normalization is realized. We denote this type of total focusing as $I'(\mathbf{r}, a)$, given by

$$I'(\mathbf{r}, a) = \left| \sum_{i,j \in a} g'_{(i)j} \left(t = \frac{|\mathbf{e_{(i)}} - \mathbf{r}| + |\mathbf{e_j} - \mathbf{r}|}{c} \right) \right| . \tag{6}$$

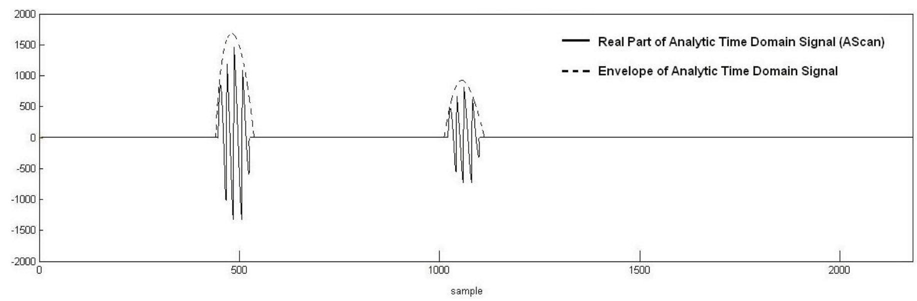

Figure 2: Real part and envelope of analytic time domain signal. Wave packets w_1 and w_2 have peaks $p_1 = 1700$ and $p_2 = 950$ respectively.

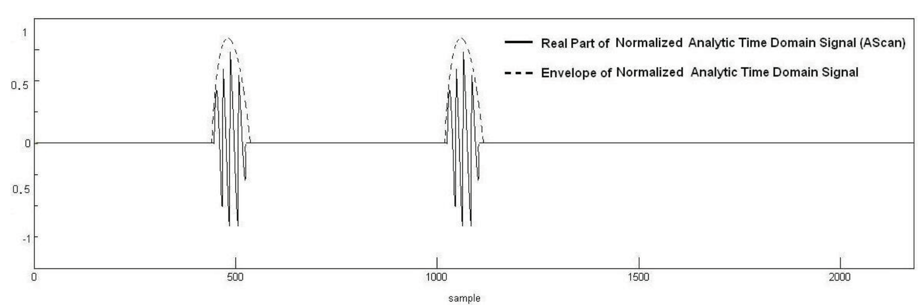

Figure 3: Real part and envelope of normalized analytic time domain signal.

4. Experimental Results

In this section we compare Equations 1, 4, and 6 in imaging a the cross section of a hand weld steel weld cap. The inspection medium is water. A 128 element probe with centre frequency 7.5 MHz is used in the inspection. The element pitch is 0.35mm while the element width is 0.25mm. The imaging of the weld cap is a good measure of the performance of the various implementations of TFM, as the sides of the weld are relatively difficult to image, as their orientations serve as poor reflectors with respect to array elements. We note from Figure 4 that grating due to the flat portions of pipe around the weld interferes with imaging the sides of the weld cap.

Of Figures 4(a), 4(b), and 4(c), the figure that best captures the entirety of the weld cap (especially the right side) is Figure 4(c) confirming that Equation 6 indeed aids in the imaging of poor reflectors when grating is present. Figure 4(a) does a second-best job of imaging the weld cap, with no beam directivity correction utilized. Figure 4(b) does a very poor job of imaging the weld cap, as intensities imaged due to grating totally drown out the true weld cap signal, thus verifying the claims made out in Section 3 on the poor performance of Equation 4 in imaging areas where grating from reflectors normal to the probe array and weak yet correctly positioned reflectors intersect.

(a) Weld cap imaged with TFM and no beam directionality correction applied (Equation 1).

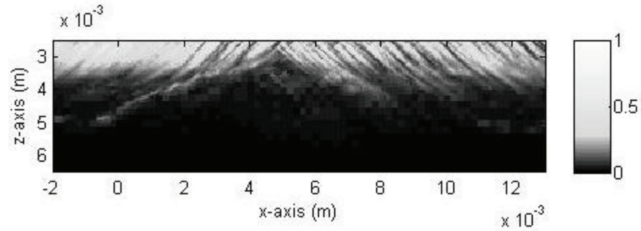

(b) Weld cap imaged with TFM and beam directionality correction applied via directionality correction factor (Equation 4).

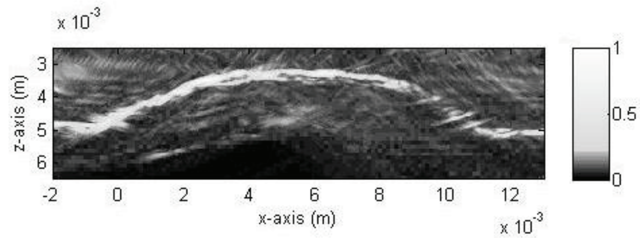

(c) Weld cap imaged with TFM and beam directionality correction applied via wave-packet normalization (Equation 6).

Figure 4: Comparison of TFM used with various strategies used to correct for beam directivity

5. Conclusions

Presented in this paper is a method to emulate beam omni-directionality through wave packet normalization. This method performs better than another method used to the same end, when imaging areas where grating from strong reflectors normal to the probe array and weak reflectors intersect.

The method outlined in the paper illustrates the ability to execute imaging correction mechanisms in post-processing. Since full matrix capture can be used to capture ultrasonic data, advanced signal processing techniques can be exploited to massage acquired data. It is the opinion of this author that further advances in post-processing techniques will be made which capitalize on the FMC / post-processing scheme used to image inspection areas.

References

[1] Caroline Holmes, Bruce W. Drinkwater, and Paul D. Wilcox. Post-processing of the full matrix of ultrasonic transmit-receive array data for non-destructive evaluation. *NDT&E International*, 38:701–711, 2005.

[2] A McNab and I Stumpf. Monolithic phased array for the transmission of ultrasound in ndt. *Ultrasonics*, 24(3):148–155, 1986.

[3] O Oralkan, A Sanh Ergun, JA Johnson, M Karaman, and U Demirci. Capacitive micormachined ultrasonic transducers: next generation array for acoustic imaging? *IEEE transactions on ultrasonics, ferroelectronics and frequency control*, 49(11):1596–1610, 2002.

[4] Paul D. Wilcox, Caroline Holmes, and Bruce W. Drinkwater. Advanced reflector characterization with ultrasonic phased arrays in nde applications. *IEEE transactions on ultrasonics, ferroelectrics, and frequency control*, 54(8):1541–1550, 2007.

Experimental Comparison of Lock-in and Pulsed Thermography for the Nondestructive Evaluation of Aerospace Materials

W. Ben Larbi, C. Ibarra-Castanedo, M. Klein , A. Bendada, and X. Maldague

Electrical and Computing Engineering Department, Université Laval,
Quebec City (Quebec) G1V 0A6 Canada.
wael.ben-larbi.1@ulaval.ca, {Bendada, IbarraC, matthieu.klein.1, MaldagX}@gel.ulaval.ca

Abstract

Infrared thermography is a nondestructive evaluation technique aimed to the detection of surface temperature variations related to the presence of subsurface defects. Several inspection techniques have been developed over the years with basically two approaches, lock-in thermography and pulsed thermography. These two techniques are based on the principle of heat diffusion and thermal wave reflection, but they differ in the way they are practically implemented. In lock-in thermography (LT), an amplitude modulated heat wave is applied to the inspected specimen in steady state. The presence of an anomaly is revealed by a phase shift between the thermal evolution for a non-defective region and a defective one. In pulsed thermography (PT), on the other hand, the inspected specimen is stimulated by a heat pulse of short duration and the surface thermal evolution is monitored in transient state. In this case, the thermal profiles of defective and non-defective regions on the surface will diverge at a given time, which is related to the defect depth. This paper presents some comparative results obtained with these two techniques for the case of aerospace materials. The advantages and limitations of each technique for both qualitative and quantitative analysis are discussed and illustrated with some examples.

1. INTRODUCTION

Infrared thermography has been successfully used as a nondestructive testing and evaluation (NDT&E) technique in many applications. Contrary to passive thermography, in which the objects or features of interest present naturally a thermal contrast with respect to the rest of the scene, the active approach [1] requires an external source of energy to induce a temperature difference between defective and non-defective areas in the specimen under examination.

There are mainly two classical active thermographic techniques based on optical excitation: lock-in thermography and pulsed thermography. We describe these techniques in the following paragraphs discussing their applicability to aerospace materials.

1.1. Pulsed thermography

In pulsed thermography (PT) [2, 3, 4] the specimen surface is submitted to a short heat pulse using a high power source such as photographic flashes, see Figure1. The duration of the pulse may vary from a few milliseconds (~2-15 ms) to several seconds depending on the thermophysical properties of both, the specimen and the flaw. After the thermal front comes into contact with the specimen's surface, it travels from the surface through the specimen. As time elapses, defective zones will appear at higher or lower temperature with respect to non defective zones on the surface, depending on the thermal properties of both the material and the defect. The temperature evolution on the surface is then monitored in transitory regime using an infrared camera. A synchronization unit is needed to control the time between the launch of the thermal pulse and the recording with the infrared camera.

The one-dimensional solution of the Fourier equation for a Dirac delta function in a semi-infinite isotropic solid is given by [5]:

$$T(z,t) = T_0 + \frac{Q}{\sqrt{k\rho c_p \pi t}} \exp\left(-\frac{z^2}{4\alpha t}\right) \tag{1}$$

where Q is the energy absorbed by the surface [J/m^2] and T_0 is the initial temperature [K]. At the surface ($z = 0$), Eq. (1) can be rewritten as:

$$T(0,t) = T_0 + \frac{Q}{e\sqrt{\pi t}} \tag{2}$$

where $e = (k\rho c_p)^{1/2}$ [W s$^{1/2}$ m^{-2} K^{-1}] is the effusivity.

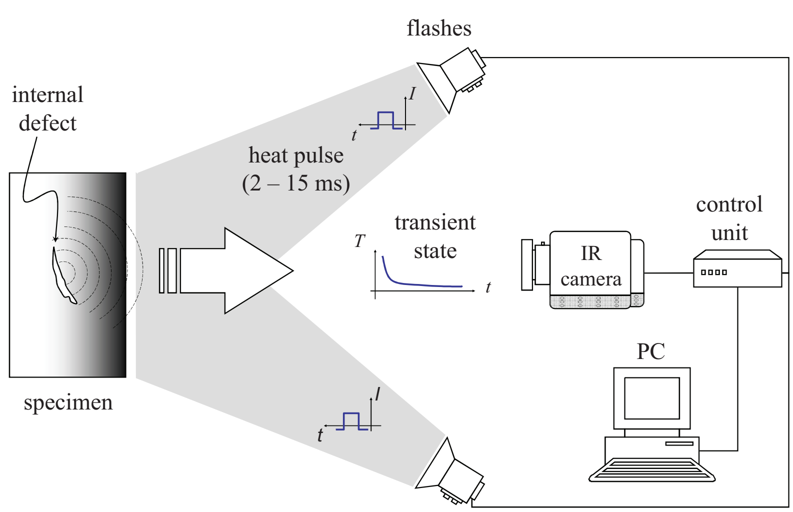

Figure1. Pulsed thermography experimental configuration.

1.2 Lock-in thermography

In lock-in thermography (LT) [6, 7], the specimen's surface is periodically illuminated by one or several modulated heating sources, e.g. halogen lamps, to inject thermal waves into the specimen. The periodic wave propagates by radiation through the air until it reaches the specimen surface where heat is produced and propagates through the material.

Internal defects, acting as barriers for heat propagation, produce changes in amplitude and phase delay of the response signal at the surface. Figure 2 depicts an LT experiment. The lamps send periodic waves (e.g. sinusoids) at a given modulation frequency ω, for at least one cycle, ideally until a steady state is achieved.

Different techniques have been developed to extract the amplitude and phase information. Fourier analysis is the preferred processing technique since it provides single images, ampligrams or phasegrams (the weighted average of all the images in a sequence).

The Fourier's law one-dimensional solution for a periodic thermal wave propagating through a semi-infinite homogeneous material may be expressed as [8]:

$$T(z,t) = T_0 \exp(-\frac{z}{\mu})\cos(\frac{2\pi z}{\lambda} - \omega t) \tag{3}$$

where T_0 [°C] is the initial change in temperature produced by the heat source, ω [rad/s] is the modulation frequency (ω=2πf, with f being the frequency in Hz), λ [m] is the wavelength; and μ [m] is the diffusion length given by [8]:

$$\mu = \sqrt{\frac{2\alpha}{\omega}} = \sqrt{\frac{\alpha}{\pi f}} \tag{4}$$

where $\alpha = k / \rho c_p [m^2/s]$ is the thermal diffusivity, with k [W/m°C] being the thermal conductivity, ρ $[kg/m^3]$ the density, c_p [J/kg°C] the specific heat; and f the thermal wave modulation frequency.

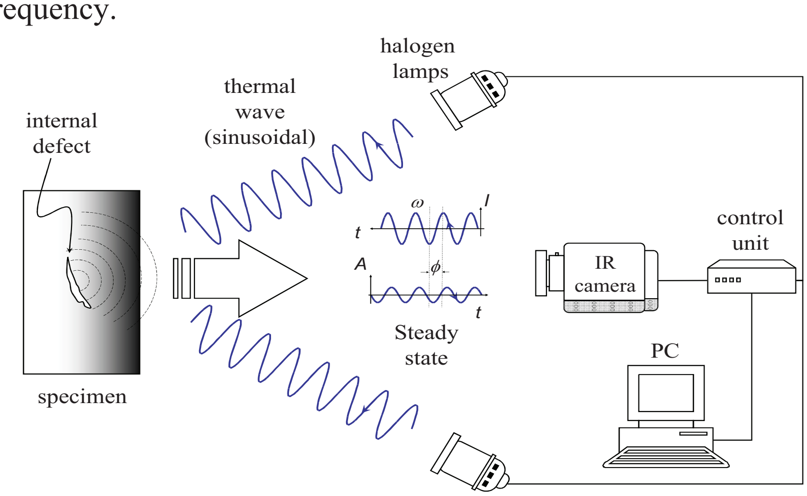

Figure2. Lock-in thermography experimental configuration.

2. EXPERIMENTAL RESULTS

2.1 Inspection of a honeycomb calibration plate

The specimen used in this experiment consisted of an NDT&E standard aluminum honeycomb core sandwich panel with a multi-layer graphite epoxy face sheet (skin) depicted on Figure 3 (a). The aluminum honeycomb core has two cell densities, and contains four types of fabricated defects: delaminations (simulated using Teflon® coated fabric), skin unbonds (fabricated using Teflon® coated fabric), excessive adhesive, and crushed core. This type of panel is commonly used in the aerospace industry for the calibration of NDT&E equipment. Figure 3 shows the results obtained by Lock-in thermography.

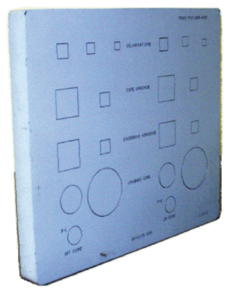

(a)

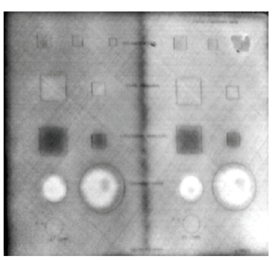

(b)

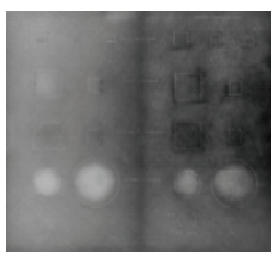

(c)

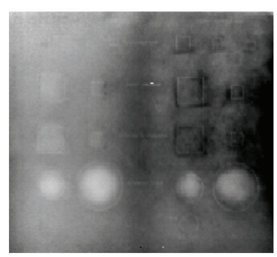

(d)

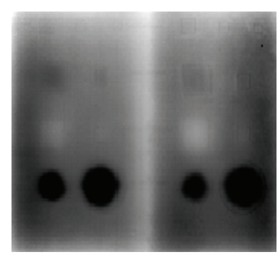

(e)

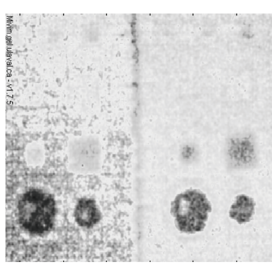

(f)

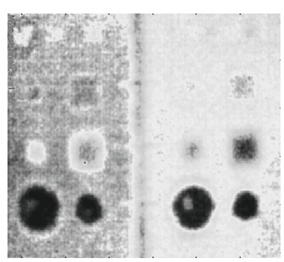

(g)

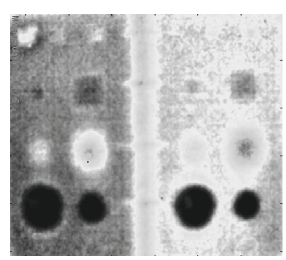

(h)

Figure 3. (a) Photo of calibration plate - **(b), (c), (d)** and **(e)** phasegrams at 0.1 Hz, 0.03 Hz, 0.02 Hz and 0.01Hz obtained by LT - **(f), (g)** and **(h)** phasegrams at 0.04 Hz, 0.03 Hz and 0.02 Hz obtained by PT.

The first line of defects consists of Teflon inserts between the first and second CFRP layers (z = 0.127 mm). It is not detected at f = 0.1 Hz and hardly visible at f = 0.02 Hz. This inserts are very thin, complicating their detection. The second line of defects is thicker and is located deeper, in the glue (type FM300) between the CFRP skin and aluminum honeycomb core. These defects are detectable at f = 0.02 Hz (see Figure 3d). The third line of defects is easily detected in Figure 3b. Finally, the circles in the fourth line of defects, representing a crushed core, are also visible at different frequencies.

These results highlight the limitations of lock-in thermography with respect to pulsed thermography. During an LT experiment, the specimen is thermally stimulated using a single frequency corresponding to the depth at which a defect, at a particular defect, can be detected. The experiment must be repeated using different frequencies to cover a wide range of depths. In addition, the experiment duration depends on the used frequency, tests at low frequencies, required to detect deep defects, last longer than tests at high frequencies. On the contrary, a PT experiment is very fast and the amplitude and phase information, at several frequencies, can be recovered from it through a Fourier transformation, following the Pulsed Phase Thermography (PPT) processing [2].

2.2 Inspection of Carbon fiber reinforced plastic (CFRP) specimens

The specimens used in this experiment have been employed as material for primary structural members of aerospace pressure vessels in launch vehicles or satellites. CFRP has excellent properties of specific strength and specific stiffness. These specimens (CFRP) have three different shapes: planar (CFRP006), curved (CFRP007) and trapeze (CFRP008). All specimens contain 25 Teflon inclusions at different depths ($0.2 < z < 1$ mm) and several sizes ($3 < D < 15$ mm).

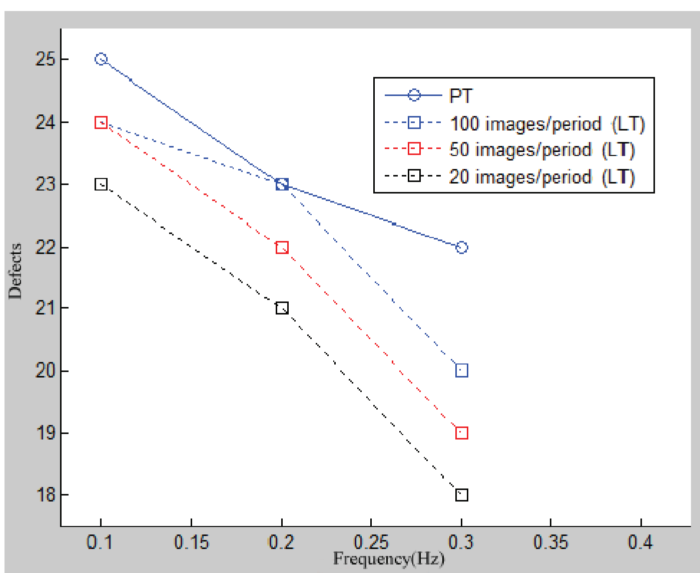

Figure 4. Results with LT and PT.

Phasegrams results obtained by optical lock-in thermography and pulsed thermography (through PPT processing) are presented in Figure 5. From this figure it can be observed that, for approximately the same modulation frequencies, PT is able to detect a greater number of inserts than LT. Interestingly, LT results improve with the number of images acquired during the experiment, see Figure 4. The objective of this experiment was to compare the number of detectable defects from both techniques.

The first tests were performed on specimen CFRP006. Specimens CFPR007 and CFPR008 were also tested by PT and LT using approximately the same modulation frequencies. LT results show that, 21 defects are detected in specimen CFRP006, 17 in specimen CFRP007 and 16 in CFRP008, whilst the corresponding numbers when inspecting by PT are; 23, 22 and 21, respectively for specimens CFRP006, CFRP007, and CFRP008.

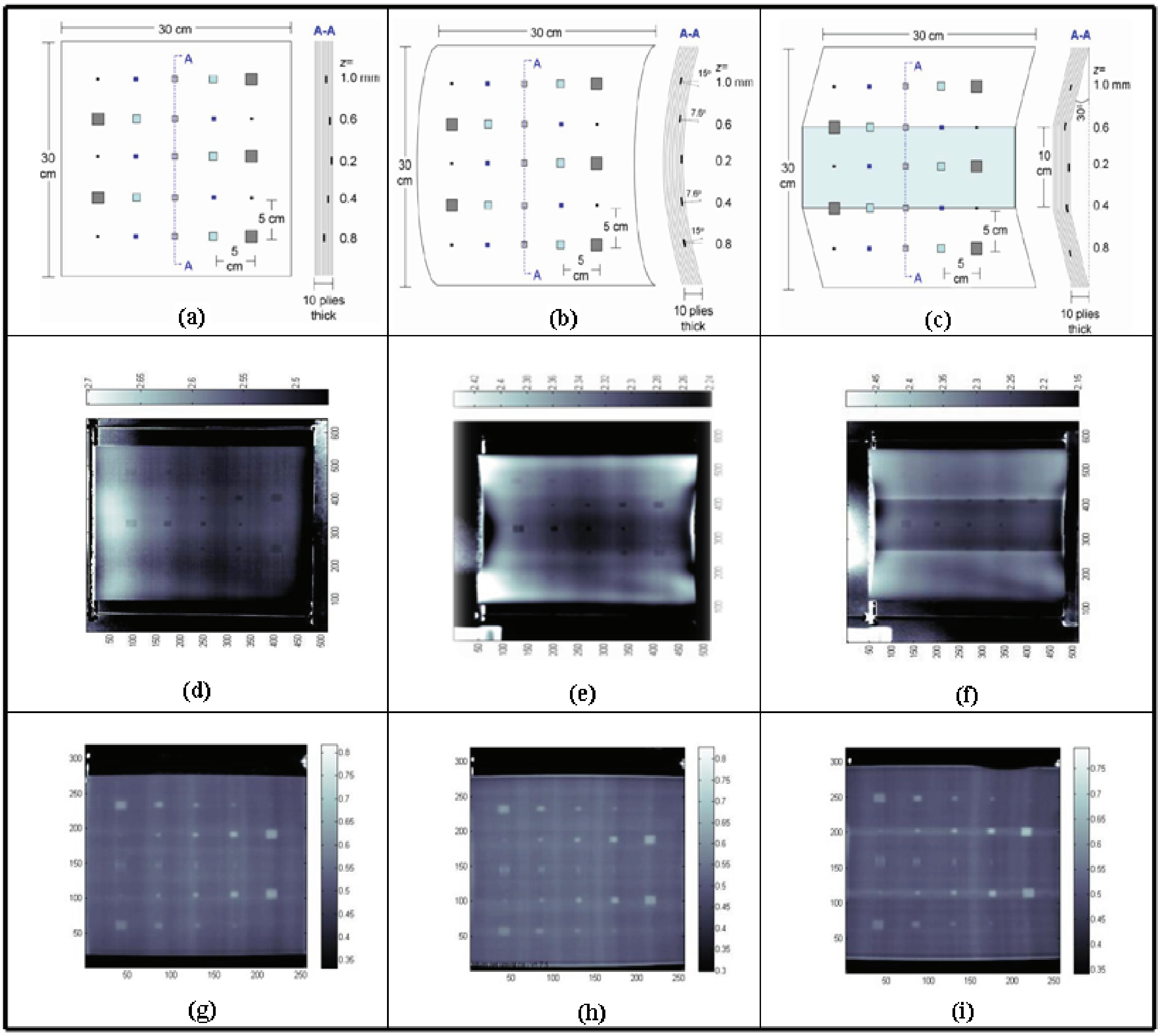

Figure 5. (a) CFRP006 - **(b)** CFRP007 - **(c)** CFRP008 - **(d)**,**(e)** and **(f)** phasegrams at 0.1 Hz obtained by LT - **(g), (h)** and **(i)**, phasegrams at 0.15 Hz obtained by PT.

2.3 Inspection of aircrafts rudders

CF18 aircrafts from the Canadian Air Forces (Figure 6a) as well as their American counterparts the F18 from the US Navy have been in service for more than 20 years. Over the lifetime of these aircrafts, some of the flight control surfaces – such as rudders and flaps – made of honeycomb sandwich structures might be subjected to water ingress or impact damage.

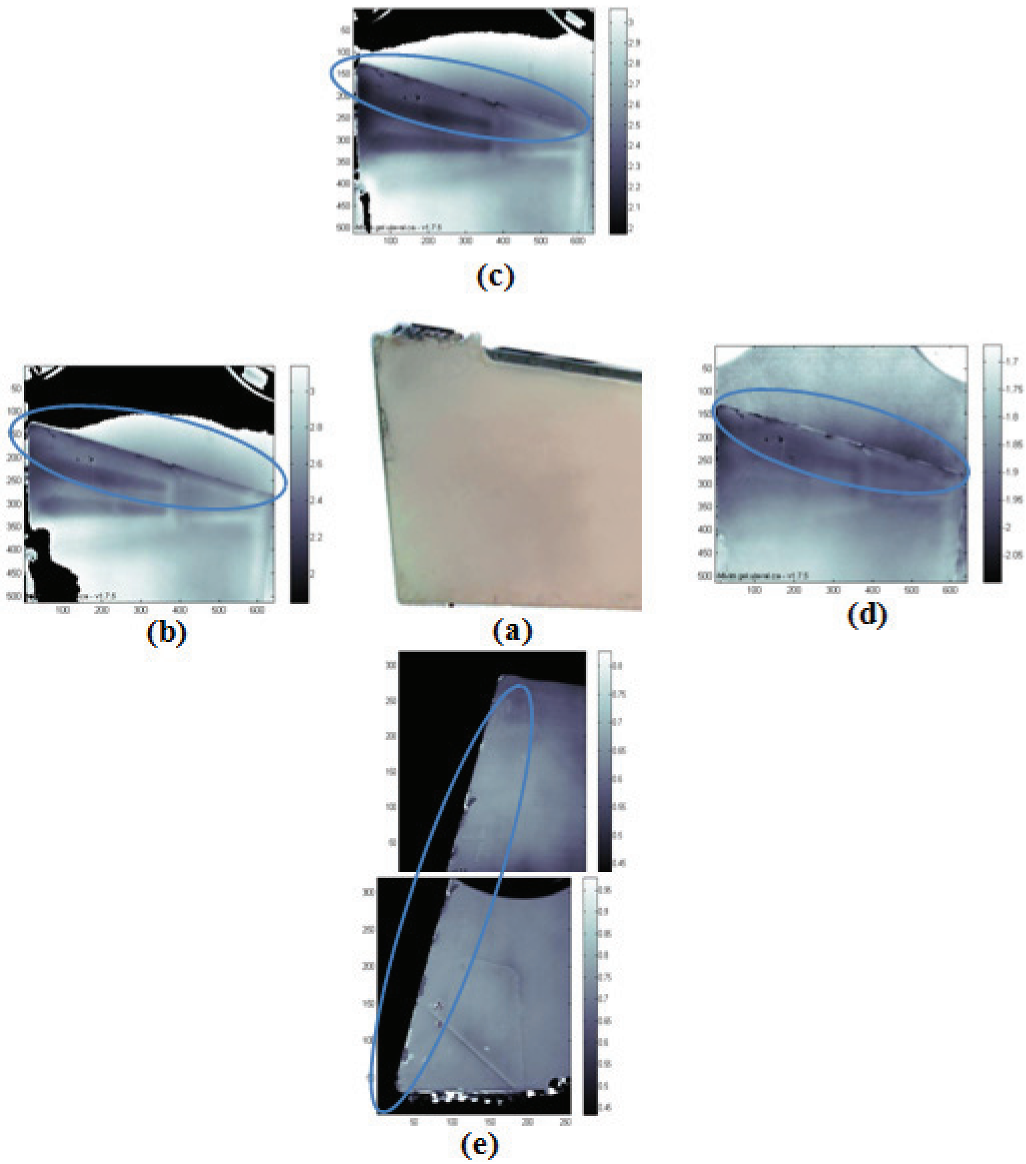

Figure 6. (a) Rudder section (picture) - **(b), (c), (d)**, phasegrams at 0.03 Hz, 0.04 Hz and 0.05 Hz obtained by LT - **(e)** phasegram at 0.045 Hz obtained by PT.

This specimen was tested by LT and PT. The frequencies used in LT were: 0.03, 0.04 and 0.05 Hz. Delaminations can be detected in at all frequencies, whilst the internal structure is better seen at low frequencies because the thermal waves probe deeper, eq. (4). Figure 6e shows a phasegram at f = 0.045 Hz. The structure of the rudder is better seen by LT, Figure 6b and c.

One of the most important parameters is the amount of energy delivered to the surface specimen. In this case, LT has a clear advantage over PT, since in LT it is possible to have a better control over the energy source more over, all the energy is devoted to the single tested frequency while in PT; the energy is dispersed among all the frequencies.

3. CONCLUSION

The two most commonly used active thermography techniques, pulsed and lock-in thermography, can be used in the NDT&E assessment of industrial materials. Selection of the most suitable energy source depends on the application. Optical pulsed thermography is fast and easy to deploy. Although data are affected by different problems (non-uniform heating, emissivity variations, environmental reflections and surface geometry), there are numerous processing techniques available to counter these problems and therefore to obtain prompt results of reliable quality, as well as quantitative information in some instances. Optical lock-in thermography allows better control of the energy deposited on a surface, which might be interesting if a low power source is to be used or if special care has to be given to the inspected part – for inspection of artworks for example. However, it requires a separate experiment for each and every inspected depth and there is a stabilization time before reaching a permanent regime.

4. ACKNOWLEDGEMENTS

The National Science and Engineering Research Council of Canada (NSERC) is thanked for its financial support as well as the Canada Research Chair MiViM – *Multipolar Infrared Vision Infrarouge Multipolaire* and the Canadian Foundation for Innovation through the LIVE installation (*Laboratory for Infrared Vision Excellence*).

5. REFERENCES

[1] Nondestructive Handbook, Infrared and Thermal Testing, Volume 3, X. Maldague technical ed., P. O. Moore ed., 3rd edition, Columbus, Ohio, ASNT Press, 2001, 718 p.

[2] Ibarra-Castanedo C. and Maldague X. “Pulsed Phase Thermography Reviewed”, QIRT Journal, 1(1):47-70, 2004.

[3] Maldague X. P. and Marinetti S. "Pulse Phase Infrared Thermography," J. Appl. Phys., 79(5):2694-2698, 1996.

[4] Ibarra-Castanedo C., Gonzalez D. A., Galmiche F., Bendada A. and Maldague X. P., “Recent Research Developments in Applied Physics On signal transforms applied to pulsed thermography”, Recent Research Developments in Applied Physics, 9:101-127, 2006.

[5] Carslaw H. S. and Jaeger J. C., “Conduction of Heat in Solids”, 2nd edition, Clarendon Press, Oxford, 1986.

[6] Wu D.and Busse G. “Lock-in Thermography for NonDestructive Evaluation of Materials” Revue Générale de Thermique, 37:693-703, 1998.

[7] Riegert G., Zweschper T., and Busse G. “Eddy-current lockin-thermography: Method and its potential”, Journal de Physique IV, vol. 125, Jun. 2005, pp. 587-591.

[8] Favro L. D. and Han X., “Thermal Wave Materials Characterization and Thermal Wave Imaging,” in Birnbaum G., Auld B. A. (eds.): Sensing for Materials Characterization, Processing and Manufacturing, ASNT TONES, 1:399-415, 1998.

Track 2

NDT Technology and Applications

Trackleader - Dave Craig, Pratt & Whitney

David M Craig (Fellow Inspection Engineering & Mgr. NDT Technology) joined Pratt & Whitney Canada (P&WC), Longueuil, Montreal in August 1988 and has been working in the field of NDT for over 30 years. Initially involved in inspection technique development and probability of detection studies, David was inducted into the P&WC Fellows program in October 2005. Current activities include working with other Pratt & Whitney aerospace businesses to consolidate NDT activities worldwide. Prior to moving to Canada David worked at The Unit Inspection Company & Rolls-Royce MatEval.

Transient thermography tools for NDT & E of composites

N. P. Avdelidis[1*], C.Ibarra-Catsanedo[2], E. Cheilakou[1], E. Saarimäki[3], T. Kauppinen[4], S. Fanou[5], M. Koui[1], X. P. V. Maldague[2], C. Ennaceur[6]

[1] NTUA – National Technical University of Athens, School of Chemical Engineering, Materials Science & Engineering Department, Zografou Campus, 157 80 Athens, Greece.
[2] University Laval, Computer Vision and Systems Laboratory, Dept. of Electrical and Computer Engineering, Quebec City (Quebec), Canada G1K 7P4.
[3] VTT - Technical Research Centre of Finland, Sinitaival 6, FI-33720 Tampere, Finland.
[4] VTT - Technical Research Centre of Finland, P.O. Box 1000, FI-02044, Finland.
[5] ENEA, Casaccia Research Centre, Via Anguillarese 301, 00123 S. Maria di Galeria, Rome, Italy.
[6] TWI Ltd., NDT Group, Granta Park, Great Abington, Cambridge, CB21 6AL, U.K.

ABSTRACT

Smart methods for assessing the integrity of a composite structure are essential to both reduce manufacturing costs and out of service time of the structure due to maintenance. Nowadays, thermal non-destructive testing (NDT) is commonly used for assessing composites. By using automated and advanced non-invasive thermography tools for the inspection of composites there could be a reduction in the use of manual, subjective inspections. It could also improve sensitivity for the detection of small defects. This way, accuracy is improved, leading to an increased "Probability of Detection" at a higher confidence level, reducing instances of catastrophic failure. Thermography NDT approaches could be used successfully in order to inspect composites at the manufacturing, assembly, maintenance and repair stages. In this work, the authors present results from thermal modelling investigation & assessment, as well as from transient thermography evaluation (pulsed, pulsed phase, vibro, etc) using a range of samples – panels of different types of defects (i.e. impact damage, delamination, drilling defects, etc). and structure in order to develop qualitative and/or quantitative procedures concerning the detection and damage assessment of composites.

[*] Correspondence: Email: avdel@mail.ntua.gr

A Comparison of Pulsed Thermography and Ultrasonic C-scanning for Inspection of Aircraft Composite Structures

Marc Genest

Abstract not available at time of printing.

Estimating a Pipe's Equivalent Wall Thickness and Elastic Properties From Ultrasonic Measurements

Darryl K. Stoyko[1], Neil Popplewell[1], and Arvind H. Shah[2]

[1]*Department of Mechanical and Manufacturing Engineering, University of Manitoba, 15 Gillson Street, Winnipeg, Manitoba, Canada, R3T 5V6, (204) 474-9888*
[2]*Department of Civil Engineering, University of Manitoba, 15 Gillson Street, Winnipeg, Manitoba, Canada, R3T 5V6, (204) 474-9674*

Email Addresses: D_Stoyko@UManitoba.ca, npopple@cc.umanitoba.ca, shah@cc.umanitoba.ca

Abstract

An inverse procedure is described that simultaneously estimates a pipe's wall thickness and elastic properties from three non-destructively measured, ultrasonic modal cut-off frequencies when given a known outer diameter and mass density. The procedure returns, with an uncertainty estimate, the uniform, right circular, hollow, homogenous, isotropic pipe that matches "best" the measured cut-off frequencies. The theory behind the inversion procedure is outlined first. The technique is next illustrated using a computer-simulated example. Then, two experimental illustrative examples, which demonstrate the viability of the technique, are presented for a steel and an aluminum pipe.

Introduction

Material and dimensional information constitute fundamental knowledge for assessing the current behaviour or "health" of a structure. From a practical perspective, in situ measurements should be used that are quick, reliable and non-destructive. An ultrasonic based approach is one plausible candidate. Indeed ultrasonic body waves are employed commonly to accurately measure fine dimensions [1]. Single or "focussed guided waves," on the other hand, can propagate over tens of metres so they have been used to remotely interrogate inaccessible locations [2]–[8]. Procedures which employ guided waves are attractive because their multi-modal and dispersive behaviour can simultaneously provide information over a range of frequencies [9]. Although the behaviour of a single, essentially non-dispersive mode is interpreted relatively easily [3]–[4], it is difficult to implement. Even if excited, a single mode is likely converted to additional modes at geometrical discontinuities [2]. These modes are generally dispersive so that the nature of a propagating wave packet changes as it travels along a structure. The objective here is to demonstrate a procedure involving several guided waves which can be automated to display material and dimensional data and can be extended, in the future, to indicate a structure's condition. Although the procedure could be applied to any plate-like structure, it is illustrated by using homogeneous, isotropic pipes. Such pipes are employed ubiquitously in industry [10].

Defining a pipe's unknown character from its measured response to a specified excitation is an example of an inverse procedure. Even an idealized computational inversion procedure, in which errors are generally less than those arising from experimental measurements, may not produce a unique solution [11]. Moreover, an inversion is often based upon a more computationally efficient, forward solver [11]. (A forward solver determines the response when both the excitation and pipe's character are known.) This indirect approach is adopted here as an uncertainty analysis can be also performed straightforwardly. The forward solver is based upon a standard Semi- Analytical Finite Element (SAFE) formulation [12]. Therefore, the novelty lies not in the numerical technique but in the insight gained from the presentation and physical interpretation of the results. On the other hand, the inherent modal decomposition produced by SAFE is crucial to understanding why simple invariant features of a pipe's temporal and corresponding frequency behaviour can be exploited in the inverse solution.

An overriding concern is that a pipe's properties should be measured as simply as possible. Therefore, a short duration excitation is applied radially at an easily accessible external surface of a pipe. No effort is made to avoid dispersive wave modes, in contrast to common practice. The modes are received at a single off-set transducer which is linked to a computer processing capability. Both the transmitting and receiving transducers' dimensions are assumed to be much smaller than the excited modes' predominant wavelengths. Therefore, they are idealized as acting at points. Software incorporates a Discrete Fourier Transform (DFT) whose output is employed as input to a curve fitting scheme for the receiving transducer's temporal signal. The aim of this contorted procedure is to refine the frequency values of only the predominant modal contributions in the received response [13]. These values correspond to the pipe's cut-off frequencies which are common to all non-nodal locations [14]. Therefore, the choice of measurement location is relatively unimportant. However, the measured cut-off frequencies still have to be reconciled with their SAFE counterparts. This task is accomplished by taking the "true" set of pipe properties as the one for which three measured and computed cut-off frequencies are closest. Likely uncertainties are estimated from a sensitivity assessment around the selected set of properties. Agreement is shown to be generally good with classically but more tediously performed destructive experiments and readily available tabulated data.

Theoretical Basis

The SAFE forward solver provides the computational foundation so that it is outlined first. Its use in finding an inverse solution is described later. An infinitely long pipe, half of which is illustrated in Figure 1, is considered. The pipe is assumed to be uniformly right circular, homogeneous, linearly elastic and isotropic. It has Lamé constants λ and μ, density ρ, a constant mean radius R, outside radius r_0 and thickness H, in addition to traction free, inner and outer surfaces. Right hand cylindrical and Cartesian coordinate systems (r, θ, z) and (x, y, z), respectively, are shown in Figure 1. Their common origin is located at the geometric centre of a generic cross section of the pipe with the z axis directed along the pipe's longitudinal (axial) axis.

The point excitation, $\boldsymbol{F}'(\theta, z, t)$, is applied normally to the external surface at $y = 0$ in the plane $z = 0$ by the transmitting transducer. (In the cylindrical coordinate system, the excitation's application coincides with $\theta = 0$.) To circumvent numerical convergence difficulties associated with a point application, the excitation is approximated by using a "narrow" pulse having a uniform amplitude over a circumferential distance $2r_0\theta_0$. This narrow pulse is represented by using a Fourier series of "ring-like" loads having separable spatial and time, t, variations. In particular,

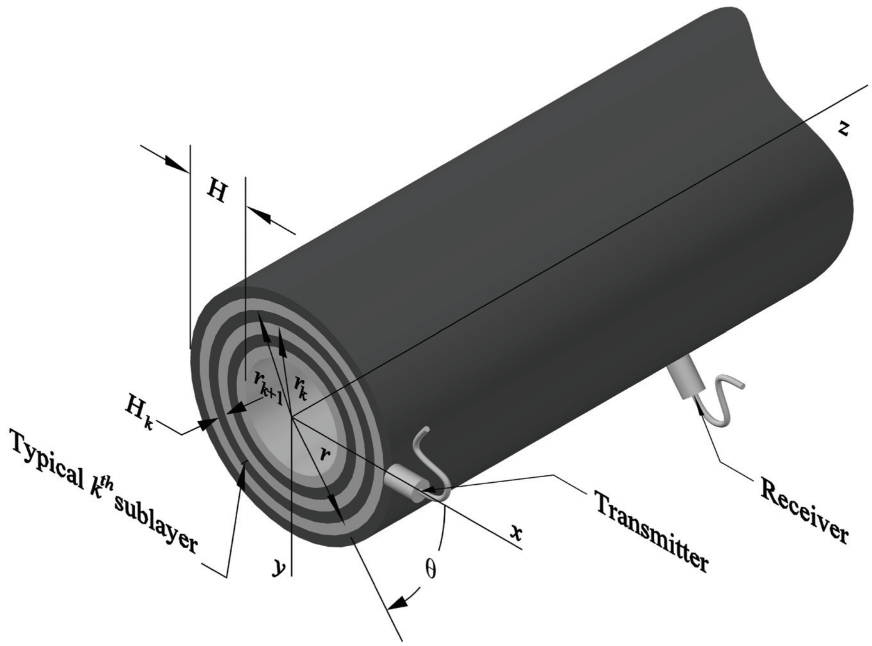

Figure 1. A pipe's discretization.

$$\boldsymbol{F^t}(\theta,z,t)=\boldsymbol{F_0}\,p(t)\delta(\theta)\delta(z)\approx\begin{cases}\dfrac{p(t)}{2r_0\theta_0}\delta(z)\boldsymbol{F_0}, & -\theta_0\le\theta\le\theta_0\\ 0, & \text{otherwise}\end{cases}=\sum_{n=-\infty}^{\infty}\frac{p(t)}{2\pi r_0}\mathrm{sinc}(n\theta_0)e^{jn\theta}\delta(z)\boldsymbol{F_0}, \quad \textbf{(1)}$$

where use has been made of the Fourier series for a rectangular pulse [15]. In equation (1) $\boldsymbol{F}_0$ and $p(t)$ are a vector and a function that describe the radial and temporal variations of the excitation, respectively, n is the circumferential wave-number, δ is the Dirac delta function, and $j=\sqrt{-1}$. The $\boldsymbol{F}_0$ is a vector of zeros except for a single element corresponding to the excitation's specified position and direction. Application of the Fourier transform integral to the series used in equation (1) transforms the excitation vector from the axial, z, domain to the wave-number, k, domain. The result is:

$$\boldsymbol{F^t}(\theta,z,t)\approx\sum_{n=-\infty}^{\infty}\frac{p(t)}{2\pi r_0}\mathrm{sinc}(n\theta_0)e^{jn\theta}\boldsymbol{F_0}, \quad \textbf{(2)}$$

in which the "sifting" property of the Dirac delta function has been applied.

In the previous equations $p(t)$ is taken commonly as the Gaussian modulated sine wave which has a non-dimensional form (always indicated by a star superscript) of:

$$p^*(t)=\frac{H}{\mu}p(t)=\begin{cases}0, & t<0\\ e^{-a(ht-\tau)^2}\sin(h\omega_0 t), & t\ge 0.\end{cases} \quad \textbf{(3)}$$

The constants a, h, τ, and ω_0 are:

$$a=2.29592\times10^{10}\ \mathrm{s}^{-2},\ h=0.28,\ \tau=1.4\times10^{-5}\ \mathrm{s},\ \text{and}\ \omega_0=(5\times10^5)\pi\ \mathrm{rad/s} \quad \textbf{(4)}$$

here. Consequently the excitation has a 70 kHz centre frequency and more than 99% of its energy is contained within a 35 to 107 kHz bandwidth. Therefore the Fourier integral transform of $p^*(t)$, $|\bar{p}^*(\omega)|$ where ω is the circular frequency, may be reasonably assumed to be contained within this finite bandwidth. The adopted $p^*(t)$ and $|\bar{p}^*(\omega)|$, where an over bar indicates a Fourier transformed variable, are illustrated in Figure 2.

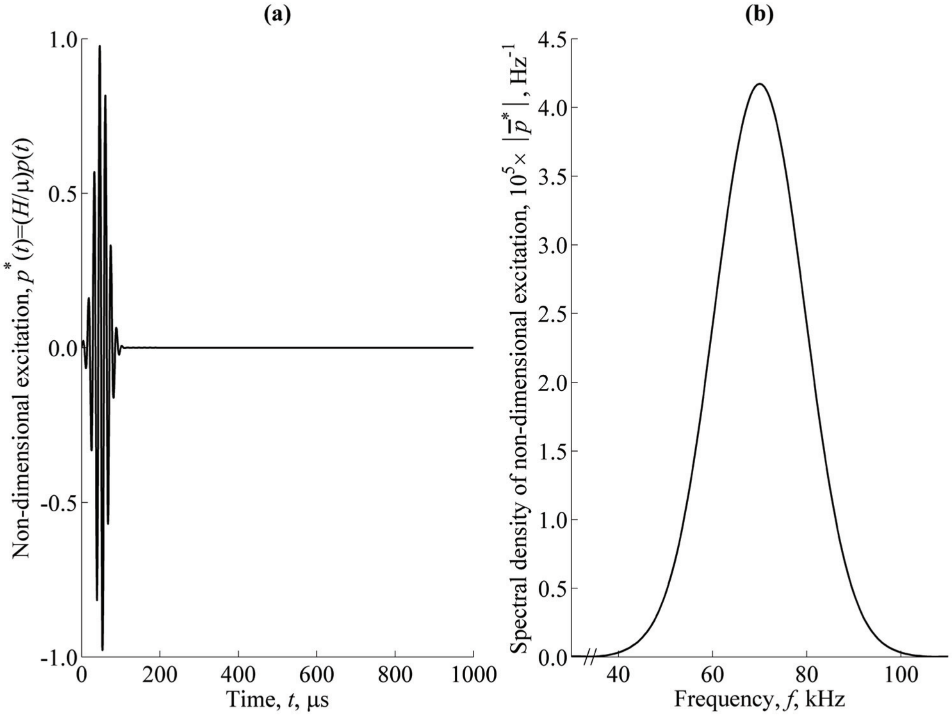

Figure 2. Applied excitation in (a) time and (b) frequency.

Having described the excitation, its effect on the pipe has to be considered next. The pipe is discretized into N layers through its thickness, where N is six in Figure 1. The thickness of the k^{th} layer is H_k and it extends radially from r_k to r_{k+1}. For simplicity, the H_k are considered to be identical. Each layer corresponds to a one-dimensional finite element in the pipe's radial direction for which a quadratic interpolation function is assumed. A conventional finite element approach is applied, layer by layer, to approximate the elastic equations of motion [12] in which the displacements, $\boldsymbol{u}^t(r, \theta, z, t)$, take the form:

$$\boldsymbol{u}^t(r,\theta,z,t)=\boldsymbol{N}(r)\boldsymbol{U}^t(\theta,z,t) \qquad \textbf{(5)}$$

The $\boldsymbol{N}(r)$ contains the set of interpolation functions assembled over the entire pipe. On the other hand, $\boldsymbol{U}^t(\theta, z, t)$ assimilates the corresponding array of nodal displacements in which the easily measured radial displacement at the pipe's external surface is principally of interest. Like the similarly approximated excitation $\boldsymbol{F}^t(\theta, z, t)$, the $\boldsymbol{U}^t(\theta, z, t)$ is assumed to be circumferentially periodic, i.e.,

$$\boldsymbol{U}^t(\theta,z,t)=\sum_{n=-\infty}^{\infty} e^{jn\theta}\boldsymbol{U}_n^t(z,t). \qquad \textbf{(6)}$$

Consider, on the other hand, a single temporally harmonic component of $\boldsymbol{F}^t(\theta, z, t)$, $\boldsymbol{F}(\theta, z, t)$, having circular frequency ω. This excitation component produces the harmonic response component $\boldsymbol{U}(\theta, z, t)$. The Fourier series of these two variables take the form:

$$\boldsymbol{F}(\theta,z,t)=e^{-j\omega t}\sum_{n=-\infty}^{\infty} e^{jn\theta}\boldsymbol{F}_{\boldsymbol{n}}(z), \tag{7a}$$

and:

$$\boldsymbol{U}(\theta,z,t)=e^{-j\omega t}\sum_{n=-\infty}^{\infty} e^{jn\theta}\boldsymbol{U}_{\boldsymbol{n}}(z). \tag{7b}$$

Equations (7a) and (7b) are substituted into approximate equations of motion obtained from Hamilton's principle [12] which are transformed into the wavenumber domain by applying the Fourier integral transform and making use of equation (2). The result for the n^{th} circumferential wave-number is:

$$\left(\boldsymbol{K_1}+jn\boldsymbol{K_2}+n^2\boldsymbol{K_4}-\omega^2\boldsymbol{M}\right)\bar{\boldsymbol{U}}_{\boldsymbol{n}}+jnk_n\left(\boldsymbol{K_3}-jn\boldsymbol{K_5}\right)\bar{\boldsymbol{U}}_{\boldsymbol{n}}+k_n^2\boldsymbol{K_6}\bar{\boldsymbol{U}}_{\boldsymbol{n}}=\bar{\boldsymbol{F}}_{\boldsymbol{n}}, \tag{8}$$

where the $\boldsymbol{K}_i$ are stiffness matrices and $\boldsymbol{M}$ is the mass matrix. Details are given in [12].

Proceeding in a classical modal analysis fashion, equation (8) takes the form of an eigensystem in the special case when $\bar{\boldsymbol{F}}_{\boldsymbol{n}}$ is the null vector. Integer values are always ascribed to n. Either k_n or ω is assigned when the wave-number or frequency is presumed. Then a linear or quadratic eigensystem is produced in ω^2 or k_n, respectively. In the latter, more commonly encountered case, equation (8) may be rewritten in the linear form:

$$\left[\boldsymbol{A}(n,\omega)-k_n\boldsymbol{B}\right]\begin{Bmatrix}\bar{\boldsymbol{U}}_{\boldsymbol{n}}\\ k_n\bar{\boldsymbol{U}}_{\boldsymbol{n}}\end{Bmatrix}=\begin{Bmatrix}\boldsymbol{0}\\ \bar{\boldsymbol{F}}_{\boldsymbol{n}}\end{Bmatrix} \tag{9}$$

where:

$$\boldsymbol{A}(n,\omega)=\begin{bmatrix}\boldsymbol{0} & \boldsymbol{I}\\ (\boldsymbol{K_1}+jn\boldsymbol{K_2}+n^2\boldsymbol{K_4}-\omega^2\boldsymbol{M}) & j(\boldsymbol{K_3}-jn\boldsymbol{K_5})\end{bmatrix},\ \boldsymbol{B}=\begin{bmatrix}\boldsymbol{I} & \boldsymbol{0}\\ \boldsymbol{0} & -\boldsymbol{K_6}\end{bmatrix} \tag{10}$$

and **0** (***I***) is the null (identity) matrix.

Normal modes are found for the nth circumferential wave-number by solving the homogeneous form of equation (9). This results in $12N$+6 eigenvalues or axial wavenumbers. A real (complex) valued wave-number corresponds to a propagating (evanescent) wave. Moreover, half the wave-numbers correspond to solutions for the positive z coordinates; the other half represent solutions for the negative z coordinates.

In addition to the wave-numbers, right and left eigenvectors, $\boldsymbol{\phi}_{\boldsymbol{nm}}^{\boldsymbol{R}}$ and $\boldsymbol{\phi}_{\boldsymbol{nm}}^{\boldsymbol{L}}$, respectively, are associated with the m^{th} eigenvalue. They are partitioned into the upper and lower halves.

$$\boldsymbol{\phi}_{\boldsymbol{nm}}^{\boldsymbol{R}}=\left[\boldsymbol{\phi}_{\boldsymbol{nmu}}^{\boldsymbol{R}}\ \ \boldsymbol{\phi}_{\boldsymbol{nml}}^{\boldsymbol{R}}\right]^{\mathrm{T}} \text{ and } \boldsymbol{\phi}_{\boldsymbol{nm}}^{\boldsymbol{L}}=\left[\boldsymbol{\phi}_{\boldsymbol{nmu}}^{\boldsymbol{L}}\ \ \boldsymbol{\phi}_{\boldsymbol{nml}}^{\boldsymbol{L}}\right]^{\mathrm{T}}, \tag{11}$$

that are represented by the subscripts u and l, respectively. The pipe's response is obtained, for the n^{th} circumferential wave-number and only those axial cross sections having positive z, by linearly superimposing the admissible $6N+3$ right eigenvector solutions. Applying first the inverse Fourier transform to this sum, and then Cauchy's residue theorem, gives the n^{th} circumferential mode of the response. The result is [12]:

$$\boldsymbol{U}_{\boldsymbol{n}}(\theta,z,t)=e^{-j\omega t}\frac{j\operatorname{sinc}(n\theta_0)}{2\pi r_0}\left[\sum_{m=1}^{6N+3}\frac{\boldsymbol{\phi}_{\boldsymbol{mnl}}^{\boldsymbol{L}\;\mathbf{T}}(\omega)\boldsymbol{F}_{\mathbf{0}}}{B_{nm}(\omega)}\boldsymbol{\phi}_{\boldsymbol{nmu}}^{\boldsymbol{R}}(\omega)\,e^{jk_{nm}(\omega)z}\right],\tag{12}$$

where,

$$B_{nm}\delta_{mp}=\boldsymbol{\phi}_{\boldsymbol{nm}}^{\boldsymbol{L}\;\mathbf{T}}\boldsymbol{B}\,\boldsymbol{\phi}_{\boldsymbol{np}}^{\boldsymbol{R}},\tag{13}$$

in which bi-orthogonality relations [16] have been used. Moreover δ_{mp} is the Kronecker delta. The linear response to a multi-frequency excitation can be found by merely superimposing the responses caused by each individual frequency component. Hence:

$$\boldsymbol{U}^{\boldsymbol{t}}(\theta,z,t)=\frac{-j}{4\pi^2 r_0}\int_{-\infty}^{\infty}\bar{p}(\omega)e^{-j\omega t}\sum_{n=-\infty}^{n=\infty}\operatorname{sinc}(n\theta_0)\left[\sum_{m=1}^{6N+3}\frac{\boldsymbol{\phi}_{\boldsymbol{mnl}}^{\boldsymbol{L}\;\mathbf{T}}(\omega)\boldsymbol{F}_{\mathbf{0}}}{B_{nm}(\omega)}\boldsymbol{\phi}_{\boldsymbol{nmu}}^{\boldsymbol{R}}(\omega)\,e^{jk_{nm}(\omega)z}\right]e^{jn\theta}\mathrm{d}\omega\tag{14}$$

after summing all the circumferential harmonic components.

Simplifying Features

It is demonstrated in [17]–[18], by using the modal decomposition component of SAFE, that the "peak" magnitudes of a pipe's radial Frequency Response Function (FRF) occur at its modal cut-off frequencies where the wave number is zero. A sharp increase there arises because the corresponding B_{nm} in equations (12), (13), and (14) tends to zero as a cut-off frequency is approached, i.e., a singularity happens in the nm mode's FRF. Although details are omitted here for brevity, this feature exists because there is a repeated root at each cut-off frequency. Hence a defective[1] eigensystem exists. Consequently the corresponding left and right eigenvectors are orthogonal to the $\boldsymbol{B}$ matrix defined in equation (10) and B_{nm} also becomes zero [19]. It is interesting that a cut-off frequency can be interpreted as a juncture at which a travelling wave problem transitions to a vibration problem because the wavelength, $2\pi/k_{nm}$, becomes infinitely long. Therefore the response at a cut-off frequency may be termed "vibration"-like [14], [19]. Also note from equations (12) and (14) that a modal response at a cut-off frequency becomes advantageously independent of an observation point's axial location. Moreover, cutoff frequencies can be calculated without knowing the corresponding eigenvectors of equation (8) with $k_n = 0$ and $\bar{\boldsymbol{F}}_{\boldsymbol{n}} = \mathbf{0}$. Cut-off frequencies depend, through the stiffness and mass matrices, on the pipe's elastic properties, mass density, and geometrical dimensions. It is assumed here that the pipe's outer diameter, D_0, and mass density, ρ, are readily available, which leaves the elastic properties and wall thickness to be determined. Two independent elastic constants are sufficient to characterize a homogeneous isotropic material. Thus, in dimensional terms, the Lamé constants, λ and μ, and the wall thickness, H, would sufficiently characterize the pipe's unknown properties. Application of the Buckingham π theorem [20] is used, however, to reduce the size of the (non-dimensional) search region, which makes calculations more

[1]A defective eigensystem is one in which an eigenvalue is repeated, say integer r times, but fewer than r unique (right) eigenvectors exist for the repeated eigenvalue [16].

tractable.

For a given circumferential wave-number n and order m, the non-dimensional cut-off frequency ratio

$$\omega^{c*}_{F(n,m)} = \frac{\omega^{c}_{F(n,m)}}{\omega_{ref}} \tag{15}$$

is introduced where $\omega_{ref}=1/H\sqrt{(\mu/\rho)}$ and $\omega^{c}_{F(n,m)}$ is the cut-off frequency of the F(n, m) flexural mode[2]. The $\omega^{c}_{F(n,m)}$ can be expressed in terms of the non-dimensional parameters (H/R) and (λ/μ). Note that the desired elastic properties and wall thickness can be calculated from (H/R) , (λ/μ), and ω_{ref} as well as the presumed mass density and outer diameter [18, 19]. The inequality $0<(H/R)< 2$ arises physically because these lower and upper bounds relate to a pipe having no wall thickness and a solid pipe, respectively. On the other hand, (λ/μ) can be bounded reasonably as $0\le(\lambda/\mu)\le 10$ from the standard elasticity relation $0\le\nu\le 0.5$, where ν is Poisson's ratio. (If the Buckingham π theorem had not been applied, the much more lax restrictions placed on λ and μ would have led to them being non-negative.) Also, the wall thickness is bounded, again on physical grounds, as $0<H<D_0/2$.

Graphical Relations Between the Cut-off Frequencies and Cylinder Properties

The key to making the inverse problem tractable is a succinct yet clear presentation showing the dependence of the forward solved cut-off frequencies upon the independent (H/R) , (λ/μ), and ω_{ref}. Transformations to obtain practical engineering properties, which also use $f=\omega/(2\pi)$ where f is frequency, are performed later. The presentation's construction may be envisaged by initially considering all the μ, H, ρ, (and thus ω_{ref}) to be unity. Then λ and R are each varied uniformly within the physically viable ranges described earlier. Forward computations to determine three non-dimensional cut-off frequencies, say $\omega^{c}_{F(10,1)}$, $\omega^{c}_{F(11,1)}$ and $\omega^{c}_{F(12,1)}$,[3] are performed within these ranges by SAFE. The corresponding values of (H/R) and (λ/μ), given ω_{ref} is simply 1 rad/s, are also noted.

In general,

$$\omega^{c*}_{F(i,1)} = \frac{\omega^{c}_{F(i,1)}}{\omega_{ref}} \quad \text{for all } i, \tag{16}$$

so that a particular $\omega^{c*}_{F(i,1)}$ is identical to $\omega^{c}_{F(i,1)}$ at this juncture. Moreover

$$\omega^{c}_{F(10,1)} \le \omega^{c}_{F(11,1)} \le \omega^{c}_{F(12,1)} \tag{17}$$

regardless of the value of ω_{ref}. Then the largest of the three $\omega^{c}_{F(i,1)}$, $\omega^{c}_{F(12,1)}$, is taken as an extreme but arbitrary 200 000 π rad/s (i.e., $f^{c}_{F(12,1)}$ is 100kHz). The non-dimensional cut-off frequencies for the selected values of (H/R) and (λ/μ) are available so that equation (16) is used to find the

[2]Modes are labelled by using the standard convention employed in [21]. Only flexural modes are considered here although the extension to torsional or longitudinal modes is obvious.

[3]These three cut-off frequencies are selected as they are the modes most easily excited with the ultrasonic transducers used in the experimental investigations.

corresponding ω_{ref} or $f_{ref} = \omega_{ref}\ /(2\pi)$. Associated values of $\omega^{c}_{F(10,1)}$ and $\omega^{c}_{F(11,1)}$ can be then determined from their non-dimensional cut-off frequencies for the selected (H/R) and (λ/μ) and ω_{ref}. Two points, corresponding to $\left(\omega^{c}_{F(10,1)}, \omega^{c}_{F(11,1)}, \omega^{c}_{F(12,1)}\right)$ and computed for the assumed (unity) and the calculated values of ω_{ref}, are converted to frequencies, in kHz, and graphed. They are joined by a line along which (H/R) and (λ/μ) are each constant but ω_{ref} varies. The line must also pass through the graph's origin because, physically, the $\omega^{c}_{F(i,1)}$ and ω_{ref} are zero there. The effects of variations in ω_{ref} due to other values of (H/R) and (λ/μ) are calculated straightforwardly. The same procedure produces a set of similar, closely spaced lines after perturbing (H/R) and (λ/μ). The resulting overall behaviour is presented in Figure 3.

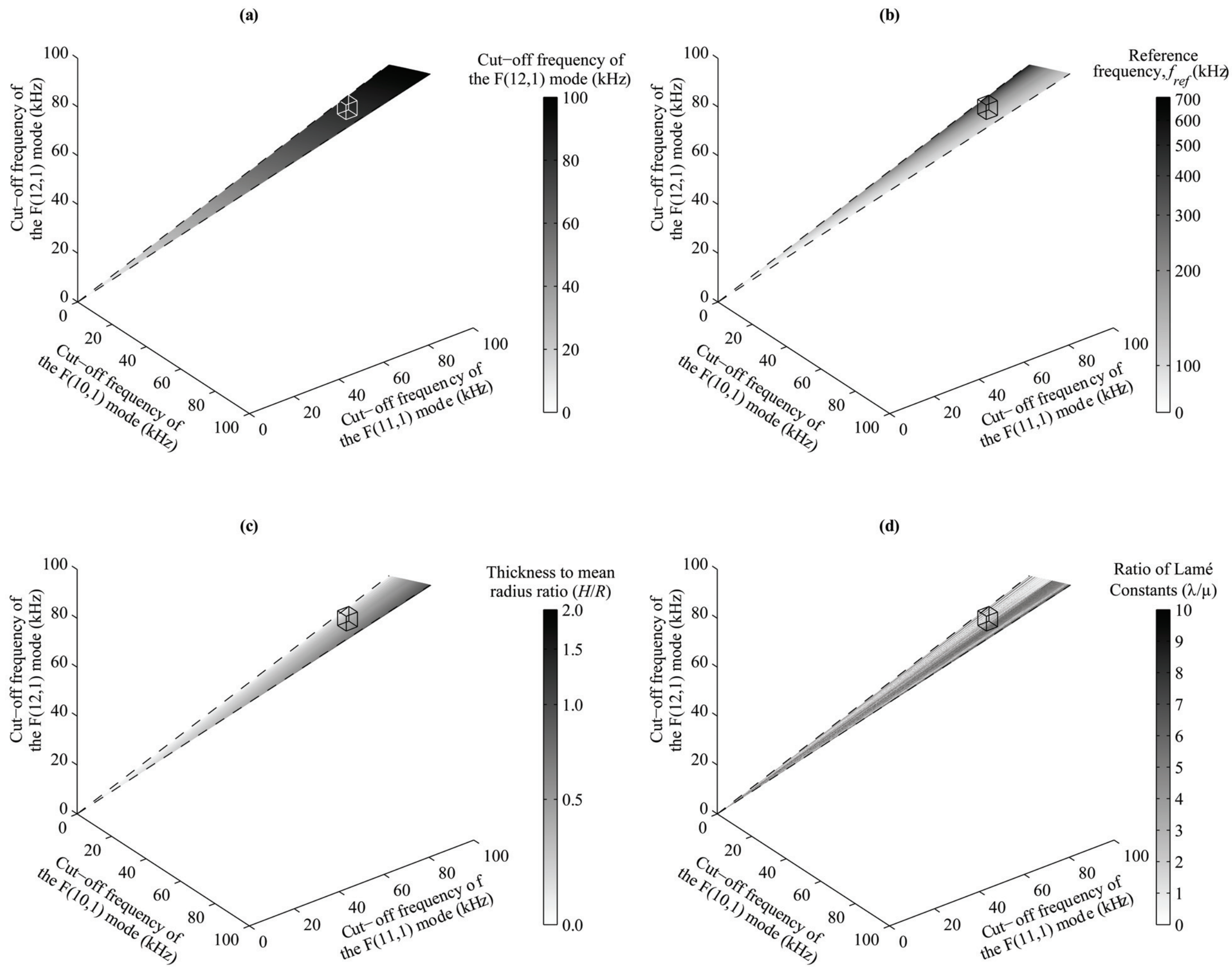

Figure 3. Dependence of the three cut-off frequencies on (a) each other, (b) $f_{ref} = \omega_{ref}/2\pi$, (c) (H/R), and (d) (λ/μ). Dashed lines (- - -) indicate the surfaces' boundaries due to constraints on (H/R).

The shaded solution surface of Figure 3 (a) shows the dependence of $\omega^{c}_{F(12,1)}$ (or, alternatively $f^{c}_{F(12,1)}$) upon $\omega^{c}_{F(10,1)}$ ($f^{c}_{F(10,1)}$) and $\omega^{c}_{F(11,1)}$ ($f^{c}_{F(11,1)}$). Note that at least three cut-off frequencies are required to determine the three unknown (H/R) and (λ/μ) and ω_{ref}. The surface seems to be a narrow bounded plane whose width increases progressively with deepening shades, i.e., higher $f^{c}_{F(12,1)}$. This is somewhat deceptive, however, because a computed inverse solution has been found empirically to exist only on the surface, not on a planar approximation. Previous research [13], [18] supports this contention because it was determined that cut-off frequencies should be measured, ideally, within 0.01%.

The shadings of Figures 3 (b) and (c) indicate that the cut-off frequencies depend strongly upon f_{ref} or ω_{ref} and (H/R), particularly at their highest values. Interestingly, a quite uniform shading emerges when these two figures are superimposed. Therefore, the effect of similar changes in f_{ref} and (H/R) counterbalance. On the other hand, the sizeable swathes of a given shading seen in Figure 3 (d) suggest that the $f^c_{\mathrm{F}(i,1)}$, i = 10, 11, 12, alter little with large (λ/μ) modifications. A comparison of Figures 3 (c) and (d) also intimates that shadings across the shorter width of the solution surface have similar tendencies for the (λ/μ) and smaller (H/R) variations. Therefore, the effect of (λ/μ) may be concealed, to some extent, by a greater one from (H/R).

Figure 4 magnifies the computed solution surface and nearby regions contained within the boxes shown in Figure 3. The illustrated points, which are offset slightly from the surface, correspond to the cut-off frequencies extracted from the simulated and experimentally measured time histories presented later. The off-sets arise from uncertainties and errors, the overall magnitudes of which are intimated by the off-set's shortest distance to the computed surface. The errors arise principally from the temporal curve fitting procedure to find the cut-off frequencies. Previous numerical studies [13] suggest that all the discernible cut-off frequencies in the measurement bandwidth should be incorporated to reduce the error. Uncertainties, on the other hand, may originate from any questionable assumption of SAFE like complete uniformity, no out-of-roundness, inhomogeneity, etc.

Inversion Scheme

The transmitter is pulsed to obtain the previously described excitation and the response is measured by the nearby receiving transducer. Three cut-off frequencies, $\hat{\omega}^c_{\mathrm{F}(n_i,m_i)}$, are "extracted" from the measured transient response using the temporal curve fitting procedure described in [13]. If these cut-off frequencies are exact and the SAFE modelling is perfect, the following relations hold:

$$\omega_{ref}\omega^{c*}_{\mathrm{F}(n_i,m_i)} - \hat{\omega}^c_{\mathrm{F}(n_i,m_i)} = 0 \text{ for } i = 1,2,3, \tag{18}$$

where $\omega^{c*}_{\mathrm{F}(n_i,m_i)}$ are the corresponding non-dimensional cut-off frequencies predicted by SAFE. Equation (18) provides three relations in three unknowns [(H/R) and (λ/μ) and ω_{ref}]. The solution of these non-linear equations provides a characterization of the pipe. Unlike the idealized forward simulation, experimental noise and errors can cause a measured point to lie outside the space spanned by the SAFE computer solutions, as seen in Figure 4. To overcome this discrepancy, the point on the surface "nearest" the measurement is sought. This point is located by minimizing the objective function:

$$\eta = \sum_{i=1}^{3} \left(\omega_{ref}\,\omega^{c*}_{\mathrm{F}(n_i,m_i)} - \hat{\omega}^c_{\mathrm{F}(n_i,m_i)}\right)^2. \tag{19}$$

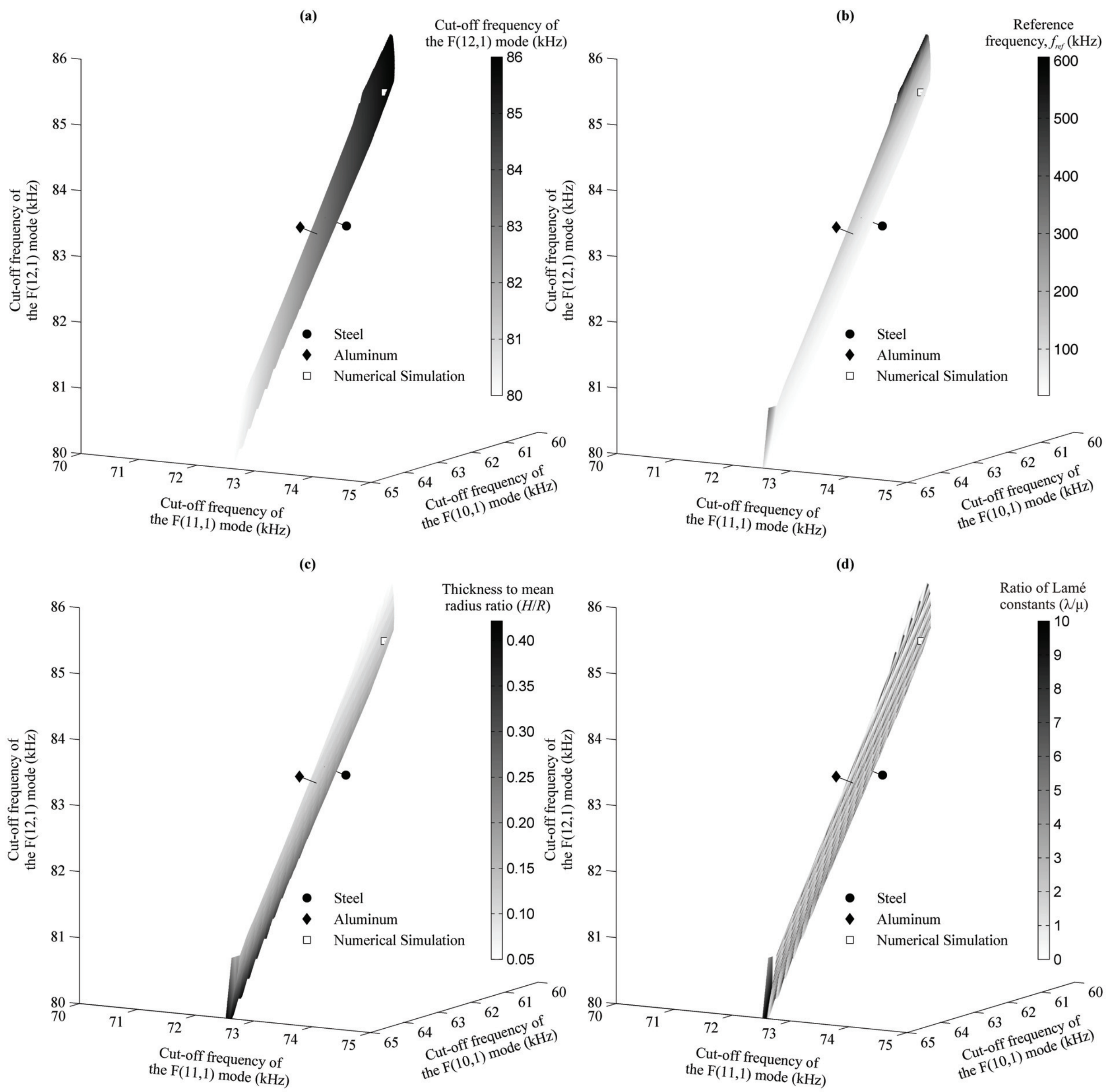

Figure 4. Magnified version of Figure 3 near the experimental and simulated data.

It is found by using the robust direct search method described in [22]. Projections between the extracted $\hat{\omega}^{c}_{\mathrm{F}(n_i,m_i)}$ and the nearest $\omega_{ref}\,\omega^{c*}_{\mathrm{F}(n_i,m_i)}$ are shown in Figure 4 for an essentially precise numerical simulation as well as the corresponding imprecise experimental data. Estimated maximum possible differences between the measured and predicted cut-off frequencies are employed to estimate the uncertainty in the recovered values of (H/R),(λ/μ), and ω_{ref}. First, the nearest found $\omega_{ref}\,\omega^{c*}_{\mathrm{F}(n_i,m_i)}$ is taken to be the initial nominal solution. This point lies, by its construction, in the space spanned by the forward solver. Use is now made of equation (18) to temporarily eliminate the effects of ω_{ref} and estimate the uncertainty in (H/R) and (λ/μ) . Three ratios:

$$Q_1 = \frac{\omega^{c}_{F(n_1,1)}}{\omega^{c}_{F(n_2,1)}} = \frac{\omega_{ref}\omega^{c*}_{F(n_1,1)}}{\omega_{ref}\omega^{c*}_{F(n_2,1)}} = \frac{\omega^{c*}_{F(n_1,1)}}{\omega^{c*}_{F(n_2,1)}},\ Q_2 = \frac{\omega^{c}_{F(n_3,1)}}{\omega^{c}_{F(n_2,1)}} = \frac{\omega_{ref}\omega^{c*}_{F(n_3,1)}}{\omega_{ref}\omega^{c*}_{F(n_2,1)}} = \frac{\omega^{c*}_{F(n_3,1)}}{\omega^{c*}_{F(n_2,1)}},$$
$$\text{and } Q_3 = \frac{\omega^{c}_{F(n_1,1)}}{\omega^{c}_{F(n_3,1)}} = \frac{\omega_{ref}\omega^{c*}_{F(n_1,1)}}{\omega_{ref}\omega^{c*}_{F(n_3,1)}} = \frac{\omega^{c*}_{F(n_1,1)}}{\omega^{c*}_{F(n_3,1)}} \tag{20}$$

can be formed. For a given (H/R) corresponding values of (λ/μ), or vice-versa, may be determined such that:

$$Q_1 - \frac{\omega^{c*}_{F(n_1,1)}}{\omega^{c*}_{F(n_2,1)}} = 0,\ Q_2 - \frac{\omega^{c*}_{F(n_3,1)}}{\omega^{c*}_{F(n_2,1)}} = 0,\ \text{and } Q_3 - \frac{\omega^{c*}_{F(n_1,1)}}{\omega^{c*}_{F(n_3,1)}} = 0 \tag{21}$$

are satisfied individually. The values of (H/R), (λ/μ), and ω_{ref} obtained by minimizing equation (19) are assumed to be sufficiently accurate to provide a reasonable starting approximation for (H/R). The values of the $\omega^{c}_{F(n,m)}$ from minimizing equation (19) are substituted into equation (20) and then into equation (21), along with the value of (H/R) corresponding to the $\omega^{c}_{F(n,m)}$. The three ratios formed in this fashion are deemed to be the nominal ratios for the Q_i. By perturbing the $\omega^{c}_{F(n,m)}$ within the range of uncertainly in the measured cut-off frequencies, maximum and minimum permissible values of the Q_i may be found. These, in turn, can be substituted into equation (21). The extreme values of (λ/μ), such that equation (21) is satisfied for all the extreme Q_i and the (H/R) arising from minimizing equation (19), are found. Then the nominal value of (λ/μ) is then taken as the mean of the extreme permissible values, and its uncertainty is taken as half the extreme range. A similar procedure is adopted to estimate the permissible variation in (H/R), taking the nominal value of (λ/μ) just found as the true value. This procedure is illustrated graphically in Figure 5 for the numerical simulation presented later. It allows a maximum perturbation in each of the $\omega^{c}_{F(n,m)}$ of 80 Hz which appears, from Table 2, to provide a reasonably conservative upper bound on the uncertainty of the extracted cut-off frequencies. The uncertainty in ω_{ref} is taken as the absolute value of the difference between the initial ω_{ref} stemming from the minimization of equation (19) and the mean value of ω_{ref} found by solving equation (16) for each of the $\omega^{c}_{F(n,m)}$, taking (H/R) and (λ/μ) as the values found from Figure 5. The uncertainties in (H/R), (λ/μ), and ω_{ref}, as well as those in D_0 and ρ are then propagated by using standard uncertainty estimation techniques (see, for example [23]) for each of the variables derived from the three properties calculated by using the inversion scheme.

Illustrative Examples

Three examples are presented next that illustrate the inversion technique. A numerical simulation, using a priori known material properties and dimensions, is given first. It is followed by an experimental example in which a real pipe has similar properties. The third example uses another real pipe which has substantially different material properties in dimensional terms, but similar properties in non-dimensional terms.

Numerical Simulation

An idealized 3 inch Nominal Pipe Size (NPS) [80 mm Diameter Nominal (DN)], Schedule 40,

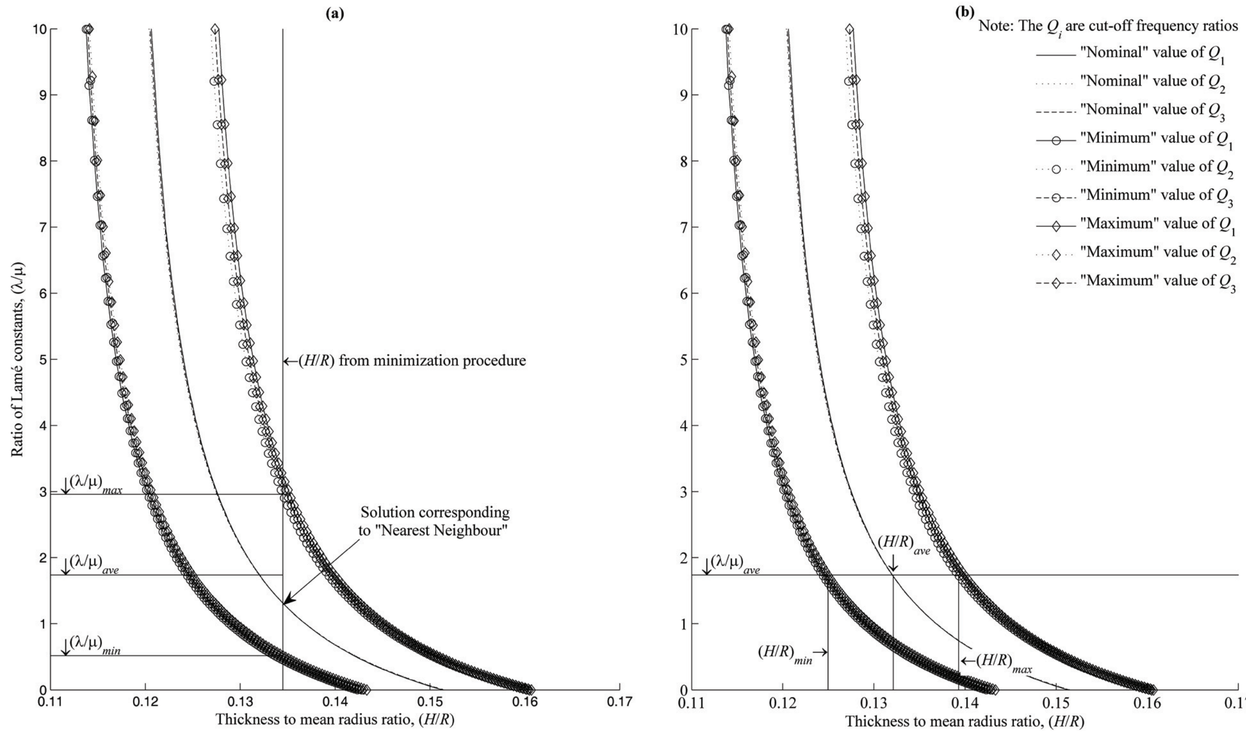

Figure 5. Graphical representation of the procedure used to assess (a) the uncertainty in (λ/μ) and (b) (H/R) for a numerical simulation.

seamless, carbon steel pipe is considered initially. Its dimensional and material properties are summarized in Table 1. This particular pipe is selected because it is commercially important. At the end of 1997, for example, there was approximately 40 300 miles (64 900 km) of such pipe in industrial use as energy-related pipeline in Alberta, Canada [10]. Consequently it has been studied extensively as in, for example, [2]–[4]. The radial displacement is calculated on the pipe's outer surface at $\theta = 0$ and $z^* = z/H = 5.1$, by using equation (14) in the manner described in [13]. The resulting time history is presented in Figure 6 (a). The corresponding DFT and temporal curve fit are given in Figures 6 (d) and (c), respectively. Table 2 compares the cut-off frequencies obtained from the computed FRF, DFT, and temporal curve fit. The inversion procedure and uncertainty estimations are applied to the cut-off frequencies found from the temporal curve fit. The results are summarized in Table 1. This table shows that the assigned and recovered material or dimensional properties generally agree within their estimated uncertainties.

Experimental Example 1

An actual 3 inch NPS (80 mm DN), Schedule 40, seamless, carbon steel pipe was examined experimentally next. The radial displacement was measured on the pipe's outer surface at $\theta \approx 0$ and $z^* = z/H \approx 5$. The time history is presented in Figure 7 (a), while the corresponding DFT and temporal curve fit are given in Figures 7 (c) and (b), respectively. The inversion procedure and the uncertainty estimations were applied to the cut-off frequencies obtained from a temporal curve fit. Results from the ultrasonic measurements are summarized in Table 3. A 7 inch (18 cm) or so length was cut from one end of the pipe. Plates and grips were welded onto this short sample after which the sample was heat treated to relieve residual stresses. Two nominally identical, three-element

Table 1. Comparing preassigned numerical values with those computed from inversion.

Property	Assigned Value	Computed Value
Mass density, ρ	8.906×10^{-3} slug/in^3 (7932 kg/m^3)	—
Outer diameter, D_0	3.496 in (88.8 mm)	—
Thickness, H	0.220 in (5.59 mm)	0.22±0.01 in (5.5±0.3 mm)
Mean radius, R	1.64 in (41.6 mm)	1.638±0.004 in (41.6±0.1 mm)
Thickness to mean radius ratio, (H/R)	0.134	0.132±0.007
Young's modulus, E	31 460 ksi (216.9 GPa)	32 000±4000 ksi (220±30 GPa)
Lamé constant (shear modulus), μ (G)	12 230 ksi (84.3 GPa)	12 000±1 000 ksi (84±9 GPa)
Lamé constant, λ	16 410 ksi (113.2 GPa)	21 000±15 000 ksi (145±103 GPa)
Ratio of Lamé constants, (λ/μ)	1.34	1.7±1.2
Poisson's ratio, ν	0.2865	0.32±0.08

Table 2. Cut-off frequencies obtained from the FRF, DFT, and temporal curve fit.

Mode	Cut-off Frequencies, kHz			Difference Between DFT and FRF, Hz	Difference Between Curve Fit and FRF, Hz
	FRF	DFT	Curve Fit		
F(8,1)	43.197	43.332	43.184	135	-13
F(9,1)	53.113	53.331	53.041	218	-72
F(10,1)	63.554	63.307	63.568	-247	14
F(11,1)	74.427	74.969	74.421	542	-6
F(12,1)	85.652	84.965	85.667	-687	15

strain gauge rosettes were bonded to the specimen. Then the instrumented sample was mounted in a standard pseudo-static test frame and loaded in either "pure" tension-compression or torsion. The tension-compression results were used to estimate Young's modulus, E; the torsional test gave the shear modulus, G. These values are also reported in Table 3, along with the independently determined mass density, outer diameter, and wall thickness. It can be seen that E, G, and the dimensional information found from the ultrasonic measurements correlate very well with those obtained pseudo-statically. However, the conventional, unlike the ultrasonic approach, calculates λ, (λ/μ), and ν from the E and G values and standard elasticity relationships whose uncertainties, therefore, are amplified.

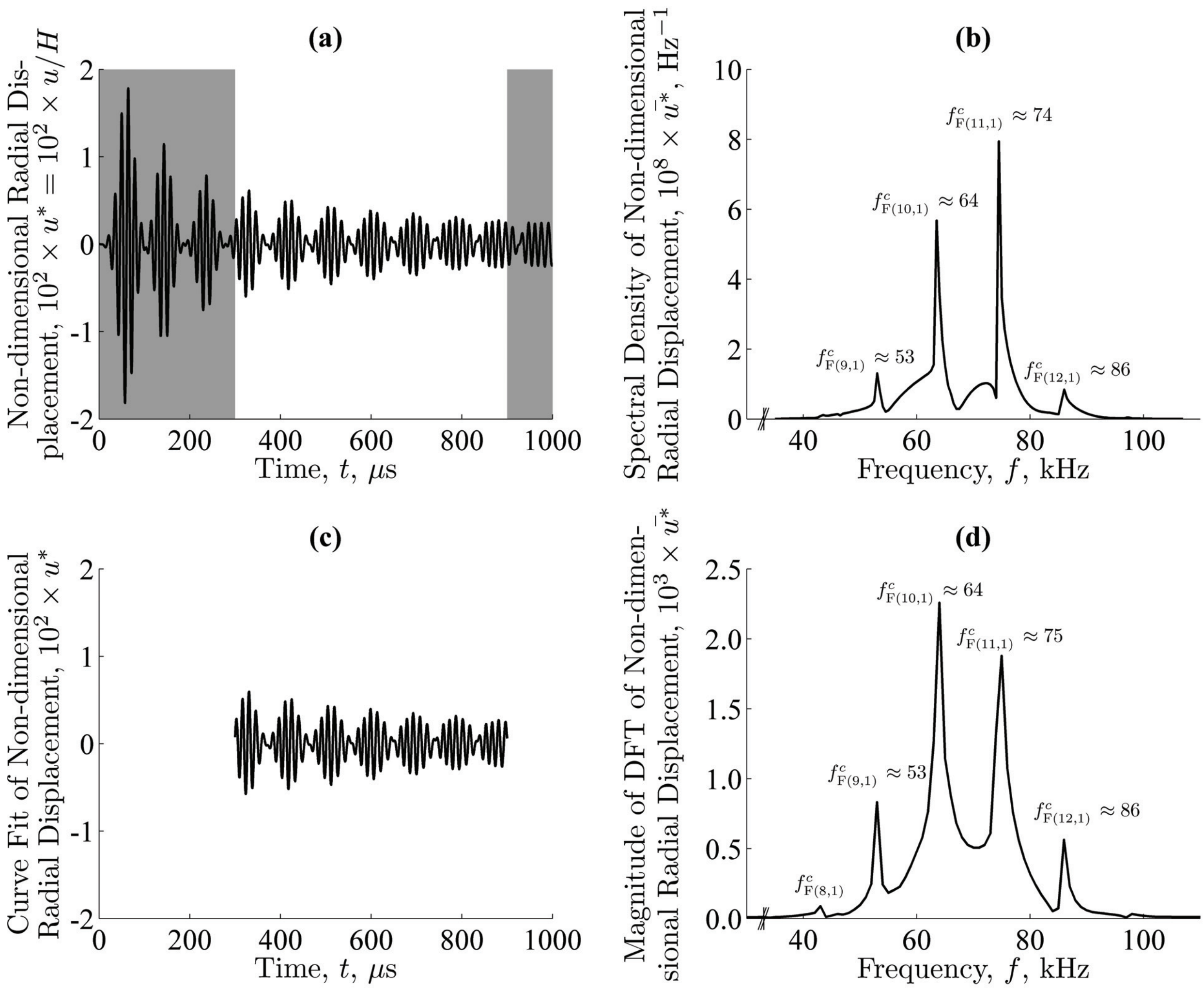

Figure 6. Giving (a) simulated radial displacement on outer surface at θ=0, $z^*=z/H$=5.1, (b) spectral density of (a), (c) curve fit of "free vibration" portion within white region of (a), and (d) DFT of time history shown before right shaded area in (a).

Experimental Example 2

A 3 inch NPS (80 mm DN), Schedule 40, seamless, aluminum pipe was also examined experimentally. The radial displacement was measured on the pipe's outer surface again at θ ≈0 and $z^* = z/H \approx 5.1$. The time history is presented in Figure 8 (a). The DFT corresponding to this time history is given in Figure 8 (c), with the temporal curve fit of the "steady state" portion of the time history shown in Figure 8 (b). The inversion procedure and uncertainty estimations were applied to the cut-off frequencies obtained from this temporal curve fit. Results from the ultrasonic measurements are summarized in Table 4. In this table, the mass density and dimensional information were measured independently. The elastic properties, on the other hand were calculated from "typical" values of *E* and *G* taken from published literature. It can be seen again that *E*, *G*, and the dimensional information found ultrasonically correlate very well with those obtained from the literature. On the other hand, the λ, (λ/μ), and ν recovered ultrasonically are somewhat lower than those derived from the ranges of *E* and *G* typically reported for aluminum. These discrepancies could be due, in part, to the assumption that Poisson's ratio is frequency independent. Experiments

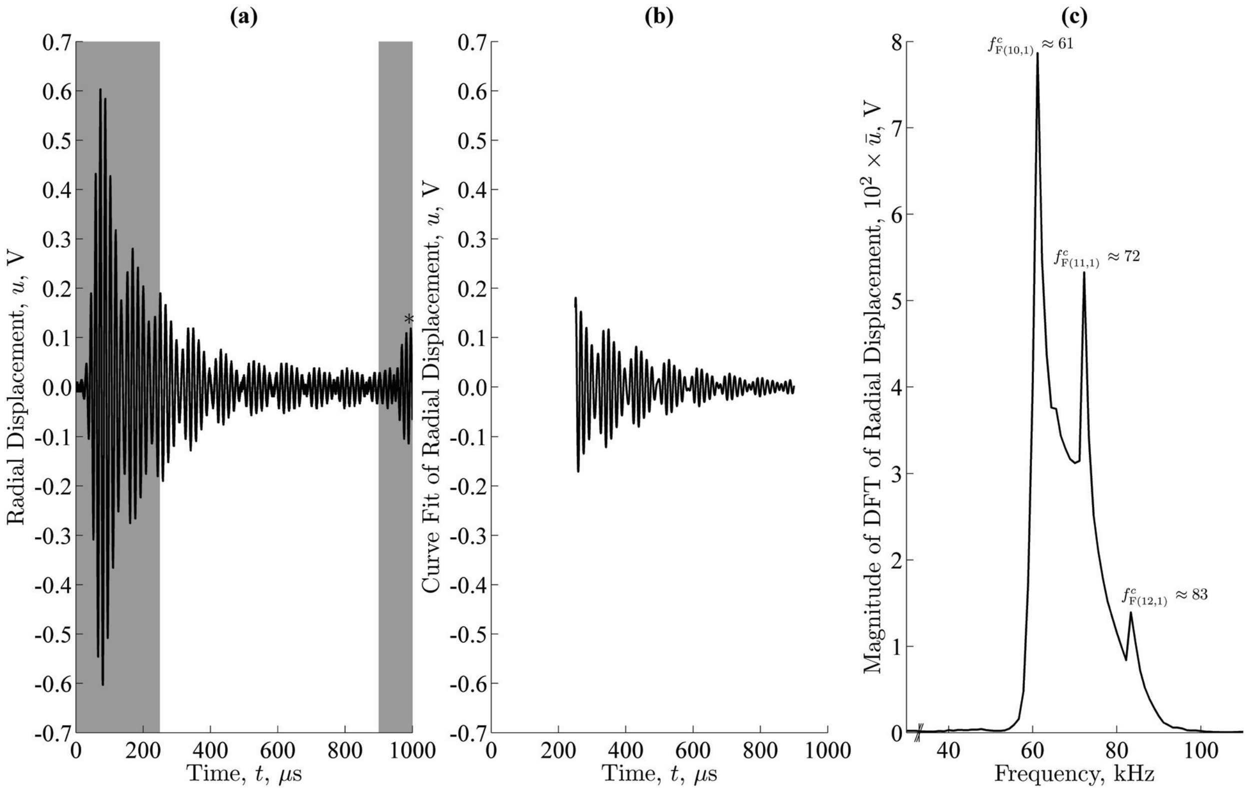

Figure 7. Showing (a) the experimental radial displacement on outer surface at $\theta \approx 0$ and $z^*=z/H\approx 5$ for a steel pipe, (b) temporal curve fit of corresponding "free vibration" portion, and (c) DFT of time history before first end reflection's arrival in (a). *End reflection.

are being planned currently to test the frequency dependance of Poisson's ratio.

Concluding Remarks

An inverse procedure was described that simultaneously estimates a pipe's wall thickness and elastic properties from three non-destructively measured, ultrasonic modal cut-off frequencies when given a known outer diameter and mass density. The procedure returned the uniform, right circular, hollow, homogenous, isotropic pipe that matches "best" the measured cut-off frequencies with an uncertainty estimate. It was illustrated by using a computer-simulated example and two physical experiments. Dimensional and elastic properties generally agreed, within estimated uncertainties, with those assigned in the simulation, measured independently, and with typical data taken from published literature. The uncertainty estimates, although somewhat conservative and yielding uncertainties comparable to conventional measurements, were calculated in a somewhat ad hoc fashion. Plans exist to statistically investigate more formally representative probability density functions for the extracted cut-off frequencies.

Table 3. Comparing conventionally measured values with those recovered ultrasonically for an actual steel pipe.

Property	Conventional Approach	Ultrasonic Approach
Mass density, ρ	$(8.6\pm0.2)\times10^{-3}$ slug/in^3 (7700 ± 200 kg/m^3)	—
Outer diameter, D_0	3.496±0.004 in (88.80±0.09 mm)	—
Thickness, H	0.220±0.004 in (5.6±0.1 mm)	0.22±0.01 in (5.5±0.3 mm)
Mean radius, R	1.638±0.004 in (41.6±0.1 mm)	1.638±0.008 in (41.6±0.2 mm)
Thickness to mean radius ratio, (H/R)	0.134±0.003	0.132±0.007
Young's modulus, E	29 300±900 ksi (202±6 GPa)	29 600±5 400 ksi (204±37 GPa)
Lamé constant (shear modulus), μ (G)	11 500±300 ksi (79±2 GPa)	11 700±13 00 ksi (81±9 GPa)
Lamé constant, λ	14 400±7 800 ksi (99±54 GPa)	12 900±10 300 ksi (89±71 GPa)
Ratio of Lamé constants, (λ/μ)	1.3±0.7	1.1±0.9
Poisson's ratio, ν	0.28±0.07	0.2(7)±0.1

Table 4. Comparing typical values for an aluminum pipe with those measured ultrasonically.

Property	Typical Values	Ultrasonic Approach
Mass density, ρ	$(2.9\pm0.2)\times10^{-3}$ slug/in^3 (2600 ± 200 kg/m^3)	—
Outer diameter, D_0	3.49±0.01 in (88.8±0.3 mm)	—
Thickness, H	0.21±0.01 in (5.5±0.3 mm)	0.22±0.01 in (5.5±0.3 mm)
Mean radius, R	1.641±0.007 in (41.7±0.2 mm)	1.64±0.01 in (41.6±0.3 mm)
Thickness to mean radius ratio, (H/R)	0.131±0.009	0.132±0.008
Young's modulus, E	10 000 – 10 400ksi (69 – 72 GPa)	10 000±1 400 ksi (69±10 GPa)
Lamé constant (shear modulus), μ (G)	3 800 – 3 900 ksi (26 – 27 GPa)	4 000±500 ksi (28±4 GPa)
Lamé constant, λ	4 800 – 13 000 ksi (33 – 87 GPa)	3 900±3 200 ksi (27±22 GPa)
Ratio of Lamé constants, (λ/μ)	1.2 – 3.3	1.0±0.8
Poisson's ratio, ν	0.28 – 0.38	0.2(5)±0.1

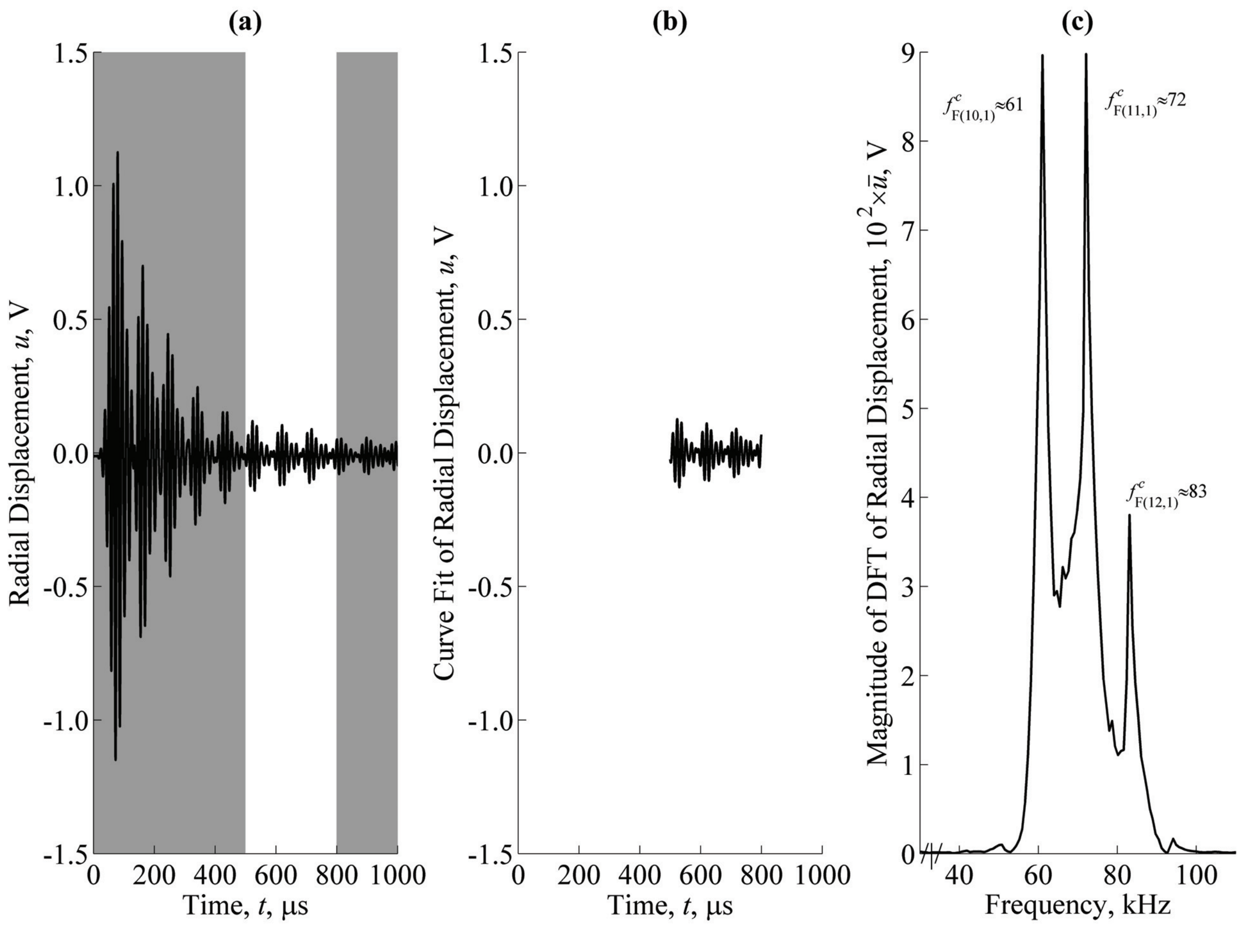

Figure 8. Showing (a) the experimental radial displacement on outer surface at $\theta \approx 0$ and $z^* = z/H \approx 5.1$ for an aluminum pipe, (b) temporal curve fit of corresponding "free vibration" portion, and (c) DFT of time history shown in (a).

Acknowledgements

All three authors acknowledge the financial support from the Natural Science and Engineering Research Council (NSERC) of Canada. The first author also wishes to acknowledge financial aid from the Society of Automotive Engineers (SAE) International, University of Manitoba, Province of Manitoba, Ms. A. Toporeck, and the University of Manitoba Students' Union (UMSU). The assistance of Messrs. B. Forzley, I. Penner, D. Rossong, V. Stoyko and Dr. S. Balakrishnan with preparation of the experimental sample is much appreciated. Recognition is given to Dr. M. Singh and Mr. A. Komus for the use and help with the load frame.

References

[1] J. Krautkrämer and H. Krautkrämer, *Ultrasonic testing of materials, Second Edition*, Springer-Verlag, Berlin, 1977.

[2] D. N. Alleyne and P. Cawley, "Excitation of Lamb Waves in Pipes Using Dry-coupled Piezoelectric Transducers," *Journal of Nondestructive Evaluation*, Volume 15, pages 11 – 20, 1996.

[3] D. N. Alleyne, M. J. S. Lowe, and P. Cawley, "Reflection of Guided Waves from Circumferential Notches in Pipes," *Journal of Applied Mechanics, Transactions of the ASME*, Volume 65, Number 3, pages 635 – 641, 1998.

[4] M. J. S. Lowe, D. N. Alleyne, and P. Cawley, "Mode Conversion of a Guided Wave by a Part-Circumferential Notch in a Pipe," *Journal of Applied Mechanics, Transactions of the ASME*, Volume 65, Number 3, pages 649 – 656, 1998.

[5] D. N. Alleyne, B. Pavlakovic, M. J. S. Lowe, and P. Cawley, "Rapid, long range inspection of chemical plant pipework using guided waves," in *Review of Progress in Quantitative Nondestructive Evaluation*, Volume 20, pages 180 – 187, edited by D. O. Thompson, D. E. Chimenti, and L. Poore, American Institute of Physics, Melville, New York, United States of America, 2001.

[6] J. L. Rose and M. J. Quarry, *Feasibility of Ultrasonic Guided Waves for Non-Destructive Evaluation of Gas Pipelines*, Gas Research Institute, Chicago, Illinois, United States of America, 1999.

[7] T. R. Hay and J. L.Rose "Flexible PVDF comb transducers for excitation of axisymmetric guided waves in pipe" *Sensors and Actuators A (Physical)*, Volume A100, Issue 1, pages 18 – 23, 2002.

[8] J. Mu, L. Zhang, and J. L. Rose, "Defect circumferential sizing by using long range ultrasonic guided wave focusing techniques in pipe," *Nondestructive Testing and Evaluation*, Volume 22, Issue n 4, pages 239 – 253, 2007.

[9] N. Rattanawangcharoen, *Propagation and Scattering of Elastic Waves in Laminated Circular Cylinders*, Ph.D. Thesis, University of Manitoba, 1993.

[10] Alberta Energy and Utilities Board. *Pipeline Performance in Alberta 1980 – 1997*. Alberta Energy and Utilities Board, Calgary, Alberta, Canada,1998.

[11] G. R. Liu and X. Han, *Computational Inverse Techniques in Nondestructive Evaluation*, CRC Press, Boca Raton, Florida, United States of America, 2003.

[12] W. Zhuang, A. H. Shah, and S. B. Dong, "Elastodynamic Green's Function for Laminated Anisotropic Circular Cylinders," *Journal of Applied Mechanics*, Volume 66, pages 665 – 674, 1999.

[13] D. K. Stoyko, N. Popplewell, and A. H. Shah, "Ultrasonic Measurement of Dimensional and Material Properties," in *Review of Progress in Quantitative Nondestructive Evaluation: 35th Annual Review of Progress in Quantitative Nondestructive Evaluation*, edited by D. O. Thompson and D. E. Chimenti, American Institute of Physics, Melville, New York, United States of America, 2009.

[14] D. C. Gazis, "Three-Dimensional Investigation of Propagation of Waves in Hollow Circular Cylinders," *Journal of the Acoustical Society of America*, Volume 31, Number 5, pages 568 – 578, 1959.

[15] C. L. Phillips and J. M. Parr *Signals, Systems, and Transforms. Second Edition*, Prentice-Hall, Incorporated, Upper Saddle River, New Jersey, United States of America, 1999.

[16] J. H. Wilkinson, *The Algebraic Eigenvalue Problem*, Oxford University Press, Oxford, England, 1965.

[17] D. K. Stoyko, N. Popplewell, and A. H. Shah, "Modal Analysis of Transient Ultrasonic Guided Waves in a Cylinder," in *Computational Mechanics Proceedings of ISCM 2007*, edited by Z. H. Yao and M. W. Yuan, Tsinghua University Press and Springer, Beijing, China, 2007, Abstract page 411, Full manuscript (pages 1215 – 1225) on accompanying CD-ROM, 211_FP-136-PopplewellN.pdf.

[18] D. K. Stoyko, N. Popplewell, and A. H. Shah, "Feasibility of Finding Properties of Homogeneous, Isotropic Pipes Using Nondestructive Guided Waves," in *Proceedings of the 7th European Conference on Structural Dynamics*, edited by M. J. Brennan, Institute of Sound and Vibration Research, Southampton, United Kingdom, 2008, Abstract page 29, Full manuscript on accompanying CD-ROM, E152.pdf.
[19] N. Moiseuev and S. Friedland, "Association of Resonance States with the Incomplete Spectrum of Finite Complex-scaled Hamiltonian Matrices," *Physical Review A*, Volume 22, pages 618 – 624, 1980.
[20] E. Buckingham, "On Physically Similar Systems: Illustrations of the Use of Dimensional Equations," *Physical Review*, Volume 4, pages 345 – 376, 1914.
[21] M. G. Silk and K. F. Bainton, "Propagation in Metal Tubing of Ultrasonic Wave Modes Equivalent to Lamb Waves," *Ultrasonics*, Volume 17, pages 11 – 19, 1979.
[22] The Mathworks, Incorporated, *Genetic Algorithm and Direct Search Toolbox™ 2 User's Guide*, The Mathworks, Incorporated, Natick, Massachusetts, United States of America, 2008, http://www.mathworks.com/products/gads/technicalliterature.html.
[23] J. P. Holman, *Experimental Methods for Engineers, Second Edition*, McGraw-Hill, Incorporated, New York, New York, United States of America, 1971.

High Temperature Flexible Ultrasonic Transducers for NDT of Pipes

M. Kobayashi[1], J.-L. Shih[2], K.-T. Wu[2], C.-K. Jen[1] and J.F. Bussiere[1]

1. Industrial Materials Institute, National Research Council Canada, 75 Blvd de Mortagne, Boucherville, Quebec J4B 6Y4, Canada
2. Department of Electrical and Computer Engineering, McGill University, 3480 University St., Montreal, Quebec H3A 2A7, Canada

Abstract

NDT of power, chemical and petroleum plants is an increasingly important element for safety improvement and extension of plant life span. Such plants contain numerous tubular structures and to obtain ultrasonic signals with sufficient signal-to-noise ratio (SNR), ultrasonic transducers (UTs) often need to conform to these structures and operate at elevated temperatures. Flexible UTs are suitable under such conditions and adaptable to different tube diameters because they ensure good self-alignment with the object's surface and a uniform couplant thickness. This results in good transmission of ultrasonic energy into the component and reduced noise.

In this study flexible UTs, consisting of piezoelectric films with thicknesses larger than 40 µm deposited on a 75 µm thick metal membrane, were developed for NDT applications up to 500°C. The piezoelectric films were made by a sol-gel spray technique and can be used for NDT of pipes of diameters larger than 25.4 mm. At room temperature the ultrasonic performances of flexible UTs were at least as good as commercially available 5 MHz and 10 MHz broadband UTs. At elevated temperatures accurate pipe thickness measurements were achieved because of the high SNR of the ultrasonic echoes obtained in the pulse-echo mode. For continuous NDT, an induction brazing technique which can be performed on-NDT-site was developed to braze flexible UTs to steel pipes. The brazing material serves as a high temperature ultrasonic couplant. Finally, the development of high temperature flexible UT arrays for NDT will be discussed.

CR and DR Inspection Capabilities

Barrie DeLong

Abstract not available at time of printing.

NDT in Canada 2009 Conference.

ECI of Gas Turbine Aircraft Engines

S. Roberge, Ing. Pratt & Whitney Canada

Eddy Current Inspection (ECI) continues to play an important role for the inspection of gas turbine aircraft engine components in both manufacturing and field / on-wing environments. At Pratt& Whitney Canada (P&WC) a limited number of rotors are subjected to a semi-automated ECI in manufacturing to meeting the engineering requirements with respect to critical flaw size. Some of these inspections have been validated by performing Probability of Detection (POD) studies. For the field / on-wing inspections required by a service bulletin these tend to be manual in nature and again some are validated by POD. This ECI paper will describe the eddy current equipment used for manufacturing & field / on-wing inspections at P&WC and provide details on number inspection applications.

Laser ultrasonics for NDE in the automotive industry

A. Blouin, D. Lévesque, S. E. Kruger and J.-P. Monchalin

Industrial Materials Institute, National Research Council of Canada
75 de Mortagne blvd, Boucherville, Quebec, Canada, J4B 6Y4
Phone: (450) 641-5112, Fax: (450) 641-5106, e-mail: alain.blouin@cnrc-nrc.gc.ca

Laser ultrasonics, which uses lasers for the generation and detection of ultrasound is now a mature nondestructive technique for evaluation of materials and structures. This technique works at a distance, without surface preparation, and is then specially adapted to inspect moving and hot parts of complex geometrical shapes. Applications of laser ultrasonics to the automotive industry have been rarely reported, and this paper is aimed to present some applications developed at the Industrial Materials Institute of the National Research Council of Canada. A first application is the evaluation of weld integrity. Welds produced by different methods such as laser stitches, spot welding, friction stir welding as well as conventional MIG welding were tested by the technique, and some examples are presented. A second application that has been explored is the evaluation of the magnesium/aluminum interface of a novel engine crankcase casting, in which delaminated and well bonded zones were clearly separated in the laser-ultrasonic images. A third application is the measurement of paint thickness, not only when it is dried but also following application when it is still wet. For this application, thickness can be obtained following a spectroscopic analysis of the laser-ultrasonic data. Finally, adhesive bonding is a new trend in the automotive industry and results are presented on the assessment of bond strength.

Evaluation of Selective Phase Corrosion Thickness on Nickel Aluminum Bronze Valves using Transient Eddy Current

T.W. Krause, Prof., D. Harlley, V.K. Babbar, Dr. and K. Wannamaker
Department of Physics, Royal Military College of Canada, Kingston, ON, K7K 7B4

ABSTRACT

Nickel Aluminum Bronze (NAB) is a material with marine environment applications. Under certain conditions the material can undergo selective phase corrosion (SPC), which involves the removal of particular elements resulting in a loss of material strength. Additional changes in material properties include a change in conductivity and permeability in comparison with the parent material. Transient eddy current (TEC) was evaluated for determination of SPC thickness on a NAB valve section with access from the surface corroded side. TEC signal characteristics were correlated with SPC thickness variations, observed along the sample's edge and averaged over 5 mm, the estimated sensing diameter of the probe. A primarily linear response of TEC amplitude, up to the maximum available SPC thickness of 4 mm, was observed for a 20 mm thick valve wall. Variability in observed TEC signal response was attributed to SPC thickness variations on surface length scales less than 5 mm and the anticipated limits to depth-of-penetration of the sensing field. Elemental analysis, using scanning electron microscopy of corroded and non-corroded regions of NAB showed a reduction in elemental Fe and Ni within the corroded phase, suggesting a corresponding reduction in magnetic permeability would occur. Conductivity was also lower by 77% relative to the base NAB material. The combination of reduced conductivity and permeability was used to explain the observed sensitivity of TEC to SPC thickness variations.

INTRODUCTION

This paper describes the development of a transient eddy current (TEC) probe configuration that is sensitive to changes in depth of selective phase corrosion (SPC) on Nickel-Aluminum-Bronze (NAB) valves as measured from the corroded surface. A previous preliminary evaluation of TEC on the same valve sample at selected locations with and without SPC was conducted by Mandache and Brothers [1]. The sample was later sectioned and measurements of the thickness of SPC at these locations were performed [2]. TEC demonstrated an ability to distinguish between SPC and the base NAB material, but did not show a clear trend in signal characteristics with varying thickness [1,2].

The penetration of transient magnetic fields into multiple layers of conducting aluminum plates has been investigated for aerospace applications with consideration of the driving coil design [3,4]. The ability to detect a hole with 5 mm diameter and 0.4 mm depth at the bottom of a stack of 2024 T3 aluminum plates of total thickness 3.3 mm has been demonstrated using the peak differential signal amplitude [3]. In addition, the application of a standard deviation analysis combined with higher driving voltages, resulted in detection of the hole at the bottom of a plate stack with thickness of 5.5 mm [4]. The conductivity of the 2024 T3 aluminum is 34% of the International Annealed Copper Standard (IACS), as compared with the 6% IACS for the corroded phase of the NAB as measured using a conventional eddy current system [1]. The reduced conductivity of SPC compared with 2024 T3 aluminum suggests that greater depth of penetration may be achieved. However, the presence of elemental iron and nickel, resulting in a finite magnetic permeability within the base and corroded material may also be a factor in the characterization of SPC depth.

Various TEC probes developed here were tested on one of the sectioned samples of the study described in [1] above. This sample demonstrated varying SPC thickness between 0 and 4 mm as observed along the sample's edge. Measurements on this sample were used to identify the TEC probe configuration with signal characteristics that could be most directly correlated to SPC thickness variations to the greatest possible depth.

THEORY

The key factor for measurement of SPC thickness from the corrosion side of the sample is the penetration of the electromagnetic sensing field through the SPC to the higher permeability parent NAB material. Models that consider circuit time constants and characteristic time for diffusion of the electromagnetic field have been used to describe the probe response as a function of plate thickness in the thin plate limit [5]. In this study, transient eddy current response under conditions of varying SPC thickness for several different probe designs, characterized by varying inductance, resistance, length and diameter were investigated.

The combined TEC driving and pick-up coil circuit may be characterized by its equivalent circuit transient response [3]. Considering only the drive coil circuit in isolation (equivalent to a simple LR circuit), the transient current through the driving (primary) coil can be obtained as [6]:

$$i_1(t) = \frac{V_0}{R_1}(1 - e^{-\left(R_1/L_1\right)t}) \ , \tag{1}$$

where V_0 is the voltage applied at time, t=0, R_1 is the total resistance of the driver circuit and L_1 is the driving circuit inductance. For a driving coil relatively unaffected by the pick-up coil circuit a time constant for the driving circuit may be taken as [6]:

$$\tau_C = L_1/R_1 \ . \tag{2}$$

Equation 2 may be used to obtain an estimate of the effective depth of penetration of the exciting field, using the time constant of the circuit in the form [5]:

$$\delta = \sqrt{\frac{\tau_C}{\mu\sigma}}, \tag{3}$$

where μ is the permeability of the material, and σ is the conductivity. This result is similar to the skin depth expression obtained under steady state excitation conditions [6,7], but with τ_c replaced by $1/(\pi f)$, where f is the steady state excitation frequency in Hz. Note that this result will be affected by probe parameters such as length and diameter of the driving coil relative to skin depth and conductor thickness, and magnitude of the applied field [3,4].

Equation 3 only addresses the initial penetration of the electromagnetic field into the material. A following stage is that of the decay of induced surface currents accompanied by the full penetration of fields into the material [8]. In this case an additional relaxation time must be considered and is given as:

$$\tau_D = \mu\,\sigma\,\ell^{\,2}, \tag{4}$$

where τ_D is the characteristic diffusion time and $\boldsymbol{\ell}$ is a characteristic length for the system. Note that $\boldsymbol{\ell}$ is dependent on the geometry of the conductor and measurement configuration.

METALLOGRAPY INVESTIGATION

Figure 1 shows the quarter NAB valve sample used for evaluation of inspection techniques in reference [1]. Dashed curves indicate where the sample was cut in order to destructively obtain SPC thicknesses at locations 2, 4, 5, 6 and 7 as indicated by the white arrows. Locations 1, 3 and 8 were exposed areas of parent NAB without SPC. The black arrow indicates the edge along the section where measurements were performed for evaluation of TEC in this study. Cut sections are labeled from A to G for ease of reference in the text.

Characterization of a number of metallurgical properties of the NAB material was conducted, since these can have a bearing on information obtained by TEC. Scanning Electron Microscope (SEM) examination was conducted on a removed section labeled B in Figure 1, containing markers 6, 7 and 8. At locations 6 and 7 the SPC thickness varied between 2 and 3 mm [2]. A thin layer of the original material was removed from the sample by progressively sanding it using 240, 320, 400 and 600 grit sandpaper, followed by a 6 μm diamond polish and finally, alumina 0.05 micron (Gamma Micropolish II).

Figures 2 and 3 show the SEM examination of sample B with 20 μm scale from sections representative of the parent NAB material and that affected by SPC in the proximity of the sample edge, respectively. In Figure 2 granular structure of non-corroded NAB is evident. Figure 3, taken within the SPC region, shows the formation of channels perpendicular to the sample surface, towards the top of the image. These channels appear to arise between grains and presumably facilitate removal of minority elements as will be examined more closely using the elemental analysis described below.

A sample with 1 mm x 1 mm cross section was sectioned from the bulk SPC phase from Sample B and fractured along one of the channel regions identified in Figure 3. Figures 4(a) shows the SEM examination of this sample at a 200 μm scale. Figure 4(b) shows the same face at a 20 μm scale, corresponding to the scales shown in Figures 2 and 3. A corroded and far less dense matrix is evident, characteristic of the entire fracture face.

An elemental analysis of the sample labeled B in Figure 1 was performed using a SEM and Energy Dispersive Analysis X-Ray (EDAX) system set at 50 μm magnification. Table 1 shows results of elemental analysis performed at eight different locations on each of the base NAB, bulk SPC phase and SPC fracture face obtained from Sample B. Results show the average weight percentage content of each detected element along with the standard deviation from the average. In going from the base NAB material to the corroded SPC phase and finally the fracture face, trends in the relative decrease of minority elements with a corresponding increase in percentage copper are observed. For example, Al shows a steady decrease from 11% in base NAB to 9% in bulk SPC and finally to 5% on the depleted face. More significantly, with regards to its potential effect on magnetic permeability, depletion of Fe and Ni is proportionally the most significant from 5 and 6% in the base material, to 3 and 4 % in the bulk SPC, and 1 and 2%, on the fracture face, respectively. Weight percent of Cu increases from 76% in base NAB, to 82% in bulk SPC and to 91% on the fracture face, reflecting that elemental Cu remains in the material matrix. The proportion of Mn, which has the smallest initial proportion of the identified elements, remains effectively unchanged.

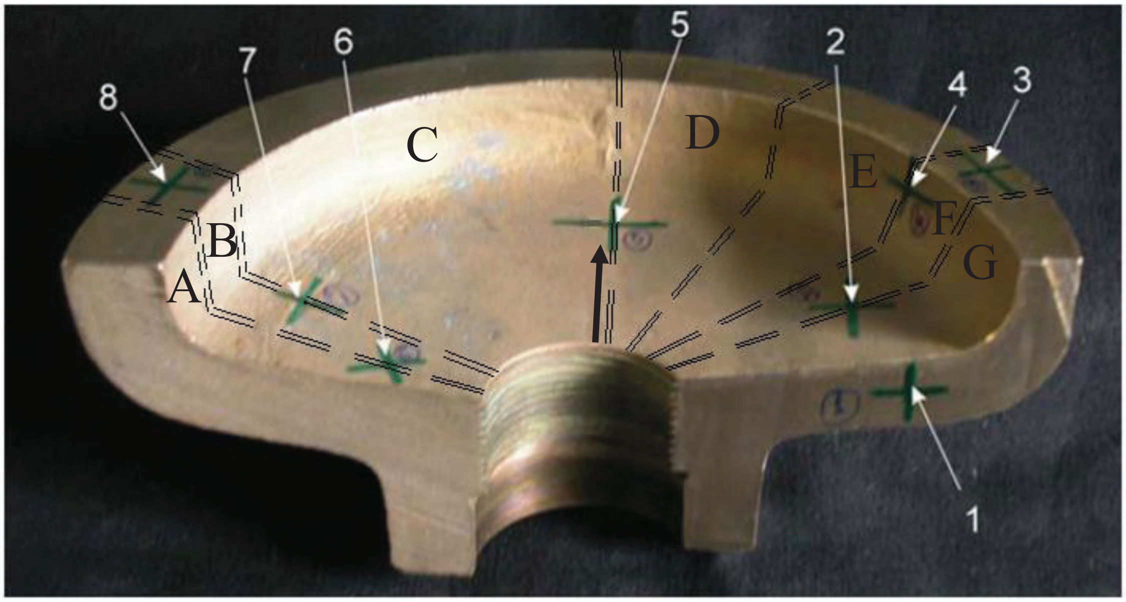

Figure #1: NAB quarter valve sample. Dashed lines indicate where valve was sectioned. The black arrow, towards location 5, is along edge where TEC measurements were performed.

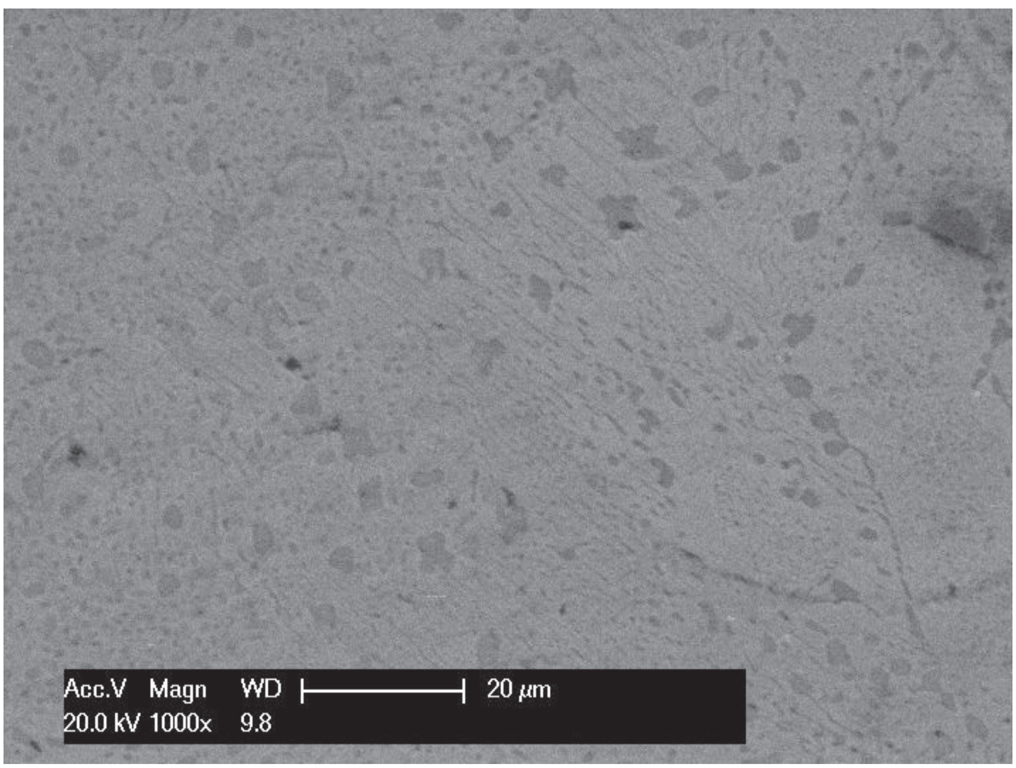

Figure #2: SEM image of central region of non-corroded NAB sample B.

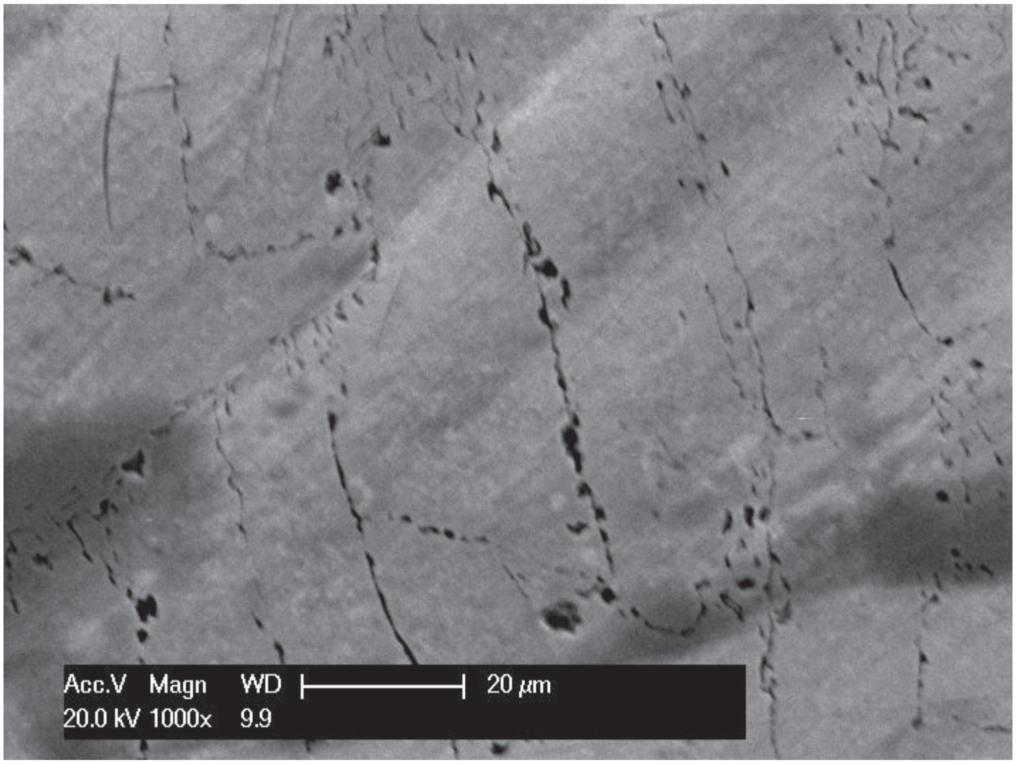

Figure #3: SEM image in the selective phase corroded region of sample B.

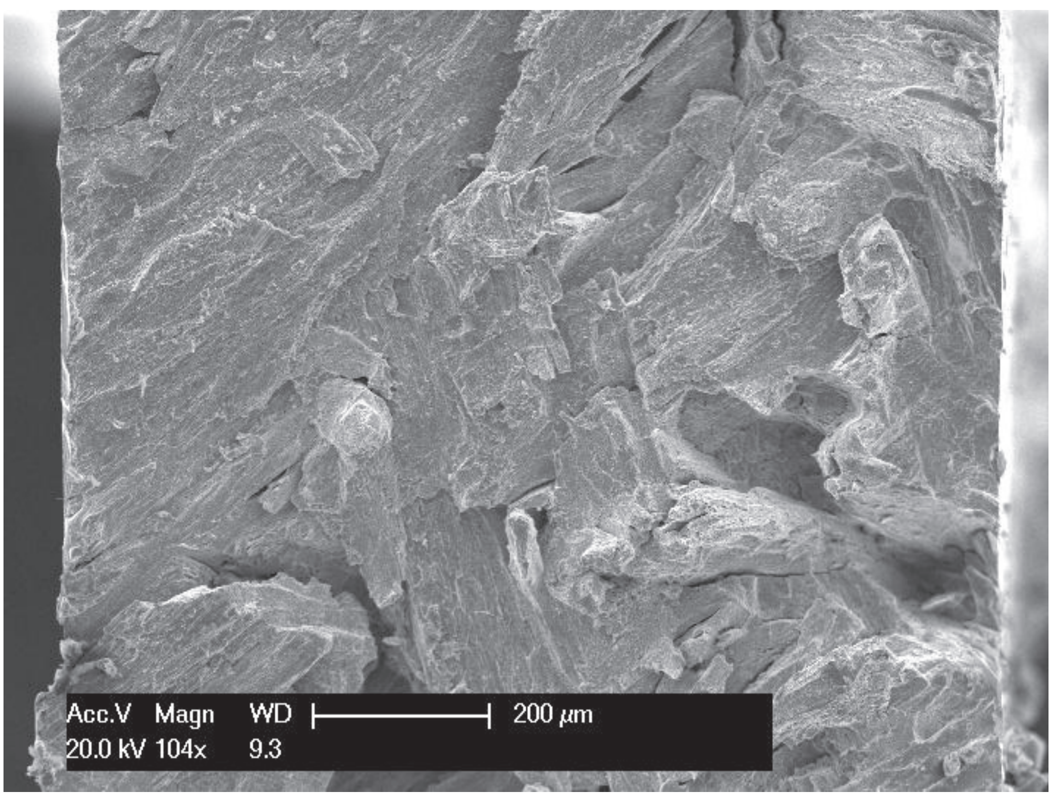

Figure #4(a): SEM image of fracture face in bulk SPC.

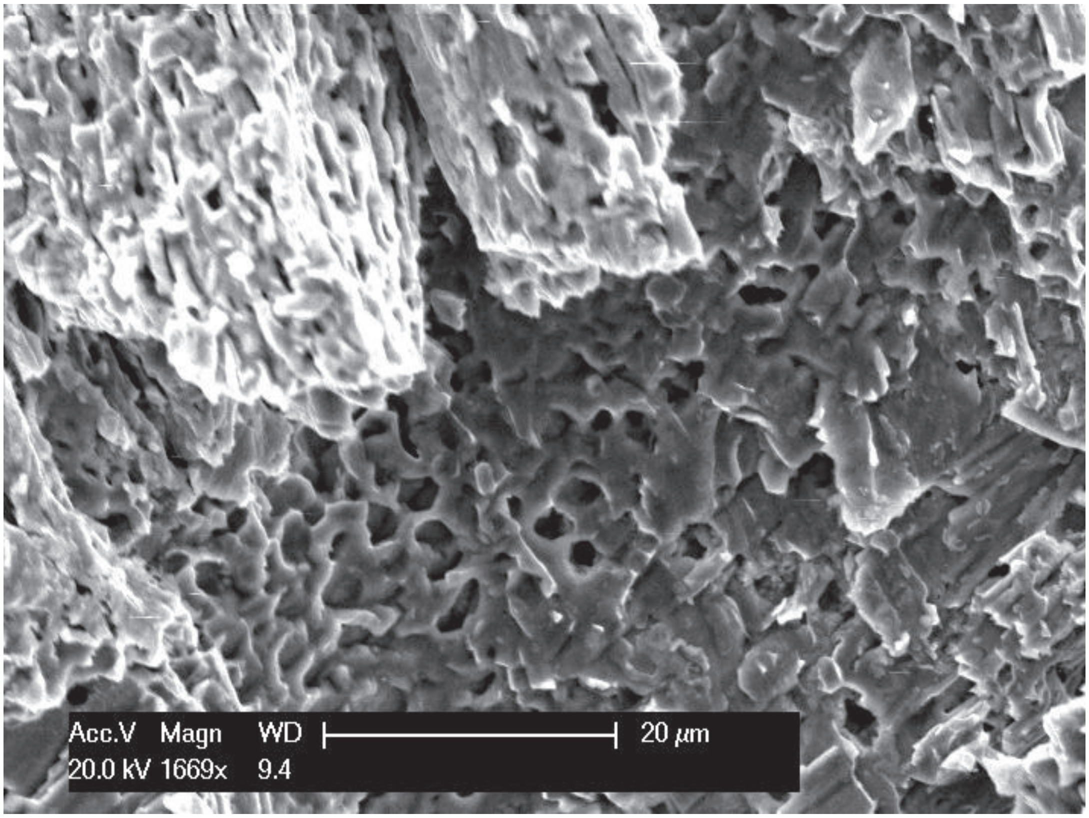

Figure #4(b): SEM image of local region of fracture face in bulk SPC at 20 μm scale.

Table #1: Percentage (%) weight of elements in base NAB, bulk SPC, and on SPC fracture face. Average of 8 measurements at different locations in each phase with one standard deviation from the average is shown.

	Weight ± standard deviation (%)				
Analyzed material	Al	Cu	Fe	Ni	Mn
Base NAB	10.9±0.4	76.3±0.9	5.0±0.3	6.4±0.4	1.4±0.1
Bulk SPC	9.4±0.9	82±1	3.4±0.7	4.2±0.5	1.3±0.1
SPC Fracture	5±1	91±2	1.1±0.1	2.1±0.2	1.1±0.2

Table #2: Dimensions and measured conductivity of base NAB and bulk SPC samples.

Sample	Area (mm^2)	Length (mm)	σ (S/m)	σ (%IACS)
Base NAB	70.09	19.63	4.61×10^6	7.9
Bulk SPC	1.30	10.04	3.53×10^6	6.1

CONDUCTIVITY OF BULK NAB AND SPC PHASES

Standard four-point direct current (DC) measurements were conducted on the bulk NAB and SPC phases of smaller longitudinal samples sectioned from sample B in order to measure conductivity. Measurements were performed using a Keithley 6221 DC and AC current source and Keithley 181 Nanovoltmeter. The DC measurement method was selected over the conventional eddy current method due to a relative permeability greater than one in the base NAB material. Dimensions for the two specimens along with the accompanying measured conductivities are listed in Table 2. The value of 6.1% IACS for the SPC phase is consistent with conductivity obtained using a conventional eddy current device as reported previously for the SPC phase of this material [1]. The bulk NAB conductivity result of 7.9% IACS is consistent with published values reported for this elemental range in NAB. See for example, NAB Alloy C63020 with composition 10.5% Al, 5% Ni and 4.8% Fe, which has reported conductivity in the range of 6 to 8.2 % IACS [9]. Note that the bulk SPC has a conductivity that is 77% of the conductivity of the base NAB material.

SPC THICKNESS MEASUREMENT

The NAB section labeled C in Figure 1 was selected for evaluation of TEC sensitivity to SPC thickness, since the right hand edge showed a significant 0 to 4 mm variation of SPC thickness in areas away from the threaded region (>5 mm). Polishing and application of Silver Nitrate (10% $AgNO_3$) solution on the edge of the sample was performed in order to obtain visible variation in SPC thickness. Figure 5 shows measured SPC thickness as a function of distance from the threaded end along the sample C's right hand edge. The estimated position of location 5 as identified in Figure 1 is indicated. Variation in SPC thickness is between 4.8 mm at the 2.5 mm position and 0 at the 44 mm position. Rapid changes in SPC thickness over short surface extent (1 mm of change in SPC thickness over 5 mm of sample surface) are observed at a number of locations.

Features relevant to TEC measurements include a 4 mm SPC thickness at 5 mm from the origin, a relatively flat region between 15 and 22.5 mm with 3.4 mm thickness and a variable and rapid decrease to 0 mm thickness at 44 mm from the threaded edge. The rate of decrease here is the steepest at 0.3 mm of SPC thickness over 6 mm of distance along the edge. The right hand edge was selected for evaluation of TEC sensitivity to SPC thickness.

EXPERMIMENTAL SET-UP

A commercial system was used to acquire the response of the transient eddy current signals. The user interface was TecView, as provided by TecScan Systems Inc. (Montreal). The driving coil voltage was provided by an HP214B Pulse Generator, which allows for driving voltages up to $50\,V$. The wave form sensed by the pickup coil, was obtained from across a 51 Ω termination, and sampled at a rate of 2 MHz over 2 ms.

Probes were mounted against the SPC sample surface at the edge of the sample where the depth of SPC into the parent NAB material was visible. Measurements were initiated at 5 mm from the origin (threaded end in Figure 1), so as not to be affected by the corner geometry, and obtained at a 2.5 mm interval along the sample edge at the locations where SPC thickness is reported in Figure 5. Measurements in air and on the parent NAB material at the previously indicated reference position [2], before and after each set of measurements were performed.

Probe characteristics were further modified with the goal of maximizing depth of penetration. The investigation reported here was performed with four different driving coils of variable length, two different diameters and 800 and 1000 turns. Table 3 shows the dimensions and characteristics of the driving coils along with the two pick-up coils used for the tests. The sensing diameter of the driver/pick-up configuration was estimated as the average of the pick-up coil outer diameter (OD) and the driving coil inner diameter (ID). This resulted in an effective sensing diameter of 5 mm, for each of the probe configurations. This dimension was consistent with the typical scale of the expected NAB thickness variation on the surface of the sample seen on the right hand edge of sample C (Figure 5) and therefore would be expected to provide a more accurate representation of thickness variations than a probe of larger dimensions.

Figure 6 shows the transient voltage obtained from a measurement across a 2 Ω resistor in the driving circuit for the four different probes. A simplified best fit expression for the driving current can be obtained from equations 1 and 2, if the additional loading introduced by the mutual coupling with the pick-up coil circuit is neglected, as [3]:

$$V = A\left(1 - e^{-t/\tau_c}\right) , \quad (5)$$

where A and τ_C are best-fit parameters. Equation 5 provides a good description of the measured voltage as shown by the dashed and solid curves in Figure 6. Table 3 shows the values of τ_C, obtained from a best fit of equation 5 to the primary circuit data. Note that R_1 in equation 2 now includes the internal resistance of the square wave generator and the equivalent resistance of the pick-up coil as seen by the driver. The results show a range of time constants reflecting the variable steepness of curves as shown in Figure 6.

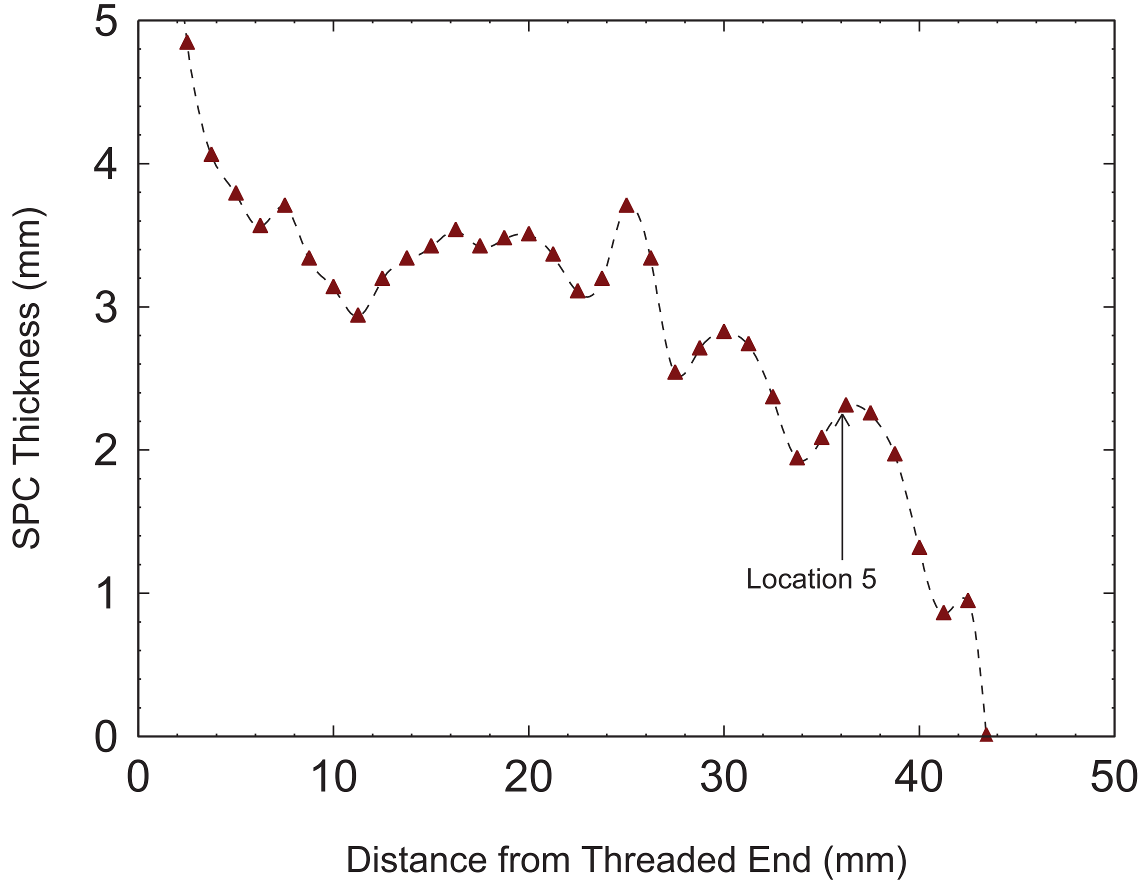

Figure #5: Selective phase corrosion thickness as a function of distance from the threaded end of right hand edge of section C shown in Figure 1. Position of Location 5 is indicated by arrow. Points are measurements and dashed curves is spline through data meant as a guide to the eye.

Table #3: Driving and pick-up coil characteristics.

Coil Serial #	Turns	Length (mm)	Outer Diameter (mm)	Inner Diameter (mm)	L (mH)	R (Ω)	τ_c (μs)
0800G38L20	800	19.8	7.3	6.0	1.26	38.5	14.7
0800G38L25	800	24.6	7.0	6.5	0.99	37.6	—
0800G38L25(2)	800	25.0	6.8	6.0	0.89	35.4	11.1
0800G38L25(3)	800	24.6	6.97	6.5	0.97	37.0	11.8
1000G38L30	1000	29.8	6.9	6.0	1.23	45.1	14.0
NAB Pickup	400	1.0	4.0	1.0	0.72	31.3	—
NAB Pickup #2	400	1.0	4.0	1.0	0.74	28.7	—

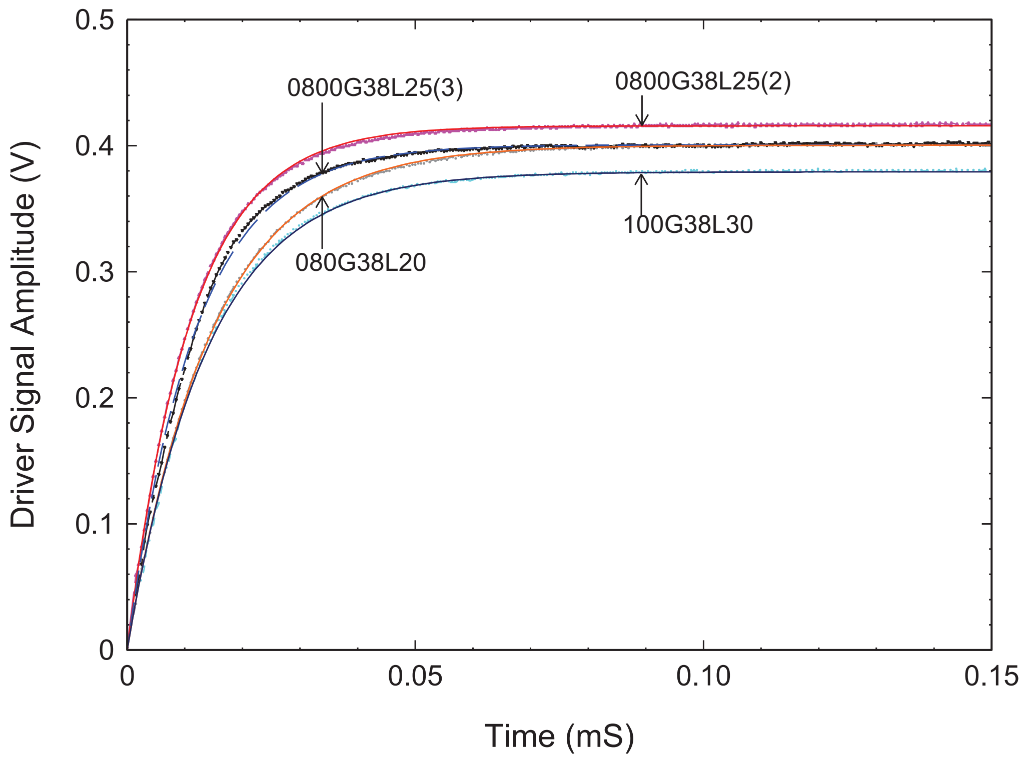

Figure #6: Driving voltage characteristics for four different driving and pick-up coil configurations. Dashed curves are a best fit of equation 5 to the data.

RESULTS

Measurements were performed with each of driving coil at 2.5 mm intervals on the SPC surface on the sample's right hand edge where thickness variation is shown in Figure 5. Results are reported here for the 0800G38L25 driving coil, the properties of which are given in Table 3. Comparable sensitivity to SPC thickness variations were obtained from the 1000G38L30 coil, while the 0800G38L20 produced inferior results. These results suggest that sufficient coil length and/or diameter needs to be present for significant field penetration to occur.

Figure 7 shows the pick-up coil response obtained using this probe configuration in air, on the NAB reference and at the 5 mm location on the right hand edge of sample C. The SPC thickness at this location, averaged over 5 mm is 4.0 mm. Reference subtracted signals are obtained by taking the difference between the signal obtained at the reference position, which is base NAB material, and the signal obtained under conditions of variable SPC. This is a similar procedure to that performed in references [3,4].

Figure 8 shows the reference subtracted waveforms obtained using the 0800G38L25 driver with pick-up coil #2 for various thicknesses along the sample's edge. The wave forms are bimodal with an initial negative voltage component followed by a positive voltage component. The negative voltage peak demonstrates large changes in SPC thickness in the thin SPC limit, but relatively smaller and less uniform changes with increasing thickness. In contrast, the positive voltage peak of the waveforms, which occurs at later times, shows a constant change up to 4.0 mm of measured SPC thickness. This is consistent with the bimodal display observed elsewhere [4] and is associated with the two stage process of initial eddy current penetration described by equation 3, followed by decay at later times as described by equation 4 [8].

Figure 9 shows the peak positive voltage amplitude as a function of SPC thickness. Thickness values were obtained by averaging the measured thicknesses shown in Figure 5 over 5 mm. This was anticipated to partially take into account the corresponding effective 5 mm diameter of the probe sensing area, although this assumes that the SPC thickness observed at the sample's edge extends relatively uniformly into the sample over length scales on the order of 5 mm. The amplitude variation exhibits a general linear trend as demonstrated by the linear best fit to the data. This suggests that sensitivity of the current TEC system up to depths of 4 mm, the maximum thickness investigated here, is possible. That the intercept of the best fit line is not zero is associated with the different wave form of the reference position, which was taken on base NAB material away from the sample's edge.

DISCUSSION

The sensitivity of TEC to SPC thickness variation on base NAB is attributed to the two stage process described by equations 3 and 4 and outlined in reference [8]. First, the response to the abruptly applied field is the generation of eddy currents within the material, which act to expel the electromagnetic field. The generation of these eddy currents is described by the associated skin depth expression, equation 3, which incorporates both the permeability and conductivity of the material. Second, the induced eddy currents decay with a characteristic diffusion time as described by equation 4. Note that the diffusion time is also a function of conductivity and permeability and will also be affected by the material thickness as this may be viewed as a characteristic length ℓ of the material. Since the difference in signal response between the measurements on the SPC phase and the reference NAB material are taken, sensitivity to SPC thickness variation on the NAB is a function of the difference in the conductivity and permeability between the two materials. A difference in conductivity between the bulk SPC and NAB phase was measured, with SPC being 77% that of the NAB phase. Potentially a more significant effect is the reduction in permeability arising from the removal of Fe and Ni in the bulk SPC phase. The relative permeabilities of the phases were not quantified here. Both reduced permeability and conductivity will affect initial penetration depth and diffusion time multiplicatively as their product, $\sigma\mu$, as described by equations 3 and 4, respectively.

As seen in Figure 9 some scatter along the best fit line of the response to SPC thickness is present, particularly at greater thicknesses. Several potential sources of variability are present in the current set of measurements. The primary source is the inferred thickness of the SPC extending into the plane of the sample. Since substantial variations are observed along the edge and differences are observed between edges at the same distance from the threads, some variation is expected even over length scales on the order of the probe sensing area. TEC sensitivity to SPC thickness is also reduced at greater thicknesses [3,4], allowing other sources of variation such as lift-off, probe tilt and the probe's proximity to the sample's edge to have a more significant effect on signal response.

SUMMARY

Transient eddy current was evaluated for the measurement of depth of corrosion on a NAB valve sample. Characteristics of the reference-subtracted TEC signal waveforms were correlated with observed SPC thickness variations along a sectioned sample's edge. SPC thicknesses, averaged over 5 mm along the edge, an extent consistent with the probe's effective sensing diameter, were compared with the positive amplitude of the TEC signal waveforms. Various driving coil designs were tested and the most successful demonstrated sensitivities to SPC thickness up to the maximum available depth of 4 mm. For this probe the response was observed to be primarily linear, suggesting that the maximum sensing depth has not yet been determined.

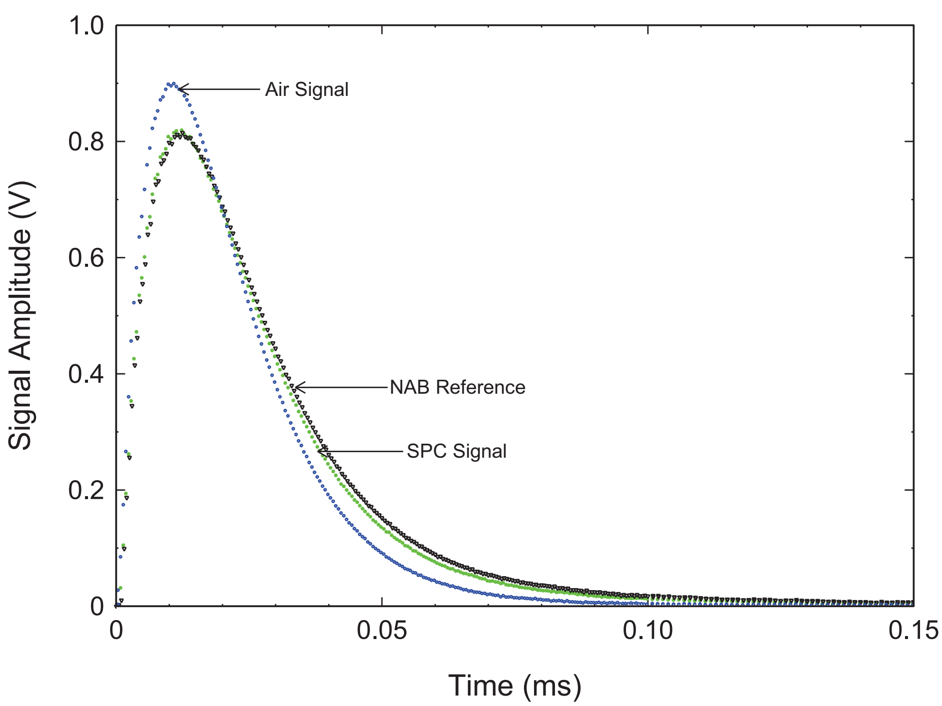

Figure #7: Measured response of pick-up coil to driving coil 0800G38L25 at 20 V in air, on NAB and on SPC with 4.0 mm thickness on NAB.

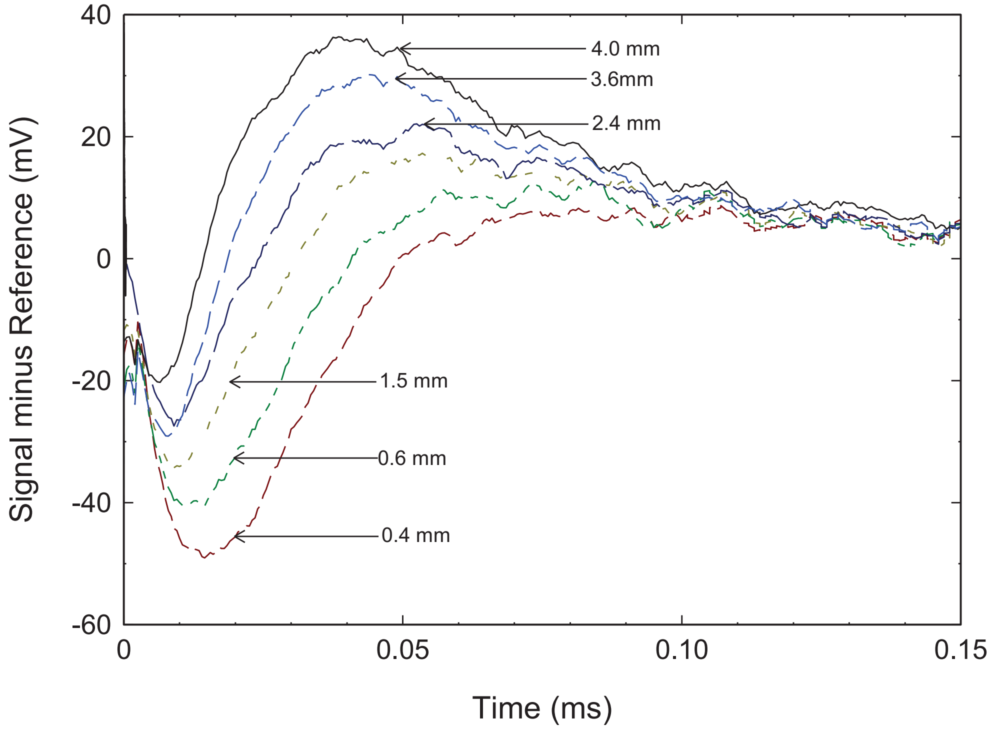

Figure #8: Measured response relative to reference obtained from driving coil 0800G38L25 at 20 V on SPC between 0 and 4 mm thickness on NAB.

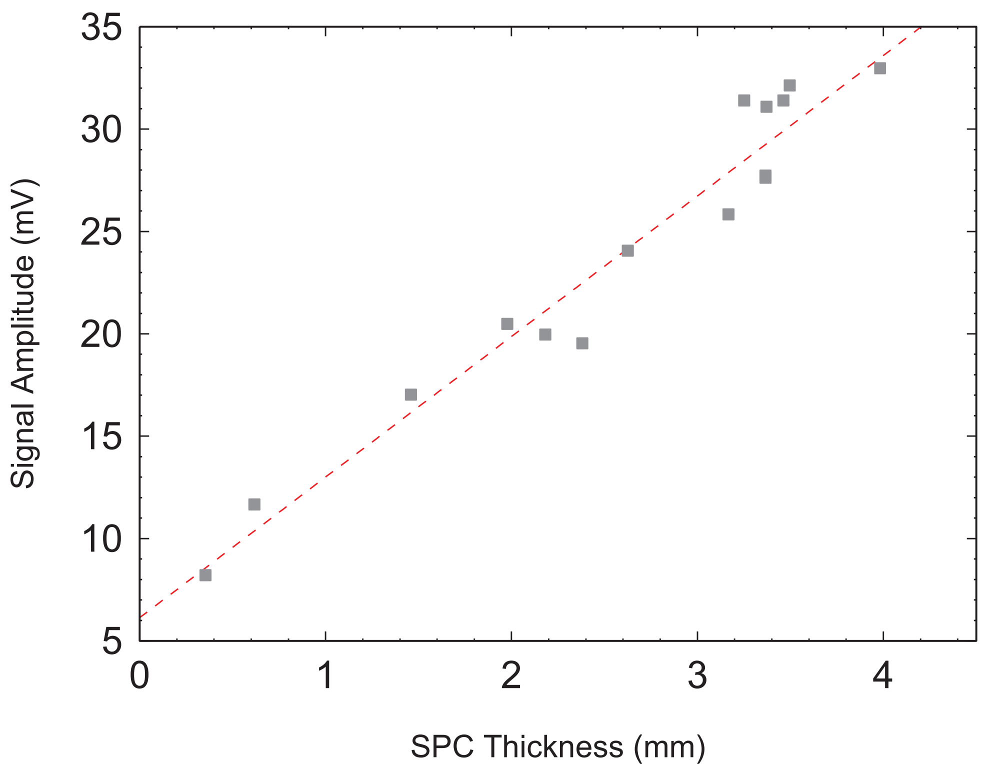

Figure #9: Measured positive amplitude response of reference-subtracted signal from pick-up coil using driving coil 0800G38L25at 20 V between 0 and 4 mm thickness of SPC on NAB. Dashed curve is a linear best fit to the data.

Scanning electron microscopy was used to perform elemental analysis of corroded and non-corroded regions of a NAB sample. SPC in the bulk phase was characterized by a relative weight increase in Cu by 6% and a reduction of Fe and Ni to 3 and 4% from the 5% and 6%, respectively, in the non-corroded NAB. In a region of severe corrosion, exposed by fracture of a smaller SPC sample, Cu was increased by a relative weight of 15% and Fe and Ni were reduced to 1 and 2%, respectively. The reduction in Fe and Ni was expected to reduce the permeability in the SPC phase relative to the non-corroded NAB. Four-point direct current resistance measurements were used to obtain conductivity values of 6.1% IACS for the SPC phase and 7.9% IACS for the bulk NAB. The combination of reduced conductivity and permeability in the SPC phase relative to base NAB was used to explain differences in transient eddy current behavior as a function of thickness along the edge of a sectioned valve sample. Variability in observed signal response was attributed to SPC thickness variations on length scales less than 5 mm, the proximity of the sample edge, and anticipated limits to depth-of-penetration of the sensing field.

Further characterization of NAB permeability in the corroded and un-corroded phase is required as this, combined with the material conductivity, directly affects transient skin depth and relaxation times. Additional work is required to fully develop this technique for in-service inspection, including production of calibration standards, development of inspection procedures and performance demonstration on valves removed from service.

ACKNOWLEDGEMENTS

The first author would like to thank Jennifer Snelgrove and Steve Lockridge for technical assistance and Dr. Pierre Roberge for useful discussions. This work was supported by Defence Research and Development Canada – Atlantic, the Natural Sciences and Engineering Research Council of Canada, and the Academic Research Program at the Royal Military College of Canada.

REFERENCES

1. C. Mandache and M. Brothers, *Overview of Potential Non-Destructive Techniques for Inspection of Nickel Aluminum Bronze Valves,* DRDC-Atlantic Contract Report, CR 20-07-212, September 2007.

2. Y. Wang, Defence R&D Canada – Atlantic, Private Communication.

3. T.J. Cadeau and T.W. Krause, *Pulsed Eddy Current Probe Design Based on Transient Circuit Analysis*, *Review of Progress in Quantitative Nondestructive Evaluation*, Vol. 28 edited by: D.O. Thompson and D.E. Chimenti, Melville, New York (© 2009 American Institute of Physics).

4. T.J. Cadeau, *Increased Field Depth Penetration with Pulsed Eddy Current*, M.Sc. Thesis, Royal Military College of Canada, April 2008.

5. T.W. Krause, C. Mandache, and J.H.V. Lefebvre, *Diffusion of Pulsed Eddy Currents in Thin Conducting Plates*, *Review of Progress in Quantitative Nondestructive Evaluation*, Vol. 27 edited by: D.O. Thompson and D.E. Chimenti, ISBN 978-0-7354-0494-6, Melville, New York (© 2008 American Institute of Physics) pp. 368-375.

6. D.J. Griffiths, *Introduction to Electrodynamics* 3rd Ed. (Prentice-Hall, Upper Saddle River, New Jersey) 1999, p. 315.

7. V.S. Cecco, G. Van Drunen, and F.L. Sharp, *Eddy Current Testing Manual on Eddy Current Method*, Vol. 1, Chalk River Nuclear Laboratories, November 1981.

8. H.C. Ohanian, *On the approach to electro- and magneto-static equilibrium,* Am. J. Phys. **51**, 1020 (1983).

9. Nickel Aluminum Bronze Alloy, Product Data Sheet, Maher Alloys http://www.maher.com/pdf/alloys/4640.pdf. 19/11/08

BIOGRAPHY

Thomas Krause has a Ph.D. in Solid State Physics from McMaster University (1992). He has seventeen years of experience in electromagnetic and ultrasonic nondestructive testing development with Level III CGSB certification in both eddy current and ultrasonic testing. He spent his first four years in NDT in the Applied Magnetics Group at Queen's University (1992-1996), ten years with Nondestructive Testing Development Branch, AECL, and the past three years as faculty at RMC:

Department of Physics,
Royal Military College of Canada,
PO Box 17000, Station Forces,
Kingston, Ontario, Canada K7K 7B4
Tel: 613 541 6000 x 6415, Fax: 613 541 6040
Email: Thomas.krause@rmc.ca

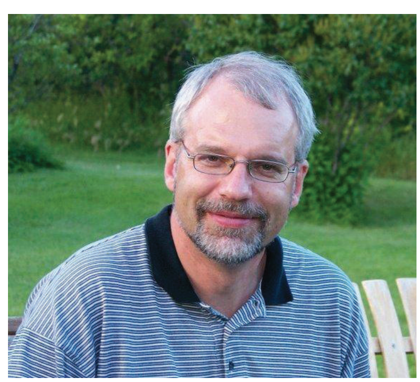

Overview of Steam Generator Tube-Inspection Technology

L. Obrutsky, J. Renaud and R. Lakhan
Atomic Energy of Canada Limited
Chalk River, Ontario, Canada, K0J 1J0
613-584-8811
obrutskl@aecl.ca, renaudj@aecl.ca, lakhanr@aecl.ca

ABSTRACT

Degradation of steam generator (SG) tubing due to both mechanical and corrosion modes has resulted in extensive repairs and replacement of SGs around the world. The variety of degradation modes challenges the integrity of SG tubing and, therefore, the stations' reliability. Inspection and monitoring aimed at timely detection and characterization of the degradation is a key element for ensuring tube integrity.

Up to the early-70's, the in-service inspection of SG tubing was carried out using single-frequency eddy current testing (ET) bobbin coils, which were adequate for the detection of volumetric degradation. By the mid-80's, additional modes of degradation such as pitting, intergranular attack, and axial and circumferential inside or outside diameter stress corrosion cracking had to be addressed. The need for timely, fast detection and characterization of these diverse modes of degradation motivated the development in the 90's of inspection systems based on advanced probe technology coupled with versatile instruments operated by fast computers and remote communication systems.

SG inspection systems have progressed in the new millennium to a much higher level of automation, efficiency and reliability. Also, the role of Non Destructive Evaluation (NDE) has evolved from simple detection tools to diagnostic tools that provide input into integrity assessment decisions, fitness-for-service and operational assessments. This new role was motivated by tighter regulatory requirements to assure the safety of the public and the environment, better SG life management strategies and often self-imposed regulations. It led to the development of advanced probe technologies, more reliable and versatile instruments and robotics, better training and qualification of personnel and better data management and analysis systems.

This paper provides a brief historical perspective regarding the evolution of SG inspections and analyzes the motivations behind that evolution. It presents an overview of regulatory issues, the current scope of SG inspections and inspection technology.

1. Introduction

Steam Generators (SG) are among the most critical components of pressurized water Nuclear Power Plants (NPP). They are large heat exchangers that use the heat generated in the reactor core, and carried by the primary reactor coolant, to make steam in the secondary side with the purpose of driving the turbines for electrical power production. The inside of the tubes carries the primary water coolant, which in turn heats the secondary-side water to produce steam. They constitute the largest surface area in the primary heat transport system. Among many other requirements, SG tubes must provide a reliable pressure boundary between the primary and secondary sides. Also, during normal operation, SGs confine the radioactivity from neutron activation or fission products to the primary side. However, since the primary coolant is at higher pressure than the secondary side, any leakage from tube defects could result in the release of radioactivity to the secondary side and even to the environment in the case of tube failure [1,2].

A variety of degradation modes challenge the integrity of the SG tubing and therefore the stations' reliability, capacity factor and cost effectiveness. Some of these modes generate volumetric material loss due to fretting wear, pitting corrosion, wastage or flow accelerated corrosion (FAC); other modes have directional properties due to intergranular attack (IGA), axial or circumferential outside diameter (OD) stress corrosion cracking (SCC), and primary water (PW) SCC. One of the key life management components for ensuring tube integrity, and thus protecting the safety of the public and the environment while maintaining cost effective operation of NPP, is inspection and monitoring aimed at timely detection and characterization of the degradation.

SG inspections can be very complex and costly operations. Inspection scope, data acquisition equipment, remote manipulators, probe drives, probe technology, data storage devices, data analysis software, data analysis methods and guidelines, personnel training and qualification, data transmission, data management, tube integrity issues, personnel radiation protection issues, need for tube plugging and their effect in the overall cost of inspections and maintenance are all elements that need to be taken into account when planning SG inspections.

In this paper we will provide a brief historical perspective regarding the evolution of SG inspections and analyse the motivations behind that evolution. We will present an overview of regulatory issues and the current scope of SG inspections and inspection technology.

2. Historical Perspective

In the late-70's and early-80's, in-service inspections of SG tubing were carried out using eddy current testing (ET) bobbin probes connected to analog single-frequency instruments, which rely on storage-type cathode ray tubes to display the EC data. In turn, the data were recorded using two-channel strip-chart recorders and analogue tape recorders and often analysed in real time or, alternatively, offline by a very slow process of reviewing the strip charts and replaying the tapes. The results were then reported on a sheet of paper with the tube list. The site engineer usually provided inspection plans in the form of a short tube listing, and in most cases the inspection scope was aimed at detection of degradation modes such as wastage or fretting wear. The inspection was limited to a small percentage of tubes, typically 3%, and in some cases expanded to no more than 20% of the tubes [3].

Probe drive technology was slow and unreliable. Remote manipulators required substantial human intervention for their installation inside the SG at the beginning of the inspections and for their repositioning during the inspection that would allow access to different areas of the tubesheet. This resulted in high cost in time and radiation exposure [3].

By the mid-80's, additional modes of degradation such as pitting corrosion, IGA, axial or circumferential inside and outside diameter SCC, particularly in non-thermally treated Inconel 600 tubing, had to be addressed. Figure 1 shows the number of tubes worldwide needing repairs over the years, classified by degradation mode [4]. The scope, and therefore the cost, complexity and time of inspections increased significantly. Bobbin probes were inadequate to detect circumferential cracking or to reliably inspect the top-of-tubesheet (TTS) locations; therefore, motorized rotating probes were used to supplement the inspections. These were very slow and prone to failure; consequently, the time and cost of inspections increased significantly.

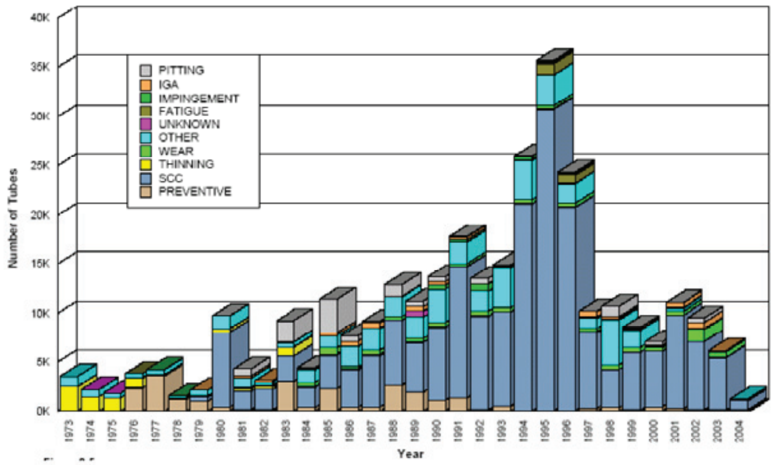

Figure 1. Worldwide Causes of SG Tube Repair Classified by Degradation Mode for Non-Thermally Treated I600

By the mid-90's, the number of tubes exhibiting SCC had increased dramatically; hence, the need for timely, fast detection and characterization of this and other modes of degradation motivated the development of inspection systems based on advanced probe technology coupled with versatile instruments operated by fast computers and remote communication systems and much improved manipulators and probe drives.

SG inspection systems have progressed through the 90's, and particularly into the new millennium, to a much higher level of automation, efficiency and reliability. The increasingly competitive market of electricity production and the demands of economic globalization required shorter and more cost effective inspections. Also, the role of Non Destructive Evaluation (NDE) evolved from simple detection tools to diagnostic tools that provide input into integrity assessment decisions, fitness-for-service and operational assessments. This new role was motivated by tighter regulatory requirements to assure the safety of the public and the environment, better SG life management strategies and often self-imposed regulations. It led to the development of advanced probe technologies, more reliable and versatile instruments and robotics, better training and qualification of personnel and better data management and analysis systems.

In addition, future SG inspections will likely be challenged by new degradation modes that might emerge as a result of life extension of NPP and their SGs or from new tube materials used in replacement SGs.

3. Inspection Requirements and Scope

SG tubes have a number of important safety functions. They are an integral part of the reactor coolant pressure boundary (RCPB) and, as such, their function is to maintain the primary system's pressure and inventory of coolant. They also provide the heat transfer surface between the primary and secondary systems such that residual heat can be removed from the primary system. The SG tubes are also relied upon to isolate the radioactive fission products in the primary coolant from the secondary system [2].

The structural integrity performance criteria (SIPC) require that SGs can withstand burst pressure under normal or postulated accident conditions. For instance in Canada, US, Belgium and Germany, the safety factor applied is approximately 3.0 against burst at normal steady-state full-power operation and 1.4 against burst under the limiting design basis accident. Also, regulations limit the allowable leakage rate at normal operating conditions [1].

To satisfy these requirements, comprehensive SG programs are written to demonstrate that SGs are fit for service. Degradation assessment, condition monitoring assessment, operational assessment and primary-to-secondary leakage assessment are important elements of such programs (5). Inspection data and results provide the information needed to establish which degradation modes are active and help determine if any flaws might have failed the SIPC during the last operating period. In this context, inspections not only provide information about flaw size and type, distribution and growth rate, but also need to do this with confidence. That is, performance of NDE capabilities needs to be demonstrated. Probability of detection (POD) and sizing accuracy must be established for different techniques, probes and flaw type and geometry combinations (6). Alternatively, technical justifications provide the basis to determine inspection uncertainties (7). Operational assessments predict end-of-cycle conditions based on beginning-of-cycle conditions using the NDE information about depth, growth and uncertainty factors of detected/hidden flaws and sizing. The objective is to estimate if any flaws would grow to exceed the SIPC during the next cycle and, consequently, to determine the length of the next operating period.

Therefore, the process of planning and defining the scope of SG inspection needs to take into account these requirements, which are normally defined in governing documents issued by the regulators such as the Nuclear Energy Institute, "Steam Generator Program Guidelines", EPRI "Pressurized Water Steam Generator Examination Guidelines: Revision 6 - Requirements", and Canadian Standard Association, "Periodic Inspection of CANDU Nuclear Power Plant Components" (2,5,8). The planning process also considers other factors such as degradation history of the component and operational experience of similar plants.

As a result, the scope of inspections could be very extensive. A typical inspection scope requires 100% full-length bobbin probe scans. Additional inspections need to be carried out with the best available and qualified technology for detection of crack-like flaws. These are either rotating probes such as MRPC or Plus Point™ Probe and/or array probes such as X-probe or Intelligent probe. This scope usually covers 100% hot leg TTS inspection, 100% of dents or dings larger than a specified voltage threshold, 100% of tubes in tight radius U-bends, typically rows 1 through 10, 20% cold leg TTS, cold leg periphery, 100% of sleeves (when present). In addition, any unusual or new indications found are re-inspected to provide further information that can help its disposition. Also historical calls with reported depths that were left in-service in previous inspections must be revisited (3). Often, additional techniques such as Ultrasonic testing (UT) are deployed for re-inspection and characterization. Furthermore, any new indication that could affect the SIPC generates an expansion to the inspection scope to include adjacent tubes to those with indications. The scope document normally has clearly defined rules for dealing with expansions.

4. Equipment Technology

In the last decade ET instruments and probe technology have progressed hand-in-hand. The availability of digital, computer-controlled, multi-channel, multi-frequency instruments, initially designed to allow the use of dual-bobbin probes simultaneously or rotating probes, led to the development of fast single-pass array probes. These probes leveraged the instruments' capabilities, but soon required further development of the instruments to satisfy the advancements in probe technology. Examples of these instruments are the Zetec MIZ-18 that led to the more advanced and versatile MIZ-30 and MIZ-70. Also, the R/D Tech TC-5700 and TC-6700 instruments evolved into the much superior TC-7700.

Until recently, inspection systems consisted of multiple individual components, i.e.: ET instrument, probe drive and probe drive controller, power supply, communication system, and manipulator controller. All this equipment was heavy and awkward to carry. It had to be transported into the reactor building by several people and was connected by a large number of cables and adapters, many of them a few hundred meters long, to allow communication with the computers located outside the reactor building. Furthermore, inspection systems comprising multiple probe-drives operating simultaneously were often used to reduce inspection time, which in turn, multiplied the overall complexity, time and dose needed for set-up.

Inspection systems have evolved in the last few years to a high degree of automation, integration, and versatility. This rapid advance was motivated by the need to reduce inspection costs, shorten outage times and to improve inspection quality. Also the levels of radiation exposure for the personnel involved in installing and operating probe manipulators and data acquisition equipment needed to be reduced to comply with ALARA (as low as reasonably achievable) objectives.

Fast evolution of electronics and computer systems in this decade led to a dramatic change in inspection systems. New inspection systems are light, easy to transport and consist of compact parts that easily assemble into an integrated single-box system comprising probe pusher, coil reel, probe drive, power supply, electronics and powerful ET instruments. These systems communicate with the acquisition computer via a standard Ethernet connection. They require plant air supply for cooling and/or to assist in probe push operation, and electric power. Figure 2 shows three examples of state-of-the-art systems: Zetec MIZ-80 *iD* system (9), Tecnatom TEDDY+ (10), and CoreStar OMNI-200-TP. In contrast, Figure 3 shows an example of a legacy set-up illustrating the cable complexity and multiplicity of "boxes". These newest ET instruments are fully digital, support simultaneous or multiplexed multi-frequency operation and use of multiple probes or array probes with channel capabilities of up to 512, 640 or 1024 channels, depending of the configuration. Their high digitization rates of 20 kHz or 40 kHz permit much higher inspection speeds.

(a)

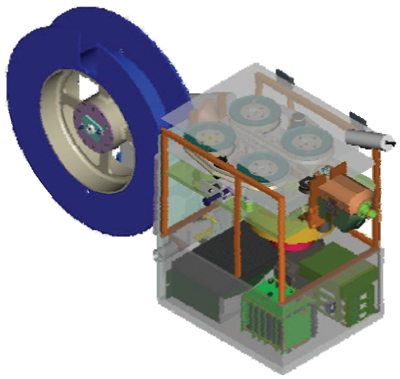

(b)

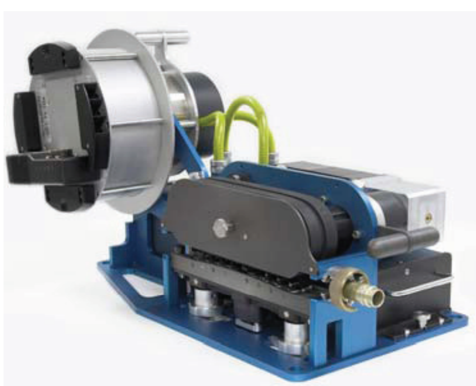

(c)

Figure 2. Images of state-of-the-art integrated inspection systems. Zetec MIZ-80iD (9), (b) Tecnatom TEDDY+SP (10), (c) CoreStar OMNI-200-TP

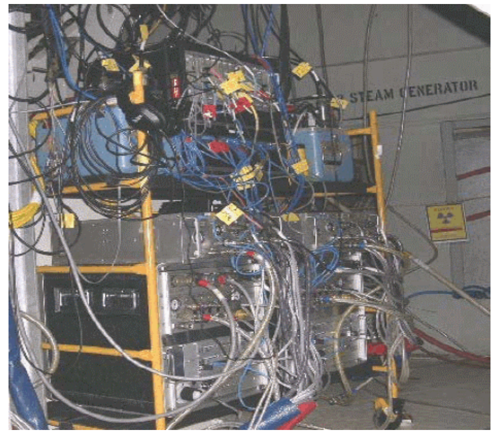

Figure 3: Illustration of cable complexity with legacy systems [(9)]

5. Probe Manipulators

Because of the high radiation fields inside a SG head, data acquisition systems rely on robotics to deliver the probes remotely. The manipulator technology has significantly evolved over the years. Early versions required substantial human intervention as the operator needed to enter the SG head to install and relocate them to cover areas where the manipulators could not reach, called exclusion zones. Also, other manipulators were sometimes needed to perform repairs. This resulted in a very high cost in terms of radiation exposure.

The design of modern probe manipulators has addressed many of these issues and, as a result, reduced considerably the radiation exposure of the personnel. They are denoted as minimum-entry or non-entry as they are either internally installed without entering the SG or externally mounted, typically on the man-way. This eliminates the need for the operators to enter the generator, although occasionally, they might need to introduce their arms inside the SG head.

Manipulators such as the Zetec SM 23, which mount on the man-way, are typically dedicated to perform only the ET inspections. They have a computer interface that allows remote semi-automatic operation using specific software. A video camera located on the arm assembly allows the operator to continuously view the guidetube and tubesheet on the remote station monitor and aid in the final tuning of the guide tube location before inserting the probe in the tube [(11)]. Figure 4 shows illustrations of the two SM 23 manipulator models.

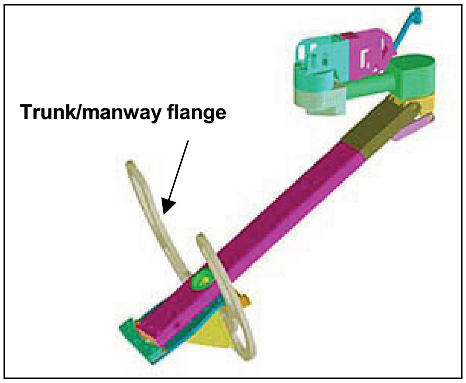

(a)

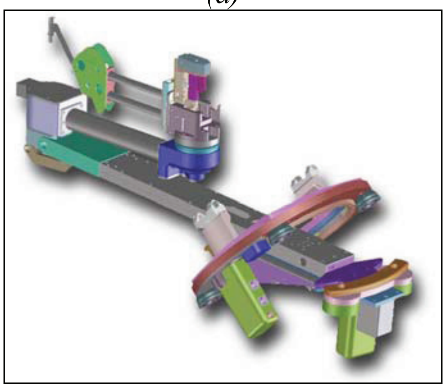

(b)

Figure 4. Examples of man-way-mounted manipulators (a) Zetec SM 23 and (b) Zetec SM 23A (11)

The limitations of these manipulators were overcome by much more robust designs that can perform the ET inspection as well as the follow-up maintenance and repairs such as tube pulling, plugging or welding of sleeves. This has helped reduce the radiation exposure and total time needed for SG maintenance activities. Their design also eliminates the need to relocate the robot within the generator in order to inspect all tubes and therefore reduces inspection time. This generation of robots, when coupled with advanced software and hardware, can perform inspections in fully automatic mode. They use vision systems to accurately locate the tube, ET data to determine probe position and tube end, encoders and information from the robot to go from tube to tube following the inspection plan without the intervention of the operator (12,13). Figures 5a and 5b show pictures of the Westinghouse ROSA III and AREVA (Framatome) Non-exclusion Zone ROGER. More recent robot models are Westinghouse PEGASYS, used for European inspections and also optimal for inspection of replacement SGs, and the Zetec ZR-1 designed specifically for CANDU® applications. They are lighter and easier to assemble than the previous models but can only perform light repairs.

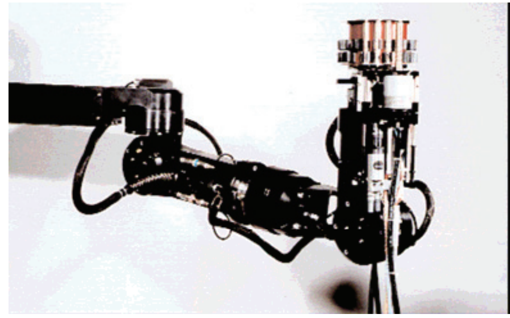

(a)

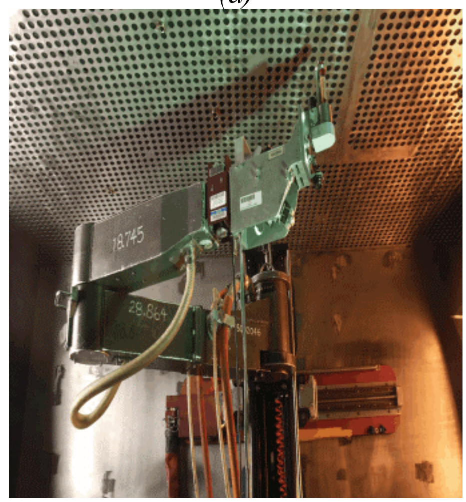

(b)

Figure 5: Examples of non-entry manipulators (a) Westinghouse ROSA III (12) *and (b) AREVA Non-Exclusion zone ROGER* (13)

6. Probe Technology

Bobbin probes have been the industry standard for general inspection of SG and heat exchanger tubes for many years. They are quite reliable and provide good general-purpose inspection of the tube, being able to reliably detect and size volumetric flaws such as fretting wear and pitting corrosion. With the new instrumentation their typical scanning speed is up to about 1 meter per second

However, one of the major limitations of bobbin probes is their inability to detect circumferentially oriented cracks because the induced current in the tube wall circulates parallel to the coil windings and is inherently unaffected by the presence of such cracks. These probes are sensitive to axial cracks at straight tube sections; however, at TTS and the U-bend transition regions, the large signals generated by geometrical tube-wall distortions significantly reduce detectability **(14,15)**.

In the 90's, the need to reliably detect SCC led to the development of Motorized Rotating Pancake Coil (MRPC) and later the Plus Point ™ probes. These surface-riding probes are connected to motor units that rotate the probe inside the tube in a helical pattern. They overcome the limitations of bobbin probes since they can detect both axial and circumferential cracks and can also provide information about flaw morphology. The presence of circumferential cracks distorts the ET pattern generated by the pancake coil giving the ability to detect these types of defects. The Plus Point™ probe comprises two orthogonal coils connected in differential mode crossing at a point so that they are affected simultaneously by material and geometric distortions such as lift-off. It has the ability to detect circumferentially and axially oriented cracks as well as discriminate between them [(1)]. Figure 6 illustrates the coil configuration of a Plus Point™ probe. In many cases rotating probe heads might incorporate both types of probes.

The main limitation of rotating probes is, however, their speed. Originally, their speed was approximately 120 times slower than that of bobbin probes, but with the development of high speed and high torque motors the gap has been narrowed to 80 times slower than the speed of bobbin probes. Also, these probes are usually spring-loaded to minimize lift-off, which makes them prone to failure. This is especially evident in CANDU® reactors where the presence of internal magnetite deposits reduces probe life significantly, and the small diameter of the motors make them more fragile. For that reason, the time required for inspections and thus the cost had increased significantly in the last decade since stations were required to inspect a large number of tubes with the Plus Point™ probe to address detection of SCC, particularly at the TTS region.

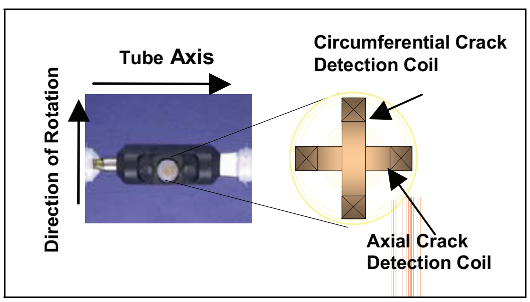

Figure 6: View of a rotating Plus Point probe for axial and circumferential crack detection

Transmit/Receive (T/R) array probes were also developed in the 90's, to address specific inspection needs of CANDU® SG tubes. These probes take advantage of the superior properties of T/R technology compared to impedance probe technology. They offer a five- to ten-fold improvement in signal-to-noise ratio, in the presence of lift-off caused by geometrical tube distortion such as U-bend deformations or the tubesheet transition. The array feature makes it unnecessary to have moving parts, which leads to increased probe reliability. Since T/R probes have directional properties, being sensitive primarily to defects in-line with the T/R coil pairs, the probe design can be optimized to maximize response to different crack orientations [(16)].

The X-probe is a fast single-pass T/R array probe that combines coils aligned for circumferential detection and for axial detection in a single probe-head as shown in Figure 7. The number of coils in each row varies from 8 to 19 depending on the tube diameter. Electronic circuits at the probe head allow the coil pairs to discriminate between axial, circumferential and volumetric flaws in a single scan and have shown performance equivalent to rotating probes, for full-length inspection at scanning speeds up to 1 meter per second [(17)]. A special design of this probe, shown in Figure 7b, can negotiate tight radius U-bends. When, combined with a bobbin probe, inspection times can decrease significantly, since the need to re-visit the tubes with different probes is virtually eliminated [(18)].

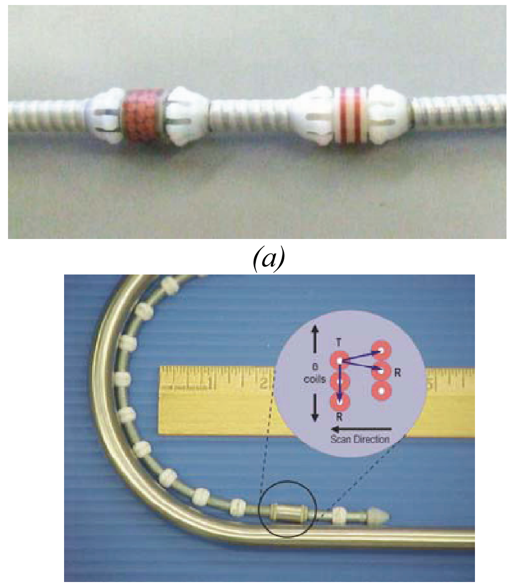

(a)

(b)

Figure 7. X-probe for axial and circumferential crack detection (a) View of an X-probe for 22.3mm diameter tubing (b) View of an X-probe for 12.9 mm diameter tight radius U-bend tubing

Another array probe currently available in the market is the Mitsubishi Intelligent probe shown in Figure 8. This is also a high-speed, high-performance alternative to rotating probe inspections. The Intelligent Probe combines bobbin and array coil technologies to detect all flaw types in a single pass. The non-surface riding probe design is durable, reliable and allows fast pull speeds. This probe technology combines an inclined drive coil arrangement and thin film pickup coils with traditional bobbin capabilities into one probe. By design, the probe coils are sensitive to all flaw types and provide characterization of indications. Each probe has a build-in electronic preamplifier circuit that optimizes the signal-to-noise ratio and EMI shielding [(19)].

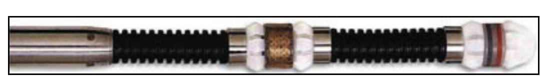

Figure 8: View of the Mitsubishi Intelligent probe [(19)]

Probe technology and the ET instruments progressed hand-in-hand. The availability of more inputs, more channels, faster acquisition rates, simultaneous, timeslot multiplexing and greater bandwidths made possible the advancements in probes seen today.

Although the initial goal of probe development was to address the need for reliable detection of SCC, the advancements in probe technology have not only fulfilled that goal, but also helped widen the scope of ET inspections. New probes, in combination with advanced software and hardware, have the ability to characterize the flaw types and their morphologies. This information is often used in integrity assessment and root cause analysis to help in identifying degradation mechanisms.

7. Data Analysis

Software packages used for analysis of SG data have also evolved significantly over the years. They function well in many other ET testing applications but typically, they have been designed with the SG application in mind. They permit very quick display of tube data and are extremely versatile having multiple features and production-oriented tools. Some examples of these features are: multiple options for display modes, process channels for multi-frequency mixes and special calibration requirements, landmarks to identify support plate locations, historical data comparison and built-in reporting capabilities that capture all the important parameters associated with an indication such as signal amplitude and phase, location, extent, depth, built-in codes to identify the type of indication, etc.

Also, before the data can be released for analysis, specific checks are performed to demonstrate that quality standards have been met. In the last few years, guideline requirements augmented the rigour and number of these verifications, and hence software for automatic checks, denoted as Data Quality Verification (DQV) has been developed. These checks can be performed in real time at the acquisition station as part of analysis software packages or additional plug-ins, minimizing the cost in time and resources needed for these verifications.

In the early days, analysis consisted of a single analyst analysing the data in real time or reviewing the data stored in strip chart recorders and analogue tapes and reporting the results on a sheet of paper listing the tubes. Today, the data analysis process consists of a multi-layer system, which provides an in-depth defence scheme that ensures high detection rate and reporting accuracy [(20)]. Two independent analysts, called primary and secondary, evaluate the data in parallel. Another more experienced analyst, called resolution, compares the reports from primary and secondary, resolves any discrepancies and confirms the accuracy of the reported indications. A second resolution analyst reviews the results again and dispositions indications that would require further diagnosis.

Often, the primary and secondary analysts operate in a highly demanding production mode, flagging indications and performing preliminary analysis only. The resolution analysts perform the detailed analysis, using more complex characterization procedures and comparing the indications to historical data. An independent analyst, reporting directly to the utility, performs a fourth level of review, verifying that the resolution analysts are consistently resolving calls and providing feedback. This role often involves spot-checking and auditing analysis results. This analyst has access to the data collected with all the probes and therefore can make informed decisions to disposition indications.

The training and qualification requisites for the SG analysis personnel are fairly demanding. In addition to national certification programs, all analysts are required to receive specific SG data analysis training and demonstrate their competence through qualification programs. Most countries required analysis personnel to be certified under the Qualified Data Analyst (QDA) testing program. This is a large database of SG data from multiple NPP and covering probable degradation modes and also different probes. In addition to this qualification, site-specific training is provided before each inspection to familiarize analysts with the specific details of the SG, operating history of the unit, method of calibration, analysis guidelines, reporting criteria, SG data, technology and procedures used at the specific site. In turn, they are required to take a site-specific test to demonstrate proficiency. In addition, analyst performance is verified by the Analyst Performance and Tracking System (APTS), with feedback to the analysts.

Technology performance is demonstrated in statistical terms or through technical justifications. All the essential variables and parameters used for probe qualification exercises such as test frequencies, multi-frequency algorithms, sizing methods, analysis guidelines, are incorporated in the acquisition and analysis procedures. Also, a site validation process compares signals in the qualification documentation to the signals from the plant being examined to ensure that the performance indices are applicable [(5)].

8. Data Management

Inspections generate an enormous amount of data, which are transmitted from the ET instrument to the acquisition computers via Ethernet connections and stored on high-speed large-capacity storage devices. These data are transmitted using high-speed communication lines, such as T1, T3 in North America and E1 lines in Europe, to centralized analysis centres that are habitually located off-site and in different parts of the continent.

In the early days of SG testing, the entire acquisition and analysis crew were located at site. To reduce costs it has become the norm to locate the analysis crew at remote sites or at centralized analysis centres. The use of these centralized analysis locations has helped in reducing costs and improve efficiency of the data analysis portion of the inspections as it makes much better and cost effective use of the resources. From the human resources point of view, personnel do not need to travel to different sites eliminating inherent travel costs and reducing the head count at site and the number of staff requiring radiation protection training and security verifications for site access. Time management is also more efficient because analysts can be made available for different jobs instead of being idle waiting for data. It also eliminates the need to transport computers and set up networks for every inspection.

This massive amount of data needs to be managed efficiently and, more importantly, reliably. Data management systems such as Eddynet Inspection Management System (EIMS), Framatome Data Management System (FDMS) etc. handle the data from thousands of tubes and several SG, in many cases from multiple scans of the same tube performed with one or various probes. Also, historical data is loaded into the database before inspections, so the analysts can use it for comparison purposes.

Often, primary and secondary analyses are carried out by different job contractors located at different sites. The data management systems integrate these locations into their network sending the data, receiving the reports and frequently operating in parallel with another management system or protocol. These systems also provide inspection plans to the acquisition computers for either semi-automatic or fully-automatic acquisition, deal with the reports from multiple levels of analysis, receive the input from DQV, generate re-scan lists and help prepare repair and plugging lists. Once the data management systems complete processing the information and all the requirements have been fulfilled, the inspection is officially finished and the equipment can be removed.

9. Advanced and Automatic Analysis Techniques

The effort required to analyse the large volume of data produced during an inspection can be enormous. Numerous analysts are required to evaluate the data at the same rate as they are acquired and often this time pressure can affect their performance and reliability. One approach to reduce costs and analysis time and to improve reliability is to use automatic analysis systems. Typically, these software packages consist of threshold and rule-based computerized data screening methods. Often, they require well-trained and experienced analysts to set them up with a fairly good understanding and knowledge of the degradation modes expected on a SG. Site-specific analysis guidelines are used to adjust signal amplitude and phase thresholds and analysis rules that will flag specific types of indications, and their performance has to be demonstrated through the site specific performance demonstration tests. They are typically used for one level of analysis, either primary or secondary, but they can be used by both teams, provided each one uses different detection algorithms (5).

These systems have shown good performance when applied in SG with well-known degradation modes. One limitation is the inherent conflict between having excessive false calls if the thresholds are set up too low for detection of very small indications versus the risk of missing flaw indications if these levels are set up too high. Also, they have a high risk of failing to identify new degradation modes. Moreover, they have not been able to replace humans, particularly when identifying indications buried in tube noise, or for indications from multiple sources found at one location.

This type of processing requires more sophisticated and flexible algorithms that incorporate the understanding of the electromagnetic phenomena in the signal interpretation. New industry efforts have concentrated on developing and testing automatic analysis systems that make use of different mathematic and multiple computer-based tools. Signal de-convolution and reconstruction, wavelet transform, feature extraction, frequency domain and spatial domain analysis, neural networks, fuzzy logic etc. are some of the methods that the industry is developing to use either individually or in combination with rule-based systems in an attempt to replace analysts (21).

These systems have shown promising results in laboratory and well-controlled environments, but have limited applicability. Furthermore, they still need to be fully qualified and demonstrated in difficult field situations.

10. Summary/Conclusions

The common wisdom is that one cannot expect exceptionally good quality products or services, to be produced quickly and at a low price because at least one of these three elements excludes the other two.

In the case of SG inspections, undoubtedly the quality has improved enormously over the years. Increased regulatory requirements for flaw detection and characterization, better probe and instrument technology, better analysis guidelines, performance demonstration requirements of the technology and personnel, noise and data quality measurements, in-depth defence analysis systems, etc have all contributed to better and more thorough inspections.

In the past, stations were shut down for long periods of time for maintenance and/or refuelling, sometimes up to three or four months. However, the electricity production market has become much more competitive in recent years, and hence stations have been compelled to reduce outage times not only to reduce costs, but also to eliminate the lost-opportunity cost associated with station downtime. As the outages became shorter, there was increased pressure to reduce inspection times as they were frequently on the outage critical path. In addition to the multiplication of resources and equipment deployed at each outage, the industry responded with significant improvements to instrument, manipulator and probe technology. Also, semi and fully automatic acquisition systems, faster communication systems for data transmission, better and more versatile and production-oriented analysis software, efficient data management systems, and automatic analysis are all main contributors to more time-effective inspections.

Finally, the costs of inspections have increased by more than an order of magnitude since the early 80's (3). This high cost is due to much more demanding regulatory requirements and the presence of active degradation modes that need to be monitored, requiring a much larger inspection scope than in earlier years. However, the trend in the new millennium has been to make inspections more cost-effective and to promote reduction in radiation exposure. In fact, remote analysis, single-box instruments, non-entry manipulators that can also perform repairs, automated acquisition and analysis, and single-pass probes have helped lower both financial and human resource costs. Moreover, shorter and better inspections have a significant economic impact on the overall station's operational cost, since one day of station shutdown can represent $1,000,000 lost revenue. Thus, shorter inspections and the prevention of unplanned shutdowns can help the stations save millions of dollars.

In summary, the SG industry has proven that better, faster and more cost effectiveness is feasible. However, there is much room for improvement through remote acquisition and further improvements to acquisition automation, fully and comprehensive automatic analysis and wide spread deployment of single-pass array probes.

11. References

1. P E MacDonald, V N Shah, L W Ward and P G Ellison, 'Steam Generator Tube Failures', Idaho National Engineering Laboratory, Lockheed Idaho Technologies Company, NUREG/CR-6365, INEL-95/0383, April 1996.
2. Nuclear Energy Institute, 'Steam Generator Program Guidelines', NEI 97-06 [Rev 1], January 2001.
3. D Mayes, S Redner and T Bipes, 'Utility Historical Perspective', 25th Annual EPRI Steam Generator Workshop, Marco Island, Florida, USA, July 2006.
4. S Swilley, 'Steam Generators – Year in Review for 2003/2004', 23rd Annual EPRI Steam Generator Workshop, Chicago, Illinois, USA, July 2004.
5. EPRI, 'Pressurized Water Steam Generator Examination Guidelines: Revision 6 – Requirements', Appendix H, Supplement H2; EPRI Report 1003138 (Final Report), October 2002.
6. M Behravesh, 'Steam Generator NDE Historical Perspective', 25th Annual EPRI Steam Generator Workshop, Marco Island, Florida, USA, July 2006.
7. M Marmonier and H Henaff, 'Qualification of Steam Generator NDE Applications Methodology According to French RSE-M Rules', 23rd Annual EPRI Steam Generator Workshop, Chicago, Illinois, USA, July 2004.
8. Canadian Standard Association, 'Periodic Inspection of CANDU Nuclear Power Plant Components', CSA 285.4 Edition 4, 2005.
9. M Burnett, M Boudreaux, N Cardillo and T Woller, 'Initial Field Experiences: MIZ®-80iD Integrated Eddy Current Inspection System', 25th Annual EPRI Steam Generator Workshop, Marco Island, Florida, USA, July 2006.
10. J Guerra and B Ribes, 'New Eddy Current Steam Generator Tube Inspection System', 5th International Conference on NDE in Relation to Structural Integrity for Nuclear and Pressurized Components, San Diego, CA, USA, May 2006.
11. Zetec Products Alphabetical Listing. SM-23 Remote Fixture, Zetec, http://www.zetec.com/pdfs/ds_sm23.pdf, August 28 2007.
12. Westinghouse Nuclear Services, 'Automated Eddy Current Acquisition System', Westinghouse Electric Company, http://www.westinghousenuclear.com/Products_&Services/docs/flysheets/NS-FS-0002.pdf, August 15 2007.
13. J C Oliver, '25 Years …The Maturing of a Process', 5th Annual EPRI Steam Generator Workshop, Marco Island, Florida, USA, July 2006.
14. V S Cecco, G Van Drunen and F L Sharp, 'Eddy Current Testing Manual, Vol.1', AECL report AECL-7523, Chalk River, Ontario, 1981.
15. V S Cecco and G Van Drunen, 'Recognizing the Scope of Eddy Current Testing', Research Techniques in Nondestructive Testing, Vol. 8, ed., R.S. Sharpe, Academic Press Inc., pp. 269-301, 1985.
16. S P Sullivan, V S Cecco J R Carter, M Spanner, M McElvanney, T W Krause and R Tkaczyk, 'Applying Computer Modeling to Eddy Current Signal Analysis for Steam Generator and Heat Exchanger Tube Inspections', CP 509, Review of Progress in Quantitative Nondestructive Evaluation, Volume 19A pp. 401-408 edited by Thomson D.O. and Chimenti D.E., American Institute of Physics, New York, 2000.
17. L S Obrutsky, N J Watson, C H Fogal, M Cantin, V S Cecco, J R Lakhan and S P Sullivan, 'Experiences and Applications of the X-Probe for CANDU Steam Generators', Presented at the 20th EPRI Steam Generator NDE Workshop, Orlando, Florida, July 2001.
18. K Davis, 'X-Probe at the Duke Plants', 6th Annual Steam Generator Inspection Technology Symposium, Zetec, Snoqualmie Ridge Golf Club, Washington, USA, August 2005.
19. Zetec Products Alphabetical Listing, 'Intelligent Probe system for Nuclear Steam Generator Inspections', Zetec, http://www.zetec.com/pdfs/ds_intelligent_probes.pdf, August 28 2007.
20. R S Maurer 'Look Back at Eddy Current Analysis Practices Over the Last Twenty-Five Years', 25th Annual EPRI Steam Generator Workshop, Marco Island, Florida, USA, July 2006.
21. K Arunachalam, R Dayana1, E Al-Sharoa1, P Ramuhalli, L Udpa, S S Udpa and J Benson, 'Development of Algorithms for Automatic Analysis of Array Probe Eddy Current Data', 25th Annual EPRI Steam Generator Workshop, Marco Island, Florida, USA, July 2006.

CIVA: Simulation Software for NDT Applications

By Erica Schumacher-Senior Applications Engineer at Magsoft Corporation & Don Roth- NDE Team Lead at NASA Glenn Research Center

Abstract

In today's environment of shrinking resources, and consistent need for accurate inspections, simulation software is an effective cost cutting tool. CIVA is an advanced NDT simulation software dedicated to modeling ultrasonic (UT), radiographic (RT) and eddy current (ET) inspections without the need for physical test sample or inspection equipment. Each inspection module is comprised of simulation, imaging and analysis tools. These tools assist the user in virtually conceiving or optimizing inspection techniques and predicting their performances in realistic NDT configurations.

While the software contains three independent modules (UT, RT, ET), this paper focuses on the UT module, which has the ability to model complex phased array UT inspections for a variety of probe styles, then automatically calculate the delay laws in an exportable format. This paper will highlight the capabilities of CIVA NDT simulation software to accurately model weld inspections using phased array ultrasound.

Introduction

The National Aeronautics and Space Administration (NASA) Glenn Research Center participated in the construction of the upper stage simulator (USS) for the Ares 1-X test rocket scheduled to launch later this year. The USS is comprised of hollow cylindrical sections that will be stacked and attached to each other. The USS contains critical welds that attach pieces to each other including a skin-to- flange weld.

NASA utilized CIVA NDT simulation software to help plan alternate inspections that if needed, could supplement the techniques that were specified and required for weld certification for the skin-to-flange weld. In the future, it is hoped that these modeling methods will be used to help qualify use of phased array ultrasonic test (PAUT) in place of a hand-held ultrasonic A-scan inspection while still meeting certification requirements.

Phased array inspection is quickly gaining acceptance in the NDT community and has many advantages over conventional A-scan inspections. These advantages include being able to complete a variety of scans with only one transducer and without any mechanical movement. Scan options include the ability to perform single point focusing, beam steering, direction and depth focusing, focusing at multiple points on a line, and focusing at multiple depths. These scan options provide greater flexibility to accurately inspect complex shapes and areas with physical restrictions (such as weld reinforcement) while being provided with a two-dimensional image of results. While the capabilities of PAUT are much greater than those of a single element transducer A-scan, the complexities of PAUT are also much greater. To improve understanding of the inspection process physics, including optimization of the inspection parameters, simulation and modeling are playing an ever increasing role. Simulation software such as CIVA can help to prove or disprove the feasibility for an inspection method or inspection scenario, help optimize inspections, and assist in approximating the limits of detectability all in significantly less time than could be accomplished through experimental trial and error only.

Body

Software Overview

CIVA is based on semi-analytical calculations in a user friendly graphical user interface. For complex shapes, the user can either import a drawing such as .DXF file, or draw the shape using the basic computer aided design (CAD) tools built into CIVA. With CIVA is it is possible to simulate the part under inspection, view the simulated inspection results and perform additional signal processing on the results such as applying filters. Because it is based on semi-analytical calculations, computation time in CIVA is significantly quicker than with finite element analysis (FEA) modeling tools.

Each module of the software is designed to let the user simulate an inspection without the use of physical test samples or inspection equipment. For each of the three modules, UT, ET and RT, the user defines the shape, size and material of the part to be inspected as well as the parameters of the inspection equipment such as ultrasonic transducer size and frequency, eddy current probe size and frequency, and radiographic source size and energy level. For each of these modules the user defines the position of the inspection equipment in relation to part. A variety of different types of flaws can be placed in the simulated part, then the inspect results calculated and displayed. The defect response obtained from the inspection results is displayed in a similar manner to what would be seen experimentally. For UT, this means that an A-scan, B-scan or C-scan can be displayed. For ET, C-scans are displayed and for RT, radiographic images are displayed.

The UT module is the oldest and most advanced of the three modules. With this module the user can either choose from 7 pre-existing specimen shapes or create their own cylindrical or planar extrusion of a CAD created profile as shown in Figure 1. The specimen material can be chosen from a large variety of isotropic materials, anisotropic materials and composites. Materials not in the database can be easily added by defining the velocity and density of the material. Additionally, a large variety of transducers shapes, sizes and types can be modeled including single element, dual element or phased array probes (linear, matrix and flexible arrays). Both single element and phased array probes (Fig. 2) can be modeled in either contact or immersion conditions. These probes can either be flat or focused. While water and oil are the two couplant choices already in the software, it is easy to add additional materials such as glycerin based gels. When a transducer is mounted on a wedge, the user defines the wedge dimensions, angle and wedge material. Several types of flaws are already defined in CIVA, where all the user needs to do is specify the dimensions and location. For more complex flaw modeling, it is also possible to create multifaceted and CAD contoured planar flaws. Examples of each of these flaw types can be seen in Figure 3.

Once the inspection parameters are defined, the user can calculate the defect response, or if they prefer, first model the beam profile to verify that the beam is angled and focused in the part as expected.

NASA PAUT Experimental Results [i]

The USS of the ARES 1-X (Fig. 4) contains several critical welds including the skin-to- flange weld. To improve their inspection planning, and hopefully qualify use of PAUT in place of conventional UT for inspection of the skin to flange weld, NASA is using a combination of experimental and simulation results.

A skin-to-flange test sample was fabricated out of carbon steel. The skin and flange portions were approximately 12 mm and 25 mm thick, respectively. The skin portion was double-beveled at one end, 45^o each side, and butt welded to the thicker flange section using the flux core arc welding (FCAW) method. Weld filler metal with a similar composition to that of the base steel was used. The external weld was machined flush. To simulate lack of fusion, a side-drilled hole (SDH) approximately 1.61 mm x 40 mm in length was located at one end of the part. (Fig. 5)

A General Electric (GE) Phasor XS portable ultrasonic flaw detector was used for the inspection of the test sample. The type used by NASA was a 32 crystal-element linear phased array transducer with 5 MHz flat focus and a total aperture of 16 mm x 10 mm. The element width was approximately 0.45 mm with a gap between elements of approximately 0.05 mm. Only 16 pulser-receivers were available in the instrument at one time, limiting the use to only 16 active elements out of a total of 32 elements. The use of only half the total elements resulted in an active aperture area of 8 mm x 10 mm. The transducer was attached to a Rexolite wedge. The wedge produced an incidence angle of approximately 36^o and a subsequent refracted shear wave angle of approximately 54^o in the steel part. Note that since a refracted angle of 54^o is beyond the critical angle for longitudinal waves in steel, this study is concerned with shear wave only. As shown in Fig. 5, whether a single element or phased array transducer is used, this is a single-sided inspection of the weld. A combination of a manual hand scan and an electronic sectorial scan from 40^o to 75^o was performed along the exterior surface of the skin to determine the detectability of the SDH in weld interior.

Using the 5MHz transducer, ultrasonic velocity and attenuation coefficient measurements were performed on the test sample base material and also on a flat area of the weld. The shear wave velocity values for the base steel and weld steel were measured to be 0.325 cm/μsec and 0.328 cm/μsec, respectively, the difference of which is close to the measurement uncertainty for the velocity measurement method. The velocity value for the base steel was used as a setup parameter in the GE Phasor.

For the inspection of the SDH, the transducer was positioned perpendicular to the axis of the flaw. Figure 6 shows the experimental sector scan results obtained at the probe position shown in Figure 5. The large amplitude indication shown in Figure 6 at the lower right portion of the sector image is from the direct path reflection off the SDH. The maximum amplitude for this indication occurs at the 66^o angle. When the probe is moved laterally away from the SDH (which is 40 mm long and extends about 2/5ths of the way across the weld) the indication from the SDH eventually disappears from sight. The Phasor display indicates that the SDH is located about 4 mm in front of the wedge and about 12.67 mm down from the surface that the probe is on. These results agreed well with actual location of the SDH in the part. The maximum amplitude from these experimental results was obtained at an angle of $66^{o.}$

NASA Validation of CIVA for PAUT[ii]

After obtaining the experimental results with the GE Phasor, NASA then used CIVA V9.1a simulation software to recreate the inspection scenario. A model of the part and transducer was created, a 1.61mm x 40 mm SDH was placed in the part at the same location and orientation as in the test sample, and a simulated 40^o to 75^o sectorial scan of the flaw was performed. To improve accuracy of simulation results, NASA used the velocity values obtained experimentally in place of the generic steel velocities in CIVA's material database. From the simulation results NASA was able to determine that the maximum amplitude obtained would occur at approximately 60^o. By exporting the defect response onto the model of the skin to flange test sample, it is easy to see that the maximum response occurs at the location of the SDH (see Fig 7). The ability to overlay the UT response onto a 3D model of the part is one of the advances of using CIVA. For complex geometry, it greatly assists in determining the physical cause of each response such as tip diffraction, corner echoes, direct reflection, etc.

Comparison of the simulation results (Fig. 7) to the experimental results (Fig. 6) shows a very good correlation in location and amplitude of response. The one measurable difference is that the simulation obtained the maximum amplitude at approximately 60°, while the maximum amplitude obtained experimentally occurred at approximately 66 °. There are several factors that could have caused the difference in angles including slight differences between the actual and modeled weld contour, flaw size and orientation, transducer setting (it is unknown whether the first or last 16 elements were turned off), and probe placement.

Comparison of Flaw Configurations

After validating the accuracy of CIVA to detect the SDH in the skin-to-flange weld, the effects of defect shape and orientation were explored. The goal was to better understand how robust the inspection would be in detecting lack of fusion. Since lack of fusion is often planar on one side, additional simulations were performed with planar defects.

Three additional simulation scenarios were created, each one containing a 1.61 mm x 40 mm planar flaw in the same location as the SDH. The flaw was oriented at 0 °, 45 °, and -45 °. The flaw orientations can be seen in Figure 8. As seen in Figure 9, the biggest response is obtained from the reflection off the SDH. Somewhat unexpectedly however, the maximum amplitude for all three planar defects is the same. The length over which the planar flaw can be easily detected differs as shown in Figure 9. Because of the difficulty manufacturing a mid-wall planar defect, there are no experimental results to compare to the simulation results. Most likely, the curvature of the weld has affected the detectability of the planar flaws.

To determine the effects of weld contour on detectability of planar flaws the weld contour was changed from concave to flat. The flaw response from the same SDH and planar flaws was compared and evaluated. As originally expected, the maximum amplitude is obtained from the SDH, the next largest is from the planar defect oriented perpendicular to the ultrasonic beam and the smallest amplitude is from the planar defect oriented parallel to the sound beam. Based on the simulation results, demonstrated in Figure 10, the defect response from the planar flaw oriented parallel to the ultrasonic beam is indistinguishable from background noise, and therefore would go undetected unless additional scans are performed.

To further bound the detectability of lack of fusion, additional simulations at the maximum and minimum weld reinforcement could be performed. The size and location of the defects could also be varied. If the phased array transducer used was not able to easily detect these flaws, then the properties of other transducers could be modeled in an effort to determine the most effect transducer and delay laws for this inspection.

Conclusion

Using the UT module of CIVA simulation software, NASA was able to create a virtual part made of steel, place a side drilled hole (SDH) in the part, create a 32 element phased array transducer where only 16 elements are used at a time, place this transducer on the part, and see how the simulated defect response compares to the experimental defect response. After validating the effectiveness of CIVA, additional defects and defect angles were analyzed, as were changes in the weld contour on detectability of the flaws. CIVA allowed the user to determine how these variances in allowable parameters such as weld contour, would affect the detectability of rejectable defects (in this case lack of fusion).

Bio

Ms. Erica Schumacher
Senior Applications Engineer
Magsoft Corporation
20 Prospect Street, Suite 311
Ballston Spa, NY 12020
erica@magsoft-flux.com

Ms. Schumacher holds a Bachelor of Science degree in Mechanical Engineering and a Master of Science degree in Industrial Engineering from Rutgers University. Currently she supports CIVA NDT simulation software, including training of new users. Prior to Magsoft, she was a Senior Quality Assurance Engineer for Bechtel Corporation specializing in NDT (PT, MT, UT, RT) and was qualified as a 250-1500-1 NDT Examiner in these methods. Her NDT expertise includes providing CIVA technical support, teaching NDT to internal and external personnel, and assisting in the NDT portion of 3rd party vendor audits. She is a co-recipient of the 2003 Bechtel Plant Machinery, Inc. General Managers Award.

---

[i] Roth, D., J.; Tokars, R., P.; Martin, R., E.; Rauser, R., W.; Aldrin, J., C.; Schumacher, E., J." Ultrasonic Phased Array Inspection Simulations of Welded Components at NASA", *Materials Evaluation,* vol. 57, no. 1, pp 60-65 (2009)

[ii] Roth, D., J.; Tokars, R., P.; Martin, R., E.; Rauser, R., W.; Aldrin, J., C.; Schumacher, E., J." Ultrasonic Phased Array Inspection Simulations of Welded Components at NASA", *Materials Evaluation,* vol. 57, no. 1, pp 60-65 (2009)


SDH

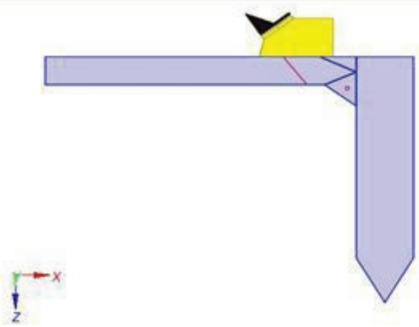

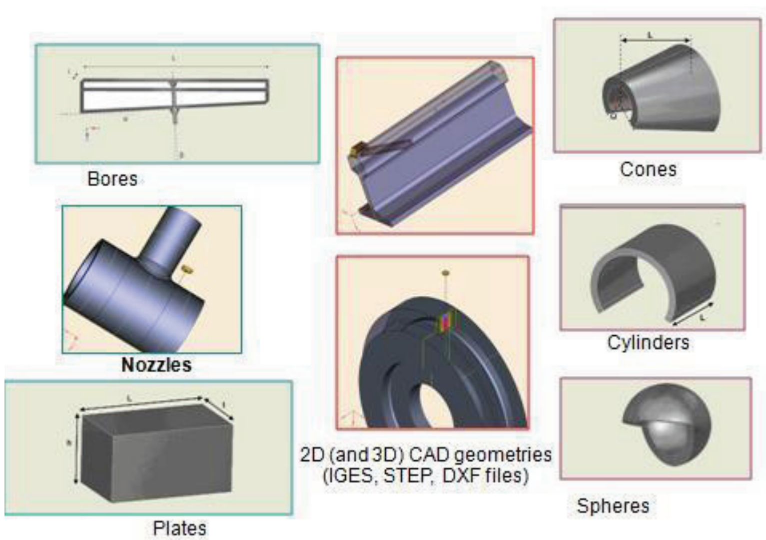
Bores
Cones
Nozzles
Cylinders
2D (and 3D) CAD geometries
(IGES, STEP, DXF files)
Plates
Spheres

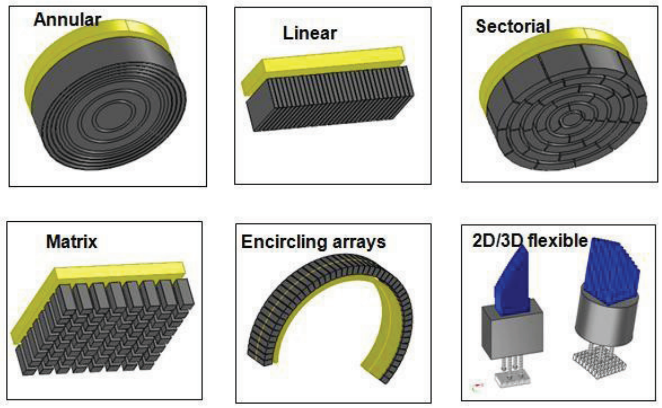
Annular
Linear
Sectorial
Matrix
Encircling arrays
2D/3D flexible

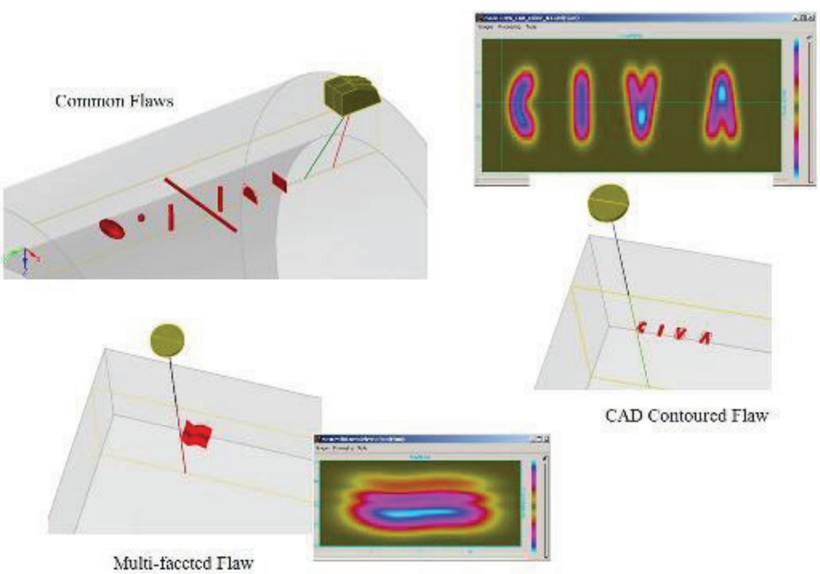
Common Flaws
CAD Contoured Flaw
Multi-faceted Flaw

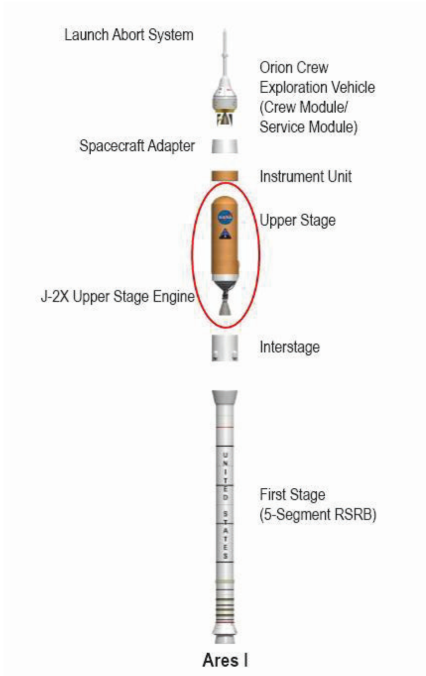
Launch Abort System
Orion Crew Exploration Vehicle (Crew Module/ Service Module)
Spacecraft Adapter
Instrument Unit
Upper Stage
J-2X Upper Stage Engine
Interstage
First Stage (5-Segment RSRB)
Ares I

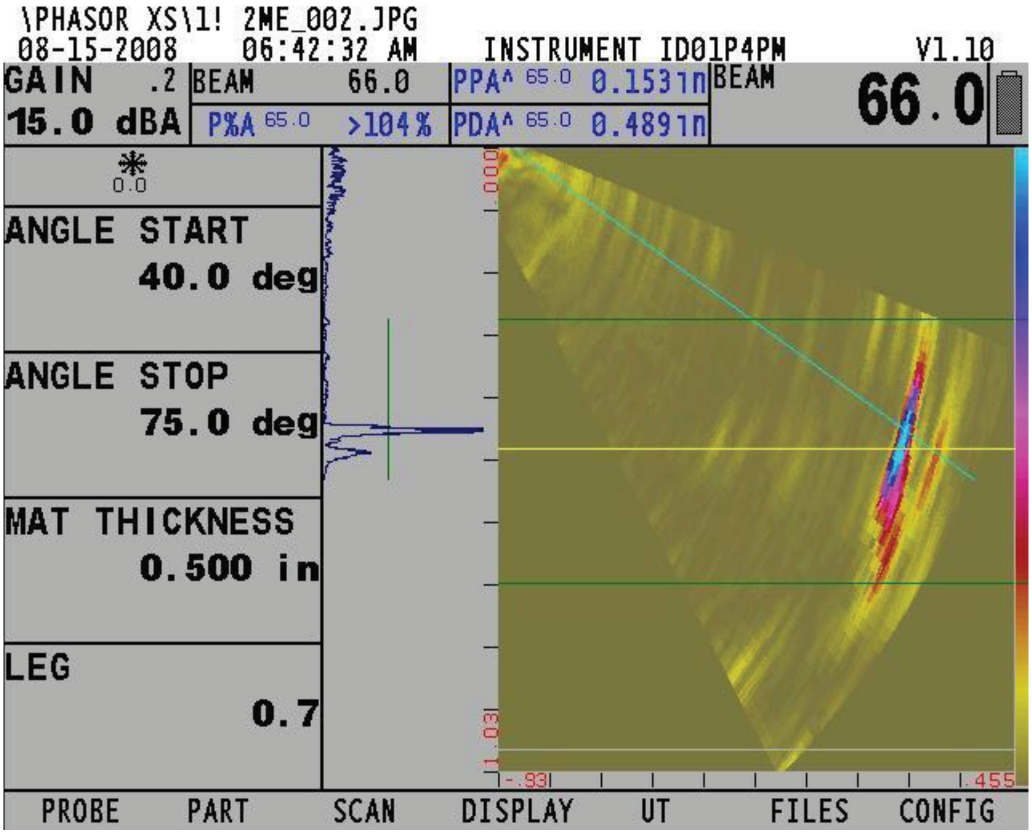
\PHASOR XS\1! 2ME_002.JPG
08-15-2008 06:42:32 AM
INSTRUMENT ID01P4PM
V1.10
GAIN .2
15.0 dBA
BEAM 66.0
P%A 65.0 >104%
PPA^ 65.0 0.153in
PDA^ 65.0 0.489in
BEAM
66.0
0.0
ANGLE START
40.0 deg
ANGLE STOP
75.0 deg
MAT THICKNESS
0.500 in
LEG
0.7
0.000
1.031
-.931
1.455
PROBE
PART
SCAN
DISPLAY
UT
FILES
CONFIG

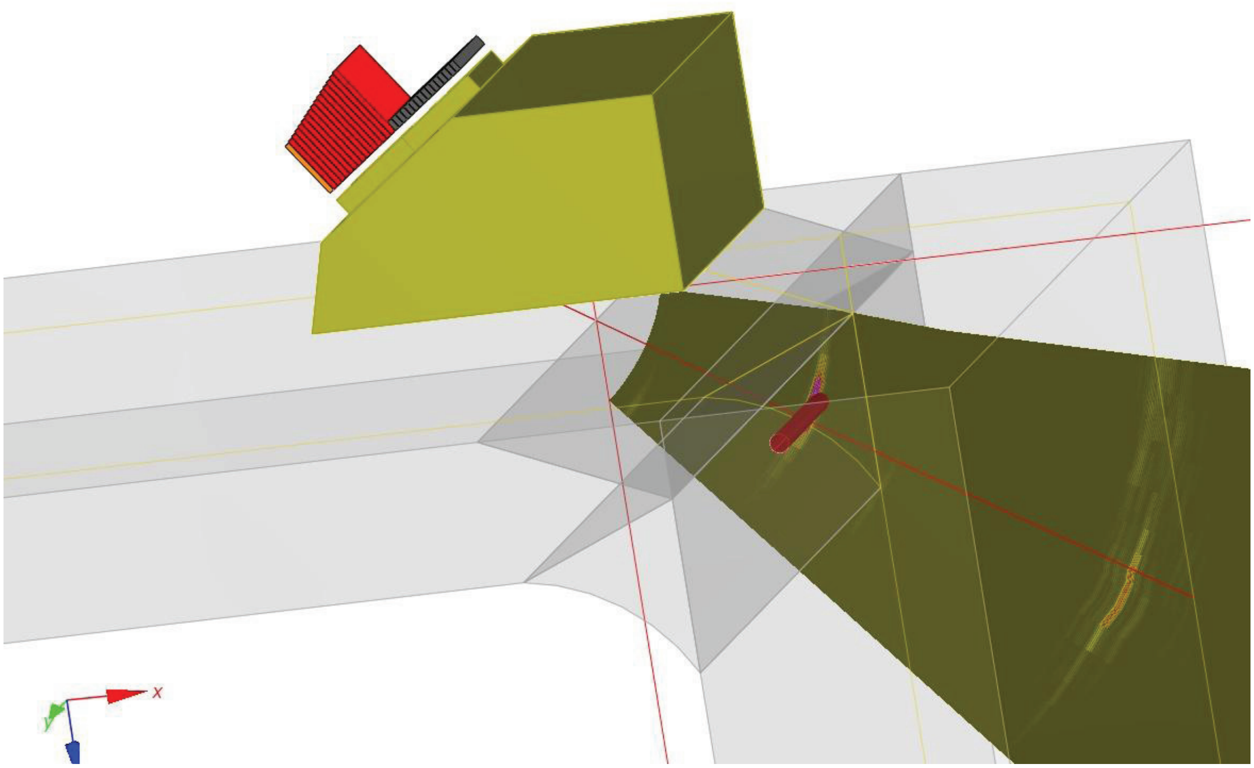
x
y

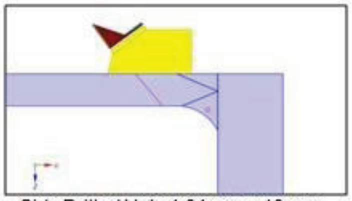

Side Drilled Hole 1.61 mm x 40 mm

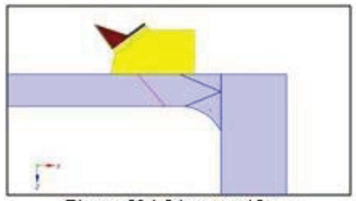

Planar 0º 1.61 mm x 40mm

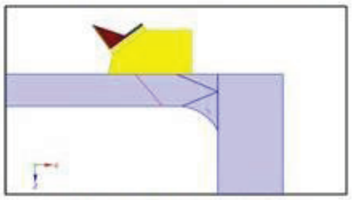

Planar 45º 1.61 mm x 40mm

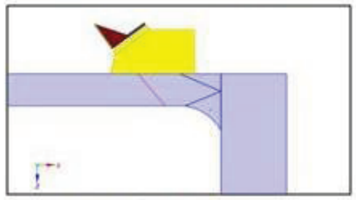

Planar -45º 1.61 mm x 40mm

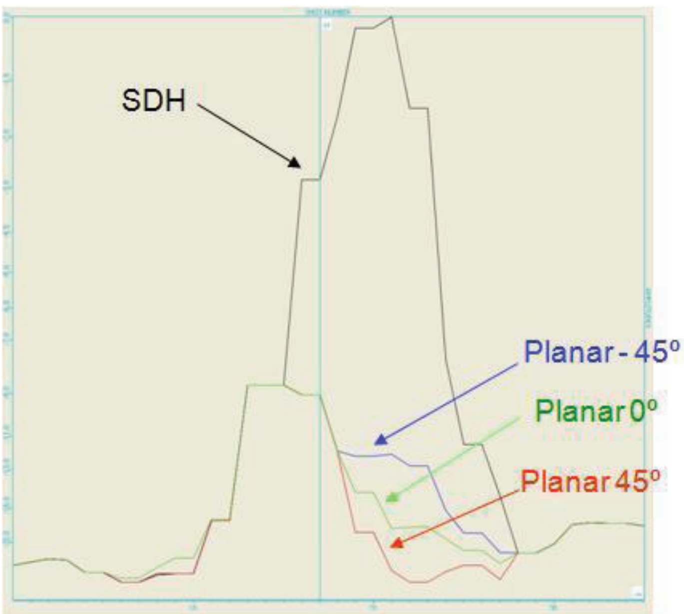

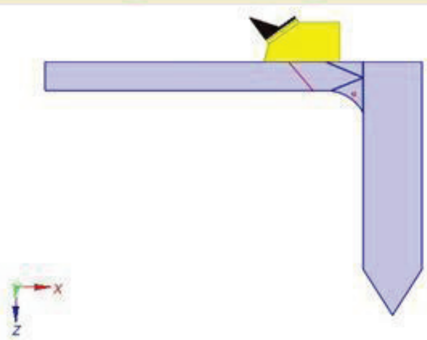

Acoustic Pulse Reflectometry

Adams, M.

Abstract not available at time of printing.

Residual Stress Measurement in Parts and Welded Elements by Ultrasonic Method

Y. Kudryavtsev and J. Kleiman

Integrity Testing Laboratory Inc., Markham, Ontario, Canada
E-mail: ykudryavtsev@itlinc.com

Residual stresses (RS) can significantly affect engineering properties of materials and structural components, notably fatigue life, distortion, dimensional stability, corrosion resistance. RS play an exceptionally significant role in fatigue of welded elements. The influence of RS on the multi-cycle fatigue life of butt and fillet welds can be compared with the effects of stress concentration. Even more significant are the effects of RS on the fatigue life of welded elements in the case of relieving harmful tensile RS and introducing beneficial compressive RS in the weld toe zones.

Different methods exist to measure the RS. One of the advantages of ultrasonic techniques for RS measurement is that they are non-destructive. Using such techniques, one can measure the RS in the same points many times, studying, for instance, the changes of RS under the action of service loading or effectiveness of stress-relieving techniques.

An Ultrasonic Computerized Complex (UCC) for non-destructive measurement of residual and applied stresses was developed recently. The UCC includes a measurement unit with transducers and basic supporting software and an advanced database and an Expert System, housed in a laptop, for analysis of the influence of RS on the fatigue life of welded elements. In general, the ultrasonic method allows one to measure the RS in both cases: averaged through thickness or in surface layers. The present version of UCC allows measuring the averaged through thickness RS in plates 2 - 150 mm thick.

The advanced ultrasonic method, the equipment and some examples of RS measurement are discussed in this paper

New Advances and Applications Using X-Ray Fluorescence Analyzers for Alloy Testing

Abstract

For more than 40 years, positive material identification (PMI) of alloys has been performed using standalone, portable, and more recently, handheld x-ray fluorescence (XRF) spectrometers. These portable spectrometers, using a focused beam of x-rays to excite key elements found in the alloy sample, produce a resultant spectrum and a digital readout of elemental concentrations. The concentrations of key elements provide industrial inspectors with the ability to verify alloy grades in critical applications, thus avoiding possible catastrophic incidents where an incorrect alloy could have been used by mistake.

The latest handheld alloy analyzers incorporate major technological advances allowing for greater accuracy, precision, and lower limits of detection for a wider range of elements. These advances illustrate how new industry problems facing inspection engineers today can now be addressed by handheld XRF. Several difficult applications will be discussed such as flow accelerated corrosion (FAC) in refinery HF Alkylation units due to chromium, copper and nickel content, and (FAC) in power generating stations due to chromium levels and carbon steel failure due to low silicon content.

Introduction

History has taught us that we should *trust, but verify*! Verification of alloys to ensure they are composed of the correct alloying elements has been the realm of handheld x-ray fluorescence for the past four decades. Industries ranging from petrochemical, aerospace and fabrication (which are mission critical for the correct material), to contract testing services, metals recycling applications and many more have employed portable XRF for alloy verification for over 40 years. The use of these tools assures users that the composition of the metal they purchase, fabricate, verify, install, or recycle is alloyed as expected. Since the late 1960s, the portable XRF market has seen several generations of increasingly sophisticated alloy analyzers become commercially available to perform this crucial task. Each generation adds new capabilities, increased speed and greater ease of use. Today, nearly all alloys are tested and identified for correct alloying content with these powerful handheld tools.

Fig. 1 Seventh generation alloy analyzer, the Thermo Scientific Niton XL3t, circa 2009

The Latest Developments

Unlike the limited quantity, hand-built and, often, highly application specific portable, two-piece, analyzers of decades past, today's one-piece handheld XRF analyzers are built in volume with modern assembly technologies and are designed on a common platform to allow a wide range of uses. The latest alloy analyzers are readily adapted, with software and calibration options, to a wide range of other materials analysis applications. Expanded alloy application examples are the addition of precious metals and electronic alloy calibrations to the base alloy model, as well as precious metals in catalytic converters.

Fig. 2 A handheld XRF being used to inspect piping systems in a refinery.

Examples of other types of analysis are environmental and toxic materials testing applications, which can be further added to the basic or expanded alloy analyzer. With user software upgrades now feasible electronically, the longer a modern XRF tool is used, the more it can evolve and the better it can perform.

In the very latest handheld XRF alloy analyzers, the most significant technology advancements are:

- Further miniaturization and field hardening
- Improved ergonomics
- Doubling of the speed of alloy and metals testing
- Enhanced performance for difficult (nearly twin) alloy separations
- Increased sensitivity for tramp & trace elements in alloys

How the XRF Works

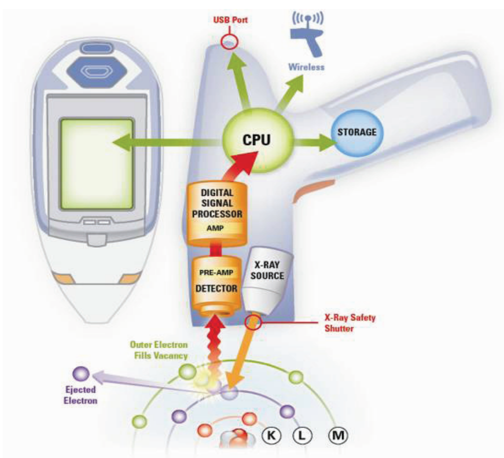

Fig. 3 Functional Diagram of HHXRF

A handheld XRF consists of a source of x-rays (radioisotope or electronic x-ray tube) that generates a beam of primary x-rays. This beam shines into the sample to be analyzed and generates a spectrum of characteristic fluorescence radiation from atoms of the elements in the sample. These characteristic x-rays are detected by a solid state detector and their electromagnetic energies are converted to electrical pulses. These pulses then are sorted into element channels in a Digital Signal Processor. From here the counts from each element are sent to the microprocessor. The microprocessor contains the algorithms to perform the calculations for computing the percentage of each element from the count rate data. The element's symbols and their concentrations are then sent to the display (see Fig. 4) and data storage, or via data transfer software to be logged in a microcomputer, laptop or PC in spreadsheet or word processor format. Entered sample names (via on-board keypad or optional bar code reader) and full spectral data for every measurement are stored along with the complete sample analysis information. All data is encrypted in accordance with US Federal Regulation 21CFR Part 11[1].

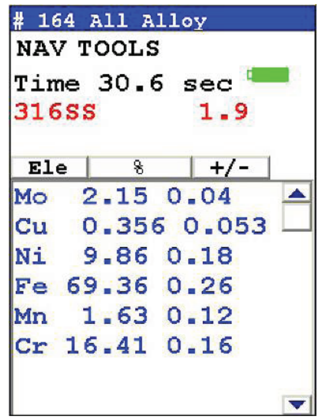

Fig.4 Example readout for SS 316

New Detector Technology

A new type of solid state detector has been introduced that is once again revolutionizing handheld XRF analysis. Silicon Drift Detectors (SDD) are high count rate, high resolution detectors that have been utilized in laboratory settings, such as in electron microscopy. The unique physical characteristics (specifically a very small anode capacitance) of this detector allow it to be used in high count rate applications with no compromise of resolution, and with excellent shaping time and signal to noise ratio.

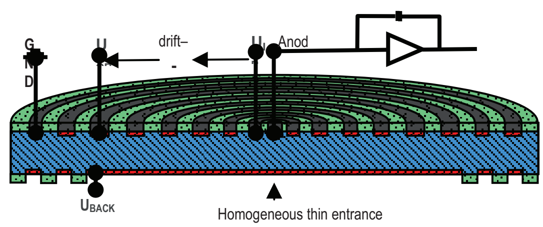

Fig. 5 Silicon Drift Detector

The ability to package these detectors in small, yet stable, systems has recently been developed, and now several handheld XRF manufacturers offer systems utilizing SDD detectors. Differences do exist however. The larger the active area of the detector, the more efficiently it can gather and process x-ray counts – translating to better statistics and sensitivities. One manufacturer utilizes an SDD offering more than two times the active area of conventional SDD units found in handheld instruments. This technology can process more than 200,000 counts per second, and can achieve, in general, up to three times better limits of detection than traditional SDD's, and up to ten times better sensitivities over conventional Si PiN detector based instruments.

Of course, in order to take advantage of this high-capacity detector, the XRF analyzer must have the ability to generate a sufficient number of fluorescent x-ray events from a sample, and position the detector to collect as many as possible. Enter the 50kV x-ray tube.

The recent introduction of a miniature 50kV gold-anode x-ray tube has led the way in x-ray tube developments. Excitation intensity is exponentially proportional to the excitation voltage. Utilization of a 50kV tube has improved precision two-fold over comparable 40kV tube systems.

As a result, the new XRF analyzers utilizing large area SDD technology have as much as a ten-fold increase in performance over conventional Si-PiN based systems. In addition, they have the distinct ability to provide analysis of light element content such as silicon, aluminum, sulfur and phosphorus – without the need for helium purging or vacuum, something that was considered impossible as recently as a year ago.

This greatly increases the ease of performing PMI on newer alloys found in high sulfur processing environments such as ZeCor®, where the 6% silicon would otherwise require measurement with a helium-purged XRF analyzer or optical emission spectroscopy. It also introduces new PMI applications which require extreme sensitivity, such as the prevention of flow accelerated corrosion in HF alkylation units. Residual element analysis can now be performed with a level of confidence once only garnered in the laboratory.

In short, technology continues to improve, and if we have learned anything, it is not to underestimate what the future might bring. Of course the real beauty of what these new generations of XRF instruments deliver is that the user need not have an understanding of the science behind them in order to benefit from their use. And that benefit can't be understated.

Spot Collimation and Camera Technology

Similar to a chain, a process system is only as strong as its weakest link. The use of proper filler materials, and the ability to obtain proper weld dilution rates while joining two pieces of a process system together are as critical to the integrity of the pressure envelope as are the base materials (pipes, valves, etc…) themselves. Up to now, clip-on "weld masks" have been available for XRF analyzers that narrow the instruments field of view, permitting these measurements. While easy to use, they made it difficult to confirm that individual measurements completely isolated the filler material from the base metal.

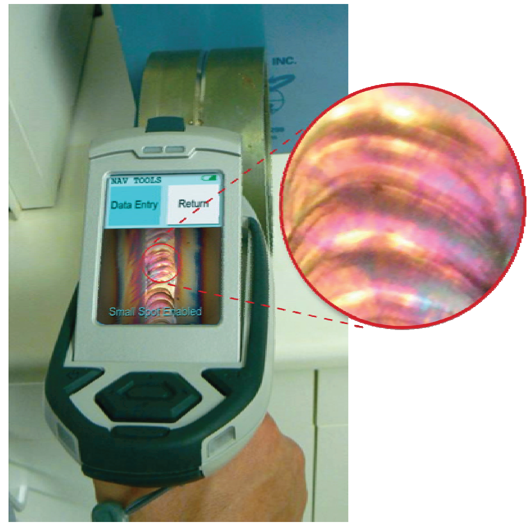

Figure 6 Isolation of a weld bead for analysis.

Recent advances to certain handheld XRF analyzers incorporate a spot collimation and CCD camera features to isolate and analyze welds. These systems incorporate a miniature CCD camera and sample imaging software that helps the user properly position the instrument in the correct location for every measurement. At the completion of each measurement, it stores a digital picture of the sample along with the analytical results. Additionally, the analyzer x-ray beam can be collimated to analyze a highly focused spot. The user can easily select a spot size appropriate for each measurement - functioning similar to an internal weld mask. While measuring base materials, the user selects the larger 8 mm diameter measurement area; when analyzing welds, a simple software switch reduces the measurement area to a smaller 3 mm diameter. The analyzer superimposes a "bull's-eye" on the camera display to ensure proper placement on the sample.

Increased Sensitivity

For tramp and trace levels of elemental contaminants, sensitivity is a critical issue. The latest breakthroughs that have improved limits of detection (LOD) for certain residual and / or tramp elements (e.g.; Cr, Mn, Sn, Cu, and Pb) are:

- 50 kV, 2W miniature x-ray tube (having 20% more output than a typical handheld XRF)
- Optimized x-ray path geometry along with "on the fly" optimization of measurement parameters

- New large area SDD's for faster measurements, greater sensitivity, better precision, and improved LOD.

TIME	2s per filter	3s per filter	5s per filter	10s per filter
Element	**Fe Base**	**Fe Base**	**Fe Base**	**Fe Base**
Sn	0.055	0.045	0.030	0.020
Nb	0.0065	0.0055	0.0040	0.0025
Cu	0.045	0.035	0.028	0.018
Ni	0.090	0.070	0.053	0.040
P	0.500	0.200	0.13	0.083
Si	1.250	0.500	0.300	0.190

Fig. 7 3-sigma LOD's Iron Base, Various Analysis Times, all units % wt.

The LOD's shown in the above chart, Fig. 7, are typically two-fold better in the LOD values than previous XRF analyzer generations.

The analyzer can now determine previously immeasurable (outside the lab) levels of trace and tramp elements. Such contaminants can poison products, or make them unusable for certain applications. For example, specifications on carbon steel piping for HF Alkylation units set a maximum concentration of 2000 ppm for the sum of residual elements Cu, Cr, and Ni. Values greater than this level have been shown to promote preferential corrosion that can lead to catastrophic failure. Other examples include, monitoring Si content at trace levels at (>0.1%) in hot sulfidation corrosion applications in Petrochemical markets and similarly Flow-accelerated corrosion (FAC) in Nuclear plants where Cr content greater than 0.1% in carbon steel piping drastically improves the corrosion rate. Many types of low concentration contaminants can now be identified using handheld XRF before the alloy is installed or the operation is seriously impacted.

Conclusion

The latest improvements in hand-held alloy analyzers for alloy testing have resulted in smaller, faster and near-lab performance in a 3 pound (1.3 kg), field-hardened package. Geometry optimization, "on the fly" parameter optimization, combined with detector improvements and faster electronics, provide faster testing, more sensitive trace and tramp element determination, the ability to quantify fractional percent alloying elements, and extremely rapid, high-precision, and accurate major element determination. Many previously difficult alloys determinations can now be performed without the need for lab testing. The essential power and reach of a lab XRF spectrometer is now available for use in harsh field environments.

Authors

Joey Cheverie,
Vice President
NITON Analyzer Division – Alloy
Elemental Controls Ltd.
3230 Wharton Way
Mississauga, On, Canada, L4X 2C1
jcheverie@elementalcontrols.com

James R. Pasmore,
Director, Key Accounts
Thermo Scientific Niton Analyzers
Thermo Fisher Scientific
62256 Nels Anderson Rd, Suite 6
Bend, OR, USA, 97701
james.pasmore@thermofisher.com

Advanced Ultrasonic Inspection Systems

David Seto

Abstract not available at time of printing.

Ultrasonic phased-array and eddy current array as approved methods for aircraft maintenance.

Ultrasonic phased-array and eddy current array technologies have shown high benefits for NDI in many industrial fields. Recently, Olympus NDT introduces its new portable array instrument with these two technologies, named Omniscan MX, specially designed for maintenance applications. This presentation will review some maintenance applications already approved by aircraft manufacturers.

André Lamarre, M. Sc., P.E.
Business Development Director - Aerospace and Defense
Olympus NDT
505, boul. du Parc-Technologique| Quebec, Qc, G1P 4S9 | Canada
Tel. (1) (418) 872-1155 | Fax (1) (418) 872-5431 | Direct line (1) (418) 263-3658
andre.lamarre@olympusndt.com
www.olympusNDT.com

A CONTRIBUTION OF PHASED ARRAY ULTRASONIC TECHNOLOGY (PAUT) TO DETECTION AND SIZING STRESS CORROSION CRACKS

Peter Ciorau - Ontario Power Generation - Canada peter.ciorau@opg.com
Chris Chartier - Acuren - Canada cchartier@acuren.com
Ken Mair - Acuren - Canada kmair@acuren.com

Abstract

The paper presents technical issues related to stress corrosion cracks (SCC) detected and sized by PAUT. SCC with height between 3 mm to 15 mm were detected and sized in the following components: welds with thickness of 9 mm, bolts at depth 21 and 63 mm, Siemens-Parson blade roots, GEC Alstom rotor steeple hook. A SOHIC (stress oriented hydrogen-induced crack) is also displayed and height evaluation is estimated (see Figure 1). Comparison with fracture mechanics, grinding measurement and optical is also presented. PAUT is capable to size cracks within ± 1 mm, with an under sizing trend (see Figure 2). Practical recommendations are also made for optimizing the PAUT parameters in sizing the last significant tip (branch) of SCC.

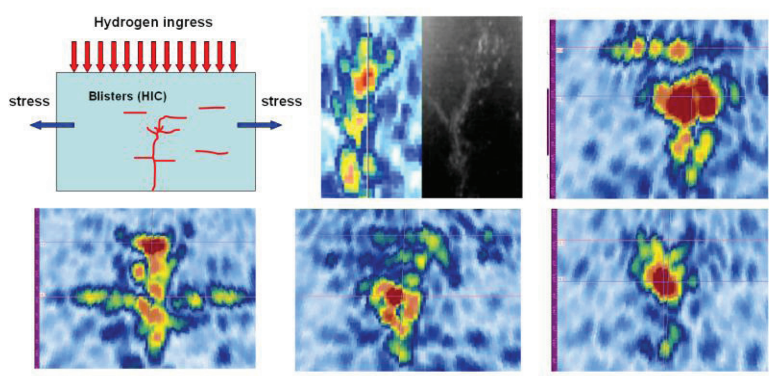

Figure 1: PAUT display of SOHIC in different locations. Crack branches also displayed.

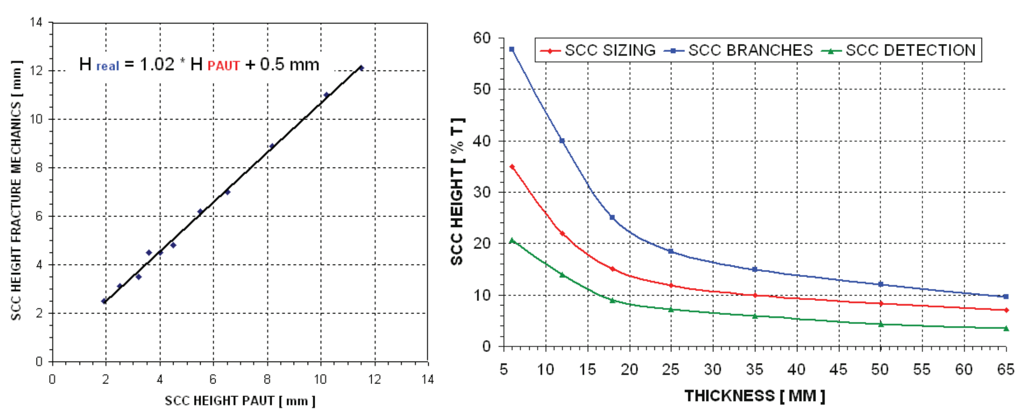

Figure 2: PAUT comparison with fracture mechanics for SCC height (left) and PAUT capability for SCC detection, height sizing and branch visualization.

DEFECT DETECTION AND IMAGING FROM PHASED ARRAY FOCUSING OF ULTRASONIC GUIDED WAVES

R. Sicard, J.-F. Martel and H. Serhan

TecScan Systems Inc., Boucherville (Québec) Canada, J4B 6Y4

ABSTRACT. The use of numerical and phased array techniques to focus guided waves and perform inspection of plates and pipes has not been widely used; it represents an interesting solution for defect detection and localization. In addition, imaging of ultrasonic guided wave results using color coded B-Scans is also considered a highly valuable tool for data interpretation. While commercial ultrasonic phased array systems have both the ability to perform focusing and present data in B or S-Scan formats, they are not designed to perform guided wave focusing. The present paper presents an experimental study for the implementation of ultrasonic guided wave focal law algorithms into phased array systems. Focal laws are calculated for the inspection of plate structures using ultrasonic Lamb waves generated by the angle beam wedge method. The wedge properties and the considerations for guided waves imaging are outlined in this work.

INTRODUCTION

The use of Phased Array focusing as a mean to perform ultrasonic inspections has become very popular in the last years. Focusing ultrasonic waves increases the signal-to-noise ratio of echoes returning from the area of interest, therefore resulting in an increased POD and, under certain conditions, fewer false calls. For that reason, Phased Array focusing has been integrated and used in applications such as conventional B-Scan imaging and angle beam and TOFD inspections of welds using either longitudinal or shear waves. However, the inspection of thin materials presents limitations mainly because of the combination of the required higher frequencies and the dead zones inherent to ultrasonic inspections.

Guided waves provide a rapid mean of inspecting large areas of a structure with minimal measurement points. Aluminum aerospace structures could benefit from the use of ultrasonic guided waves as a rapid screening tool. However, their interpretation often requires skilled inspectors, mainly because of their multi-modal and dispersive nature. Representing the result of an inspection as an image often represents an excellent solution which helps in the identification of defects. Work has been carried out by many authors using tomography [1-2] and, more recently, phase superposition algorithms such as the Synthetic Aperture Focusing technique (SAFT) [3-4] to produce images from guided waves signals in plates, namely Lamb waves. The feasibility of using Phased Array as a guided waves imaging tool has also been studied numerically by *Sicard* et al. [5].

In this paper, we present an experimental study of Lamb waves based on phased array imaging of plate structures. Linear scan (depth focusing) and sectorial (azimuthal) scan were performed using a commercial phased array system. The results of this study are presented for thin plates containing artificial defects in a 1.82 mm stainless steel plate with simulated corrosion pitting and a 2-layer aluminum riveted aluminum plate arrangement with EDM notches on the first layer. Good detection is obtained on both samples, highlighting potential applications of Phased Array Guided Waves.

LAMB WAVE

Lamb waves represent, along with the shear horizontal modes, a group of guided ultrasonic wave modes propagating in an elastic plate. Lamb waves propagating in a plate of thickness $2h$ are defined by the mode phase velocity $V_p(\omega)$, obtained from the dispersion relation [6]:

$$(k^2 - q^2)^2 cos(ph + \alpha) sin(qh + \alpha) + 4k^2 pq\ sin(ph + \alpha) cos(qh + \alpha) = 0, \quad (1)$$

where the wavenumbers p and q are given by:

$$p^2 = \frac{\omega^2}{V_L^2} - p^2 \text{ and } q^2 = \frac{\omega^2}{{V_T}^2} - k^2 \quad (2)$$

Here, k is the frequency-dependant angular wavenumber ($V_p(\omega) = \omega/k$) and V_L and V_S are respectively the longitudinal and shear bulk wave velocities of the material. Symmetric ($\alpha = 0$) and antisymmetric ($\alpha = \pi/2$) solutions are provided by the roots of (1) and correspond to the dispersion curves of the different Lamb modes, which can be represented as phase and group velocity as a function of the product of frequency and plate thickness. As an example, figure 1 shows the dispersion curves calculated for an aluminum plate.

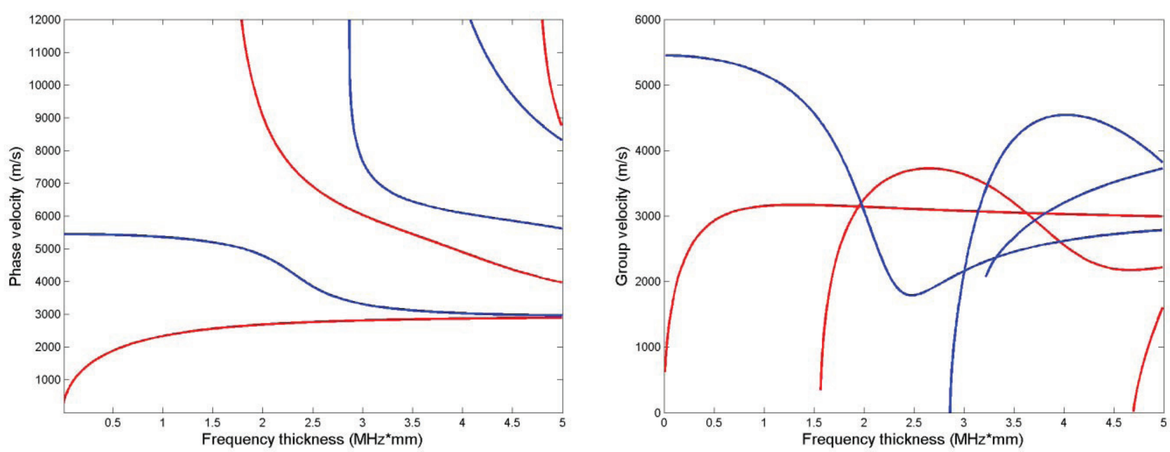

(a) **(b)**

FIGURE 1. (a) Phase and **(b)** Group velocity dispersion curves of an aluminum plate (V_L = 6348 m/s; V_T = 3133 m/s).

One of the common ways to generate Lamb waves is to use an angle wedge with the angle selected considering a refracted angle of 90° in Snell's law of refraction:

$$\theta = sin^{-1}\left(\frac{V_W}{V_P}\right) \tag{3}$$

where V_W is the wedge longitudinal velocity and V_P is the phase velocity of the selected Lamb mode at the selected frequency. Figure 2 illustrates the beam divergence of Lamb waves in an isotropic plate as a function of the wedge incidence angle.

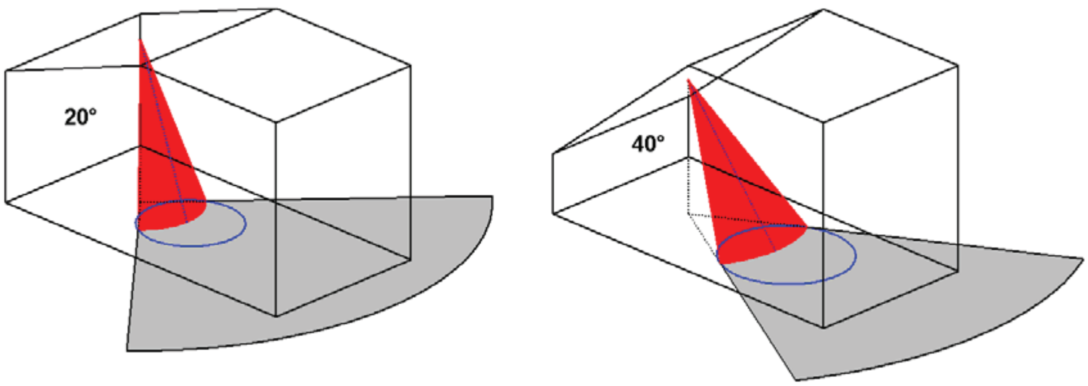

(a) (b)

FIGURE 2. Illustration of a conic wave beam projected on the plate and the subsequent Lamb wave beam for incidence angles of **(a)** 20° and **(b)** 40°. The filled section in the wedge corresponds to a constant incidence angle within the incident beam, while the flat filled area corresponds to the Lamb wave field.

PHASED ARRAY THEORY

The principle of phased array imaging is based on the phase matching of waves propagating through different paths by applying proper delays on the wave generation and/or reception. The ability to focus at a certain point within a material resides in the application of individual delays on each element of the array in order to create a constructive interference of the waves at the desired point. This implies and requires some level of beam divergence from the array elements, which is generally not problematic. The delays can be applied at both the wave generation and reception, and they can be computed from a simple ray tracing approach.

The time delays requiring to be applied at wave generation (Δt_T) and reception (Δt_R) are computed relative to the time-of-flight of the element that is closest to the focal target (the time delay of this element is zero). If Δr is the difference between the propagation path from the current element to the target focal point and the propagation path between the target point and the closest array element, then the time delays are calculated using the wave velocity V within the material as:

$$\Delta t_{T,R} = \frac{\Delta r_{T,R}}{V} \tag{4}$$

with indices T and R representing wave generation and reception respectively. The principle of phased array focusing is illustrated in figure 3.

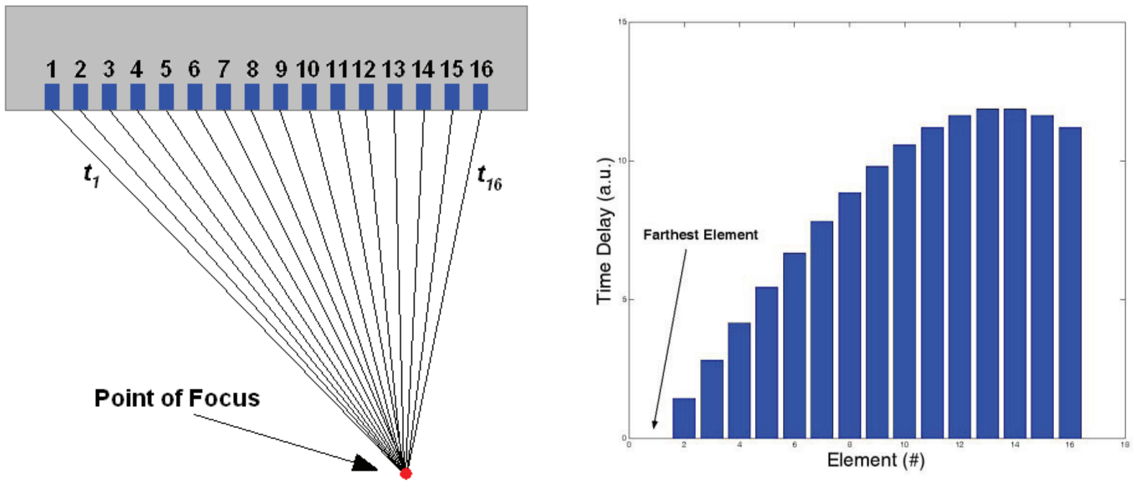

(a) (b)

FIGURE 3. Illustration of the generation and reception delays for of phased array focusing at a given point using a linear array. **(a)** 16 element linear array with time-of-flights t_h necessary to reach the desired point of focus (without delays); **(b)** Example of delays that need to be applied to the array of (a) in order to synchronize the time-of-arrival of each waves at the defect position.

GUIDED WAVES FOCAL LAW CALCULATOR

Guided waves require particular calculations in order to obtain the proper focal law delays, as presented in an earlier work [5]. A focal law calculator was developed with the ability to calculate delays for guided Lamb waves focusing (figure 4).

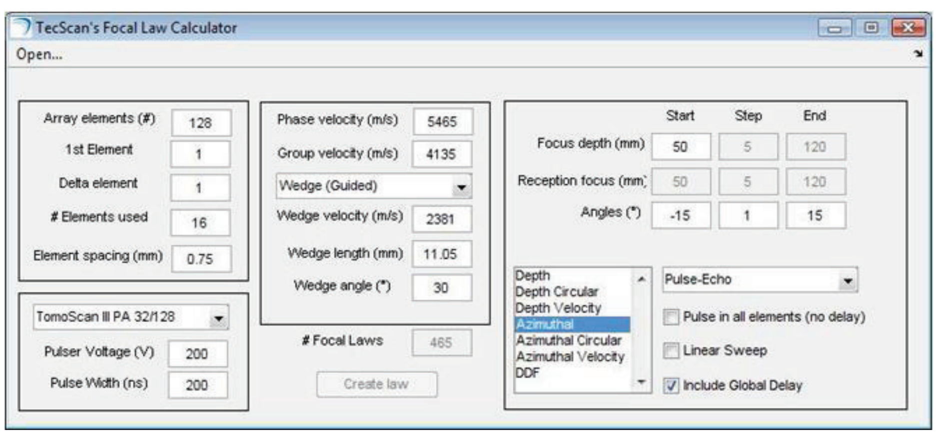

FIGURE 4. Interface of the focal law calculator developed for guided waves focusing.

EXPERIMENTS AND RESULTS

For our experiments, a TomoScan III PA 32/128 unit was used to perform guided wave focusing. A 2.25 MHz array probe with 128 elements and pitch of 0.75mm (2.25L128-I3) was mounted on a 30° LOTEN wedge to generate and receive the guided Lamb modes (figure 4a). The first set of experiments was conducted on a 1.82 mm thick, 302 stainless steel plate with simulated corrosion pitting (1 mm deep FBH with a diameter of 3 mm). The objective of these tests was to demonstrate the potential imaging capabilities of phased array with multiple reflectors.

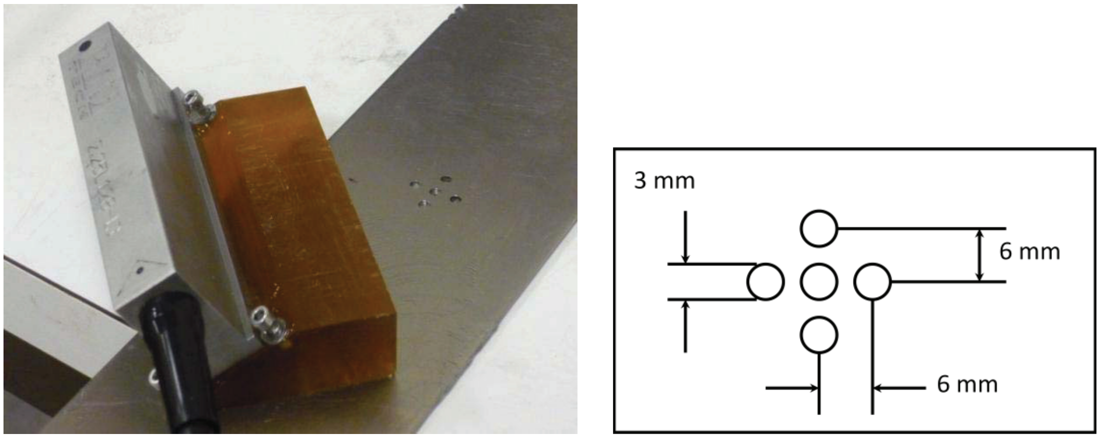

(a) (b)

FIGURE 4. (a) Picture of the array and wedge on the stainless steel sample. **(b)** Dimensions and separation of the simulated pits cluster.

A comparison between standard B-Scan and phased array imaging was performed using the A_1 mode in the stainless steel plate around 2.21 MHz. Depth focusing was performed at 25 mm using 16 elements of the array to do a linear scan across the array. Figure 5 shows the results obtained (a) from a B-Scan performed using 1 element at a time (~0.75 mm wide transducer, no delays) across the array, (b) from phased array focusing at 25 mm, and (c) from a B-Scan perform using 8 elements at a time (~6 mm wide transducer, no delays) across the array. The first B-Scan (1 element – figure 5a) show the defect cluster with a very low SNR and show the cluster as a single indication. The B-Scan obtained with 8 elements (figure 5c) provides some indication of the shape of the defect cluster by displaying a cross pattern, but defect separation is once again impossible. The phased array result in 5b however does display a clear defect separation and a strong SNR for all five defects.

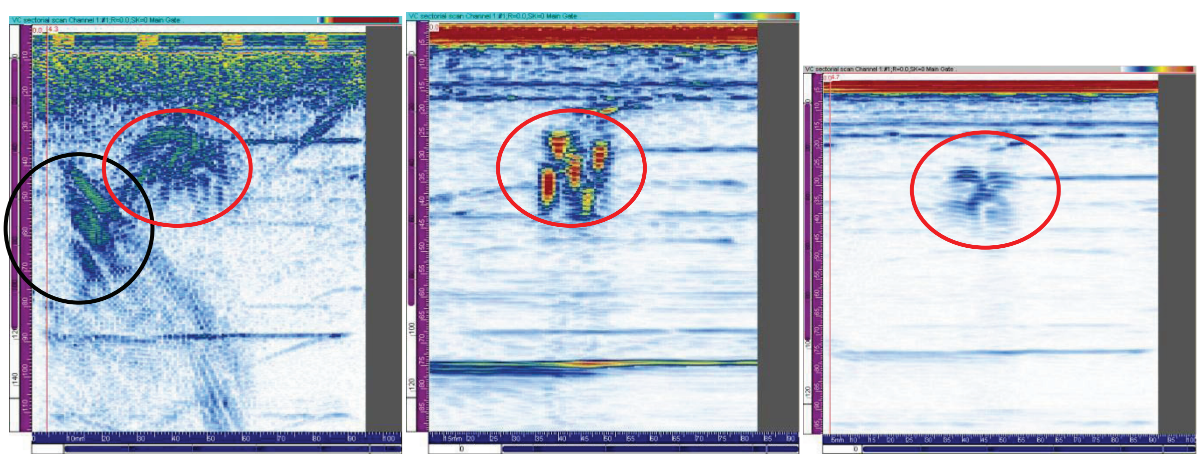

(a) (b) (c)

FIGURE 5. (a) B-Scan obtained from a linear scan using 1 element. **(b)** Linear scan (16 elements) with a focusing depth of 25 mm. **(c)** B-Scan obtained from a linear scan (8 elements, no focusing). Defects are encircled in red, specimen edge reflections are encircled in black.

A second linear scan (16 elements) and a sectorial scan (32 elements) were also performed on the same sample at a greater distance from the defects (50 mm), as shown in figure 6 (a) and (b) respectively. Again, these results demonstrate the validity of the method and the benefits of focusing guided waves to improve defect detection and imaging; four of the five FBH can be easily identified while traces of the fifth FBH can also be observed. It should be noted that additional indications appear in the results, which are artifacts resulting from internal reflections due to the geometry of the wedge that was used.

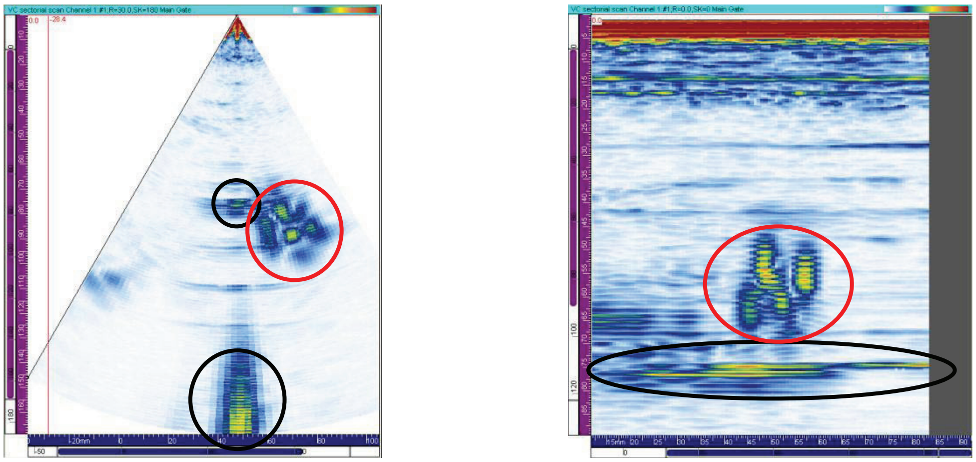

(a) **(b)**

FIGURE 6. (a) Picture of the array and wedge on the stainless steel sample. **(b)** Dimensions and separation of the simulated pits cluster. Defects are encircled in red, wedge artifacts are encircled in black

The results in figure 5 highlight the benefits of phased array focusing in this case; both the signal-to-noise ratio of the defects and their separation was increased by phased array focusing and imaging.

The second set of experiments aimed at verifying the potential in detecting and sizing EDM notches in thin plates. The example presented here is an eddy current reference standard composed of two riveted 1.02 mm thick (0.040") aluminum plates containing a total of 6 rivets. Four EDM notches are present in the sample with lengths of 6.35 mm (0.250"), 5.08 mm (0.200"), 3.81 mm (0.150") and 2.54 mm (0.100"), as illustrated in figure 7. In that case, the S_0 Lamb mode was used for the imaging at 1.93 MHz.

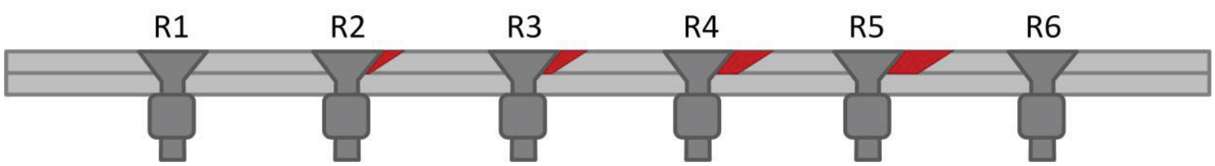

FIGURE 7. Illustration of the riveted plates and the EDM notches in the top layer plate. Notches are present in rivets R2 (2.54 mm), R3 (3.81 mm), R4 (5.08 mm) and R5 (6.35 mm).

A sectorial scan (32 elements) was performed on rivets R1 to R5 at a focal depth of 40 mm. Figure 8 presents the results obtained on the EDM notches. Please note that all rivets were inspected by centering the array on the EDM notch, not the rivet itself, with the expection of rivet R1, which does not have any defect around it. As it can be observed on figure 7, the EDM notches signals are very strong when compared to the reflection from the rivet hole itself and their lateral size increases coherently with that of the real notches. Plus, indication coming from the rivet hole and from the EDM notch are fairly well separated, especially for rivet R5, as it illustrated in figure 7f. This leads to a possible interresting application of guided waves focusing, where cracks could be detected around rivets.

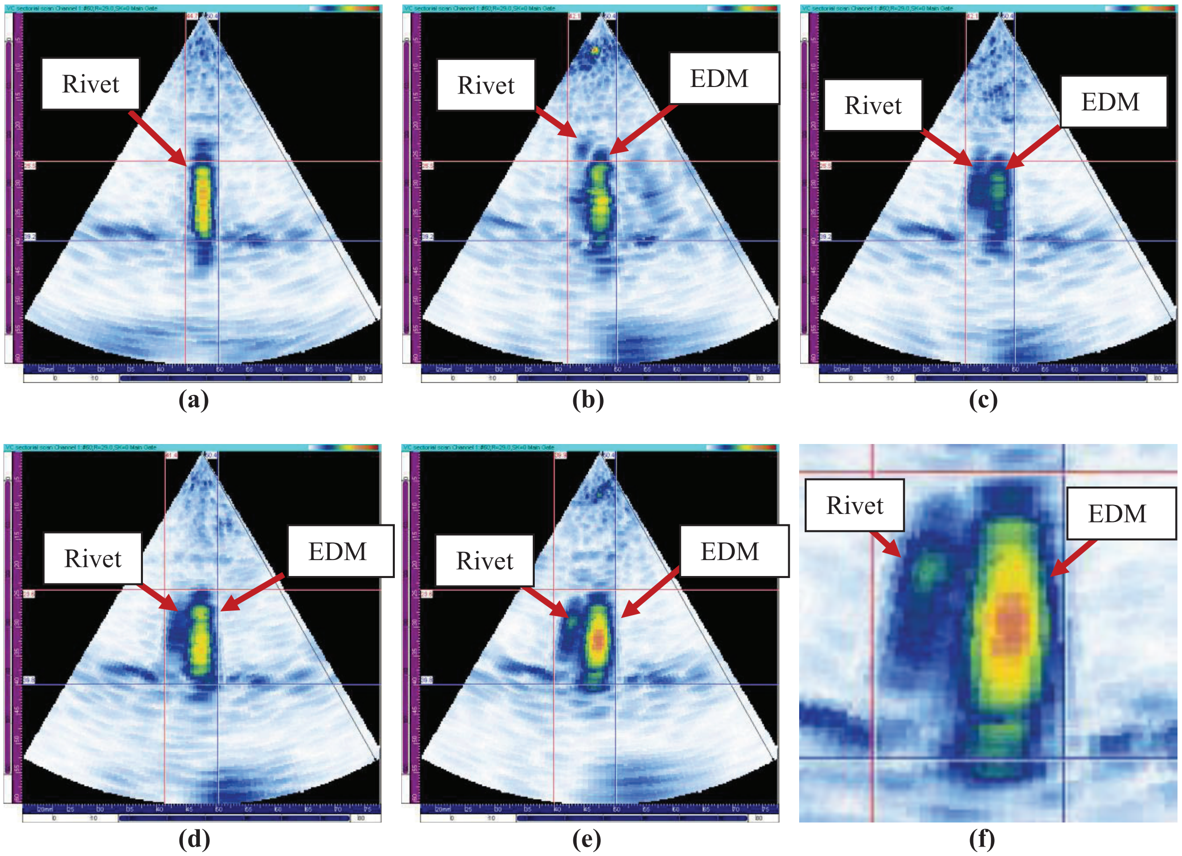

FIGURE 8. Sectorial scan (focal depth of 40 mm) obtained on rivet **(a)** R1; **(b)** R2; **(c)** R3; **(d)** R4; **(e)** R5. **(f)** Enlarged view of the rivet R5 and its associated EDM notch.

CONCLUSION

In this paper, we have shown the applicability of phased array focusing to guided waves in plates using the angle wedge method. The developed guided waves focal law calculator was successfully tested for linear and sectorial scans for multiple scans performed using a commercial phased array instrument. A cluster of FBH simulating corrosion pitting was successfully detected and displayed in a 1.82 mm stainless plate, and phased array focusing proved to increase both the SNR and the ability to separate individual reflectors when compared to conventional B-Scan imaging. EDM notches of lengths ranging from 2.54 mm to 6.35 mm were also successfully inspected and detected by performing phased array focusing of the S_0 mode in the upper skin of a 2-layers, riveted aluminum eddy current reference sample. Experiments showed strong reflections from all notches when compared to the reflection from the rivet hole itself, leading to a potential application of the technology.

ACKNOWLEDGEMENTS

TecScan would like to thank Zetec Inc. (Quebec facilities) for the utilization of their phased array unit and array probe.

REFERENCES

1. Wright, W., Hutchins, D., Jansen, D. and Schindel, D., *IEEE Trans. Ultrason., Ferroelect., Freq. Contr.*, **44** (1), 53–59, (1997).
2. Malyarenko, E. V. and Hinders, M. K., *Ultrasonics*, **39**, 269–281, (2001).
3. Sicard, R., Chahbaz, A. and Goyette, J., *IEEE Trans. Ultrason. Ferroelec. Freq. Cont.* **51** (10), 1287-1297, (2004).
4. Wilcox, P. D., *IEEE Trans. Ultrason., Ferroelect., Freq. Contr.*, **50** (6), 699–709, (2003).
5. Sicard, R., Serhan, H., *Review of progress in QNDE, AIP Conf. Proc.*, Vol. 894, pp. 185-192 (2007).
6. D. Royer and E. Dieulesaint, *Elastic Waves in Solids I, Free and Guided Propagation*, Berlin: Springer-Verlag, 2000, chap. 5.

Ultrasonic evaluation of friction stir welds and dissimilar intermixing using synthetic aperture focusing technique

D. Lévesque[1], L. Toubal[1], X. Cao[2] and L. Dubourg[2]

[1]Industrial Materials Institute, National Research Council Canada, Boucherville, Quebec, Canada
[2]Aerospace Manufacturing Technology Centre, National Research Council Canada, Montreal, Quebec, Canada
Phone: (450) 641-5240, Fax: (450) 641-5106, e-mail: daniel.levesque@cnrc-nrc.gc.ca

Friction stir welding (FSW) is a recently developed solid-state joining process that uses a specially shaped rotating tool to produce lap or butt joints. At the National Research Council, an inter-institute collaboration was started in 2007 with the goal of exploiting the NDE expertise and applying it for the characterization of friction stir welds for various industrial applications. In particular, very good performance was obtained using ultrasonic immersion or laser-ultrasonics combined with the synthetic aperture focusing technique (SAFT) for detecting lack of penetration in butt joints, discontinuities such as wormholes and hooking in lap joints. Dissimilar metal welds of aluminum and magnesium by FSW are also considered for automotive and aerospace applications. Complex vortex flows are produced during the FSW process that may create intercalated lamellar structures with the possible formation of intermetallic compounds, causing variable hardness and degradation in mechanical properties. A modified version of SAFT that takes into account the difference of ultrasonic velocity in the joint between that of Al and Mg has been developed to study the dissimilar intermixing. Welded samples in the butt configuration with different welding speeds and seam offsets are tested using the immersion technique with the modified SAFT. Results will be presented for both defect detection and weld characterization, and the capabilities and limitations will be discussed.

Standard compliance - NDT performance demonstration in the CANDU industry

Evan Choi, **P.Eng.**
Project Manager – CANDU Owners Group

Abstract: *CANDU nuclear power plants are operated in 3 provinces in Canada for electric power generation. A table in the paper will show the built and operating plants in Ontario, Quebec, New Brunswick and overseas. The regulator for nuclear power in Canada is the Canadian Nuclear Safety Commission (CNSC). The CNSC holds the plant licensees accountable for compliance to CSA N285.4 for periodic inspections. The Standard basically specifies the "what, when, where, how, how much and how frequently" NDT is to be done on pressure retaining systems and components in CANDU nuclear power plants. In inspection methods, the Standard specifies they must be non-destructive. The NDT methods were grouped into visual, dimensional, surface, volumetric and integrative. The Standard also specifies that the licensees are responsible for the performance demonstration (PD) of the adequacy of the procedures and the proficiency of the personnel.*

This paper describes the Standard's requirement in NDT PD and presents a joint project participated by Canadian and overseas CANDU owners. The sub-project for NDT included providing evidence and technical justification on the adequacy of the procedures and the proficiency of the personnel. The paper describes the PD methodology followed by the participants. This will be followed by how the participants produced Inspection Specification, tools and procedures, personnel training and qualification programs, test and qualification samples, independent peer reviews and Technical Justification.

Introduction of CANDU, its Regulator and Governing Standard for Inspection

CANDU is the Canadian designed pressurized heavy water reactor (PHWR) used in Ontario, Quebec, New Brunswick and several countries in the world for electric power generation. As of 2009, there are 25 operating CANDU reactor units in the world. In addition, there are 13 similar design PHWR units operating in India. CANDU users and India's NPCIL are members of the CANDU Owners Group (COG). There are 2 units in Ontario Power Generation's (OPG) Pickering A plant that are laid up, and there are 10 other CANDU or PHWR units around the world being refurbished or under construction.

Table 1 below lists the COG member utilities, the number of operating units, laid-up units and under construction or refurbishment units.

The nuclear industry is regulated by individual country's regulator. In Canada, the regulator is the Canadian Nuclear Safety Commission (CNSC).

The Standard that governs periodic inspections of critical components in CANDU reactors in Canada is the CSA N285.4[1]. The current version of the Standard is the 2005 version. In this paper, the terms CSA N285.4-05 and the Standard will be used interchangeably.

	COG Members	Operational Units	Laid-up Units	Units under Construction/ Refurbishment
	BP(LP) Canada	6		2
	HQ Canada	1		
	NBPN Canada	0		1
	OPG Canada	10	2	
	NASA Argentina	1		
	SNN Romania	1		1
	KHNP Korea	3		1
	TQNPC China	2		
	NPCIL India	13		5
	PAEC Pakistan	1		
	AECL Canada	-		
	Totals:	38	2	10

Table 1 List of CANDU and PHWRs

Periodic Inspection for CANDU Reators

CSA N285.4 specifies the periodic inspection requirements for pressure retaining systems and components such as pipe, nozzle and vessel welds. It also includes mechanical couplings, pump and valve welds and supports. There are also supplementary section specifically for pressure tubes, feeder pipes and steam generators.

The Standard calls for inspection methods that are “non-destructive”, hence it includes NDT methods such as visual & dimensional (direct or using visual aids), surface test (PT & MT), volumetric (RT, ET and UT) and integrative (leak test, acoustic emission and strain gauge).

When stating NDT requirements, the Standard generally specifies the what, when, where, how, how much and how often for the in-scope components.

NDT Qualification and Performance Demonstration

In the CSA N285.4-05 Standard, it specifies that NDT must have “performance demonstration” (PD) and it puts this responsibility to the licensee (clause 3.6). In other words it holds the power utility, such as OPG who holds the licenses to operate, responsible for providing evidence that the NDT done on the components are performance demonstrated. The responsibilities of the licensees include, in clause 3.6d, verification of the qualification and proficiency of inspection personnel; and in clause 3.6e, PD of the adequacy of the procedures & proficiency of the personnel using assigned equipment, to detect & size flaws. PD is therefore a dynamic combination of 1) procedure, 2) qualified personnel and 3) equipment; and the capabilities requiring PD are detecting and sizing.

Although the Standard specifies this PD requirement, it does not specify how to conduct PD and how to present the evidence of PD.

Different ways to conduct PD

In different part of the world and in different jurisdictions, NDT PD has been conducted with various methodologies and approaches in the nuclear power industry. The more significant PD programs are the European Network for Inspection Qualification (ENIQ)[2] and Performance Demonstration Initiative (PDI) administered by Electric Power Research Institute (EPRI) in the USA. Table 2 below lists some key differences between methodologies:

Inspection Specification	ASME XI	PDI administration of ASME XI	ENIQ	IAEA
Components	Specified	Specified	DBO	DBO
Flaw types/size	Specified	Specified	DBO	DBO
Acceptance Criteria	Specified	Modified to meet technical need	DBO	DBO
Effectiveness / Reliability Criteria	Included in Design	Included in Tech Basis for Code Modifications	Should be in TS	Should be in TS
Technical Justification	Embedded in Code	PDD and Technical Basis	Required	Required
Practice & Procedure Development	Not addressed	yes –samples provided-(A)	Could use open procedure trial	Could use open procedure trial

Inspection Specification	ASME XI	PDI administration of ASME XI	ENIQ	IAEA
Procedure Trials	Blind	Blind – with feedback	Blind or open	Blind or open
Personnel qualification	Blind (C)	Blind – with feedback (C)	Blind	Blind
Independent Qualification Body	Not addressed	Yes	Required	Required
Documentation of Qualification	To be determined by organization	PDD, Procedure, Essential variables, Demo Records	Dossier -	Dossier -

Table 2 comparison of major PD Programs

PDD = Program Description Document (includes compliance comparison, deviations from Code and TJ for deviations)
Open = has knowledge of specific flaw size shape and location
Blind = without knowledge of flaw size, shape, location or quantity
DBO = Developed by Owner
(C) Individuals who qualify the procedure can receive personnel qualification

In a generic sense, the principle of a PD process should contain at least the following major milestones (or a similar variation of them):

1. An Inspection Specification (IS) written by experts on a component. The expert should have assessed the fitness-for-service (FFS) criteria and determine the extent and detail of NDT results required to conduct the proper assessment. The specified extent and detail should include, but not limited to:

   - "what" and "where" to inspect, including surface and volume coverage requirements,
   - the types of degradations to look for,
   - results repeatability, accuracy, or error tolerance,
   - probability of detection,
   - reportable and rejectable criteria,
   - results reporting requirement and format.

2. Based on the IS, the NDT practitioners develop and write the Inspection Procedure (IP) including specifying the method and equipment. The IP targets to meet the requirements in the IS and it will be tested and qualified in laboratory sessions. To complete the procedure qualification, NDT personnel training and qualification will be included.

3. A Technical Justification (TJ) will be written by the NDT practitioners. The TJ will refer to evidence collected from IP development, training and qualification exercises, field use experiences and destructive examination results (if available); to declare how well the IP, equipment & personnel combination meets the requirements in the IS. The TJ may state exceptions where some of the IS requirements cannot be met, or can only be met partially.

4. Finally, the whole process is subject to an independent peer review. Usually a panel of experts will be assembled to review the PD process. Members of the panel should not have been directly involved in the process of steps 1-3 above. The panel will issue an assessment report based on its observations and the technical arguments in the TJ. There will be back-and-forth interaction between the author(s) of the TJ and the Panel to address comments and questions raised.

Some necessary tasks during the PD process

During the development of the IS, the FFS experts may or may not consult the NDT practitioners on the limitations of NDT. There are pros and cons in this respect. If NDT practitioners were not consulted, the IS may specify requirements that is not achievable by present or foreseeable NDT capabilities. On the other hand, if NDT practitioners were consulted, the quality of FFS analysis may be limited by whatever results current NDT capabilities can provide.

During the development of the procedure, test samples will be designed and made and specialized calibration blocks will be made if necessary. After the procedure has been technically qualified, the next task is to train and qualify NDT personnel. To do that, a training package including documents and other materials has to be designed and fabricated. A training program will be developed within which pass/fail criteria will be specified.

NDT personnel will be trained and qualified. The qualification process includes open or blind tests. The independent peer review panel may be present during the training and testing. The panel may even select trainees to run through its own set of testing.

A dossier of all the documents produced during the PD process will be assembled and file. Finally, a formal submission may be made to the Regulator for its acceptance of the PD evidence and process.

The CANDU Independent Qualification Bureau

COG has established a CANDU Inspection Qualification Bureau (CIQB). CNSC has recognized the COG CIQB as a qualification body. The CIQB has started full operating since 2008.

An example of a PD submission to the CNSC

The example is a project jointly participated by Canadian, Korean (KHNP) and Romanian (SNN) members of COG. The component is the CANDU reactor's feeder pipes. Feeders of concern are 2" and 2.5" schedule 80 carbon steel pipes circulating PHT water in and out of the reactor fuel channels. Flaw types are Flow Accelerated Corrosion (FAC) thinning, and cracking at bends. NDT method used is UT.

Inspection tools are mostly remote controlled or automatic mainly because the inspection is operated in a very high radiation dose rate area (right at the reactor faces). Reliability and accuracy of the results are critical because confirmed rejectable flaws could cause replacement of the feeder – an operation that is expensive and which causes significant outage extension. Accuracy of wall thickness measurement and location repeatability are crucial because thinning trends are monitored to predict remaining life.

Inspection tools

The IPs and tools were developed under the COG joint project NDT sub-team. The NDT sub-team consists of representatives from AECL, BPLP, HQ, KHNP, NBPN, OPG and SNN. Photographs of some of the inspection tools are shown below:

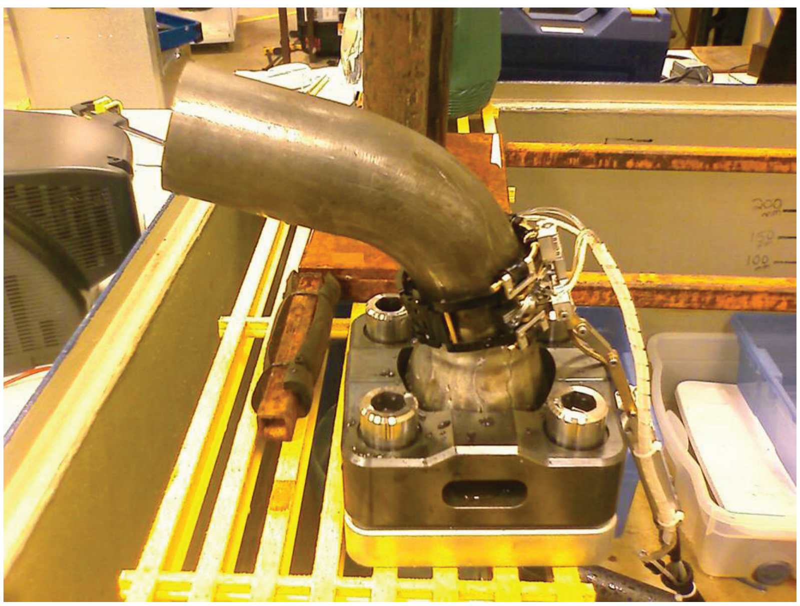

The bend crack crawler (BCC) mounted on a mockup is being tested at the factory.

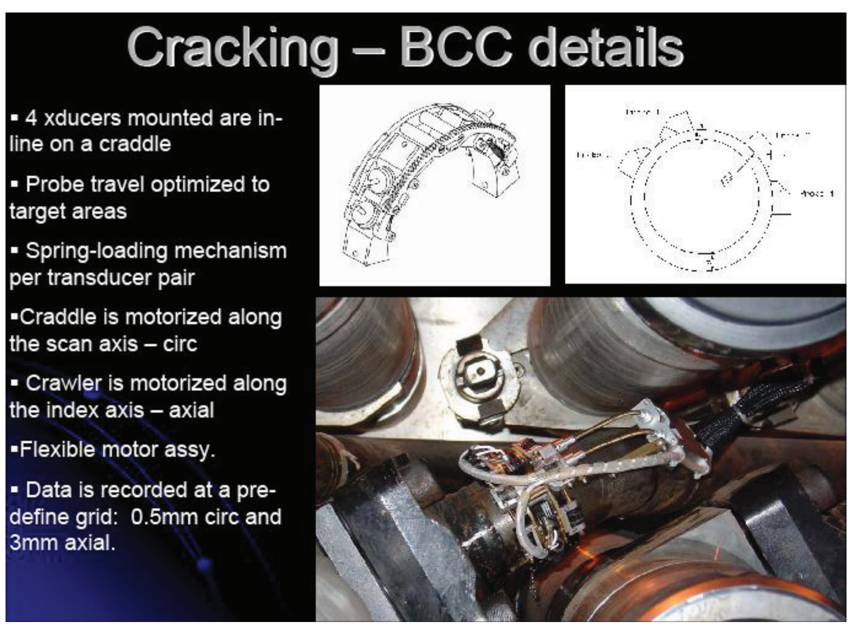

The BCC mounted on a real feeder pipe about to to start a crack detection inspection.

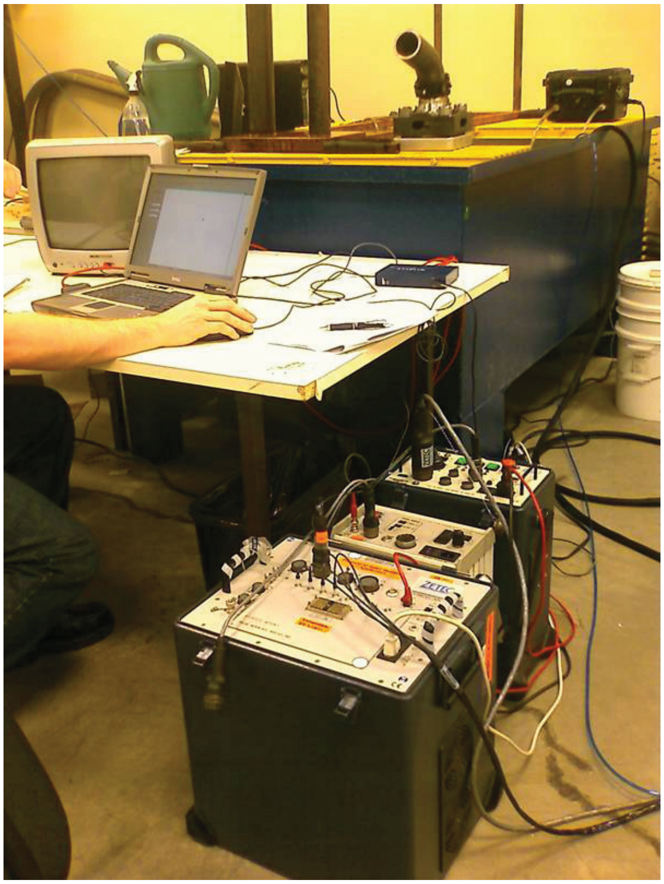

This picture shows the electronic instrumentation operated through a note-book computer.

A thickness measurement crawler. This picture shows drive-wheels, U-joint, an array of UT probes. There is a sample feeder beside the crawler.

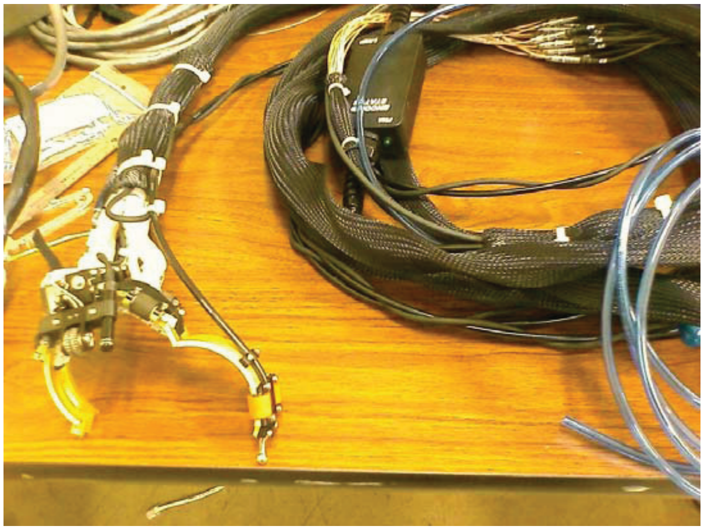

Another view of the thickness measurement crawler. This view shows the encoder and the front-viewing camera

The Grayloc Area Inspection Tool (GAIT) for inspecting for wall thickness right adjacent the Grayloc hub weld.

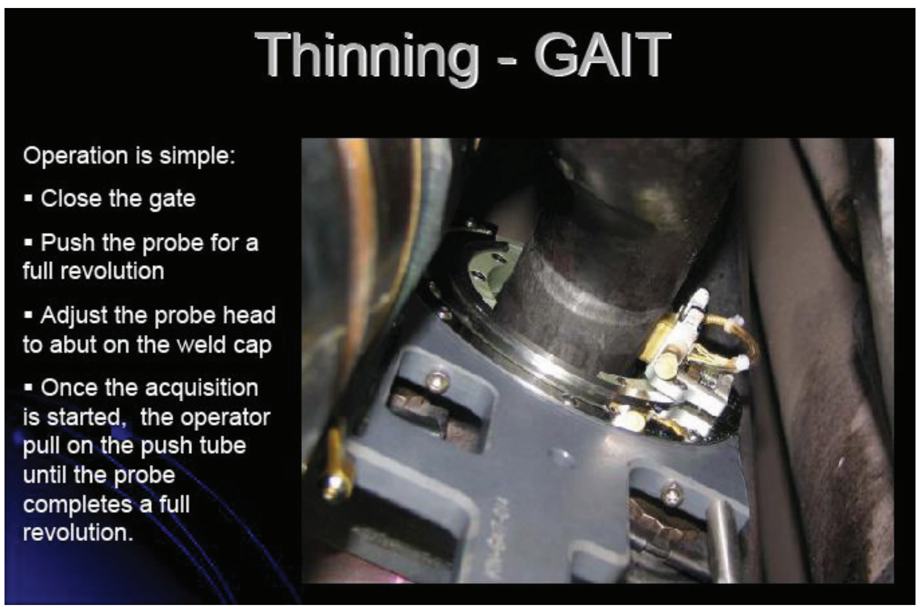

The COG joint project PD submission

Participants of this joint project have chosen the ENIQ PD methodology. A common industry IS was written by a joint FFS team. Procedures and tools were developed by industry qualified NDE engineers and technicians. Guided practice test pieces and calibration blocks were designed and produced.

Training program and material were developed. Participants and service providers conducted and/or received training of NDT personnel in Canada and from Korea. Trainees passed qualification test. The training and qualification processes was audited and reviewed by CIQB. Numerous real inspection campaigns were subsequently conducted. Many destructive examinations were performed to compare to the NDT results. These field experiences and finding were included or later added to the TJs.

Two TJs were written – one for thickness measurement and one for crack detection. The TJs were reviewed by CIQB. Comments were addressed and then the TJs were finalized. Two document dossiers were assembled – again, one for thickness measurement and one for crack detection. OPG took the TJs and made a formal submission to CNSC in 2004. CNSC reviewed it and later contracted an external consultant to further review the submission. CNSC accepted the submission.

Conclusion

It is a regulatory and CSA N285.4-05 compliance requirement for NDT to be performance demonstrated. Nuclear power plant licensees are responsible for meeting this requirement. COG established the CIQB and it has been recognized by the Regulator. COG administered a joint project to successfully complete the PD requirement for the NDT of one of the reactor's most critical component. The ENIQ methodology was proven to be adaptable to specific development suitable for feeder inspection.

This experience is very valuable to the CANDU licensees and CIQB in executing present and future PD projects.

References:

1. *CSA Standard N285.4-05 Periodic Inspection of CANDU nuclear power plant components. Published in June 2005 by Canadian Standards Association.*

2. *European Methodology for Qualification of Non-Destructive Testing - Third Issue - August 2007 ENIQ Report nr. 31 EUR 22906 EN.*
   http://safelife.jrc.ec.europa.eu/eniq/docs/method/ENIQ_31.pdf

Best Practices for Personnel Certification

Larry Cote CET, CLS, CMRP
Managing Director
Canadian Institute for NDE (CINDE)

Abstract
The term "best practices" was introduced to the author when he worked in the steel industry on quality improvement and reliability improvement projects. Best practices are not as esoteric as "World Class performance", nor are they as mundane as a "standard operating procedure" The term denotes a well thought out approach to achieve an important goal by using every good idea possible to "do the right things" and just as importantly, to "do the right things well"

This paper provides an overview of why personnel certification schemes were started and are still needed. Influences and issues affecting personnel certification programs are discussed, along with some best practices to address them. Examples to illustrate the best practices are provided from a variety of personnel certification schemes for different occupational areas.

Introduction
The amount of knowledge in the world has grown exponentially over the last several hundred years. It has been so explosive that "pencil and paper" institutions and "bricks and mortar" companies of the 19th century face serious challenges from competitors that only exist in a virtual sense within the realm of digital technology. This relatively new technology is enabled, aided and abetted by computers, software and the Internet. As the world becomes increasingly digitized and globally connected, individuals and their organizations must adapt to survive in the information age. For those that do, significant opportunities exist. For those that don't, problems leading to their demise may be imminent.

Countries such as the United States, Canada, Britain and Australia that have the aging population demographic ubiquitously known as the "boomer generation" can be said to have two types of "immigration". The first is immigration in the traditional sense whereby people from other countries arrive to become citizens in a host country. The benefit to the immigrant is personal opportunity to improve their lot in life. The benefit to the host country is to have a workforce that can support economic growth that could otherwise not be maintained by the host country's fertility rate and birth rate. However, this has introduced a significant amount of cultural diversity to the host countries, which sometimes creates problems due to the native residents of the host country misunderstanding the culture of their new citizens. And the new citizens sometimes struggle; as they perceive that their cultural identity is being assimilated into the culture of their new home.

On a different note, Marc Prensky defines a second type of "immigration" that has produced a digital immigrant. [1, 2] Digital immigrants are the people born into the analog world before the personal computer (PC) was invented. They either became fascinated with PC's and wanted to use them as they became mainstream, or eventually had no choice but to use them to compete in the job market. The new competition is what Mark Prensky describes as a digital native. A digital native is a person who was born into and grew up as a native speaker of the language of computers, software and the Internet. They are the youngsters who taught their parents how to program the VCR! The differences between digital immigrants and digital natives are vast not only in age. The synergistic growth of knowledge and digital technology extends directly into the fundamental concepts of how people are taught, learn and subsequently demonstrate their knowledge and skills. In terms of their education, Marc Prensky asserts, *"Our students have changed radically. Today's' students are no longer the people our educational system was designed to teach.* But this is not just a joke. It is very serious, because the single biggest problem facing education today is that *our Digital Immigrant instructors, who speak an outdated language (that of the pre-digital age), are struggling to teach a population that speaks an entirely new language."*

The growth of digital technology, cultural diversity and demographic differences are exerting tremendous pressure on everyone in the business of education, training and personnel testing. It has become imperative for people in leadership positions to adapt what they do, and how they do it, to meet the needs of the next generation workforce. To that end a best practices approach for education, training and personnel certification is more than sensible, it is practically mandatory and should be always be investigated. Otherwise the education, training and personnel certification programs so highly regarded to date might suffer the same fate as phonographs, LP records, 8-track cassettes, Walkmans, CD's and DVD's, i.e. will people want to keep using them?

What is Certification?
A definition of certification found on the Internet is: [3]
• the act of certifying or bestowing a franchise on.
• validating the authenticity of something or someone.
• a document attesting to the truth of certain stated facts.

And a standard dictionary definition is: [4]
• The act of certifying or guaranteeing.
• The state of being certified.
• A certificate.

In addition to the definitions above, the context of this discussion is further assisted by the description of a personnel certification body as provided by the Standards Council of Canada, which is: *Personnel certification bodies provide services for many professional and trade persons such as auditors, welders, and doctors. The role of certification bodies involves assessing the individuals'*

necessary competencies, and ensuring these are appropriate to the work being performed. [5]
Another organization that defines a professional credentialing is the National Organization for Competency Assurance (NOCA). In the publication "Guide to Credentialing Concepts" [6] primary author Cynthia C. Durley notes, *"There are 5 major criteria that distinguish a professional credentialing (certification, licensure or registration) examination from an end-of-course examination:"*

1. A professional role delineation or job analysis is conducted and periodically validated.
2. A demonstration of how the examination is linked to a defined body of knowledge, based on the professional role delineation or job analysis, is provided.
3. A demonstration of reliability and validity of the examination, based on psychometrically accepted statistical methods, is provided.
4. A minimum passing score is developed psychometrically accepted statistical methods.
5. When a professional credentialing examination is part of a professional certification, credential maintenance or recertification is (or should be) required.

The Value Proposition for Certification

In the early 1900's many countries underwent a massive shift from an agricultural economy to a manufacturing economy. The new manufacturing economy replaced craftsman who produced something from start to finish, with assembly line workers who worked on just some portion of an overall product. One problem with the new assembly line method was that defects produced in one area were passed along to create a problem in another area, or even worse, to the customer. This was remedied by the introduction of a new job, that of the Inspector. The originator of the modern scientific management movement, Frederick Winslow Taylor, described the new role in 1911 as: *"The Inspector is responsible for the quality of the work, and both the workman and (speed) bosses must see that the work is all finished to suit him. This man can, of course, do his work best if he is a master of the art of finishing work both well and quickly"* [7]

Many years later, personnel certification schemes serve to ensure many more people, not just limited to Inspectors, can live up to today's version of Frederick Taylor's original expectations. The people being certified are pilots, doctors, nurses, financial planners; fitness trainers and educators, to name just a few. They are often known as technicians, practitioners or subject-matter-experts (SME's). They gain value from the professional development they first undertake to become certified, and the additional professional development they need to remain certified. Their certification has value because it credentials the special knowledge, skills and competencies that often can't be attested to by an academic diploma or degree. Personnel certification programs can be indispensable in discriminating between "people who <u>know and can do</u>" and "people who <u>don't know and cannot do</u>". For example, the Society of Tribologists and Lubrication Engineers (STLE), after almost 10 years of development, in 1994 launched the Certified Lubrication Specialist (CLS) program in direct response to requests from people employed in the lubrication business who wanted a way to raise their profile and demonstrate the expertise brought to their profession.[8] People seek certification in high risk occupations such as finance, investment banking, healthcare, education, aerospace, civil aviation, power generation, oil and gas exploration, refinery operations, petrochemical processing, boiler and pressure vessel manufacture and operation, and the military. The public at large places value on the skills of people who have been certified in those occupations because of their expertise.

Some people see value in pursuing multiple levels and types of certification. Their motivation often stems from wanting a holistic understanding of a subject, or to be outstanding in the job market, or to have the self-satisfaction of demonstrable achievement. Hence personnel certification bodies deliver value by developing and maintaining personnel certification programs to ensure employers and the public confidently benefit from the expert and efficient application of knowledge and skills, while enhancing on-the-job satisfaction of the certificants.

The Business Case for Personnel Certification

In addition to the value proposition for personnel certification, there is also a business case, especially when viewed as a risk mitigation strategy. Risk management methodologies are used to deal with hazardous events of low probability but having very undesirable high-impact consequences such as multiple fatalities or environmental damage. When thinking about personnel certification as a risk mitigation strategy, it could be said they deal with two types of human error: 1) having sound knowledge and good skills, but following a bad plan in good faith and getting the wrong result, or 2) not having sound knowledge and using poor skills to produce the wrong result, even while following a good plan. Some of the worst catastrophes of the 20th century that resulted in the loss of human life and millions of dollars of environmental damage are the result of human error. [10, 11] The training and skills development invested in personnel certification can have a return-on-investment (ROI) of several thousand percent, or a payback period of less than days or weeks when calculated for high-risk industries.

Figures One and Two are examples from a risk assessment method known as the tie-line method. While originally developed in the 1970's for the railroad industry in Australia [9], it is used here to simulate the difference in risk levels for the hazards associated with doing something right or wrong. To more accurately put the tie-line method in the context of training and certification, further research and study would be needed to qualitatively and quantitatively assess how human factors and training variables influences error and reliability, and how effectively a personnel certification process "guarantees" or "predicts" competent, accurate and reliable human performance. That is beyond the scope of this paper, but certainly within the means of the organizations seriously engaged in personnel certification.

Figure One – *Tie-line method for Risk Analysis: Case #1*

- Frequently allowed to do work with hazardous consequences.
- Potential for serious injury or damage.
- Almost certain to do something wrong because of poor training and certification testing

= **High Risk**

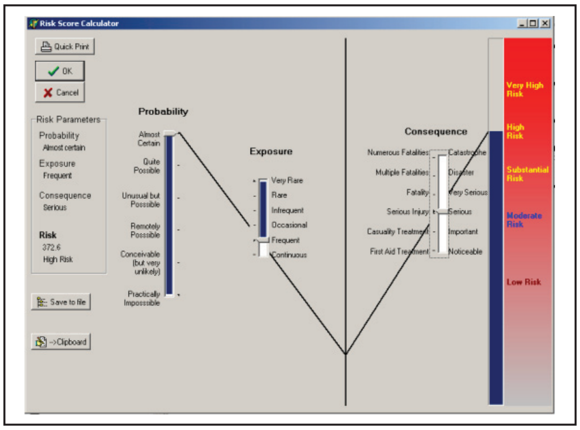

Figure Two – *Tie-line method for Risk Analysis: Case #2*

- Frequently allowed to do work with hazardous consequences.
- Potential for serious injury or damage.
- Practically impossible to do something wrong because of good training and certification testing

= **Low to Moderate Risk**

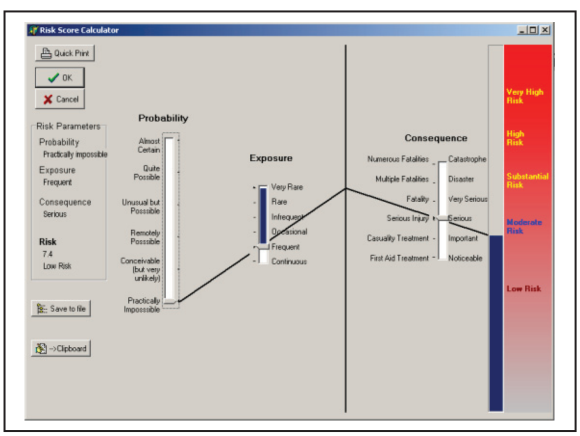

Regulatory requirements are often created as a result of catastrophes affecting the public on a large scale. Even when no regulatory requirements are mandated, industry will often voluntarily become self-regulating and seek out better approaches that include specialized training and personnel certification. For example, the Society of Maintenance and Reliability Professionals (SMRP), after 5 years of development, launched in 1998 the Certified Maintenance and Reliability Professional (CMRP) certification program. It was a direct response to people in manufacturing industries who wanted to identify the skills and competencies needed to improve the reliability of physical assets and reduce the exorbitant costs of unreliable designs and reactive maintenance programs. [12]

Types of Personnel Certification Schemes

A quick reminder is provided as to the various types of personnel certification schemes that are available. They all co-exist in the market place, and that in and of itself sometimes leads to confusion and mistrust in any type of certification at all. The three main types of certification are:

- 1st. Party (self assessment or pronouncement)
- 2nd. Party (supplier or employer assessment)
- 3rd. Party (independent certification body assessment)

While they should all theoretically be able to discriminate between people who know and people who don't, it is the authors' experience that any of them can be diluted or trivialized and rendered irrelevant to the subject domain unless a best practices approach is followed.

Best Practices for Personnel Certification

Complex work involving difficult problems and daunting tasks rarely have one easy, single way to be done. In other words, there is no "silver bullet" for success. This is also true for the best practices for personnel certification. Ignoring or giving lip service to them impugns the integrity of the certification program and disrespects individuals who would place their trust in it. It is far more desirable and meaningful to develop a personnel certification program that embraces all known best practices. With that encouragement in mind, the best practices are:

1. Public domain and access
2. Peer reviewed body of knowledge (BoK)
3. Standards referenced
4. Psychometric analysis of test items
5. Preparation and training
6. Surveillance and renewal
7. Recertification
8. Program accreditation

Following are the rationale for each best practice along with some examples and further references.

1. Public domain and access

Public domain and access is usually intrinsic to personnel certification programs, because personnel certification bodies want people in a given profession to be attracted to their programs. Anyone reasonably competent and familiar with the subject domain should be encouraged to attempt the certification test(s). People should be able to attempt the certification without having to satisfy extraneous obligations such as purchasing a society membership, or paying usurious amounts of money. For example, if membership in a society is a mandatory eligibility requirement for certification, the program works at cross-purposes of membership recruiting and retention versus failing or passing candidates. If the certification process requires excessive and unjustifiable amounts of training, work experience or money, those too will become deterrents that discourage candidates and direct them to inferior options for professional recognition.

For occupations requiring licenses or certification, public domain and access encourages labor mobility so that people can work in their specialized occupation wherever opportunities exist. Many tradespeople must be licensed before they can do their work, and this is analogous to people who need certification before doing theirs. An example of a system that encourages workforce mobility is the Interprovincial Standards Red Seal Program that was established more than 45 years ago in Canada. [13] It is a very good program encompassing hundreds of occupational roles that can be practiced across Canada. It has many ideas for best practice that other organizations can consider. For example, the Red Seal Program acts as a cohesive national umbrella to unify regional requirements for trades people.

2. Peer reviewed Body of Knowledge

The Body of Knowledge (BoK) is also sometimes referred to as a training syllabus. The BoK is a vitally important document because it defines the scope of what is to be taught, tested and sometimes demonstrated for a given subject domain. A panel of subject matter experts who are thoroughly familiar with the necessary occupational skills and competencies initially develops the technical depth and breadth of the BoK. The BoK must be reviewed and updated at regular intervals to remove obsolete content and add new knowledge and skill requirements. It is a key reference that provides an interface between educators, personnel certification bodies and certification candidates. Used correctly, it prevents educators from "teaching the test questions", because they should not know exactly what they are. And the BoK helps certifying bodies test knowledge at the proper level, because of the expertise of the panel of SME's who define and maintain the BoK.

An example of a BoK is provided by the American Society for Quality (ASQ) for its' Certified Reliability Engineer (CRE) program. [14] The CRE exam is developed according to Blooms Taxonomy [15] for the required levels of cognition to be demonstrated for the subject domain. For those unfamiliar with Bloom's groundbreaking taxonomy, it is the division of learning into three domains:

1. the cognitive - knowledge based domain at 6 levels
2. the affective - attitudinal based domain at 5 levels
3. the psychomotor - skills based domain at 6 levels.

Defining the minimum and maximum level of cognition at which a subject must be taught and tested is a complex and challenging process. Mary Forehand revisits Blooms Taxonomy to describe how his original taxonomy of learning levels can be used for developing a BoK. [16] This ensures the challenge level of a certification exam is neither too simple, i.e. tests only lower level knowledge based on recall and rote memorization, nor too difficult, i.e. testing based on inventing new information from abstract theoretical concepts. In general, most personnel certification programs test at the level associated with applying knowledge correctly, and problem solving. Once developed, the BoK must be updated at regular intervals by a panel of SME's. The underlying reasons and the process for this must be understood and respected so that personnel certification remains valid, relevant and fair to everyone involved in any way with the program.

3. Standards and Guidelines referenced

Many standards are available to describe the requirements, guidelines or policies for personnel certification schemes. At the international level, the Committee on Conformity Assessment (CASCO) provides terms, definitions and general requirements for certification programs. [17] The International Standards Organization (ISO) in 2003 released a new standard, ISO/IEC 17024, Conformity assessment - General requirements for bodies operating certification of persons. As described at the time by Dr. Thomas Facklam, the Chairman of the International Accreditation Forum (IAF) and convener of the working group that developed the new standard. *"It provides a uniform set of guidelines for organizations managing the qualifications and certification of persons, including procedures for the development and maintenance of a certification scheme. It is designed to help bodies operating certification of persons conduct well-planned and structured evaluations using objective criteria for competence and grading in order to ensure impartiality of operations and reduce any conflict of interest."* [18]

The ISO standard 9000 for quality management systems is also useful and applicable to personnel certification programs, because ISO 17024 identifies the need to use a Quality Management System (QMS), or similar system. The ISO 9000 standard for QMS's requires employees to receive appropriate training, and for employers to document and measure the effectiveness of the training. Personnel certification programs are a very effective way to satisfy that requirement.

Apart from the standards that are directly applicable to personnel certification programs, many others have been developed for specific occupational areas. They may be international, national or regional in scope, and overlap with or reference other standards developed for specific industries. Like personnel certification programs, standards are often developed in response to a request from industry. For example, the Society of Automotive Engineers (SAE) developed the SAE Standards JA1011 [19] and JA1012 [20] for Reliability-Centered Maintenance (RCM). These are intended for use by any organization that operates physical assets or systems that it wishes to manage and maintain responsibly by using an acceptable RCM methodology. As another example, the American Petroleum Institute (API) publishes a host of equipment and practice standards for the petroleum and petrochemical processing industries. Standards from technical organizations often contain important information pertaining to personnel certification, and for both of the above examples, certification schemes are in place for RCM practitioners and API inspectors.

Standard developing organizations play an important role in guiding the development and growth of personnel certification programs by bringing technical advances in the subject domain, as well as advances in the field of education, training and testing to the attention of personnel certification bodies. Those engaged in personnel certification activities should use standards judiciously. The information and advice provided by a good standard should never be ignored. However, if a standard was developed for a technical context that no longer exists, then it may no longer serve the purpose for which it was originally intended. Rigidly adhering to a standard that is out of synch with current needs and demands will keep a personnel certification program stuck in the past. Fortunately, most standards development organization have mechanisms for updating standards, albeit sometimes very slowly or with great difficulty. Neither should the use of standards be overly rigid, as that could handicap the people operating or using the personnel certification program by preventing them from making sensible use of up to date information and best practices. For example, ISO standards are updated and revised on a 5 year cycle, and this may be too long a period to wait to make changes that make sense.

Therefore as a minimum it is recommended to acknowledge applicable standards and adopt them wherever it makes sense to do so. This can be done within a personnel certification scheme by identifying a standard as a normative or information reference, and following it accordingly. Doing so demonstrates that the certification program is keeping up to date by paying attention to current information.

4. Psychometric analysis of test forms and test items

"Archaeologic research has shown that more than 1,000 years ago examinations were administered for the licensing of physicians in China. Examinations were available to license physicians in the Middle East a few hundred years later. As Western culture took time to grow out of the Middle Ages, testing also became a means of issuing licenses for physicians. Thus, there is a long history to our current enterprise of testing for competence in the health fields." [21]

In the last 1000 years, the science of measuring knowledge, skill and competency has advanced as fast and as far as any other technical discipline. The specific field of study dedicated to understanding and improving the testing process is called psychometric analysis. Some of the reasons psychometrics emerged are: 1) a desire to improve the reliability of a test as a measuring instrument, 2) being better able to define standards to help advance a profession, and 3) to improve the defensibility of personnel certification bodies and certification processes.

As an example, psychometric analysis improves the accuracy of multiple-choice question formats on high volume screening tests such as university entrance exams. Exams using only multiple-choice questions can be a very inaccurate test of knowledge and therefore unfair to the test candidate. Essay style tests can be very subjective to grade. And other question types such as True/False or Yes/No offer the candidate a 50% successful guess rate. No matter what type of question format was used, testing error exists. [22] Therefore the need for better accuracy and fairness in standardized testing emerged in the 19th century. Eric Haughton criticized terms such as "knows," "understands," or "is able" because they do not delineate learning well. [23] Therefore the testing of knowledge and skill has become a specialized technical discipline with statistical tools provided by psychometric analysis. As described by Marvin Trimm, "*In the US, The American National Standards Institute's ANSI-PCAC-GI-502,* Guidance on Psychometric Requirements for ANSI Accreditation, *was developed to provide guidance about compliance with ISO/IEC 17024 Conformity Assessment - General Requirements for Bodies Operating Certification of Persons to certification bodies interested in ANSI accreditation. It does not prescribe specific statistics that should be computed and displayed. Rather, it emphasizes* ***methodologies, procedures, types of analyses, and how they are applied****, as a basis for the accreditation standards in ISO/IEC 17024"*. [24] Through tools and techniques such as the Angoff method for cut-score workshops, the performance of test forms and items as measuring systems can be refined and improved. [25, 26, 27, 28] For example, the American Society for Nondestructive Testing (ASNT) publishes *"Guidelines for the development of Test Questions for NDT exams"* [29], a very useful primer with best practices for developing test forms and test items. Some psychometric analysis tools are available at no cost on the Internet. [30, 31] Statistics such as the point biserial measure the ability of test items to discriminate equitably between those who know and those who do not know. Psychometric analysis guards against types of errors such as passing and accepting candidates who are ignorant and incompetent and who <u>should not pass</u>, or failing a knowledgeable and competent candidate who <u>should pass</u> the certification test.

There are other reasons to use statistically based tests developed using psychometric analysis. For example, if someone sues a personnel certification body for being denied employment because they are lacking a certification they repeatedly failed, or if an employer denies someone advancement because of a failed certification effort, then the psychometric analysis can be introduced by counsel to help prove the technical soundness of the test. Another very good use of psychometric analysis is to correlate the performance of test forms and test items as they are translated into other languages. This is useful whenever personnel certification bodies address cultural diversity and promote their certification programs around the world. The psychometric analysis of the same test forms and test items that are translated into different languages ensures that multilingual candidates do not have access to a certification test form in one language that is easier to pass than a test form in another language.

The author suspects that a gold mine of information lies within the mountain of test data accumulated by personnel certification bodies over the past several decades. Analysis of the data using the analysis techniques and software tools available today would yield useful information; providing great insight relevant to certification in terms of what people learned and can do, versus what they should have really learned and should know how to do.

5. Preparation and training

The path to higher knowledge through learning proceeds in distinct phases. The first and often most problematic is "not knowing what you don't know". This gap in knowledge is often unseen and totally transparent to people. Once aware of that gap though, then the pursuit of education, training, practice and experience can begin to fill it. However, just knowing some facts and concepts and witnessing demonstrations is not enough; you need to be able to do something with them! Therefore further education and on-the-job experience leads to the correct application of skills and knowledge to useful activities and that is a function of accumulated useful experience over time. As they become embedded in the brain, mastery can be demonstrated at the higher levels of analysis and problem solving in the cognitive, affective and psychomotor domains.

Formal academic education provides a measure of a person's ability to demonstrate knowledge at a certain point in time. Evidence in the form of a college diplomas or university degree is proof that a person was capable of meeting a learning requirement for a subject domain at a certain cognitive level at a given point n time. In short, it means a person knows how to learn. Once gained, keeping knowledge and skills current and up to date is not easy. Huge changes have occurred within education systems in terms of 1) the amount and type information to be delivered, 2) the learning environment it is delivered in, and 3) the delivery methods used, and the student on the receiving end who is doing the learning. Long gone is the era of the one-room schoolhouse where a teacher wrote lessons on a chalk blackboard for the three R's of **R**eading, W**r**iting and A**r**ithmetic to a class with students from grades 1 to 8 in it. Today, those entrusted to educate the people who will be the workforce of tomorrow have different demands and multiple roles to play that are more complex and multi-dimensional. Significant insight to this has been provided by Eric Haughton, who found that teachers and other professionals in education can take advantage of the visual, auditory or kinesthetic "learning channels" to avoid vague descriptions of learning behavior and their outcomes. [23] Researchers have proven that education and training should relate to a person's experiential world, and be designed to use the learning channel that is inherently best suited for them.

In the world of adult education, the four most common sources of failure in adult learning are content overload, content mismatch, memory loss and learning style mismatch. Therefore a training needs analysis must be used for the design and delivery of information to the adult learner. Learning-centered instructional design should follow a process of design and prototyping to meet specific learning parameters. A variety of assessments can be used to identify the context, content, user needs, and work or job parameters. This is followed by evaluating training suitability and a cost-benefit analysis. The result should be education and training that instills the correct knowledge, skills and competencies for targeted training outcomes. No training or certification program can declare itself a success until the student validates that new knowledge and skills were gained and transferred to the job to the benefit of themselves, their employer and their customers. As an example, to ensure that Instructor skills are commensurate with the design and delivery of training, the Canadian Society for Training and Development (CSTD) provides two certification programs for people to demonstrate a thorough understanding of the training profession. The Certified Training and Development Professional (CTDP) and the Certified Training Practitioner (CTP) are based on the competency categories in the Training Competency Architecture, commonly called the 'TCA", a common body of knowledge for the training and development profession. [32]

6. Surveillance and renewal

Initial and ongoing surveillance of people seeking and maintaining certification is necessary to ensure they represent themselves honestly, and remain engaged in their occupational field. Applications should be statistically sampled and the information checked for completeness and accuracy. Subsequent to the initial application and assuming successful certification, ongoing renewal is needed to update the history of employment and work experience. This is needed because periods of significant interruption will erode important skills and competencies through memory leakage and lack of practice. So the renewal should serve to remind people that they need to keep active and engaged in their chosen profession. This best practice links to the next best practice of recertification.

7. Recertification

Academic achievement is proof of what was achieved once, and that becomes part of <u>the past</u>. A best practice for a personnel certification program is to measure skills and competencies that need to be maintained over a continuum of time. It provides proof of current knowledge and skills to be demonstrated <u>today</u>. Recertification will be necessary whenever advances are made or new technology relevant to the certification becomes available. The practice of requiring evidence of continued competence to retain certification is an important part of a well-designed certification program. The requirements should be reasonable and appropriate, such as collecting Continuing Education Units (CEU's) or proving ongoing technical engagement in other ways such as authoring articles, developing curriculum and delivering training, conducting and publishing research, or serving on panels as a SME for a BoK.

The argument for recertification also has to do with the fact that to perform at a consistently high level, people need continuous reinforcement and repetition to drive knowledge into long-term memory, and fluidly connect it with muscle memory and eye-hand coordination. People in every field of human endeavor including the performing arts, professional sports, civil aviation, aerospace, all branches of the military, and many technical occupations rely on the expertise gained through practice and repetition. For example, hockey great Guy Lafleur of the Montreal

Canadiens NHL hockey team was famous for spending extra time skating alone and shooting pucks to learn and improve every nuance of his shooting and passing. The military submits recruits to exhausting simulated combat operations to condition them to automatically and properly respond under the stress of battlefield conditions. And the National Aerospace Agency (NASA) subjects astronauts to hours of rigorous operational drills to ensure they will perform reliably under the stress of working in outer space. An interview with famed musician Ray Charles illustrates the connection between practice time and performing at a high level:

ROBERT SIEGEL: You practice a lot?

RAY CHARLES: Whenever I can. I don't -- I don't practice as much as I would like to, because I'm not around a big piano all the time. But I try to, you know, I try to practice a little bit every day for the most part.

ROBERT SIEGEL: And when you practice, I mean, do you practice the tunes that you'll be playing at the next concerts......?

RAY CHARLES: Oh, no, no, no, no, no, no, no, no, no.....

ROBERT SIEGEL: I guess the answer is no, you're saying?

RAY CHARLES: No. No. I practice things like scales and chords and movement of my hands and things like that, because, I mean, I -- what I'm going to play on stage, I know. What I'm practicing for is to try to improve what I might play, you know. You gotta practice. I mean you gotta keep your fingers loose, you gotta keep your mind active, you know, because what your mind think of -- the question is: what your mind thinks of, can your fingers play it?

ROBERT SIEGEL: Right. [33]

Put in simple terms, practice makes perfect, and repetition is the key to keeping essential skills finely honed.

Authors Repenning and Sterman also provide a compelling reason for maintaining and upgrading competencies and skills: *"The bias towards blaming people rather than the system within which those people are embedded means managers are prone to push their organizations into the capability trap."* [33] They assert that a "capability trap" occurs when organizations choose to work harder using the same old time-worn approaches as have always been used, instead of looking for ways to improve the way work gets done, i.e., work smarter. Beyond that, they also maintain it is necessary to improve the system that manages resources and work as a whole. Personal improvement cannot be ignored and management cannot excuse themselves or their organizations from seeking out best practices in the interest of continuous improvement.

Figures Three, Four and Five illustrate the differences between what Repenning and Sterman describe as the "Physics of Improvement" and the two ways in which improvement is sought and implemented: Work Harder versus Reinvestment / Reinforcement.

Figure Three - *The "Physics" of Improvement*

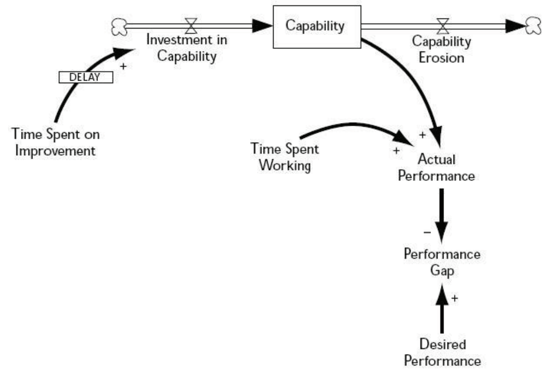

Figure Four - *The Work Harder Balancing Loop*

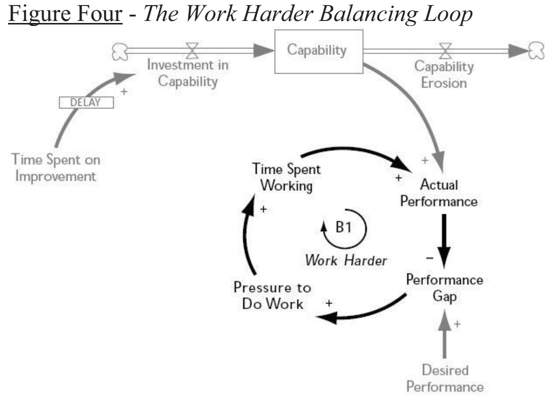

Figure Five – *Reinvestment for Improvement*

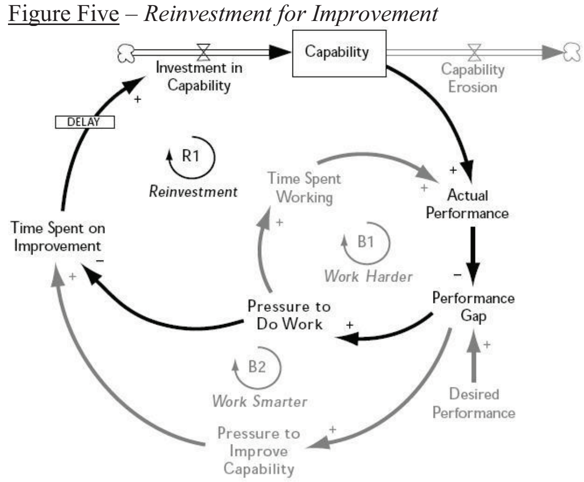

Note that Reinvestment / Reinforcement in Figure Five simultaneously uses the Work Harder, Work Smarter and Reinvestment (improvement) mechanisms to close the gap between desired and actual performance. Put in terms of personnel recertification, working harder using skills and competencies as tested by the original certification requirements is not as good as learning to additionally work smarter by taking advantage of new knowledge or technology. Better still is to also improve at the same time the fundamental process for how something is done. Recertification assures that the original capabilities are maintained, while further enhancing and updating skills through lifelong learning and development. This requires a reinvestment of time and money on an ongoing basis, but as previously noted in the business case for certification, the waste and risk of failure associated with the loss of knowledge and erosion of essential skills should generate an acceptable ROI for personnel recertification.

8. Program accreditation

A personnel certification body inspects the credentials of candidates and through testing, makes decisions about whether they will be certified. To do so in the best way possible, a Quality Management System (QMS) is needed to deliver products, services and information that reflect the "Voice of the Customer" at a level that inspires customer confidence and loyalty. But who decides whether the QMS is adequate, if in fact one is present at all?

Conformity assessment is the practice of determining whether a product, service or system meets the requirements of a particular standard. The International Accreditation Forum is the world association of Conformity Assessment Accreditation Bodies in the fields of management systems, products, services, personnel and other similar programs of conformity assessment. [35] Program accreditation is an excellent way to ensure that a QMS approach is intrinsic to the management of a personnel certification program. Organizations such as the Standards Council of Canada (SCC) accredit conformity assessment bodies in areas such as testing and calibration laboratories, greenhouse gas verification and validation bodies, management systems certification bodies, personnel certification bodies, product and service certification bodies and inspection bodies. [36] In the same way that most countries have a standards developing body, they can also have an accreditation agency. For example, the SCC in Canada, the American National Standards Institute (ANSI) in the United States [37], and the United Kingdom Accreditation Service (UKAS) in Britain [38] provide accreditation to specific standards. Those and other agencies like them provide accreditation in a variety of diverse technical occupations. For example, the Canadian Association for Co-operative Education (CAfCE) develops resources to promote the highest quality of co-op education programs in Canada. It does this through a national forum of professional co-op practitioners; by establishing national standards and promoting the value of post-secondary Co-operative Education; and by delivering opportunities for learning and sharing of best practices. The CAfCE also provides co-op program accreditation services for co-op education programs, and lists over 80 accredited educational institutions. [39]

Accreditation should establish whether the QMS meets the requirement of *"Say what you do, do what you say, prove it and then improve it."* If it does, then the QMS will contribute to the long-term sustainability of the certification program and the customers using the certification. As an example, Appendix One contains a form that could be used to evaluate a personnel certification program against the requirements of ISO standard 17024.

Summary

The background relating to personnel certification has been reviewed, along with some best practices for developing and maintaining a high performing personnel certification process. It should be obvious that education and training, along with the science of measuring knowledge and testing competency, is now much more sophisticated than it used to be. In the occupational areas where certification is offered and used, it is up to business leaders and decision-makers to be aware of the best practices for personnel certification programs, and much more importantly, to be willing to use them to maintain and improve personnel certification schemes.

When all is said and done, a best practices approach is applicable to just about anything worth doing. Pursuing an approach based on best practices is a test of our determination to learn to do the right things, and to do them well.

Author Information:
Larry Cote CET, CLS, CMRP
Managing Director
Canadian Institute for NDE (CINDE)
135 Fennell Avenue West
Hamilton, ON L8N 3T2
Canada

ph (905) 387-1655 ext. 225
fax (905) 574-6080
l.cote@cinde.ca
http://www.cinde.ca
http://events.cinde.ca

References

1. Prensky, M., *Digital Natives, Digital Immigrants - Part One*, On the Horizon, MCB University Press, Volume 9 No. 5, October 2001
2. Prensky, M., *Digital Natives, Digital Immigrants - Part Two*, On the Horizon, MCB University Press, Volume 9 No. 6, December 2001
3. Internet dictionary website: http://www.thefreedictionary.com/certification
4. Funk & Wagnalls Standard Desk Dictionary, Deluxe Edition (1982), Lippincott & Crowell Publishers, USA
5. Standards Council of Canada website: http://www.scc.ca/en/programs/personnel_cert/index.shtml
6. Durling C., *Credentialing Concepts*, National Organization for Competency Assurance (NOCA) website: http://www.noca.org/portals/0/CredentialingConcepts.pdf
7. Taylor, W.F. "*Shop Management"* (1911) Harper and Bros. Publishers, New York, NY, p. 101
8. Society of Tribologists & Lubrication Engineers (STLE) Certification website: http://www.stle.org/certifications/cls/default.aspx?
9. Fine, W. T. *"Mathematical evaluations for controlling hazards*." (1971) Journal of Safety Research, 3, 157-166
10. Kletz, T. "*What Went Wrong? 4th Edition"* (1999) Gulf Professional Publishing, Houston, TX
11. Perrow, C. *"Normal Accidents, Living with High Risk Technologies"* (1999) Princeton University Press, NJ
12. Society of Maintenance & Reliability Professionals website: http://www.smrp.org/SMRP_certification/index.htm
13. Interprovincial Standards Red Seal website: http://www.red-seal.ca/Site/index_e.shtml
14. Reliability Engineer Certification website: http://www.asq.org/certification/reliability-engineer/bok.html
15. Bloom, B.S., Krathwohl, D.R. (1956) "*Taxonomy of educational objectives: The classification of educational goals, by a committee of college and university examiners. Handbook 1: Cognitive domain." Longmans,* New York, NY
16. Forehand, M., (2005). *Bloom's taxonomy: Original and revised.* Website: http://www.coe.uga.edu/epltt/bloom.htm.
17. Conformity Assessment Committee (CASCO) website: http://www.iso.org/iso/iso_technical_committee.html?commid=54998
18. International Standards Organization (ISO) (2003) *International benchmark for personnel certification schemes* News 2003 Reference 847
19. Society of Automotive Engineers (SAE) Standard JA1011 for Reliability-Centered Maintenance (RCM)
20. Society of Automotive Engineers (SAE) Standard JA1012 for Reliability-Centered Maintenance (RCM)
21. Early, L.A, *Writing Test Questions: Part III* Journal of Diagnostic Medical Sonography.1987; 3: 194-196
22. Osterlind, S. J.,(2001) *Constructing Test items: Multiple Choice, Constructed Response, Performance, and other formats*, Kluwer Academic Publishers 2nd edition, The Netherlands, pp. 11-13
23. Haughton, E. C. (1980). *Practicing practices: Learning by activity.* Journal of Precision Teaching, 1(3), 3-20.
24.
25. Trimm, M., *The Use of Psychometrics in NDT Certification Programs*, 5th International Conference on Certification and Standardization in NDT - Lecture 24
26. Early, L. A., *Human Factors: How to Measure Competency in a Valid and Reliable Way, Materials Evaluation,* Vol. 57, No. 4, April 1999, pp. 444-445.
27. Glasch K. J., *Human Reliability in Nondestructive Evaluation*, Materials Evaluation, Vol. 45, No. 8, August 1987, pp. 907–908, 910–912, 932.
28. Tiratira, N.L, (2009) *Cut Off Scores: The Basic Angoff Method And the Item Response Theory Method,* International Journal of Educational and Psychological Assessment 2009; Vol. 1(1)
29. Ricker, K. L., *Setting Cut Scores: Critical Review of Angoff and Modified-Angoff Methods*, Centre for Research in Applied Measurement and Evaluation, University of Alberta Edmonton, Alberta, Canada
30. Early, L. A., Wheeler, George C. 2005, *Guide for Developing NDT Certification Examinations, Columbus Ohio*, The American Society for Nondestructive Testing, Inc.
31. Item analysis website: http://www.hr-360.com/cgi-local/ItemAnalysis.cgi
32. Test form analysis website: http://people.jmu.edu/meyerjp/resources.asp
33. Canadian Society for Training and Development (CSTD) website: http://www.cstd.ca/ProfessionalDevelopment/Certification/tabid/231/Default.aspx
34. Binder, C. (2003) *Removing the Ceiling on Performance* Precision Teaching Conference, Columbus, OH citing the Interview on National Public Radio Celebrating Ray Charles 50 years in recording September 23, 1997 http://www.npr.org/
35. Repenning, N. P., Sterman, J.D., (2001) *Nobody Ever Gets Credit for Fixing Problems that Never Happen, Creating and Sustaining Process Improvement.* California Management Review, 43(4),77.
36. International Accreditation Forum website: http://www.iaf.nu/
37. Standards Council of Canada (SCC) website: http://www.scc.ca/en/programs/personnel_cert/index.shtml
38. American National Standards Institute (ANSI) website: https://www.ansica.org/wwwversion2/outside/Default.asp
39. United Kingdom Accreditation Services (UKAS) website: http://www.ukas.com/default.asp
40. Canadian Association for Co-operative Education website: http://www.cafce.ca/pages/home.php

APPENDIX

Table One – Personnel Certification Program Evaluation Form (based on ISO Standard 17024)

Section 4 – Requirements for Certification Bodies

4.1 Certification Body Requirements	Overall Assessment	Recommendations
4.1.1 *Fair and equitable policy and procedures for all candidates.*	☐ Fully meets standard ☐ Only partially meets standard ☐ Does not meet standard	
4.1.2 *Defined policy and procedures for granting, maintaining, renewing expanding, reducing scope, suspending and withdrawing of certification*	☐ Fully meets standard ☐ Partially meets standard ☐ Does not meet standard	
4.1.3 *Certification body confines requirements, evaluation and decision on certification to matters relating to scope of the desired certification.*	☐ Fully meets standard ☐ Partially meets standard ☐ Does not meet standard	

4.2 Organizational Structure Requirements	Overall Assessment	Recommendations
4.2.1 *Structured to give confidence to interested parties in its competence, impartiality and integrity.*	☐ Fully meets standard ☐ Partially meets standard ☐ Does not meet standard	
4.2.2 *Documented structure to safeguard impartiality, with provisions to assure impartiality of operations.*	☐ Fully meets standard ☐ Partially meets standard ☐ Does not meet standard	
4.2.3 *Appointment of a scheme committee(s) for the development and maintenance of the certification scheme.*	☐ Fully meets standard ☐ Partially meets standard ☐ Does not meet standard	
4.2.4 *Certification body requirements regarding financial resources, confidentiality, objectivity and impartiality*	☐ Fully meets standard ☐ Partially meets standard ☐ Does not meet standard	
4.2.5 *Certification body shall not offer training or aid others, with demonstration of how training is independent of evaluation.*	☐ Fully meets standard ☐ Partially meets standard ☐ Does not meet standard	
4.2.6 *Certification body policies and procedures for the resolution of appeals and complaints.*	☐ Fully meets standard ☐ Partially meets standard ☐ Does not meet standard	

4.2 Organizational Structure Requirements	Overall Assessment	Recommendations
4.2.7 *Education, training, technical knowledge and experience of certification body personnel, including contracts.*	☐ Fully meets standard ☐ Partially meets standard ☐ Does not meet standard	

4.3 Development & Maintenance Requirements	Overall Assessment	Recommendations
4.3.1 *Definition of the methods and mechanisms to be used to evaluate competence of candidates.*	☐ Fully meets standard ☐ Only partially meets standard ☐ Does not meet standard	
4.3.2 *Review and validation of changes by scheme committee members for any change in requirements for certification*	☐ Fully meets standard ☐ Only partially meets standard ☐ Does not meet standard	
4.3.3 *Notice to certified persons of any change in requirements for certification.*	☐ Fully meets standard ☐ Partially meets standard ☐ Does not meet standard	
4.3.4 *Criteria for competence defined by certification body against ISO 17024 and other relevant documents as developed by experts and endorsed by the scheme committee.*	☐ Fully meets standard ☐ Partially meets standard ☐ Does not meet standard	
4.3.5 *Certification not restricted on grounds of undue financial or other limiting condition.*	☐ Fully meets standard ☐ Partially meets standard ☐ Does not meet standard	
4.3.6 *Evaluation of the methods for examination of candidates for reliability, with annual review.*	☐ Fully meets standard ☐ Partially meets standard ☐ Does not meet standard	

4.4 Management System requirements	Overall Assessment	Recommendations
4.4.1 *Management of the certification body is documented and covers all aspects to ensure effective application of the standard.*	☐ Fully meets standard ☐ Only partially meets standard ☐ Does not meet standard	
4.4.2 *Establishment and implementation of a management system that is understood at levels of the organization.*	☐ Fully meets standard ☐ Partially meets standard ☐ Does not meet standard	

4.4 Management System requirements	Overall Assessment	Recommendations
4.4.3 *Document control, audit and management review systems are in place.*	☐ Fully meets standard ☐ Partially meets standard ☐ Does not meet standard	

4.5 Subcontracting requirements	Overall Assessment	Recommendations
4.5.1 *Development and documentation of agreement(s) with subcontractors.*	☐ Fully meets standard ☐ Only partially meets standard ☐ Does not meet standard	
4.5.2 Certification body responsibility for assessing subcontracted work per documented procedures.	☐ Fully meets standard ☐ Partially meets standard ☐ Does not meet standard	

4.6 Records requirements	Overall Assessment	Recommendations
4.6.1 *Certification body to maintain a record system for certificant status, forms, evaluation, surveillance and compliance to regulations.*	☐ Fully meets standard ☐ Only partially meets standard ☐ Does not meet standard	
4.6.2 *Records identification, management and disposal.*	☐ Fully meets standard ☐ Partially meets standard ☐ Does not meet standard	

4.7 Confidentiality requirements	Overall Assessment	Recommendations
4.7 *Certification body to maintain confidentiality of Information obtained.*	☐ Fully meets standard ☐ Only partially meets standard ☐ Does not meet standard	

4.8 Security requirements	Overall Assessment	Recommendations
4.8 *Security of exams maintained by certification body and subcontractors in a secure environment to maintain confidentiality.*	☐ Fully meets standard ☐ Only partially meets standard ☐ Does not meet standard	

Section 5 – Requirements for Persons employed or Contracted by certification body

5.1 Personnel requirements	Overall Assessment	Recommendations
5.1.1 *Certification process defines the personnel competence requirement.*	☐ Fully meets standard ☐ Only partially meets standard ☐ Does not meet standard	
5.1.2 *Certification body personnel commitment to the rules and independence from commercial interests.*	☐ Fully meets standard ☐ Only partially meets standard ☐ Does not meet standard	
5.1.3 *Certification body documents experience, education, technical expertise, duties and responsibilities of personnel.*	☐ Fully meets standard ☐ Only partially meets standard ☐ Does not meet standard	
5.1.4 *Certification body maintains documentation on the relevant qualifications of personnel.*	☐ Fully meets standard ☐ Only partially meets standard ☐ Does not meet standard	

5.2 Examiner requirements	Overall Assessment	Recommendations
5.2.1 *Requirements of Examiners based on applicable competence standards.*	☐ Fully meets standard ☐ Only partially meets standard ☐ Does not meet standard	
5.2.2 *Recorded measures to ensure Examiner conflict of Interest does not compromise certification process.*	☐ Fully meets standard ☐ Only partially meets standard ☐ Does not meet standard	

Section 6 – Certification Process

6.1 Application requirements	Overall Assessment	Recommendations
6.1.1 *Description of certification process.*	☐ Fully meets standard ☐ Only partially meets standard ☐ Does not meet standard	
6.1.2 *Application for individuals seeking certification.*	☐ Fully meets standard ☐ Only partially meets standard ☐ Does not meet standard	

6.2 Evaluation requirements	Overall Assessment	Recommendations
6.2.1 *Application review for ability to meet requirements*	☐ Fully meets standard ☐ Only partially meets standard ☐ Does not meet standard	
6.2.2 *Competence examined by written, oral, practical, observational or other means*	☐ Fully meets standard ☐ Only partially meets standard ☐ Does not meet standard	
6.2.3 *Examination structure covers scheme objectively and systematically.*	☐ Fully meets standard ☐ Only partially meets standard ☐ Does not meet standard	
6.2.4 *Reporting procedures to document performance and results.*	☐ Fully meets standard ☐ Only partially meets standard ☐ Does not meet standard	

6.3 Decision on Certification requirements	Overall Assessment	Recommendations
6.3.1 Certification decision not awarded by anyone involved in the examination or training of candidates.	☐ Fully meets standard ☐ Only partially meets standard ☐ Does not meet standard	
6.3.2 *Certificate awarded for sole ownership.*	☐ Fully meets standard ☐ Only partially meets standard ☐ Does not meet standard	
6.3.3 *Certificate information to meet minimum requirements.*	☐ Fully meets standard ☐ Only partially meets standard ☐ Does not meet standard	

6.4 Surveillance requirements	Overall Assessment	Recommendations

6.4 Surveillance requirements	Overall Assessment	Recommendations
6.4.1 *Proactive surveillance process used to monitor compliance with provisions.*	☐ **Fully meets standard** ☐ **Only partially meets standard** ☐ **Does not meet standard**	
6.4.2 *Procedures and conditions in place for maintenance of certification according to the scheme.*	☐ **Fully meets standard** ☐ **Only partially meets standard** ☐ **Does not meet standard**	

6.5 Recertification requirements	Overall Assessment	Recommendations
6.5.1 *Certification body defines recertification requirements according to the competence standard.*	☐ **Fully meets standard** ☐ **Only partially meets standard** ☐ **Does not meet standard**	
6.5.2 *Procedures and conditions for recertification include frequency and content as endorsed by the scheme committee.*	☐ **Fully meets standard** ☐ **Only partially meets standard** ☐ **Does not meet standard**	

6.6 Use of certificates and logos / marks requirements	Overall Assessment	Recommendations
6.6.1 *Certification body provides certification mark or logo and documents conditions for use.*	☐ **Fully meets standard** ☐ **Only partially meets standard** ☐ **Does not meet standard**	
6.6.2 *Certification body requires certified persons to sign an agreement to comply with certification scheme and provisions for use.*	☐ **Fully meets standard** ☐ **Only partially meets standard** ☐ **Does not meet standard**	
6.6.3 *Certification body applies corrective measures for nappropriate or misleading use of certification logos or marks.*	☐ **Fully meets standard** ☐ **Only partially meets standard** ☐ **Does not meet standard**	

Informative Aspects for the development and maintenance of a personnel certification scheme

A.1 Certification schemes for persons should only be established in response to specific government requirements (i.e. protection of the public) or a demonstrated market need / desire. (i.e. credibility, confidence and improvement of the profession)

A.2 The certification body or organization proposing the certification scheme should consult the interested parties on the following:

a) a description of the field for which the persons will be certified;

b) a description of the qualification/competence requirements, evaluation requirements and procedures, including those for surveillance and recertification;

c) the degree of support for the scheme by the interested parties and evidence of their acceptance of the contents of the scheme;

d) which organization should be responsible for the development of the proposed scheme.

A.3 A job / practice analysis should be conducted periodically (at least every 5 years) to produce or confirm the following:

a) a description of the target candidate population and a statement of purpose or intended outcome for certification;

b) a list of the important and critical tasks performed by competent people working in the profession;

c) a list of the certification requirements, including the rationale and evaluation mechanism(s) selected for each requirement.

d) a specification for the construction of the examination(s), where a formal oral or written examination forms part of the evaluation process. Including content outline., types) of questions being posed, cognitive level(s) of the questions, number of questions for each subject, time length of the examination, method for establishing the acceptance level of the mark, and methods9) for marking;

e) a specification for the construction of the examination(s), where a formal oral or written examination forms part of the evaluation process. Including content outline., type9s) of questions being posed, cognitive level(s) of the questions, number of questions for each subject, time length of the examination, method for establishing the acceptance level of the mark, and methods for marking.

A.4 All mechanisms should be prepared by persons who are thoroughly familiar with the certification profession and the relevant subject matter, and are skilled at preparing such mechanisms.

A.5 All examinations should conform to the examination specification, ensure a uniform application, and be free from bias.

A.6 The certification body should define the controls for rotation of examination or revision in order to maintain their objectivity and confidentiality.

Quality Assurance in NDT

Kris Krishnamoorthy, P. Eng
Atomic Energy of Canada Ltd

Abstract:

The importance of Nondestructive Testing (NDT) as a Quality Control/ Quality Assurance tool in the industrial domain cannot be over-emphasized. With the rapid advancement in research and technology, the NDT field is becoming larger and more sophisticated day by day. Innovative research in materials science and digital technology is paving the way for more and more new methods in NDT technology.

Although the NDT technology has improved over the years, the basic 'human factor' underlying the success of the NDT field remains the same. There are two major factors that influence the 'Quality Assurance in NDT'. First, knowledgeable and skilled NDT Operators are the most important factor in assuring the reliable test results. Second, the Management oversight of the NDT operations plays a major role in assuring the overall quality of NDT.

Management responsibilities include the implementation of a Quality Management System (QMS) that focuses on the NDT operations and apply all the elements of Quality Assurance relevant to NDT.

Whether the NDT operations are performed in-house or by a contractor, periodic Management Self-assessments should include the following question: How can the Management assess and improve the 'Quality Assurance in NDT'?

This paper attempts to answer the above question. Some practical examples are provided to illustrate the potential quality incidents that could lead to costly failures, and the role of NDT Operator and the Management in preventing such quality incidents. Also, some guidelines are provided on how the Management can apply the elements of Quality Assurance to NDT in order to assess and improve the 'Quality Assurance in NDT'.

Introduction

Nondestructive testing (NDT) plays a vital role in assuring the quality and reliability of several critical products whose integrity is of paramount importance for safety. As an inspection, condition monitoring and diagnostic tool in a variety of applications, NDT plays a key role in the safety of our lives. Billions of parts in the manufacturing, power generation and transportation industries throughout the world are being inspected on a daily basis using one or more NDT methods. Many potential accidents are avoided due to the timely detection and elimination of the defects in materials and products through careful application of the principles of 'Quality Assurance in NDT'.

Most of us agree that Quality and Safety go hand in hand. In other words, a quality product is a safe product. In this context, quality is defined as 'freedom from defects'. There is a considerable risk associated with the inspection of the pressure boundary structures, systems and components. However, the importance of NDT is often not realized until serious accidents occur that lead to personal injury and/or economic losses. A single major accident in the field could seriously damage the reputation of the organization responsible for the product and/or testing service. On the other hand, undesirable quality incidents in the manufacturing plants or research laboratories could also lead to costly rework and delayed shipments.

"Quality Assurance in NDT" means all those planned and systematic actions needed to provide adequate confidence to the customers, regulators and other stake holders that the NDT operations were performed and documented in accordance with the specified requirements.

There are two major factors that influence 'Quality Assurance in NDT'- the qualified NDT personnel who perform the tests, and the Management oversight on NDT operations.

The purpose of this Paper is to review the key elements of Quality Assurance (QA) relevant to NDT and emphasize the role of the Management in implementing a Quality Management System (QMS) that focuses on NDT. It is beyond the scope of this Paper to discuss the technical details of the essential variables that affect the reliability of NDT.

The Role of the NDT Operator in Quality Assurance

Despite the automation of several NDT techniques, NDT technology today is very much operator dependant. There is no doubt that the reliability of the test results depends on the experience, knowledge and skill of the NDT Operator. The testing environment, accessibility and other site conditions during the test have major influence on the operator performance. Therefore, the 'human factor' plays a major role in the reliability of NDT. From this point of view, it is possible that a critical defect might be missed even by an experienced and skilled NDT operator. On the other hand, the root cause of a component failure could be traced to the inadequate NDT technique applied, poor sensitivity of the test setup or incorrect procedure employed during the test, which are operator dependent. Also, there are several important essential variables that affect the test results. For example, the test sensitivity and resolution are the most important parameters, which depend on the capability of the equipment, selection of the appropriate techniques, calibration standards, surface preparation and the procedure employed. Such factors can be controlled by a qualified NDT Operator to the best of his ability by applying the correct techniques and following the approved procedures. Hence, NDT Operator is taken into consideration while determining the Probability of Detection (POD) during the qualification of the Ultrasonic Testing (UT) examination system.

Thus the NDT Operator plays a key role in the reliability of the test results. It is the responsibility of the qualified NDT Operator to follow the Code of Ethics and apply his/her technical knowledge and skills to ensure the best results possible out of the tests.

The Role of the Management in Quality Assurance

'Quality Assurance in NDT' depends not only on the qualified NDT Operators, but also on the Management who is responsible for execution of the NDT operations. Quite often, the apparent causes of the field failures or quality incidents related to NDT could be attributed to the weakness in the Quality Management System (QMS) of the organization responsible for the production and/or testing of the product. Sometimes, quality incidents of potential risk may go unnoticed by the Management in the manufacturing plants or research laboratories.

To illustrate the above point, consider the following practical examples.

A) The Radiographic Testing (RT) crew completed radiography on the welder qualification test specimen in a **Piping Fabrication Facility.** However, the radiographs were rejected due to poor density, although the exposure time and technique were correct. The production was delayed due to the repetition of radiography on the test specimen.

- ***Reason***: It was discovered that the processing chemicals had passed the shelf-life for sometime. It could also be the result of under-developed films due to the weak chemicals which were not replenished on time. *There was no inventory checklist maintained in the lab for the chemicals (and their shelf-life), nor was a logbook of films processed in the dark room.*

B) Three process tanks were supplied by a contractor to a **Waste Management Facility** sometime ago. They were held back from commissioning, as the NDT reports and radiographs could not be located in the history dockets. The supplier of the tanks is no longer in business. As a result, radiography was repeated on the tanks which led to significant cost overruns and delayed the commissioning schedules.

- ***Reason***: The source inspection was not performed when the tanks were released from the supplier. *There was a communication gap between the Quality and Purchasing departments. Also, there was no system established for records management concerning NDT reports.*

C) A radiography job in the **NDT Laboratory** was temporarily suspended by the supervisor due a safety issue. One of the technicians discovered that the guide tube of the Ir-192 exposure device was found damaged. There was a nick at the center of the guide tube caused by a sharp object, which could have led to a serious accident resulting in over exposure of the personnel, if the source was stuck while operating the exposure device. Luckily, a serious radiation accident was avoided by quickly replacing the damaged guide tube.

- ***Reason****:* The source of the damage to the guide tube was not known, *as there were no daily safety checklists maintained in the lab.*

D) During the review of the assembly drawings in a **Gas Turbine Assembly Plant**, the Quality Engineer discovered that unrealistic inspection requirements were specified in the engineering drawings. The field welds between the burners and their supports had to be inspected by the Liquid Penetrant Inspection (LPI) method. However, LPI was not practical due to the limited space available between the burner and the support. The production was stopped until the Design Engineer evaluated the alternatives and revised the drawing requirement from LPI to Visual Inspection (VT) at 10X magnification. As a result, the overall engine assembly schedule was delayed.

- ***Reason*:** Critical inspection requirements were not reviewed earlier at the design stage. *Concurrent engineering did not involve the Quality Engineer knowledgeable in NDT.*

The above quality incidents are only a sample of several possibilities in the field or in-house testing, which could have serious impact on the organization with respect to the quality and safety. Further, each of the above quality incidents indicates some weakness in the Quality Management System (QMS) of the respective organizations.

The chances of serious accidents or costly rework could be prevented by the Management through pro-active planning and execution of the NDT operations. Also, it is the responsibility of the Management to provide adequate training, equipment and environment to minimize the operator's contribution to the quality incidents.

The importance of "Human Factor" in NDT

The 'Human Factor' plays a key role in the quality and reliability of NDT. If the testing environment is not adequate, even the most skilled operator may not produce the satisfactory test results. Often, the NDT personnel are exposed to the harsh environmental conditions and undue stress during the field testing. For example, inadequate access to the field welds, incomplete surface preparation, poor lighting conditions, unexpected equipment failures and other noise factors at site affect the operator performance. Also, prolonged testing under inadequate site conditions contribute to the stress and fatigue of the NDT personnel leading to less than satisfactory performance. The Management should be wary of such human factors while planning and execution of the NDT operations and necessary precautions should be taken ensure that the NDT personnel are free from extraneous pressure and unnecessary administrative burdens while carrying out the tests. Motivation of the NDT personnel during the critical field testing is very important for reliable test results.

Key elements of Quality Assurance in NDT

1. Personnel Qualification & Certification

Personnel Qualification and Certification is one of the basic requirements of 'Quality Assurance in NDT'. It is the responsibility of the Management to ensure that the NDT personnel are adequately qualified and certified prior to engaging them on the job.

A knowledgeable and skilled NDT Operator is no doubt the most important factor in assuring the quality and reliability of NDT. Although rapid advancement in digital technology has led to automation of several NDT techniques in the manufacturing plants and research laboratories, much of the field NDT today is still operator dependent. Since each NDT method has certain advantages and limitations, proper application of the techniques and interpretation of the results require the qualified NDT personnel in the respective methods. The regulatory codes and standards require that only NDT personnel qualified and certified to certain level in the applicable NDT method shall perform the testing. Further, in the case of Radiographic Testing (RT), it is a regulatory requirement that only certified Exposure Device Operators (EDO) shall handle the exposure devices.

Minimum training and qualifying NDT experience are among the pre-requisites for initial certification of the NDT personnel. Although there is no minimum education specified for the qualification of NDT personnel, there are three distinct competency levels of qualification (Levels 1, 2 and 3) that are graded based on the knowledge, skill and experience in the specific NDT method. Each level of qualification has certain defined responsibilities. This is an important point to be kept in view by the Management, while planning and deploying the resources for various projects involving NDT.

There are two types of certification schemes available for NDT personnel. The first type is based on the employer certification after in-house training and qualification of the NDT personnel. The second is based on independent central certification. It is beyond the scope of this Paper to discuss the merits or demerits of such certification schemes. There has been considerable skepticism in the employer based certification schemes for qualification and certification of NDT personnel, such as the SNT-TC-1A Recommended Practice [1], which is prevalent in the United States. However, the rest of the world is keen on the central certification schemes based on independent evaluations. From the Quality Assurance point of view, independency and consistency of the certification process are the two important properties of the certification schemes that are recognized internationally. Therefore, it is expected that ISO 9712-2005 will soon become the common international standard for NDT personnel qualifications and certifications throughout the world. In a global economy, NDT personnel certified to this standard will be transparent to the national boundaries and meet the demands of the NDT projects around the world. Fortunately, Canada has already adopted this international standard as a Canadian National Standard, CAN/CGSB-48.9712-2006 [2].

2. Training and Motivation

As noted above, minimum training and qualifying NDT experience are the two basic pre-requisites for certification of NDT personnel. It is very important to ensure that the NDT personnel are knowledgeable, competent and fully trained at the appropriate level prior to certification. In order to assure the reliability of the test results, it is important that the NDT Operator should be able to clearly distinguish a 'defect' from a 'discontinuity' in a test specimen.

However, it is not just enough to engage the certified personnel and expect everything to be run smoothly in NDT operations. It is extremely important to motivate the NDT personnel by recognizing their efforts and rewarding the good results. Management should recognize that skilled and experienced NDT Operators are an asset to the organization. A motivated NDT Operator can save the organization from huge economic losses by timely detection and reporting of the defects through diligence and careful examination. Treating the NDT personnel with respect and dignity would go a long way in motivating them. Management should strive to retain the experienced and skilled NDT personnel and find the means to keep them fully engaged during the gap between the projects. Re-training through periodic refresher courses is often required to keep current with the new technology. This will be a real motivation for some NDT personnel with the thirst for knowledge. On the other hand, continuous observation and coaching by the direct supervisors and On-the-Job Training (OJT) would increase the confidence and sharpen the skills of the new NDT Operators. Other management techniques for training and motivation of employees include encouragement to exchange ideas and sharing of lessons learned among the staff. Creating a learning environment and providing the opportunities for improvement are some of the measures the Management can take to motive the NDT personnel.

3. Facilities and Equipment

Adequate facilities and equipment are necessary for achieving optimum results in NDT. For example, in the case of Radiographic Testing (RT), maintenance of the dark room facility, processing chemicals, storage of films are among the major factors that influence the quality of the radiographs. The hard work of the NDT personnel in the plant or field could be wasted, if the radiographs turn out to be too dark or too light due to inadequate processing of films. Similarly, the test facilities for the liquid penetrant tanks and magnetic particle wet bench should be designed such that handling and storage of the test specimen as well as the consumables result in high quality and productivity.

Management oversight on the regular maintenance of the equipment is very important to assure the quality and reliability of the inspection results. For example, regular quality control checks for penetrant bath contamination and sensitivity should be performed as per the established test procedures and the results should be recorded. Similarly, Ultrasonic and Eddy current instruments, probes and calibration blocks should be regularly cleaned and maintained.

In the global economy, ever growing competition in the manufacturing and service sectors has resulted in the NDT facilities and equipment being automated and modernized to meet the demands of the customers. Automation is the key to success in the automotive and aerospace industries where billions of parts are being produced and inspected on a daily basis. New automated inspection techniques in several NDT methods, combined with the computerized vision systems, are contributing significantly to the high productivity and quality in several industries. Not only the automation improves the efficiency of inspection, it also helps in increasing the reliability of NDT by minimizing the 'human errors' such as operator fatigue in routine operations. However, automation also means due care and regular maintenance of the facilities and equipment. Therefore, creating and maintaining the suitable and adequate facilities and test equipment are among the key Management responsibilities to maintain the 'Quality Assurance in NDT'.

4. Procedures

The purpose of the NDT procedure is to ensure that the inspection process is applied consistently so that expected results can be achieved with confidence. This is one of the basic principles of Quality Assurance. Each NDT method has certain essential variables which should be captured in the written procedure and monitored during the implementation. NDT procedures should be reviewed and approved by the authorized and qualified personnel in the respective NDT methods. Any change in the essential variable is a cause for revision of the procedure.

Typically, an NDT procedure should identify the scope and limitations of the test, personnel qualification requirements, health and safety precautions, surface preparation requirements, equipment and calibration standards to be used, applicable techniques, reference codes and standards, acceptance criteria and the records to be maintained. The acceptance criteria should be clearly specified in the procedure, or a reference should be made to the relevant sections of the codes and standards, or the customer specifications. It is very important that the NDT procedure provides clear instructions on the acceptance criteria and the reporting levels of indications found.

Also, the NDT procedures should provide clear instructions on the pre-and post cleaning of the test specimen. For example, certain critical nuclear applications require that the penetrant materials should be free of chemical impurities due to halogens and phosphorous. Therefore, the NDT procedure should clearly identify the type of penetrant materials permitted and the quality control measures required to verify such materials. Similarly, instructions for demagnetization following the magnetic particle inspection on rotating equipment should be clearly specified in the NDT procedure. Although the qualified NDT personnel should be aware of such requirements, a precautionary checklist in the NDT procedure would help to assure that these steps are promptly completed.

Also, it is important to distinguish an ‘NDT procedure’ from an ‘NDT technique’. Usually, one NDT procedure may be applied to several products within the scope of the project. However, an NDT technique is written to a specific application. Therefore, it is important to ensure that the NDT techniques are promptly reviewed and approved by the authorized and qualified personnel in the respective NDT method prior to implementation.

From the Quality Assurance point of view, it is important to ensure that only approved procedures and techniques are employed by the NDT personnel, and such documents are maintained and controlled by the Management.

5. Codes and Standards

NDT personnel who interpret and evaluate the test results should be familiar with the codes and standards relevant to the products being inspected, in addition to the customer specifications. Certain codes and standards have specific requirements on the qualification of the NDT personnel, test sensitivity and acceptance criteria. Evaluation of the indications against the accept/reject criteria is an important step in the NDT operations, where the experience and skill of the NDT personnel are often put to test. Knowledge of the product as well as the applicable codes and standards would help the NDT personnel in the evaluation of the indications without ambiguity. In certain critical applications, ‘acceptance criteria’ could play a major role during the third party inspection and investigation into the root cause analysis of major failures. Therefore, NDT personnel should be aware of the customer requirements as well as the applicable regulatory codes and standards. Management should be aware of the occupational health and safety rules and the regulations pertaining to radiation protection, handling of nuclear substances and exposure devices. In this respect, maintenance of a library of codes and standards relevant to various NDT methods will benefit the NDT personnel as well as the Management. Pressure boundary codes and standards, Radiation Protection regulations, and other NDT books and magazines should be accessible to the NDT personnel. Periodic in-house testing on the NDT knowledge including codes and standards could help increase the confidence of the NDT personnel. Such tests could also be conducted as a part of internal or external training for certification/re-certification.

6. Calibration Standards

NDT is a non-destructive method of flaw detection and material characterization based on a reference standard. In other words, NDT is essentially a comparative study between an 'unknown' test specimen and a 'known' reference standard or calibration standard. The test system must be calibrated against the reference standard so that proper test sensitivity and resolution are established. Such calibration data is essential for the meaningful evaluation of the indications in any NDT method. The NDT procedures should clearly identify the type of calibration standards to be used and the process for calibration of the equipment. The NDT techniques should clearly identify the specific calibration standards to be used during the test set-up, in order to assure the sensitivity and resolution of the test results. For some applications, special calibration blocks should be prepared to suit the geometry (thickness and curvature range) of the test specimen. The material properties and geometry of calibration standards should closely match the characteristics of the test specimen. Error corrections to compensate for the differences between the specimen and the calibration standard should be considered in the evaluation of the indications. This is an essential variable which has a major impact on the reliability of the test results. Therefore, the NDT reports should invariably identify the calibration standard, against which the test system has been calibrated. Management oversight on the identification and maintenance of the calibration standards is very important for 'Quality Assurance in NDT'.

7. Design Quality Assurance

One of the reasons products fail in service could be attributed to the design errors in the product development, particularly with respect to the specification of Inspection and Testing. As illustrated in example 'D' above, engineering drawings and technical specifications should be reviewed by qualified NDT personnel for proper selection of the NDT methods and techniques. Sometimes, design engineers tend to over specify the NDT requirements, without realizing the practicality of the inspection or limitations of the NDT methods. In general, Radiographic Testing (RT) is usually preferred to Ultrasonic Testing (UT), even though the latter method is more economical and provides similar results in detecting the volumetric flaws. Similarly, Liquid Penetrant Inspection (LPI) is a common method applied for detecting the surface flaws, even though the wet magnetic particle method would save the inspection time significantly on ferrous materials. Some products with complex geometry (size and shape) may require more than one NDT method for thorough inspection. On the other hand, a full inspection using any NDT method would be impossible or uneconomical on certain applications due to the geometry or accessibility of the test specimen. Therefore, a thorough knowledge of the capabilities and limitations of the NDT methods is important for the design engineers who specify the inspection requirements. Design quality assurance in NDT should consider such factors as accessibility, field conditions, safety issues, sample size, and other regulatory requirements. Management should ensure that concurrent engineering teams include qualified NDT personnel. Also, at the procurement stage, technical specifications and purchase orders should be reviewed by the qualified NDT personnel to ensure that proper NDT requirements are specified. Subsequently, NDT procedures and techniques submitted by the suppliers should be reviewed and approved by the authorized and qualified NDT personnel.

Selection of the appropriate sample size for NDT is another challenge often faced by the design engineers. In order to demonstrate the capability and reliability of the NDT test systems, design engineers should consider conducting Repeatability and Reproducibility (R&R) studies involving multiple operators. Site conditions should be kept in mind while analyzing the test results based on ideal laboratory conditions. Management should consider a risk assessment prior to embarking on critical projects involving NDT.

8. Work Management

Work management typically includes resourcing, planning and scheduling of activities. It also includes safety management and emergency planning. Health and Safety of the operators are an integral part of the planning for NDT. Also, public safety should be considered, particularly in the case of field radiography. Preparations for RT should consider ALARA (As Low As Reasonably Achievable) principles. When planning for field radiography, management should ensure that the ALARA principles (Time/Distance/Shielding) are followed by the NDT personnel. If necessary, the radiographers should be rotated to avoid over exposure to radiation. Although it is not a mandatory requirement in Canada per the Nuclear Substances and Radiation Devices Regulations [3], it is prudent on the part of the Management to engage a minimum of two persons (a qualified NDT Operator and a helper) while performing the field radiography. However, the Regulations require that only certified Exposure Device Operators (EDO) shall be permitted to operate the exposure devices.

In addition to the resourcing and scheduling, work management for NDT operations should also consider the following:

- Site clearance for carrying out the NDT operations
- Emergency support for unplanned events, including fire hazards
- Radiation safety and ALARA measures in the case of field radiography
- Preparations for field inspection, such as scaffolding, and adequate lighting
- Surface preparations for the specimen to be tested
- WHIMS training for handling hazardous chemicals and MSDS catalogues
- Surface preparations and post cleaning of the test specimens
- Disposal of hazardous chemicals, and
- Housekeeping

It is the joint responsibility of the qualified NDT personnel and the Management to ensure the personnel safety and the safety of the equipment while performing the operations. In addition, Management should consider all human factors that could affect the performance of the NDT personnel, either in-house or at site. Management assistance in facilitating and coordination of the pre-inspection activities would remove the administrative burden on the part of the NDT personnel so that they can focus on the technical aspects of the NDT operations. Management should also ensure that necessary daily log books and safety checklists are completed and maintained regularly at all NDT facilities and sites. Obviously, the management representative should be an individual knowledgeable in the NDT methods and the associated health and safety regulations.

Housekeeping is an important factor for the safety as well as efficiency of operations. Housekeeping includes identification and labeling of the equipment and accessories, calibration blocks, penetrant materials and their batch certificates, inventory controls for chemicals and other NDT consumables such as the radiographic films.

Tables 1 and 2 show some typical examples of daily log books and safety checklists.

Table 1
Daily Log book for NDT activities

Form#:________________ **Rev# ______**

Project #	Operator Name	NDT method / Technique#	Time Start	Time Finish	Equipment Used (Model / Serial#)	Safety Checks Completed - Form# (Y/N)	Remarks

Reviewed by: __________ Sign / Date: ______________

Such Daily Log books should be maintained for each NDT laboratory, production facility or Field work, where NDT is routinely carried out.

Table 2
NDT Safety Checklist – Field RT (Ir-192)

Form#: ____________ **Rev#: ______**

Safety check	Yes/ No	Operator Name	Sign/ Date	Remarks
1. Check the Exposure device and determine if this is the correct source you need for the job.				
2. Check the locking mechanism for cleanliness and good condition.				
3. Check for any physical damage to the control cable, cranking mechanism or the source guide tube.				
4. Does the cranking mechanism move freely throughout its length of travel?				
5. Check the surface leak from the camera. Is there any abnormal radiation from the surface of camera?				
6. Do you have the personnel protective equipment (PPE) in good working condition? Is the pocket dosimeter in working condition and calibrated?				
7. Do you have a calibrated survey meter in working condition?				
8. Have you placed the Radiation warning boards in all directions where public access is possible?				
9. Do you have adequate number of films loaded and ready to go?				
10. Do you have all other accessories (lead numbers, penetrameters (IQI), shielding etc.				
11. Did you cordon off the distance correctly to control radiation dose for the public?				
12. Did you receive the site clearance before proceeding for RT.				

Similar checklists should be designed for each facility and each NDT method.

If designed well, the work management tools could assist the Management in identifying the potential safety and performance issues in NDT operations. Logbooks and safety checklists are very important objective evidences for investigation of major events of significance. They could assist in the trend analysis of the quality incidents and identify the areas of concern so that appropriate corrective actions can be implemented. To explore the opportunities for improvement in the work management, NDT personnel assigned for each job should be encouraged to explain the reasons why the job took more time than planned and what safety issues or other difficulties were faced during the testing (such as accessibility, poor surface preparation and other noise factors). Regular review of the logbooks by the Management could identify the performance issues, and necessary corrective actions can be taken to improve the overall efficiency of NDT operations. Therefore, work management is a powerful tool in the maintenance of 'Quality Assurance in NDT'.

9. Records Management

Records management is a basic element of the Quality Management System (QMS). Without the clean and legible reports, the NDT operations do not have much value to the customers. Therefore, quality of the NDT reports should be verified for information to be 'complete', 'correct' and 'consistent' prior to submitting to the customers. Most of the pressure boundary Codes and Standards require that NDT reports and radiographs shall be kept as permanent records, including the qualification of the NDT personnel. Therefore, qualification and certification records of all NDT personnel, their level of qualification together with the training history should be saved in a database, and be readily retrievable when required. Also, the annual vision test records of the NDT operators should be saved together with the personnel qualification records. As a minimum, all NDT reports should contain proper identification of the project (customer) and the test specimen inspected, location of the test specimen, equipment used, procedure and technique employed and the personnel qualification. NDT procedures and revisions should have been approved by the authorized and qualified personnel in the respective NDT methods.

In the case of Radiographic Testing (RT), there are certain mandatory records that must be maintained by the Licensee. Reference should be made to the Nuclear Substances and Radiation Devices Regulation (SOR/2000-207) [3]. Clauses 36 of the Regulations describes the records to be kept and retained with respect to the 'Nuclear substances', and Clause 37 describes the records to be maintained with respect to the 'Exposure devices'.

It is the responsibility of the Management to ensure that all NDT records are completed and secured for a minimum period as required by the customers and regulatory standards for future reference.

10. Audits & Assessments

Internal audits and Self-assessments are the two important management tools through which the adequacy and effectiveness of the Quality Management System (QMS) can be evaluated. Unfortunately, the true contribution of the NDT operations to the overall effectiveness of the QMS may not be realized by the Management, since the scope of the internal quality audits and self-assessments often fail to include NDT. Failure to include NDT in the audit plans or self-assessment plans would mean the missed opportunity for improvement in a key area of Quality Assurance. Sometimes it is too late to realize the potential problems and risks involved in the NDT operations and implement necessary preventing actions.

Therefore, it is very important for the Management to plan and execute independent audits and assessments periodically on NDT operations in order to improve the 'Quality Assurance in NDT'. At the minimum, ongoing assessments in the form of coaching and performance monitoring by the supervisor would assist the Management in maintaining a competent NDT team. Periodic review of the work management records should also help the Management in the assessment of the quality as well as the performance issues associated with the NDT operations.

Table 3 below shows a typical Self-assessment Checklist for NDT. Such checklists should be developed to suit the individual organizations.

Table 3
Typical Management Self-assessment Checklist for NDT

Area of Concern	**Description**
Potential Risks	Type of Projects / Customer specific requirements/ Cost and Delivery schedules for NDT operations / Health & Safety issues.
	Additional precautions to be taken for inspection of safety related / pressure boundary work including regulatory oversight.
Capabilities	NDT Methods, particularly Field RT vs. In-house inspection
	NDT Equipment capabilities to meet the customer requirements, including the dark room facilities for RT.
	Adequate Facilities qualified for various NDT methods.
	Adequate number of qualified and certified NDT personnel
	Adequate training facilities for NDT personnel
	Adequate calibration standards to meet the requirements of codes and standards and customer specifications.
Performance Issues	Accidents or quality incidents related to NDT at site or in the plant
	Customer complaints or rejects/ Failure rates due to operator errors
	Customer feedback on the quality of NDT reports
Compliance Issues	Incidents due to non-compliance of NDT procedures?
	Issues due to the use of un-approved procedures or NDT techniques
	Non-compliance to the codes and standards, or customer specifications
Work Management Issues	Overall efficiency of NDT operations – productivity, overtime, cost etc.
	Inventory controls
	Management of Field operations (NDT)
	Housekeeping

Summary

There are two major factors that influence the 'Quality Assurance in NDT'– Qualified NDT personnel who perform the tests and the Management oversight on NDT operations. Knowledgeable and skilled NDT Operators are very important for reliable test results in NDT. On the other hand, Management oversight in planning, coordination and execution of the NDT operations would help in achieving the quality and safety objectives. If managed properly, the right application of NDT by the qualified NDT personnel under adequate testing conditions can prevent accidents and save the organization from huge economic losses.

The overall quality and effectiveness in NDT depend on the Management involvement in pro-active planning and execution of the NDT operations. Management should consider implementing a Quality Management System (QMS) that focuses on NDT, and apply all the elements of Quality Assurance relevant to the NDT operations. Qualification and Certification of NDT personnel, Training and Motivation, Facilities and equipment, Codes and standards, Calibration standards, Procedures, Design Quality Assurance, Work management, Records management are among the key elements that should be monitored by the Management in addition to the periodic Audits and Self-assessments on NDT operations. Work management is a powerful tool in identifying potential quality, safety and performance issues associated with the NDT operations. Management oversight should include periodic audits and self-assessments covering the NDT operations in order to assess and improve the 'Quality Assurance in NDT'.

Acknowledgements

The author is grateful to the AECL Technical Conference Review Panel (TCRP) for the timely review and approval of this Paper.

References

[1] SNT-TC-1A (2006) – *Recommended Practice: Personnel Qualification and Certification in Nondestructive testing,*

[2] CAN/ CGSB-48.9712-2006 (ISO 9712:2005) – *Non-destructive testing – Qualification and Certification of personnel*

[3] SOR/2000-207 – *Nuclear Substances and Radiation Devices Regulations (Nuclear Safety Control Act Canada)*

Dedication

This paper is dedicated to the thousands of NDT operators around the world whose Diligence, Integrity and Dedication (DID) to the NDT profession keep our lives safe.

The Case for Inspection Qualification

John Baron
Program Manager, CANDU Inspection Qualification Bureau
CANDU Owners Group

ABSTRACT

Nondestructive examination (NDE) is the primary means of measuring the structural integrity of industrial pressure boundary components. In many jurisdictions such inspections are mandatory either through regulatory requirements or, for example, in order to obtain insurance coverage. The mandatory requirements universally require personnel who conduct the inspection to be certified – either through a central system such as ISO 9712 or an employer based system such as that used in the USA and elsewhere.

It was generally accepted that the results of these inspections represented the 'truth' however, in the late 1970s – early 1980 three significant situations clearly challenged the 'truth' assumption. All these situations were in the nuclear power industry – exactly where correct results are of paramount importance.

This issue was first addressed in the USA under the auspices of ASME Section XI, the nuclear in-service inspection section of the ASME Boiler and Pressure Vessel Code and subsequently in Europe under the European Network for Inspection and Qualification (ENIQ). Although the approaches are quite different both have the common goal of confirming, to the extent possible, that inspection procedures and personnel are capable of detecting and sizing flaws of the defined degradation mechanism when applied to specific components.

Although the nuclear industry is the leader in terms of demanding post base-level certification demonstration of inspection performance, the lessons learned are clearly applicable to other industries where NDE plays a key rôle in assuring the safety of the public, workers and the environment - as well as protecting economic interests.

The paper discusses the merits of the various inspection qualification systems currently in use or in development.

The Case for Inspection Qualification

John Baron
Program Manager, CANDU Inspection Qualification Bureau
CANDU Owners Group

Introduction

Nondestructive Evaluation (NDE) processes, when applied to industrial plant, may be viewed as being in the same category as quality control processes. The most prevalent application of NDE is to provide information on the structural integrity of materials, components and systems. The basic rôle is to confirm, or otherwise, that the particular component is within the bounds of the design parameters or is fit for service projected out to the next inspection cycle.

Should the inspection process return an incorrect result, for example a false call (a flaw where one does not exist) or a missed call (failure to detect a flaw) then potential threat to economic considerations is likely to ensue. In the extreme case, an incorrect NDE result could threaten public, worker or environmental safety.

Traditionally, it was assumed that NDE results were correct. However, in the late 1970s – early 1980s, three situations arose that caused this assumption to be challenged. All of these were in the nuclear industry.

In 1978, under the auspices of the OECD, a round robin exercise was conducted using two nuclear reactor pressure vessel segments containing nozzles with defects implanted in the vessel to nozzle welds[1]. The mandatory use of ASME Section V ultrasonic procedures was found to be inadequate for the particular inspections.

In 1982, the UK regulatory body initiated the Defect Detection Trials[2] (DDT) prior to approval of Sizewell B nuclear plant. This was somewhat similar to the PISC I exercise but without the restriction on inspection method/technique. These trials confirmed that representative flaws could be detected and sized successfully albeit using non-traditional techniques.

Circa 1982, soon after being given a clean bill of health by experienced NDE personnel, the austenitic piping of a US nuclear plant began to exhibit leakage due to a stress corrosion cracking mechanism.

The conclusion reached was that it is prudent to ensure, to the extent possible, that NDE processes, that is the procedure, equipment and personnel, are capable of detecting and sizing flaws due to experienced or postulated degradation mechanisms in the specific components to be inspected.

---

[1] PISC 1 (Plate Inspection Steering Committee that evolved into the Program for the Inspection of Reactor Steel Components) S. Crutzen et al, CEC, EUR 6371EN, Vols 1-6, OECD, CSNI report 48

[2] "CEGB Inspection of Plates 1 and 2 in the UKAEA Defect Detection Trials", K.J Bowker et al, Brit. Journal of NDT, 1983, vol 25, No 5.

This requirement is clearly outside of the realm of the general qualification/certification process such as that defined in ISO 9712.

The Development of Inspection Qualification Systems

It is clear that a central certification system such as ISO 9712 cannot test candidates on every conceivable combination of component and inspection technique. Thus, ISO 9712 contains a clause that places the responsibility on the employer of NDE personnel to ensure that individual inspectors are competent to perform the assigned tasks.

Under other certification schemes, such as that developed by the American Society for NDT, even the basic evaluation of competence is the employer's responsibility.

In either case, confirmation of capability, or competence, is in-house and may be considered somewhat a conflict of interest with respect to generally accepted practices of quality control and quality assurance.

In 1989, ASME Section XI, the nuclear in-service inspection code, introduced the mandatory Appendix VIII, "Performance Demonstration for Ultrasonic Examination Systems". This code details the required testing of personnel when using ultrasonic inspection procedures on nuclear plant components. Although Appendix VIII does not specifically define who or what organization is to conduct the performance demonstration testing, it is strongly implied that this is an independent body.

In the mid-1990s, the European Network for Inspection and Qualification (ENIQ) developed an inspection qualification scheme. Although the goal is completely consistent with that of Appendix VIII, that is, to ensure that the inspection process returns the correct results, the methodology is quite different. If Appendix VIII may be considered to define what has to be achieved in detail, ENIQ concentrates more on the method of independently ensuring NDE process performance.

ASME Section XI, Appendix VIII is part of the mandatory nuclear NDT code. In about 2002, ASME Section V, the "NDT Section", introduced Article 14 which is an inspection qualification code aimed at non-nuclear applications. This appeared in the 2004 Addenda. Article 14 maybe viewed as a hybrid between ASME XI App. VIII and ENIQ.

ASME Section XI, Appendix VIII

As written, this Appendix is aimed at the inspection personnel performing in-service inspection of nuclear plant components. It pertains only to ultrasonic testing of specified nuclear plant components. It defines applicable degradation mechanisms, (fatigue or stress corrosion cracking) and the sizes of cracks the inspector is to be tested on. The code defines pass-failure criteria for both detection and sizing.

For example, Supplement 2 – "Qualification Requirements for Wrought Austenitic Piping Welds" provides a table of the number of flawed and non-flawed grading units to be used in the personnel qualification process, and defines the allowable 'missed' and 'false' call rates. An illustration of this is that, if ten flawed grading units are used, a detection rate of at least eight is required. This is coupled with twenty non-flawed grading units and no more than three false calls. (The distribution of implanted flaw sizes is also defined)

There are also requirements on flaw sizing that are based on root mean square error. (for length sizing, RMS error not to exceed 0.75 inches, for depth sizing RMS error not to exceed 0.125 inches).

Early in the implementation of Appendix VIII, it was realized that even a ‘good’ inspector would have difficulty should the procedure be inadequate. Thus EPRI Performance Demonstration Initiative (PDI), the accepted independent qualification body in the USA, implemented a process to pre-qualify inspection procedures.

ASME Section XI, Appendix VIII works well because its application is limited to a single NDE method, (ultrasonics), a single application, (in-service inspection of light water reactor system components constructed according to ASME code) and limited degradation mechanisms of concern.

European Network for Inspection and Qualification (ENIQ)

The approach taken under ENIQ is quite different from that of ASME Section XI. However, both processes have the common aim of improving the reliability of inspection results. ENIQ is neither a code nor a standard but rather a methodology that may be applied within any industry, any inspection method, any component and any degradation mechanism. The methodology is supported by a number of ‘recommended practice’ – or guideline – documents that are freely available[3].

The base of the ENIQ methodology is a document which we in Canada term the Inspection Specification (other jurisdictions refer to this as the Technical Specification or Technical Requirements or Input Requirements).

The Inspection Specification is an engineering document – not an NDE document. It describes the component or group of components, including the material and configuration. It notes environmental issues such as hazardous conditions and access to the component(s), experienced and postulated degradation mechanisms and what the inspection must achieve. In general, it provides all the information an Inspection Service Provider (ISP) needs to design and operate the inspection system.

The Inspection Specification is the document that gives the ENIQ methodology its flexibility. In comparison, ASME Section XI, App. VIII provides a prescriptive definition of requirement which, by its very nature, must be limited in its scope and application. However, generating the Inspection Specification can require significant engineering analysis effort, often requiring fracture mechanics analysis. Another issue is the challenge of specifying NDE performance in quantitive terms that can be used by the ISP and the Inspection Qualification Body (IQB). For example, it is tempting to state the inspection must be ‘highly reliable’ but, although this term presents a worthy sentiment, it is subjective and cannot be used to evaluate the performance of either the Inspection Procedure or personnel unless all parties agree how ‘highly reliable’ is to be interpreted.

Once the Inspection Specification is in place it is the rôle of the ISP to develop the Inspection Procedure that meets the requirements of the Inspection Specification.

[3] http://safelife.jrc.ec.europa.eu/eniq

A second document that the ISP must produce is the Technical Justification (TJ). This document sets out the evidence that the procedure meets the requirements of the Inspection Specification.

The Inspection Procedure and its associated TJ are then put before an individual or team to independently confirm, or otherwise, that the Inspection Procedure does, in fact, meet the stated requirements. This is largely based on the degree to which the evidence in the TJ is considered convincing. In some cases, the independent review team may ask for further evidence.

The CANDU Inspection Qualification Bureau (CIQB), established by seven CANDU nuclear utilities, considers the independent review to be non-adversarial. Dialogue and collaboration between the review team and the ISP is expected and encouraged as the aim is to achieve a robust Inspection Procedure – not just a pass or fail decision.

Following qualification of the procedure, the Inspection Qualification Body (IQB) may engage in testing of inspection personnel using representative physical test pieces or recorded data. The approach taken by the CIQB is to review training programs, test pieces and written test questions but leave the post-training tests to the ISP. However, the CIQB maintains the right to observe and audit actual training situations.

ASME Section V, Article 14

ASME Section V, Article 14,"NDE System Qualification" was designed to provide an inspection qualification process within the ASME Boiler and Pressure Vessel code but outside of the nuclear arena. It is more recent that its ASME Section XI counterpart and also more recent than ENIQ. However, the approach is more consistent with that of ENIQ rather than ASME Section XI. For example, there is a requirement for a TJ.

The issue of the Inspection Specification is circumvented by stating that is expected that it originates elsewhere, typically the "referencing code section" (see "T-1410 Scope").

The document defines three level of rigour, with accompanying levels of Probability of Detection (PoD), allowable missed call and false call rates and statistical confidence levels. At the high level of rigour, with high confidence (>90%) and high PoD (>90%), the number of test pieces quickly ramps up to several hundred.

As with ENIQ, specifying and justifying the appropriate quantitive qualification requirements in engineering terms is a challenge but outside of Article 14.

Other Qualification Schemes

Other qualification schemes exist but these tend to be very specific in their application. One example is the EPRI Steam Generator Inspection Guidelines which, as the name suggests, is specific to in-service inspection of nuclear steam generator tubing (heat exchangers).

Recently, there has been a drive to produce an international standard on inspection qualification under ISO, ISO 11774. The draft ISO document circumvents the issue of an engineering approach to defining inspection performance requirements but placing this requirement on “Industrial Sector Committees”. (There seems little onus on the owner of the plant.) Some of the elements under this draft standard are prescriptive, for example, requalification period and the number of personnel test pieces while other elements are open-ended, e.g. the basis and from where the required inspection performance is developed.

However, regardless of the specifics or the inspection qualification processes, all have the common objective of ensuring, to the extent possible, that NDE processes (procedures, equipment and personnel) are capable and competent of producing the correct results.

Are Inspection Qualification Systems Justified?

The exercises of the late 70s and early 80s did challenge the assumption that NDE results could be trusted blindly. We have moved forward twenty or thirty years and there is no doubt that NDE instrumentation has become more complex, new techniques and methods have been developed and our reliance on NDE results has significantly increased. It is not unusual for a large industrial plant to have a down-time cost of more than $1million per day. Thus, even if we set aside the issue of public, worker and environmental safety, an unscheduled forced outage due to an incorrect NDE result is a daunting proposition.

A further reality is that, under a base-level NDE personnel certification system such as ISO 9712, it is clearly impossible to cover all techniques and adaptations of the modern NDE methods and it is certainly impossible to design all-encompassing practical tests of personnel. Further, some would argue that the implementation of certification standards such as ISO 9712 have not kept pace with the realities of industrial use of current NDE technologies.

Without Inspection Qualification, this leaves us totally reliant on the Inspection Service Provider to train and qualify inspection personnel not only in the specifically assigned task but also the nuances of modern day electronic instruments, often employing remotely operated or automated manipulators. This does not infer that such training by ISPs is inadequate but it most certainly lacks the independence consistent with quality assurance/control protocols. In Canada, we accept our national certification body as an independent and impartial organization to test and qualify/certify inspection personnel. If we accept this process at the general base levels, why should we not demand it at levels beyond ISO 9712? Even the pre-amble to ISO 9710 recognizes that qualification beyond Levels 1,2 and 3 are the responsibility of the ISP.

For the plant owner, (here I include aircraft, oil and gas pipelines etc.) independent qualification of inspection procedures and personnel is simply a sound idea in terms of due diligence, protecting assets and safety of the public, workers and the environment.

A further consideration is the use of statistical methods to determine the risk levels of industrial plant systems and components. Here, I define risk as the likelihood of failure multiplied by the consequence of failure. Thus, inspection processes may be deployed to mitigate risk by providing information that may be used to reduce the likelihood of system/component failure. This suggests concentration on areas where the level of risk is highest (but not completely abandon lower risk areas). If we are to use NDE in this mode, it is necessary to have knowledge of the effectiveness of inspection thereby providing the extent to which probability of failure is reduced. This is typically expressed in terms of probability of detection (PoD) , false call probability (FCP) and confidence level (CL). This knowledge must be derived from objective evaluation of the inspection process – Inspection Qualification.

Independence of Inspection Qualification

All of the above considerations are a mirror of quality control applied to normal engineering processes. Just as quality control would be overseen by an independent entity, so should be Inspection Qualification.

Further, almost all industrial NDE practice is governed by a regulatory authority, an insurance company, or through contractual agreements. The most effective and practical manner of satisfying these agencies or customer performance requirements is by an independent, arm's length organization. This is now the norm in all nuclear jurisdictions and there is growing interest in developing similar organizations and processes wherever NDE represents a critical information system.

It is not good enough to declare inspection results as being correct, they must be shown to be so.

Summary

There are a number of inspection qualification schemes in existence. Some are general in scope whereas others are either industry specific, e.g. nuclear industry, or largely deployed within a single industrial sector. There are different approaches but all schemes have the objective of confirming the effectiveness of the inspection process (equipment, procedure and personnel) that is, to the extent possible, ensure NDE results are correct.

The most widely used protocols (ASME Section XI, Appendix VIII and ENIQ) require an independent assessment of inspection performance. This is the most effective manner in which third parties such as regulatory and insurance agencies may be satisfied that the application of NDE processes will return the correct result. Additionally, it is of benefit to the NDE customer to have an independent body attesting to the effectiveness, that is the quality of inspection delivery.

The global nuclear industry is at the forefront of independent inspection qualification but, given the high cost of downtime of industrial plant and the increasingly complex technology associated with NDE, it is forecast that this process will be developed in other industries where NDE is a critical information system with respect to structural integrity.

Biography – Dr John Baron

John has well in excess of thirty years experience in the nuclear industry involving NDE. He is a graduate of the University of Manchester and the University of Waterloo. His current rôle in the CANDU Owners Group is that of Program Manager, CANDU Inspection Qualification Bureau (CIQB). Currently John is a member of the ENIQ Steering Committee and a member of the founding committee of the international working group of inspection qualification bodies.

In addition to his rôle in COG, John is the proprietor of 'Folville Consulting' and is an eddy current instructor for CINDE.

Author index

Index

É. du CAO

à la frontière des connaissances
at the cutting edge of knowledge

ISBN 978-2-9809199-2-3